A psychologist probes the roots of unconscious bias p. 1418

Changing sexual harassment policy p. 1430

A resilient superconductor p. 1454

Science

$15
27 MARCH 2020

AAAS

COVID-19

How the coronavirus targets human cells p. 1444

AAAS
ANNUAL MEETING

2020 AAAS Student E-poster Competition Winners

The 2020 AAAS Student E-poster Competition took place at the AAAS Annual Meeting in Seattle, WA on February 13-16. The competition recognizes the individual efforts of students who are actively working toward an undergraduate, graduate or doctoral-level degree. The winners' presentations displayed originality and understanding that set them apart from their peers. Eligible students can apply to present at the 2021 E-poster Competition in Phoenix, AZ starting in July 2020.

BIOCHEMISTRY AND MOLECULAR BIOLOGY

Graduate Student First Place: Luyi Cheng, Northwestern University

Graduate Student Honorable Mention: Edna Chiang, University of Wisconsin-Madison

Undergraduate First Place: Mario Rodriguez, University of California, Irvine

Undergraduate Honorable Mention: Tal Sneh, Arizona State University

BRAIN AND BEHAVIOR

Graduate Student Winner: Ellen Brennan, University of Michigan

Graduate Student Honorable Mention: Jessica Y. Chen, University of Michigan

Undergraduate First Place: Angelique Cortez, University of California, Irvine

Undergraduate Honorable Mention: Olumide Fagboyegun, University of Maryland, Baltimore County

CELL BIOLOGY

Graduate Student First Place: Melody Tan, Rice University

Graduate Student Honorable Mention: Nathan Sunada, University of Hawaii at Hilo

Undergraduate First Place: Cuauhtemoc Ramirez, University of California, Irvine

Undergraduate Honorable Mention: Kelsey N. Salcido, University of California, Irvine

DEVELOPMENTAL BIOLOGY GENETICS AND IMMUNOLOGY

Graduate Student First Place: Caryn Carson, Washington University in St. Louis

Graduate Student Honorable Mention: Luz Milbeth Cumba Garcia, Mayo Clinic Graduate School of Biomedical Sciences

Undergraduate First Place: Isaryhia Maya Rodriguez, University of California, Irvine

Undergraduate Honorable Mention: Ieeshiah Otarola, University of California, Irvine

ENVIRONMENT AND ECOLOGY

Graduate Student First Place: Jean P. González-Crespo, University of Puerto Rico, Mayagüez

Graduate Student Honorable Mention: Michelle Elise Spicer, University of Pittsburgh

Undergraduate First Place: Patrick Robichaud, Washington State University

Undergraduate Honorable Mention: Ananth Udupa, Arizona State University

MEDICINE AND PUBLIC HEALTH

Graduate Student First Place: Catherine Steffel, University of Wisconsin, Madison

Graduate Student Honorable Mention: Alexandra G.Hammerberg, University of Washington

Undergraduate First Place: Jack Shanahan, University of California, Irvine

Undergraduate Honorable Mention: Anit Tyagi, University of Denver

PHYSICAL SCIENCES

Graduate Student First Place: Rachael Knoblauch, University of Maryland, Baltimore and The Institute of Fluorescence

Graduate Student Honorable Mention: Soochan Kim, Sungkyunkwan University

Undergraduate First Place: Joe C. Gonzales, University of California, Irvine

Undergraduate Honorable Mention: Amelia Cuomo, The University of North Carolina at Chapel Hill

SCIENCE AND SOCIETY

Graduate Student First Place: Taran Lichtenberger, Northwestern University and Chicago Botanic Garden

Graduate Student Honorable Mention: Suyog Padgaonkar, Northwestern University

Undergraduate First Place: Richa Venkatraman, Arizona State University

Undergraduate Honorable Mention: Madison Frazier, Arizona State University

SOCIAL SCIENCES

Graduate Student First Place: Luis Alexis Rodríguez-Cruz, University of Vermont

Graduate Student Honorable Mention: Theora Tiffney, Arizona State University

Undergraduate First Place: Delaney Bucker, Arizona State University

Undergraduate Honorable Mention: Sheldon Rosa, University of Hawaii—Hilo

TECHNOLOGY, ENGINEERING AND MATH

Graduate Student First Place: Andrés J. Arroyo Colón, University of Puerto Rico, Rio Piedras

Graduate Student Honorable Mention: Brandon Hunter, Duke University

Undergraduate First Place: Daniela Gonzalez, University of California, Irvine

Undergraduate Honorable Mention: Jai Singh Rajput, University of Texas, Dallas

aaas.org/2020-eposter-sessions

CONTENTS

1422 & 1443
Neanderthals see seashells on the sea shore

27 MARCH 2020 • VOLUME 367 • ISSUE 6485

1418

NEWS

IN BRIEF

IN DEPTH

FEATURES

INSIGHTS

PERSPECTIVES

POLICY FORUM

BOOKS *ET AL.*

PHOTOS (FROM TOP): JOSÉ PAULO RUAS; LIPO CHING

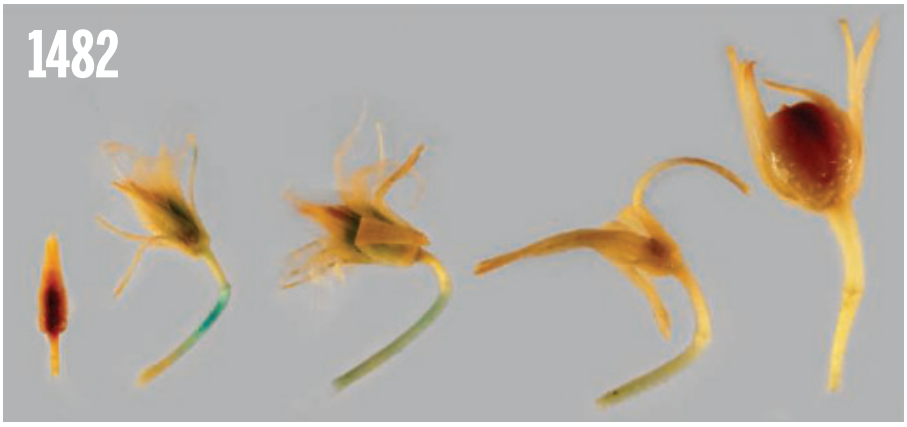

ON THE COVER

The novel coronavirus (SARS-CoV-2; blue) approaches a human cell (pale pink). The viral spike protein (gray) binds to a receptor (ACE2; dark pink) on the cell surface. This allows SARS-CoV-2, the virus responsible for the COVID-19 pandemic, to infect human cells. The structures of the viral spike protein, the full-length ACE2, and the complex of ACE2 with the receptor binding domain of SARS-CoV-2 have been elucidated, providing structural basis for development of antiviral drugs and vaccines. See page 1444 and www.sciencemag.org/coronavirus-research-commentary-and-news.
Illustration: V. Altounian/Science; Data: PDB ID 6VSB (viral spike protein), PDB ID 6M17 (ACE2)

PHOTO: REICHARDT *ET AL.*

SCIENCE (ISSN 0036-8075) is published weekly on Friday, except last week in December, by the American Association for the Advancement of Science, 1200 New York Avenue, NW, Washington, DC 20005. Periodicals mail postage (publication No. 484460) paid at Washington, DC, and additional mailing offices. The title SCIENCE is a registered trademark of the AAAS. Domestic individual membership, including subscription (12 months): $165 ($74 allocated to subscription). Domestic institutional subscription (51 issues): $2148; Foreign postage extra: Air assist delivery: $98. First class, airmail, student, and emeritus rates on request. Canadian rates with GST available upon request, GST #125488122. Publications Mail Agreement Number 1069624. **Printed in the U.S.A.**
Change of address: Allow 4 weeks, giving old and new addresses and 8-digit account number. **Postmaster:** Send change of address to AAAS, P.O. Box 96178, Washington, DC 20090–6178. **Single-copy sales:** $15 each plus shipping and handling available from backissues.sciencemag.org; bulk rate on request. **Authorization to reproduce** material for internal or personal use under circumstances not falling within the fair use provisions of the Copyright Act can be obtained through the Copyright Clearance Center (CCC), www.copyright.com. The identification code for *Science* is 0036-8075. *Science* is indexed in the *Reader's Guide to Periodical Literature* and in several specialized indexes.

EDITORIAL

Underpromise, overdeliver

H. Holden Thorp
Editor-in-Chief, *Science* journals.
hthorp@aaas.org;
@hholdenthorp

The majority of crises that most of us have lived through have not looked to science for immediate answers. In many cases, much of the scientific analysis came after the fact—the effects of climate change on extreme weather events; the causes of nuclear accidents; and the virology of outbreaks that were contained such as severe acute respiratory syndrome (SARS) in 2002–2003 or Middle East respiratory syndrome (MERS) in 2012. Now, science is being asked to provide a rapid solution to a problem that is not completely described.

I am worried that science may end up overpromising on what can be delivered in response to coronavirus disease 2019 (COVID-19). This isn't because I think the scientific community has bad intentions or will purposefully overhype anything, but because of what science can report in real time. It is difficult to share progress with adequate caveats about how long things might take or whether they will work at all. The scientific method is a very deliberate process that has been honed over time: Basic research, which describes the problem, is followed by applied research that builds on that understanding. Now, scientists are trying to do both at the same time. This is not just fixing a plane while it's flying—it's fixing a plane that's flying while its blueprints are still being drawn.

> "...engendering false hope will cause... lasting damage if science overpromises."

On the testing side, polymerase chain reaction (PCR) technology is allowing folks to know quickly whether they are infected with SARS coronavirus 2 (SARS-CoV-2), the cause of COVID-19. However, a negative PCR test result may lead a person to erroneously conclude that they're in the clear, which is a danger to controlling the spread. We urgently need serology tests that show whether someone has had the infection and recovered. And we must be able to identify individuals who have some immunity to SARS-CoV-2 because understanding their biology may contribute to helping the world recover.

When it comes to drug trials, we've now seen the first negative result on the lopinavir-ritonavir combination, which performed no better than placebo. Efforts are underway to identify other possible drugs—remdesivir, novel antivirals, and numerous antibodies. These are exciting possibilities, but also extremely speculative. Political overhyping of such approaches is extremely dangerous—it risks creating false expectations and depleting drugs needed to treat diseases for which they are approved. And it sets science up to overpromise and underdeliver.

As for vaccines, we know so little about SARS-CoV-2. Developing a vaccine could take at least a year and a half—as many experts have suggested—or maybe won't happen at all. Fortunately, a clinical trial for a vaccine is already underway in the United States, but the public must be told that these early vaccines may not work or be safe—that this vaccine is only being tested for safety, not efficacy, at this point.

Scientists involved in COVID-19 research know these caveats. But the general public—who are agonizing over how long this pandemic will last, how it will affect the economy, and whether they and their loved ones will be safe—are looking for hope wherever they can find it. If science can deliver answers, public trust in science could increase substantially (the high point for trust in science in the United States was at the end of World War II). But if the scientific community contributes to building up hope in the fight against COVID-19, but then doesn't deliver, the consequences for science could be dire, especially if politicians continue to amplify the false hope irresponsibly.

When science addressed the HIV/AIDS crisis, it took years of careful virology, drug development, and epidemiology. The global scientific assault on COVID-19 is faster, and as I see the research that comes to *Science* and that appears on preprint servers, I am hopeful that science will deliver on this challenge, too. But I worry that engendering false hope will cause complacency that will deprive us of the time needed to find a lasting solution. And I worry about lasting damage if science overpromises.

Let's underpromise. Let's overdeliver

–H. Holden Thorp

PHOTO: CAMERON DAVIDSON

Published online 23 March 2020; 10.1126/science.abb8492

Science AAAS

Editor-in-Chief Holden Thorp, hthorp@aaas.org

Executive Editor Monica M. Bradford

Editors, Research Valda Vinson, Jake S. Yeston **Editor, Insights** Lisa D. Chong

DEPUTY EDITORS Julia Fahrenkamp-Uppenbrink (UK), Stella M. Hurtley (UK), Phillip D. Szuromi, Sacha Vignieri **SR. EDITORIAL FELLOW** Andrew M. Sugden (UK) **SR. EDITORS** Gemma Alderton (UK), Caroline Ash (UK), Brent Grocholski, Pamela J. Hines, Paula A. Kiberstis, Marc S. Lavine (Canada), Steve Mao, Ian S. Osborne (UK), Beverly A. Purnell, L. Bryan Ray, H. Jesse Smith, Keith T. Smith (UK), Jelena Stajic, Peter Stern (UK), Valerie B. Thompson, Brad Wible, Laura M. Zahn **ASSOCIATE EDITORS** Michael A. Funk, Priscilla N. Kelly, Tage S. Rai, Seth Thomas Scanlon (UK), Yury V. Suleymanov **LETTERS EDITOR** Jennifer Sills **LEAD CONTENT PRODUCTION EDITORS** Harry Jach, Lauren Kmec **CONTENT PRODUCTION EDITORS** Amelia Beyna, Jeffrey E. Cook, Chris Filiatreau, Julia Katris, Nida Masiulis, Suzanne M. White **SR. EDITORIAL COORDINATORS** Carolyn Kyle, Beverly Shields **EDITORIAL COORDINATORS** Aneera Dobbins, Joi S. Granger, Jeffrey Hearn, Lisa Johnson, Maryrose Madrid, Ope Martins, Shannon McMahon, Jerry Richardson, Alana Warnke, Alice Whaley (UK), Anita Wynn **PUBLICATIONS ASSISTANTS** Jeremy Dow, Alexander Kief, Ronmel Navas, Hilary Stewart (UK), Brian White **EXECUTIVE ASSISTANT** Jessica Slater **ASI DIRECTOR, OPERATIONS** Janet Clements (UK) **ASI SR. OFFICE ADMINISTRATOR** Jessica Waldock (UK)

News Editor Tim Appenzeller

NEWS MANAGING EDITOR John Travis **INTERNATIONAL EDITOR** Martin Enserink **DEPUTY NEWS EDITORS** Elizabeth Culotta, Lila Guterman, David Grimm, Eric Hand (Europe), David Malakoff **SR. CORRESPONDENTS** Daniel Clery (UK), Jon Cohen, Jeffrey Mervis, Elizabeth Pennisi **ASSOCIATE EDITORS** Jeffrey Brainard, Catherine Matacic **NEWS REPORTERS** Adrian Cho, Jennifer Couzin-Frankel, Jocelyn Kaiser, Kelly Servick, Robert F. Service, Erik Stokstad, Paul Voosen, Meredith Wadman **INTERNS** Eva Frederick, Rodrigo Perez Ortega **CONTRIBUTING CORRESPONDENTS** Warren Cornwall, Ann Gibbons, Mara Hvistendahl, Sam Kean, Eli Kintisch, Kai Kupferschmidt (Berlin), Andrew Lawler, Mitch Leslie, Eliot Marshall, Virginia Morell, Dennis Normile (Shanghai), Elisabeth Pain (Careers), Charles Piller, Michael Price, Tania Rabesandratana (Barcelona), Emily Underwood, Gretchen Vogel (Berlin), Lizzie Wade (Mexico City) **CAREERS** Donisha Adams, Rachel Bernstein (Editor), Katie Langin (Acting Editor) **COPY EDITORS** Julia Cole (Senior Copy Editor), Cyra Master (Copy Chief) **ADMINISTRATIVE SUPPORT** Meagan Weiland

Creative Director Beth Rakouskas

DESIGN MANAGING EDITOR Marcy Atarod **GRAPHICS MANAGING EDITOR** Alberto Cuadra **PHOTOGRAPHY MANAGING EDITOR** William Douthitt **WEB CONTENT STRATEGY MANAGER** Kara Estelle-Powers **SENIOR DESIGNER** Chrystal Smith **DESIGNER** Christina Aycock **GRAPHICS EDITOR** Nirja Desai **INTERACTIVE GRAPHICS EDITOR** Xing Liu **SENIOR SCIENTIFIC ILLUSTRATORS** Valerie Altounian, Chris Bickel **SCIENTIFIC ILLUSTRATOR** Alice Kitterman **SENIOR GRAPHICS SPECIALISTS** Holly Bishop, Nathalie Cary **SENIOR PHOTO EDITOR** Emily Petersen **PHOTO EDITOR** Kaitlyn Dolan

Chief Executive Officer and Executive Publisher Sudip Parikh

Publisher, Science Family of Journals Bill Moran

DIRECTOR, BUSINESS SYSTEMS AND FINANCIAL ANALYSIS Randy Yi **DIRECTOR, BUSINESS OPERATIONS & ANALYSIS** Eric Knott **DIRECTOR OF ANALYTICS** Enrique Gonzales **MANAGER, BUSINESS OPERATIONS** Jessica Tierney **SENIOR BUSINESS ANALYST** Cory Lipman, Meron Kebede **FINANCIAL ANALYST** Alexander Lee **ADVERTISING SYSTEM ADMINISTRATOR** Tina Burks **SENIOR SALES COORDINATOR** Shirley Young **DIGITAL/PRINT STRATEGY MANAGER** Jason Hillman **QUALITY TECHNICAL MANAGER** Marcus Spiegler **ASSISTANT MANAGER DIGITAL/PRINT** Rebecca Doshi **SENIOR CONTENT SPECIALISTS** Steve Forrester, Jacob Hedrick, Antoinette Hodal, Lori Murphy **DIGITAL PRODUCTION MANAGER** Lisa Stanford **CONTENT SPECIALIST** Kimberley Oster **ADVERTISING PRODUCTION OPERATIONS MANAGER** Deborah Tompkins **DESIGNER, CUSTOM PUBLISHING** Jeremy Huntsinger **SR. TRAFFIC ASSOCIATE** Christine Hall **SPECIAL PROJECTS ASSOCIATE** Sarah Dhere

ASSOCIATE DIRECTOR, BUSINESS DEVELOPMENT Justin Sawyers **GLOBAL MARKETING MANAGER** Allison Pritchard **DIGITAL MARKETING MANAGER** Aimee Aponte **JOURNALS MARKETING MANAGER** Shawana Arnold **MARKETING ASSOCIATES** Tori Velasquez, Mike Romano, Ashley Hylton **DIGITAL MARKETING SPECIALIST** Asleigh Rojanavongse **SENIOR DESIGNER** Kim Huynh

DIRECTOR AND SENIOR EDITOR, CUSTOM PUBLISHING Sean Sanders **ASSISTANT EDITOR, CUSTOM PUBLISHING** Jackie Oberst

DIRECTOR, PRODUCT & PUBLISHING DEVELOPMENT Chris Reid **DIRECTOR, BUSINESS STRATEGY AND PORTFOLIO MANAGEMENT** Sarah Whalen **ASSOCIATE DIRECTOR, PRODUCT MANAGMENT** Kris Bishop **SR. PRODUCT ASSOCIATE** Robert Koepke **DIGITAL PRODUCT STRATEGIST** Michael Hardesty **SPJ ASSOCIATE** Samantha Bruno Fuller

DIRECTOR, INSTITUTIONAL LICENSING Iquo Edim **ASSOCIATE DIRECTOR, RESEARCH & DEVELOPMENT** Elisabeth Leonard **MARKETING MANAGER** Kess Knight **SENIOR INSTITUTIONAL LICENSING MANAGER** Ryan Rexroth **INSTITUTIONAL LICENSING MANAGER** Marco Castellan **MANAGER, AGENT RELATIONS & CUSTOMER SUCCESS** Judy Lillibridge **SENIOR OPERATIONS ANALYST** Lana Guz **FULFILLMENT COORDINATOR** Melody Stringer **SALES COORDINATOR** Josh Haverlock

DIRECTOR, GLOBAL SALES Tracy Holmes **US EAST COAST AND MID WEST SALES** Stephanie O'Connor **US WEST COAST SALES** Lynne Stickrod **US SALES MANAGER, SCIENCE CAREERS** Claudia Paulsen-Young **US SALES REP, SCIENCE CAREERS** Tracy Anderson **ASSOCIATE DIRECTOR, ROW** Roger Goncalves **SALES REP, ROW** Sarah Lelarge **SALES ADMIN ASSISTANT, ROW** Bryony Cousins **DIRECTOR OF GLOBAL COLLABORATION AND ACADEMIC PUBLISHING RELATIONS, ASIA** Xiaoying Chu **ASSOCIATE DIRECTOR, INTERNATIONAL COLLABORATION** Grace Yao **SALES MANAGER** Danny Zhao **MARKETING MANAGER** Kilo Lan **ASCA CORPORATION, JAPAN** Kaoru Sasaki (Tokyo), Miyuki Tani (Osaka) **COLLABORATION/CUSTOM PUBLICATIONS/JAPAN** Adarsh Sandhu

DIRECTOR, COPYRIGHT, LICENSING AND SPECIAL PROJECTS Emilie David **RIGHTS AND LICENSING COORDINATOR** Jessica Adams **RIGHTS AND PERMISSIONS ASSOCIATE** Elizabeth Sandler **CONTRACTS AND LICENSING ASSOCIATE** Lili Catlett

---

MAIN HEADQUARTERS
Science/AAAS
1200 New York Ave. NW
Washington, DC 20005

SCIENCE INTERNATIONAL
Clarendon House
Clarendon Road
Cambridge, CB2 8FH, UK

SCIENCE CHINA
Room 1004, Culture Square
No. 59 Zhongguancun St.
Haidian District, Beijing, 100872

SCIENCE JAPAN
ASCA Corporation
Sibaura TY Bldg. 4F, 1-14-5
Shibaura Minato-ku
Tokyo, 108-0073 Japan

EDITORIAL
science_editors@aaas.org

NEWS
science_news@aaas.org

INFORMATION FOR AUTHORS
sciencemag.org/authors/science-information-authors

REPRINTS AND PERMISSIONS
sciencemag.org/help/reprints-and-permissions

MEDIA CONTACTS
scipak@aaas.org

MULTIMEDIA CONTACTS
SciencePodcast@aaas.org
ScienceVideo@aaas.org

INSTITUTIONAL SALES AND SITE LICENSES
sciencemag.org/librarian

PRODUCT ADVERTISING & CUSTOM PUBLISHING
advertising.sciencemag.org/products-services
science_advertising@aaas.org

CLASSIFIED ADVERTISING
advertising.sciencemag.org/science-careers
advertise@sciencecareers.org

JOB POSTING CUSTOMER SERVICE
employers.sciencecareers.org
support@sciencecareers.org

MEMBERSHIP AND INDIVIDUAL SUBSCRIPTIONS
sciencemag.org/subscriptions

MEMBER BENEFITS
aaas.org/membercentral

AAAS BOARD OF DIRECTORS
CHAIR Steven Chu
PRESIDENT Claire M. Fraser
PRESIDENT-ELECT Susan G. Amara
TREASURER Carolyn N. Ainslie
CHIEF EXECUTIVE OFFICER
Sudip Parikh
BOARD Cynthia M. Beall
Rosina M. Bierbaum
Ann Bostrom
Stephen P.A. Fodor
S. James Gates, Jr.
Laura H. Greene
Kaye Husbands Fealing
Maria M. Klawe
Robert B. Millard
Alondra Nelson
William D. Provine

EDITORIAL

COVID-19 needs a Manhattan Project

Seth Berkley
is the chief executive officer of Gavi, the Vaccine Alliance, in Geneva, Switzerland.
sberkley@gavi.org

There is an unprecedented race to develop a vaccine against severe acute respiratory syndrome coronavirus 2 (SARS-CoV-2). With at least 44 vaccines in early-stage development, what outcome can we expect? Will the first vaccine to cross the finish line be the safest and most effective? Or will it be the most well-funded vaccines that first become available, or perhaps those using vaccine technologies with the fewest regulatory hurdles? The answer could be a vaccine that ticks all these boxes. If we want to maximize the chances for success, however, and have enough doses to end the coronavirus disease 2019 (COVID-19) pandemic, current piecemeal efforts won't be enough. If ever there was a case for a coordinated global vaccine development effort using a "big science" approach, it is now.

There is a strong track record for publicly funded, large-scale scientific endeavors that bring together global expertise and resources toward a common goal. The Manhattan Project brought about nuclear weapons quickly (although with terrible implications for humanity) through an approach that led to countless changes in how scientists from many countries work together. The Human Genome Project and CERN (the European Organization for Nuclear Research) engaged scientists from around the world to drive basic research from their home labs through local and virtual teamwork. Taking this big, coordinated approach to developing a SARS-CoV-2 vaccine will not only potentially save hundreds of thousands of lives, but will also help the world be better prepared for the next pandemic.

"In the race to develop a SARS-CoV-2 vaccine, everyone must win."

An initiative of this scale won't be easy. Extraordinary sharing of information and resources will be critical, including data on the virus, the various vaccine candidates, vaccine adjuvants, cell lines, and manufacturing advances. Allowing different efforts to follow their own leads during the early stages will take advantage of healthy competition that is vital to the scientific endeavor. We must then decide which vaccine candidates warrant further exploration purely on the basis of scientific merit. This will require drawing on work already supported by many government agencies, independent organizations like the Coalition for Epidemic Preparedness Innovations, and pharmaceutical and biotech companies to ensure that no potentially important candidate vaccines are missed. Only then can we start to narrow in on those candidates to be advanced through all clinical trial phases. This shortlist also needs to be based on which candidates can be developed, approved, and manufactured most efficiently.

Trials need to be carried out in parallel, not sequentially, using adaptive trial designs, optimized for speed and tested in different populations—rich and developing countries, from children to the elderly—so that we can ultimately protect everyone. Because the virus is spreading quickly, testing will be needed in communities where we can get answers fast—that means running trials anywhere in the world, not just in preset testing locations. Working with regulators early in the process will increase the likelihood of rapid approvals, and then once approved, a coordinated effort will ensure that sufficient quantities are available to all who need the vaccine, not just to the highest bidder.

All of this will require substantial funding, which is the big ask of big science. Late-stage clinical trials are not cheap, nor is vaccine manufacturing. Although new modular manufacturing methods may speed up the process and cut costs, a single vaccine facility can cost half a billion dollars. Distribution comes at a cost, too. So, to guarantee sufficient production of SARS-CoV-2 vaccines, incentives are needed to engage manufacturers for large-scale capacity. As for dissemination, those organizations with experience in global vaccine distribution, like Gavi, will be at the ready.

Ideally, this effort would be led by a team with a scientific advisory mechanism of the highest quality that could operate under the auspices of the World Health Organization (WHO), for example. But none of this will be possible without political will and a global commitment from leaders of the G7 and G20 countries and multilateral organizations, like the WHO and the World Bank. A pandemic of this magnitude, affecting so many lives, livelihoods, and economies, demands this.

In many ways, COVID-19 is more like the Manhattan Project than other big science efforts, not just because it involves the application of science and not just in terms of scale, but because it is a global security issue. In the race to develop a SARS-CoV-2 vaccine, everyone must win.

–Seth Berkley*

PHOTO: GAVI/TONY NOEL (2018)

*Hear more from the author about a vaccine for SARS-CoV-2 at go.ted.com/sethberkley

Published online 25 March 2020; 10.1126/science.abb8654

NEWS

IN BRIEF

Edited by **Jeffrey Brainard**

Cambodia's Lower Sesan 2 hydroelectric dam, built on a Mekong River tributary and opened in 2018, drew criticism.

BIODIVERSITY

Cambodia halts Mekong dams

In a victory for conservation, the Cambodian government announced on 18 March that it is suspending for 10 years plans to build two hydropower dams on the Mekong River. The move helps preserve a freshwater ecosystem that, after the Amazon, is the world's most biologically diverse. It also supports a vast fishing industry. Cambodia now relies on hydropower for nearly 50% of its electricity, but will turn to coal, natural gas, and solar energy to meet its future power needs. The Mekong begins on the Tibetan Plateau and flows through several countries, including Cambodia and Vietnam, before emptying into the South China Sea. It has been under increasing pressure from development, pollution, and climate change; drought and upstream dams in China have exacerbated recent low water levels in the lower Mekong. Adding to the river system's woes, Laos opened two hydropower dams on the Mekong's main branch in the past 6 months, and Cambodia said it may yet build dams on Mekong tributaries. Still, conservationists praised Cambodia's decision. Maintaining the free flow of the lower Mekong is "the best decision for both people and nature," Teak Seng, Cambodia country director for the World Wildlife Fund, said in a statement.

Computer mimics neurons

ARTIFICIAL INTELLIGENCE | The computer got a nose job. Intel researchers reported last week that they trained Loihi, the company's "neuromorphic" processing chip, to identify 10 odors based on input from 72 chemical sensors—an ability they say could be used to sniff out bombs and drugs. After just one exposure, the chip could identify each odor even when others masked it. Unlike traditional circuits, neuromorphic processors intermingle logic and memory. That makes them energy efficient, and good at artificial intelligence tasks such as pattern recognition. Loihi contains more than 2 billion transistors, which mimic the behavior of 130,000 neurons and 130 million synapses. This month, Intel said, researchers could access its neuromorphic computing system, containing 64 Loihi chips, through a cloud-based server.

A call for waterworks

GLOBAL WARMING | To adapt to climate change and improve health and living standards, countries should triple spending, to $114 billion annually, to build safe drinking water and wastewater management systems, the United Nations says in a 22 March report. Warming temperatures threaten to deplete groundwater supplies, among other risks. But increased spending on unconventional technologies—such as collecting water from fog and using low-volume irrigation—could help provide adequate supplies while decreasing the overall carbon footprint of water and wastewater utilities, the report says. Few countries say much about water projects in their plans for reducing carbon emissions under the Paris agreement. And in 2016, water management projects directly received only about 3% of financing to mitigate and adapt to climate change. Half the world's population lacks safely managed wastewater systems.

Iran, France swap detainees

INTERNATIONAL RELATIONS | A French sociologist jailed in Tehran, Iran, since

PHOTO: SION ANG/SOPA IMAGES/LIGHTROCKET VIA GETTY IMAGES

June 2019 has been freed in exchange for an Iranian engineer held in France. Roland Marchal of the Paris Institute of Political Studies (Sciences Po) is known for his analyses of civil war in sub-Saharan Africa, particularly Somalia. Marchal had traveled to Iran to visit his friend Fariba Adelkhah, a social anthropologist at Sciences Po. The two were charged with "collusion against national security," a charge that was never substantiated, says Sciences Po political scientist Sandrine Perrot. Adelkhah was also charged with "propaganda against the political system of the Islamic Republic." Adelkhah remains imprisoned and reportedly suffered kidney damage during a hunger strike. France released Jalal Rohollahnejad, who faces U.S. charges "related to the illegal export of equipment with military applications in violation of U.S. sanctions," according to the U.S. Department of State, which had sought his extradition.

Deep-sea fish may migrate

MARINE ECOLOGY | Every year, great herds of land animals migrate across the African continent. Now, marine biologists report hints of another seasonal movement of animals, this one off Africa: deep-sea fish traveling in search of food. A research team counted fish by analyzing 7 years of photos taken by observing systems at two sites 1400 meters deep off the coast of Angola. The numbers showed fluctuations that correlate with seasonal changes in abundance of plankton at the ocean surface, which drives food availability in the depths. Births and deaths alone couldn't explain the changing numbers of fish, so the researchers conclude that these species, from 10 different families, regularly migrate in search of food. If confirmed, the migration would be one of the first documented in the deep sea. As the oil and gas industry increasingly drills there, understanding its ecological patterns becomes more important, says the team, which published its findings last week in the *Journal of Animal Ecology*.

SETI@home shutters computing

ASTRONOMY | Almost 21 years after its debut, SETI@home—a pioneering citizen science effort to employ idle home computers to sift radio signals for alien messages—will end this month. Scanning the radio sky has been a mainstay of the search for extraterrestrial intelligence since the 1980s, but processing the data was a challenge. In 1999, researchers at the University of California (UC), Berkeley, asked the public to download a screensaver program that would crunch data during computer downtime. More than 1.8 million people joined in, and the project identified several patches of sky worth further study because signals there rise above random noise. The project announced earlier this month that it was "at the point of diminishing returns" and would write up the results for publication. This week SETI@home urged participants to donate time instead to a UC Berkeley project on the coronavirus pandemic.

BY THE NUMBERS

15,506

Instances of social scientists testifying in Congress, 1946–2016. About two-thirds of the testimonies came from economists; social scientists made up about 2% of all testimonies in that period. (*PLOS ONE*)

Irreverent science reporter dies

POLICY | Daniel Greenberg, a journalist who pioneered coverage of the intersection of science and politics and was an influential early leader of *Science*'s News section, died on 9 March in Washington, D.C., at the age of 88. From 1961 to 1970, he reported for *Science* on research funding and the regulation of new technologies, applying a somewhat skeptical view of the research community's pleadings for money and promises of breakthroughs. Many scientific leaders winced when he wrote about them, but also consumed his work with gusto. Greenberg next founded the Science & Government Report, an influential newsletter. For decades, he delighted many readers with his satirical interviews of a fictional character he created when at *Science*—Dr. Grant Swinger, who later became head of the Center for the Absorption of Federal Funds. Greenberg also wrote more serious tomes, including *Science for Sale: The Perils, Rewards, and Delusions of Campus Capitalism*, published in 2007.

PLANETARY SCIENCE

Lost on the Moon? Check GPS

To find your way on Earth, GPS is a lifeline; now, it could be on the Moon, too. To examine whether the U.S. system of global positioning satellites and similar spacecraft from Europe and Russia could guide a new generation of astronauts exploring the Moon, scientists at NASA's Jet Propulsion Laboratory made calculations about radio signals from 81 of the satellites. They found that signals from five to 13 of them would reach the Moon at any one time—enough for astronauts to locate their position to within 300 meters or so, they reported at the IEEE Aerospace Conference this month. Crater rims might block the signals at the lunar surface, especially at the poles—but a small relay satellite could bridge that gap. GPS would provide a marked improvement from the Apollo era, when astronauts relied on directional gyros and odometers to navigate the lunar buggy.

PHOTO: NASA/EUGENE CERNAN

Businesses in Germany have erected temporary walls to protect people from infection.

INFECTIOUS DISEASE

Coronavirus impact on research spreads

As China this week reported few new cases of coronavirus disease 2019 (COVID-19) and eased lockdown restrictions intended to control its spread, caseloads rose in other countries. Scientists stepped up their research on the disease while other work was suspended. Read more at /tags/coronavirus.

U.S. agencies, projects shut

FACILITIES | Research agencies have shut down key facilities and postponed projects across a span of disciplines to stem transmission of SARS-CoV-2, the virus that causes COVID-19. The U.S. National Institutes of Health, for example, said that as of 23 March its more than 20,000 staff members can enter their labs and offices only to perform "mission-critical" work that cannot be done remotely, such as studies on COVID-19 and caring for patients in medically necessary clinical trials or for research animals. The consortium that operates oceanographic research vessels for the National Science Foundation and the Office of Naval Research recommended a 30-day pause in operations for 16 of its ships. The Department of Energy has restricted access and ramped down activities at its 17 national laboratories, which every year serve more than 30,000 visiting researchers. And the European Space Agency suspended instrument operations and data gathering on four of its Solar System science probes sent to explore Earth, Mars, and the Sun.

A race to develop virus tests

DIAGNOSTICS | To monitor and stop the pandemic's spread, companies are seeking tests for SARS-CoV-2 that return results more quickly. The traditional polymerase chain reaction (PCR)-based method can take 4 days. Last week, diagnostics company Cepheid won emergency approval from the U.S. Food and Drug Administration to use its GenXpert device, a small PCR system developed to detect influenza viruses and other microbes, to test for SARS-CoV-2 in physicians' offices; it can produce a result in 45 minutes. Two other companies are developing tests based on the CRISPR genome editor that may be faster still.

Old vaccine, new use?

IMMUNOLOGY | Researchers in four countries this week began a clinical trial of an unorthodox intervention: bacillus Calmette-Guérin. It is a century-old vaccine against tuberculosis, a bacterial disease, that they hope can rev up the human immune system so it can better fight SARS-CoV-2 and, perhaps, fend off infection altogether. The trial will study two high-risk populations—health care workers and older patients.

Fetal tissue ban blocks study

POLICY | The Trump administration's restrictive 2019 policy on research use of human fetal tissue is stopping a U.S. researcher from testing potential therapies for COVID-19, *The Washington Post* reported last week. The ban prevents National Institutes of Health (NIH) scientists from using human fetal tissue donated after elective abortions. Kim Hasenkrug of NIH's Rocky Mountain Laboratories has unsuccessfully sought an exemption to study mice with humanlike lungs created with fetal tissue. Unlike normal mice, these can be infected with coronaviruses closely related to SARS-CoV-2.

THREE QS

Rubella's lingering lessons

In the mid-1960s, rubella swept the United States, infecting an estimated one in 15 Americans. The virus responsible was about twice as contagious as the novel coronavirus spreading around the world today seems to be. That rubella epidemic resulted in about 20,000 babies born with serious birth defects. (There's no evidence that SARS-CoV-2 infects or hurts fetuses.) In 1964, working in his Wistar Institute lab, Stanley Plotkin invented the rubella vaccine used today the world over. Now 87, he is advising six companies developing COVID-19 vaccines. A longer version of this interview is at https://scim.ag/PlotkinQA.

Q: Before the vaccine was licensed in 1969, rubella came in cyclical outbreaks every 4 to 6 years. Should we expect that with the novel coronavirus?
A: That is the $64,000 question. We all hope—and I underline hope—that the [novel] coronavirus will not persist in the population in some mild form that could pop up again and again. That's why the effort to develop a vaccine in the shortest possible time is so important. Because obviously if next winter [it] returns, we must have a vaccine by that time.

Q: How does the rubella story inform today's coronavirus vaccine race?
A: Perhaps [that] not only one should be licensed. There are at least 40 [COVID-19] vaccine candidates being developed in various companies and biotechs not only in the United States, but elsewhere in the world. There may be advantages to having more than one anticoronavirus vaccine because if—and it's a big if—one needs millions of doses, asking a single manufacturer to produce enough for the world is unlikely. One is going to need multiple manufacturers.

Q: Do we have advantages now that we didn't have in the 1960s?
A: It took at least 5 years before a [rubella] vaccine was on the market. And we cannot afford to have that kind of delay when you have an emergency such as this one. So, the prospect that we have of getting a coronavirus vaccine by next year, which I think is a reasonable hope, is a big difference.

S /NEWS
Read more news from *Science* online.

PHOTO: JENS BÜTTNER/DPA/PICTURE-ALLIANCE/NEWSCOM

eppendorf & Science

PRIZE FOR NEURO BIOLOGY

2019 Winner
Lauren Orefice, Ph.D.

For research on the causes and potential therapies for autism spectrum disorders

Application Deadline
June 15, 2020

Now It's Your Turn!

Eppendorf & Science Prize for Neurobiology
The annual Eppendorf & Science Prize for Neurobiology is an annual international prize which honors young scientists for their outstanding contributions to neurobiological research based on methods of molecular and cell biology. The winner and finalists are selected by a committee of independent scientists, chaired by *Science's* Senior Editor, Dr. Peter Stern. If you are 35 years of age or younger and doing great research, now is the time to apply for this prize.

As the Grand Prize Winner, you could be next to receive
> Prize money of US$25,000
> Publication of your work in *Science*
> Full support to attend the Prize Ceremony held in conjunction with the Annual Meeting of the Society for Neuroscience in the USA
> 10-year AAAS membership and online subscription to *Science*
> Complimentary products worth US$1,000 from Eppendorf
> An invitation to visit Eppendorf in Hamburg, Germany

It's easy to apply! Write a 1,000-word essay and tell the world about your work. Learn more at:

www.eppendorf.com/prize

eppendorf Science AAAS

IN DEPTH

Medical staff treat a patient with the novel coronavirus this month in Wuhan, China.

PHOTO: STR/AFP/GETTY IMAGES

INFECTIOUS DISEASES

Race to find COVID-19 treatments accelerates

WHO launches megatrial to test repurposed drugs and experimental drug candidates

By **Kai Kupferschmidt** *and* **Jon Cohen**

With cases of the new coronavirus disease 2019 (COVID-19) climbing steeply everywhere from Madrid to Manhattan, overwhelming one hospital after another and pushing the global death toll past 17,000, the sprint to find treatments has dramatically accelerated. Drugs that stop the novel coronavirus, severe acute respiratory syndrome coronavirus 2 (SARS-CoV-2), could save the lives of severely ill patients, protect health care workers and others at high risk of infection, and reduce the time patients spend in hospital beds.

The World Health Organization (WHO) last week announced a major study to compare treatment strategies in a streamlined clinical trial design that doctors around the world can join. Other trials are also underway; all told, at least 12 potential COVID-19 treatments are being tested, including drugs already in use for HIV and malaria, experimental compounds that work against an array of viruses in animal experiments, and antibody-rich plasma from people who have recovered from COVID-19. More than one strategy may prove its worth, and effective treatments may work at different stages of infection, says Thomas Gallagher, a coronavirus researcher at Loyola University Chicago's Health Sciences Campus. "The big challenge may be at the clinical end determining when to use the drugs."

Researchers want to avoid repeating the mistakes of the 2014–16 West African Ebola epidemic, in which willy-nilly experiments proliferated but randomized clinical trials were set up so late that many ended up not recruiting enough patients. "The lesson is you start trials now," says Arthur Caplan, a bioethicist at New York University's Langone Medical Center. "Make it a part of what you're doing so that you can move rapidly to have the most efficacious interventions come to the front."

To that end, WHO on 20 March announced the launch of SOLIDARITY, an unprecedented, coordinated push to collect robust scientific data rapidly during a pandemic. The study, which could include many thousands of patients in dozens of countries, has emphasized simplicity so that even hospitals overwhelmed by an onslaught of COVID-19 patients can participate. WHO's website will randomize patients to local standard care or one of the four drug regimens, using only ones available at the patient's hospital. Physicians will simply record the day the patient left the hospital or died, the duration of the hospital stay, and whether the patient required oxygen or ventilation. "That's all," says Ana Maria Henao Restrepo, a medical officer at WHO's Department of Immunization Vaccines and Biologicals.

The design is not blinded: Patients will know they received a drug candidate, and that could cause a placebo effect, Henao Restrepo concedes. But it is in the interest of speed, she says. "We are doing this in record time." The agency hopes to start to enroll patients this week.

Rather than taking years to develop and test compounds from scratch, WHO and others want to repurpose drugs that are already approved for other diseases and have acceptable safety profiles. They're also looking at experimental drugs that have performed well in animal studies against the other two deadly coronaviruses, which cause SARS and Middle East respiratory syndrome (MERS). And they are focusing on compounds plentiful enough to treat a substantial number of patients.

For its study, WHO chose an experimental antiviral called remdesivir; the malaria medication chloroquine (or its chemical cousin hydroxychloroquine); a combination of the HIV drugs lopinavir and ritonavir; and that combination plus interferon-beta, an immune system messenger that can help cripple viruses. The treatments would stop the virus by different mechanisms, but each has drawbacks.

Remdesivir, developed by Gilead Sciences to combat Ebola and related viruses, shuts down viral replication by inhibiting a key viral enzyme, the RNA polymerase. It didn't help patients with Ebola in a test during the 2019 outbreak in the Democratic Republic of the Congo. But in 2017, researchers showed in test tube and animal studies that the drug can inhibit the SARS and MERS viruses.

The drug, which is given intravenously, has been used in hundreds of COVID-19 patients in the United States and Europe under what's known as compassionate use, which required Gilead to review patient records; some doctors have reported anecdotal evidence of benefit, but no hard data. Gilead says it is now starting to supply remdesivir under a simpler "expanded use" designation. Five other clinical trials underway in China and the United States are testing it and may have preliminary results soon. Of the drugs in the SOLIDARITY trial, "remdesivir has the best potential," says Shibo

Jiang of Fudan University, who works on coronavirus therapeutics.

Like most drugs for acute infections, remdesivir may be much more potent if given early, says Stanley Perlman, a coronavirus researcher at the University of Iowa—and that could be a challenge. "What you really want to do is give a drug like that to people who walk in with mild symptoms," he says. "And you can't do that because it's an [intravenous] drug, it's expensive, and 85 out of 100 people don't need it" because they won't develop severe disease.

Chloroquine and hydroxychloroquine have received intense attention because of positive results from small studies and an endorsement from President Donald Trump, who said, "I feel good about it." The drugs decrease acidity in endosomes, compartments that cells use to ingest outside material and that some viruses co-opt during infection. But SARS-CoV-2's main entryway is different: It uses its so-called spike protein to attach to a receptor on the surface of human cells. Studies in cell culture have suggested chloroquine can cripple the virus, but the doses needed are usually high and could cause severe toxicity. "Researchers have tried this drug on virus after virus, and it never works out in humans," says Susanne Herold, an expert on pulmonary infections at the University of Giessen.

Results from COVID-19 patients are murky. Chinese researchers who treated more than 100 patients touted chloroquine's benefits in a letter in *BioScience*, but they did not publish data. And WHO says "no data has been shared" from more than 20 other COVID-19 studies in China using chloroquine or hydroxychloroquine. French microbiologist Didier Raoult and colleagues published a study of hydroxychloroquine in 20 COVID-19 patients that concluded the drug had reduced viral load in nasal swabs. (It seemed to work even better with the antibiotic azithromycin.) But the trial, reported in the *International Journal of Antimicrobial Agents*, was not randomized, and it didn't report clinical outcomes such as deaths.

Hydroxychloroquine might actually do more harm than good. It has many side effects and can, in rare cases, harm the heart—and people with heart conditions are at higher risk of severe COVID-19, says David Smith, an infectious disease physician at the University of California, San Diego. "This is a warning signal, but we still need to do the trial," he says. There have also been reports of chloroquine poisoning in people who self-medicated.

Many coronavirus researchers are similarly skeptical of the lopinavir-ritonavir combination. Abbott Laboratories developed the drugs to inhibit the protease of HIV, an enzyme that cleaves a long protein chain during assembly of new viruses. The combination has worked in marmosets infected with the MERS virus, and has also been tested in patients with SARS and MERS, though those results are ambiguous. But the first trial with COVID-19 was not encouraging. When doctors in Wuhan, China, gave 199 patients standard care with or without lopinavir-ritonavir, the outcomes did not differ significantly, they reported in *The New England Journal of Medicine* on 15 March. The authors say the patients were very ill and treatment may have started too late.

The fourth arm of SOLIDARITY combines these two antivirals with interferon-beta, a molecule involved in regulating inflammation that has lessened disease severity in marmosets infected with MERS. But interferon-beta might be risky for patients with severe COVID-19, Herold says. "If it is given late in the disease it could easily lead to worse tissue damage, instead of helping patients," she cautions.

SOLIDARITY is designed to provide a quick, useful verdict, based on the outcomes that are the most relevant for public health, says virologist Christian Drosten of the Charité University Hospital in Berlin. More detailed data could come from an add-on trial in Europe, announced on 23 March by the French biomedical research agency INSERM. To include 3200 patients, it will test the same drugs, including hydroxychloroquine but not chloroquine, and collect additional data such as blood gas levels or lung imaging.

Other approved and experimental treatments are in testing against coronavirus or likely soon to be. They include drugs that can reduce inflammation, such as corticosteroids and baricitinib, a treatment for rheumatoid arthritis. Some researchers have high hopes for camostat mesylate, a drug licensed in Japan for pancreatitis, which inhibits a human protein involved with infection. Other antivirals will also get a chance, including the influenza drug favipiravir and additional HIV antiretrovirals. Researchers also plan to try to boost immunity with "convalescent" plasma from recovered COVID-19 patients or monoclonal antibodies directed at SARS-CoV-2.

Perlman says the smartest way to test the drugs is in people in early stages of disease who doctors think are most likely to get much worse. How would you determine that? "That is the key question," he says. Researchers might find a biomarker in blood that helps them predict disease course.

Crucially, doctors and researchers around the world are tackling the problem with urgency, Henao Restrepo says. "This is a crisis like no other and we will have to work together," she says. "That is the only way perhaps we are going to find a solution." ■

Lines of attack

Experimental treatment strategies attempt to interfere with different steps (numbered) in the coronavirus replication cycle.

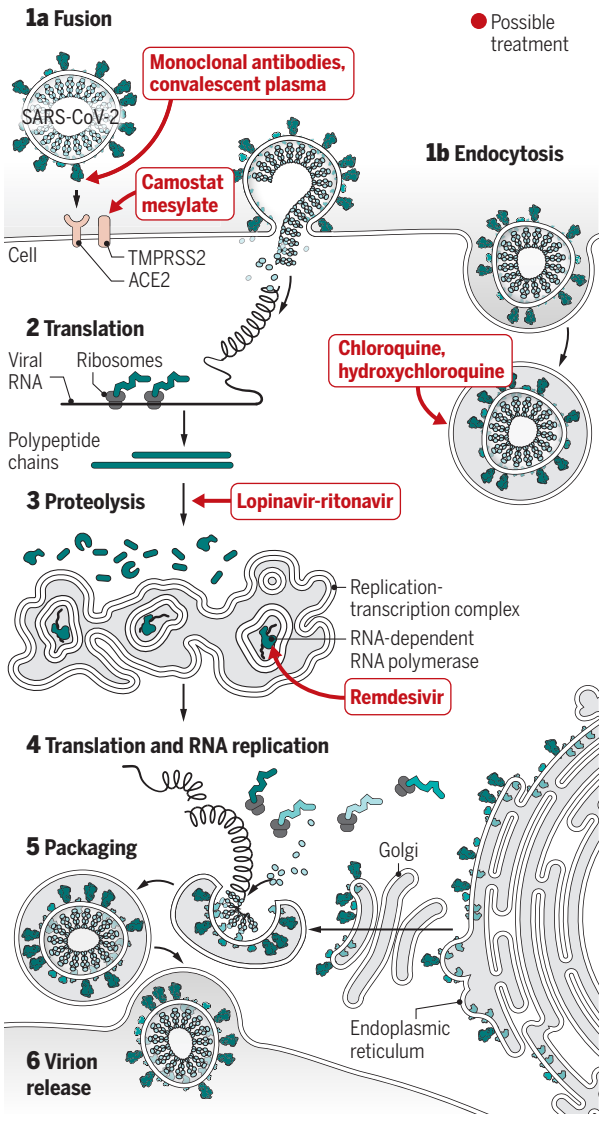

GRAPHIC: V. ALTOUNIAN/*SCIENCE*

PANDEMIC Qs

Fauci's straight talk

To many watching the White House press briefings on the coronavirus pandemic, veteran public health expert Anthony Fauci has become the voice of science and reason on how the country should respond. He made national news this week for his careful but candid assessment to *Science*'s Jon Cohen of the challenges of working for President Donald Trump during the crisis. "When you're dealing with the White House, sometimes you have to say things one, two, three, four times, and then it happens. So, I'm going to keep pushing," says Fauci, longtime director of the National Institute of Allergy and Infectious Diseases. His full interview is at https://scim.ag/QAFauci.

Q: The first question everyone has is how are you?
A: Well, I'm sort of exhausted. But other than that, I'm good. I mean, I'm not, to my knowledge, coronavirus infected. To my knowledge, I haven't been fired [laughs].

Q: How are you managing to not get fired?
A: To [Trump's] credit, even though we disagree on some things, he listens. He goes his own way. He has his own style. But on substantive issues, he does listen to what I say.

Q: You've been in press conferences where things are happening that you disagree with, is that fair to say?
A: Well, I don't disagree in the substance. It is expressed in a way that I would not express it, because it could lead to some misunderstanding about what the facts are about a given subject.

Q: You're standing there saying nobody should gather with more than 10 people and there are almost 10 people on the stage [and] more than 10 journalists.
A: I know that. I'm trying my best. I cannot do the impossible.

Q: We've had all this pandemic preparedness. What went wrong?
A: I think we'll have to wait until it is over and we look back before we can answer that. It's almost like the fog of war. After the war is over, you then look back and say, "Wow, this plan, as great as it was, didn't quite work once they started throwing hand grenades at us." Obviously, testing [for the new coronavirus] is one clear issue that needs to be relooked at. Why were we not able to mobilize on a broader scale? But I don't think we can do that right now. I think it's premature. We really need to look forward. ■

Dutch models of COVID-19 are designed to help prevent overloading of hospitals and the need to transfer patients.

PHOTO: THOMAS ANGUS/IMPERIAL COLLEGE LONDON

CORONAVIRUS

With COVID-19, modeling takes on life and death importance

Epidemic simulations shape national responses

By **Martin Enserink** *and* **Kai Kupferschmidt**

Jacco Wallinga's computer simulations are about to face a high-stakes reality check. Wallinga is a mathematician and the chief epidemic modeler at the National Institute for Public Health and the Environment (RIVM), which is advising the Dutch government on what actions, such as closing schools and businesses, will help control the spread of the novel coronavirus in the country.

The Netherlands has so far chosen a softer set of measures than most Western European countries; it was late to close its schools and restaurants and hasn't ordered a full lockdown. In a 17 March speech, Prime Minister Mark Rutte rejected "working endlessly to contain the virus" and "shutting down the country completely." Instead, he opted for "controlled spread" of the virus while making sure the health system isn't swamped with COVID-19 patients. He called on the public to respect RIVM's expertise on how to thread that needle. Wallinga's models predict that the number of infected people needing hospitalization, his most important metric, will taper off next week. But if the models are wrong, the demand for intensive care beds could outstrip supply, as it has, tragically, in Italy and Spain.

COVID-19 isn't the first infectious disease scientists have modeled—Ebola and Zika are recent examples—but never has so much depended on their work. Entire cities and countries have been locked down based on hastily done forecasts that often haven't been peer reviewed. "It's a huge responsibility," says epidemiologist Caitlin Rivers of the Johns Hopkins University Center for Health Security, who co-authored a report about the future of outbreak modeling in the United States that her center released this week.

Just how influential those models are became apparent over the past 2 weeks in the United Kingdom. Based partly on modeling work by a group at Imperial College London, the U.K. government at first implemented fewer measures than many other countries—not unlike the strategy the Netherlands is pursuing. Citywide lockdowns and school closures, as China initially mandated, "would result in a large second epidemic once measures were lifted," a group of modelers that advises the government concluded in a statement. Less severe controls would still reduce the epidemic's peak and make any rebound less severe, they predicted.

But on 16 March, the Imperial College group published a dramatically revised model that concluded—based on fresh data from the United Kingdom and Italy—that even a reduced peak would fill twice as many intensive care beds as estimated previously, overwhelming capacity. The only choice, they concluded, was to go all out on control measures. At best, strict measures might be periodically eased for short pe-

riods, the group said (see graphic, below). The U.K. government shifted course within days and announced a strict lockdown.

It's not that the science behind epidemic modeling is controversial. Wallinga uses a well-established model that divides the Dutch population into four groups, or compartments in the field's lingo: healthy, sick, recovered, or dead. Equations determine how many people move between compartments as weeks and months pass. "The mathematical side is pretty textbook," he says. But model outcomes vary widely depending on the characteristics of a pathogen and the affected population.

Because the virus that causes COVID-19 is new, modelers need estimates for key model parameters. Wallinga is now confident that the number of new infections caused by each infected person when no control measures are taken—which epidemiologists call R_0—is just over two. And he trusts data showing that 3 to 6 days elapse between the moment someone is infected and the time they start to infect others.

From a 2017 survey of the Dutch population, the RIVM team also has good estimates of how many contacts people of different ages have at home, school, work, and during leisure. Wallinga says he's least confident about the susceptibility of each age group to infection and the rate at which people of various ages transmit the virus.

Compartment models assume the population is homogeneously mixed, a reasonable assumption for a small country like the Netherlands. Other modeling groups don't use compartments but simulate the day-to-day interactions of millions of individuals. Such models are better able to depict heterogeneous countries, such as the United States, or all of Europe. The World Health Organization organizes regular calls for COVID-19 modelers to compare strategies and outcomes, Wallinga says: "That's a huge help in reducing discrepancies between the models that policymakers find difficult to handle."

In their review of U.S. outbreak modeling, Rivers and her colleagues note that most of the key players are academics with little role in policy. They don't typically "participate in the decision-making processes … they sort of pivot into a new world when an emergency hits," she says. Rivers argues for the creation of a National Infectious Disease Forecasting Center, akin to the National Weather Service. It would be the primary source of models in a crisis and strengthen outbreak science in "peacetime."

Policymakers have relied too heavily on COVID-19 models, says Devi Sridhar, a global health expert at the University of Edinburgh. "I'm not really sure whether the theoretical models will play out in real life." And it's dangerous for politicians to trust models that claim to show how a little-studied virus can be kept in check, says Harvard University epidemiologist William Hanage. "It's like, you've decided you've got to ride a tiger," he says, "except you don't know where the tiger is, how big it is, or how many tigers there actually are."

Models are at their most useful when they identify something that is not obvious, says Adam Kucharski, a modeler at the London School of Hygiene & Tropical Medicine. One valuable function, he says, was to flag that temperature screening at airports will miss most coronavirus-infected people.

There's also a lot that models don't capture. They cannot anticipate, say, an effective antiviral that reduces the need for hospital beds. Nor do most models factor in the anguish of social distancing, or whether the public obeys orders to stay home. In Hong Kong and Singapore, "It's 2 months already [of such measures], and people are really getting very tired," says University of Hong Kong modeler Gabriel Leung. Recent data suggest the virus may be spreading faster again in both cities, putting them on the brink of a major outbreak, he adds.

Long lockdowns to slow a disease have catastrophic economic impacts and may devastate public health themselves. "It's a three-way tussle," Leung says, "between protecting health, protecting the economy, and protecting people's well-being and emotional health."

The economic fallout isn't something epidemic models address, says Ira Longini, a modeler at the University of Florida—but that may have to change. "We should probably hook up with some economic modelers and try to factor that in," he says. ■

Modeling a bleak future

U.K. control measures could be let up once in a while, a model suggests, until demand for intensive care unit (ICU) beds hits a threshold.

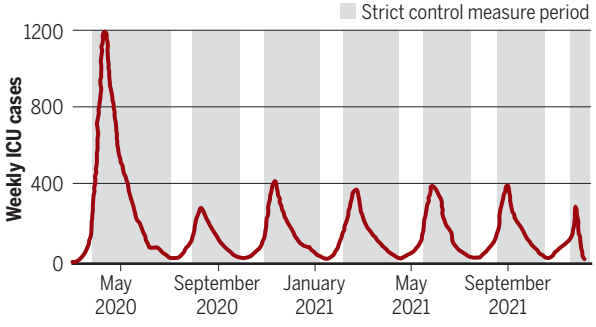

GRAPHIC: IMPERIAL COLLEGE COVID-19 RESPONSE TEAM. ADAPTED BY C. BICKEL/*SCIENCE*

TOXICOLOGY

New mercury compound spotted in mass poisoning

Chemical found in 60-year-old cat brain reopens debate over Minamata disaster

By **Joshua Sokol**

The city of Minamata, Japan, is dotted with monuments commemorating victims of an industrial mass poisoning decades ago. High in the hills, a small stone memorial honors other deaths—of cats sacrificed in secret to science. Now, after restudying the remains of one of those cats, a team of scientists is arguing, controversially, that the long-standing explanation for the tragedy is wrong.

No one questions the root cause of the disaster, which at minimum poisoned more than 2000 people: mercury in a chemical factory's wastewater that was dumped into Minamata Bay and taken up by seafood eaten by fishermen and their families. At first, the chemical form of the mercury, which ultimately killed many of its victims and left many babies with severe neurological disorders, was unknown. But in 1968, the Japanese government blamed methylmercury, a common byproduct of mercury pollution. Many studies supported that conclusion, finding methylmercury spikes in shellfish, bay sludge, and even hundreds of umbilical cords from babies delivered during the time. But methylmercury is not the culprit, says Ingrid Pickering, an x-ray spectroscopist at the University of Saskatchewan. "Our work is indicating that it's something else": an unusual mercury compound that may say little about the broader threat of mercury pollution.

Minamata has long been a vivid case study of mercury's dangers. The metal is toxic on its own, but it becomes far more dangerous when bacteria in natural environments convert it into methylmercury, an organic compound, readily absorbed by living tissues, that can be concentrated and passed up food chains. Since the 1990s, scientists have argued that the Chisso chemical factory in Minamata produced

In 1986, decades after the Minamata disaster, workers still discarded mercury-tainted fish from the bay.

PHOTO: THE ASAHI SHIMBUN/GETTY IMAGES

methylmercury and dumped it directly into the bay.

The dead cat now challenging that picture dates to 1959, when the then-mysterious neurological disease was sweeping through the city. A doctor working for the Chisso factory mixed wastewater with cat food and fed it to cats, which started to convulse and were paralyzed before dying. He autopsied two of them, known only as 400 and 717. Their behavior and lesions in their brains suggested the same disease as the one raging outside. Factory supervisors hushed up the finding.

The Chisso cats were lost until 2001, when Komyo Eto, a pathologist at the National Institute for Minamata Disease, studied samples of the cats and the wastewater that had been found in storage at nearby Kumamoto University—along with lab notebooks lent by the factory doctor's wife. His measurements showed that less than half of the mercury in the cats' brain samples occurred as methylmercury; the rest was inorganic. Only a minuscule fraction of the wastewater's mercury was methylmercury, but Eto thought that was probably because the compound had broken down over the 4 decades since the samples were taken.

Now, Pickering and her colleagues have reanalyzed samples of cat 717's cerebellum at the Stanford Synchrotron Radiation Lightsource, blasting them with x-rays and analyzing the resulting spectrum for the fingerprints of specific molecules. The molecules that best fit the spectrum don't contain any methylmercury at all, they found. Instead, three-quarters of the sample's mercury appears to be an obscure organic compound called alpha-mercuri-acetaldehyde that likely came straight from the wastewater, they argue. The rest was inorganic mercury.

The finding suggests the Minamata disaster—and methylmercury poisoning more generally—is due for a rethink, the researchers argue in their study, published in *Environmental Science & Technology* in January. Methylmercury played no significant role in the poisoning, says Graham George, Pickering's husband and co-leader of the experiment, who is also at the University of Saskatchewan. Because previous studies used less sensitive techniques, they missed the major form of mercury in Minamata samples, he argues. "Were there other more prevalent forms of mercury present that were not detected? Yes, we think so."

But to other researchers, the team may be overstating its conclusions in the service of a larger agenda. Many of the authors have downplayed the toxicity of methylmercury for years, says Philippe Grandjean, an environmental toxicologist at Harvard University. The work doesn't do anything more than identify an unusual chemical in one preserved cat brain, he says. "They did an admirable piece of chemistry, but it should not be interpreted beyond what it really shows."

Charles Driscoll, an environmental scientist at Syracuse University, says the new mercury compound might be a product of the cat's metabolism or an artifact of the sample's long preservation. And even if it did spew directly from the factory, the residents of Minamata were exposed to mercury from seafood they ate, not from factory wastewater, he says. "Quite a few things in [the study] give me pause," he says. "I was, frankly, surprised it would get published."

The dispute reflects a schism dating to the 1980s, when dueling research teams looked at the neurological consequences of methylmercury from seafood. One team, at the University of Rochester, studied the brain development of children in the Seychelles islands, where the diet is heavy in fish that can acquire methylmercury in the open ocean from natural and human sources of mercury. "We have not been able to confirm any adverse effects of methylmercury from fish," said Gary Myers, a University of Rochester neurologist who also participated in the study on cat 717. But a competing study by Grandjean and others in the Faroe Islands concluded methylmercury from seafood was harming children.

In 2000, when the U.S. Environmental Protection Agency (EPA) defined the maximum daily amount of mercury thought to be safe to ingest, the agency found the Faroe Islands evidence more convincing, and set a low limit. In 2019, EPA began to reassess this limit; Grandjean fears the new study could be used to support relaxing the standard. At the same time, the Trump administration is working to weaken a separate rule called the Mercury and Air Toxics Standards, which limits mercury emissions from power plants.

Last year, Grandjean, Driscoll, and other mercury researchers submitted a comment to EPA as part of the agency's reassessment. They pointed out that Minamata is not the only example of methylmercury toxicity; the compound caused another industrial poisoning in Iraq in 1971, and studies of babies and children around the world have found that even low-level exposure can harm brain development, Grandjean says. Compared with past decades, "We know better now."

Eto, who loaned the samples and was credited as a study co-author, said in an email that he still believes methylmercury was the most important cause of the tragedy. But Pickering and George plan to move beyond a single cat sample to bolster their controversial claim. They have already borrowed preserved samples from human victims from the National Institute for Minamata Disease, and plan to test for the same obscure compound. ■

Joshua Sokol is a journalist in Cambridge, Massachusetts.

FOREST SCIENCE

Can 'sentinel trees' warn of devastating pests?

By planting groves of exotic species, nations hope to identify potential insect invaders

By **Gabriel Popkin**

It's become an all-too-common tale: An introduced insect takes hold in a new home and then spreads, wreaking havoc with ecosystems and economies. Take, for instance, the emerald ash borer, an Asian beetle first spotted in North America in 2002; researchers estimate it has killed hundreds of millions of ash trees and caused more than $10 billion in damage.

Now, in a bid to prevent such catastrophes—and get an early warning of which exotic pests are likely to cause trouble—researchers from the United States, Europe, and China are trying a new approach: planting "sentinel trees" from their own regions in distant nations, and then observing which insects attack. The findings should help authorities more quickly recognize and snuff out threatening introduced insects if they show up in the trees' native countries. Sentinel trees are "the new frontier" in fighting forest pests, says entomologist Jiri Hulcr at the University of Florida.

Sentinel trees could help prevent the spread of exotic insects, such as the emerald ash borer of Asia.

PHOTO: STEPHEN AUSMUS/USDA/SCIENCE SOURCE

Already, groves of North American and European trees planted in China have enabled scientists to identify and start to study more than a dozen insects of concern. In Europe, 23 nations have launched a €5 million project that will, among other activities, establish sentinel nurseries in North America, Asia, and South Africa—and enable researchers to plant trees from those areas in Europe. And next month, if the coronavirus pandemic doesn't interfere, researchers will plant the first sentinel grove of Asian trees in the United States.

A team led by entomologist Alain Roques of France's National Institute for Agriculture, Food, and Environment pioneered the approach between 2007 and 2011, when it planted seven tree species in Fuyang and near Beijing in China. By 2015, the researchers had identified more than 100 kinds of insects that had sampled the trees. They considered five species to be dangerous, and they took one—a bagworm moth—back to Europe to study its appetite for broadleaved trees. That study, conducted under quarantine, showed the moth can destroy numerous trees, Roques reported in January at a U.S. Department of Agriculture conference in Annapolis, Maryland.

Hulcr became a convert after colleagues in China discovered a beetle demolishing American sweetgum trees that had been planted near Shanghai. Sweetgum is an ecologically and economically important species in the southeastern United States. If the beetle, which he and his colleagues named the sweetgum inscriber, gained a foothold in North America, it could pose a serious threat, they reported in 2017.

The discovery prompted China to ban imports of the tree, to avoid further damage. And it spurred Hulcr in 2018 to plant his first sentinel grove of North American trees in China's Fujian province. Hulcr and colleagues in China has since established two additional plantations, which hold pines, oaks, and citrus trees, in Yunnan and Shandong provinces, and plans a fourth in Liaoning province.

So far, Hulcr's team has detected eight insect species of concern, which the researchers are now rearing and studying. Such studies could alert authorities to look for the pests, some of which were unknown to science, and lead to better monitoring traps and control measures.

Establishing sentinel orchards in a foreign nation can be fraught, Roques says. A Chinese farmer destroyed one of his plantings after seeing insect damage, not realizing the attacks were by design. He lost access to other potential sites after collaborators balked, fearing his trees would also bring European pests to Asia.

Funding agencies are ramping up support for sentinel groves. Europe's new project, called Holistic Management of Emerging Forest Pests and Diseases, is expected to run through 2024. And the U.S. Forest Service (USFS) is funding several projects, including one led by Ohio State University, Columbus, plant pathologist Enrico Bonello that, in April, is scheduled to plant the first sentinel trees from Asia and Europe—including beeches, hollies, maples, and pines—in Ohio and New Hampshire. Collaborators have already planted North American and Asian trees in Sweden and Italy.

It could take years to know whether the sentinels provide useful intelligence. Some insects won't attack young trees, for instance, so researchers will have to wait to see what the mature trees attract. And some trees become stressed and more vulnerable to insects when growing outside their native range, potentially making observations less relevant to predicting the impacts of invasions.

Governments, meanwhile, are still figuring out how they might incorporate any findings into biosecurity policies and practical actions. "Science and regulation are disjoint a lot of times," Roques says. But Elizabeth Lebow, who directs invasive species programs for USFS's international office, believes new sentinel trees are "a really smart approach … [to] informing our early detection efforts." ■

Gabriel Popkin is a journalist in Mount Rainier, Maryland.

THE BIAS DETECTIVE

Psychologist Jennifer Eberhardt explores the roots of unconscious bias—and its tragic consequences for U.S. society

By **Douglas Starr**; *Photography by* **LiPo Ching**

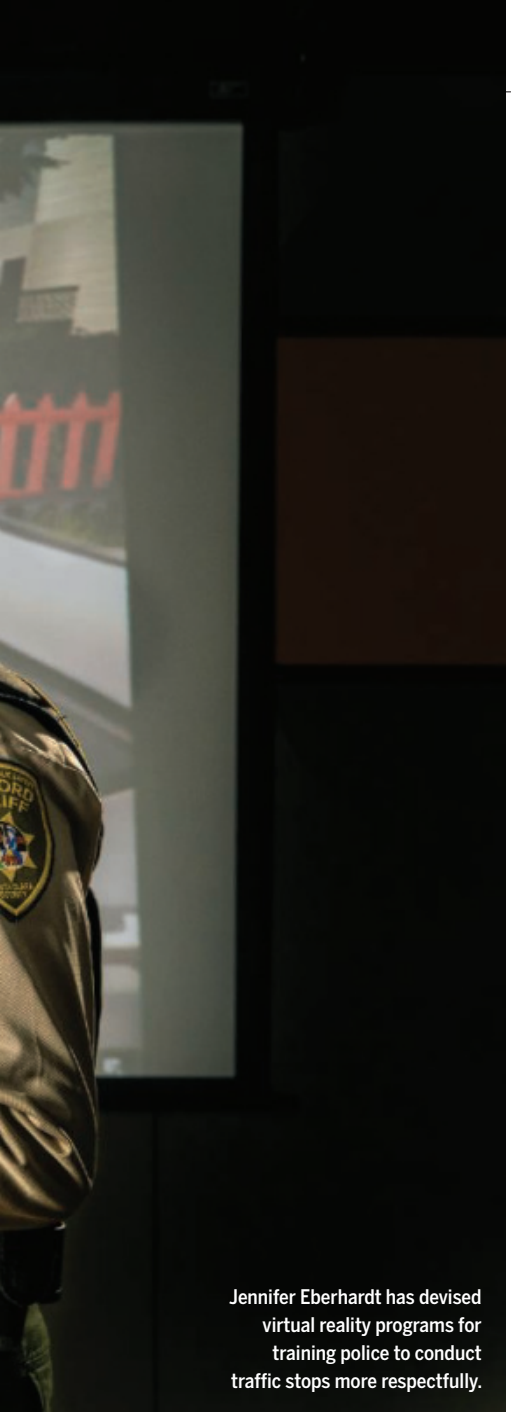

Jennifer Eberhardt has devised virtual reality programs for training police to conduct traffic stops more respectfully.

When Jennifer Eberhardt appeared on *The Daily Show* with Trevor Noah in April 2019, she had a hard time keeping a straight face. But some of the laughs were painful. Discussing unconscious racial bias, which she has studied for years, the Stanford University psychologist mentioned the "other-race effect," in which people have trouble recognizing faces of other racial groups. Criminals have learned to exploit the effect, she told Noah. In Oakland, California, a gang of black teenagers caused a mini–crime wave of purse snatchings among middle-aged women in Chinatown. When police asked the teens why they targeted that neighborhood, they said the Asian women, when faced with a lineup, "couldn't tell the brothers apart."

"That is one of the most horrible, fantastic stories ever!" said Noah, a black South African.

But it was true. Eberhardt has written that the phrase "they all look alike," long the province of the bigot, "is actually a function of biology and exposure." There's no doubt plenty of overt bigotry exists, Eberhardt says; but she has found that most of us also harbor bias without knowing it. It stems from our brain's tendency to categorize things—a useful function in a world of infinite stimuli, but one that can lead to discrimination, baseless assumptions, and worse, particularly in times of hurry or stress.

Over the decades, Eberhardt and her Stanford team have explored the roots and ramifications of unconscious bias, from the level of the neuron to that of society. In cleverly designed experiments, she has shown how social conditions can interact with the workings of our brain to determine our responses to other people, especially in the context of race. Eberhardt's studies are "strong methodologically and also super real-world relevant," says Dolly Chugh of New York University's Stern School of Business, a psychologist who studies decision-making.

"She is taking this world that black people have always known about and translating it into the principles and building blocks of universal human psychology," adds Phillip Atiba Goff, a former graduate student of Eberhardt's who runs the Center for Policing Equity at John Jay College of Criminal Justice.

Eberhardt hasn't shied away from some of the most painful questions in U.S. race relations, such as the role of bias in police shootings. "What's distinctive about her work is how bold she is," says Susan Fiske, a psychologist at Princeton University who wrote the authoritative textbook about social cognition. "She's not the only one working in social cognition or on police issues or on implicit bias. But she dares to go where other people don't."

Eberhardt, a MacArthur Foundation "genius grant" award winner in 2014, has long been putting her insights to work. At Stanford, she co-directs Social Psychological Answers to Real-world Questions, a group of researchers who aim to solve problems in education, health, economic mobility, and criminal justice. Eberhardt has been especially active in criminal justice, playing a key role in the court-ordered reform of the Oakland police department, which has a history of toxic community relations.

"She has been working tirelessly on this issue and brought a whole new series of concepts to the department," says Jim Chanin, an attorney whose class action suit prompted the court order and who has seen the department's record improve. "The whole culture has changed, and Dr. Eberhardt has been part of that."

EBERHARDT HAS AN EARNEST manner that suggests a deep sense of mission. After growing up in a black Cleveland neighborhood, she had a formative experience in middle school when her family moved to a predominantly white suburb. Contrary to her fears, her new classmates were welcoming. But as much as she tried to reciprocate their attention, she had trouble telling them apart. So she trained herself to recognize features she had never paid attention to before—"eye color, various shades of blond hair, freckles," she wrote in her book, *Biased: Uncovering the Hidden Prejudice That Shapes What We See, Think, and Do*. It also became clear to her how different her world was from that of her classmates—how her relatives routinely got pulled over by the police, for example, whereas those of her classmates almost never did.

Those memories never left her as she made her way through her undergraduate years at the University of Cincinnati and her Ph.D. in cognitive psychology at Harvard University. Still, she hadn't planned to study race until the issue came up while she was a teaching assistant. She introduced the class to the quizmaster test, in which one student poses as a quiz show host, like Alex Trebek on *Jeopardy!*, and another poses as a contestant. Observers almost always say they see the quizmaster as more intelligent, despite knowing that's simply because the host already has the answers. It's a textbook example of what's known as the fundamental attribution error, a tendency to credit or blame other people for actions or qualities for which they bear no responsibility.

Eberhardt's students committed the same error—except when the quizmaster was black and the contestant was white. "The effect was just flat," she says: The student observers did not see the quizmaster as any more intelligent than the contestant. "And I was like, wow, because normally this experiment always works." She began to wonder how unconscious bias influences our perceptions. For her dissertation, she decided to study one of the best-known examples—the "other race" face recognition bias.

To explore how hardwired the effect

might be, Eberhardt and colleagues at Stanford recruited 10 black and 10 white students and put them in an MRI machine while showing them photographs of white and black faces. When students viewed faces of their own race, brain areas involved in facial recognition lit up more than when viewing faces of other races. Students also had more trouble remembering faces of races other than their own.

Same-race recognition isn't inborn, Eberhardt says. It's a matter of experience, acting on biology: If you grew up among white people, you learned to make fine distinctions among whites. "Those are the faces our brain is getting trained on."

Such learned perceptual biases, she thought, might shape reactions, too—in particular those at work in tense confrontations that can have a tragic outcome, such as when a police officer shoots an unarmed black man. She and colleagues did a series of experiments using the dot-probe paradigm, a well-known method of implanting subliminal images. She asked subjects (largely white) to stare at a dot on a computer screen while images—of a black face, a white face, or no face at all—flashed imperceptibly quickly off to one side.

Then she would show a vague outline of an object that gradually came into focus. The subjects, who included both police officers and students, were asked to press a key as soon as they recognized the object. The object could be benign, such as a radio, or crime-related, such as a gun. Subjects who had been primed with black faces recognized the weapon more quickly than participants who had seen white faces. In other words, seeing a black face—even subconsciously—prompted people to see the image of a gun.

Subjects recognize a gun that gradually comes into focus faster when "primed" with a glimpse of a black face.

Then the researchers tried the experiment in reverse, flashing subliminal images of crime objects, such as a gun, followed by a brief image of a face in various parts of the screen. Those subjects primed by crime-related objects were quicker to notice a black face.

Eberhardt's finding, added to earlier studies showing similar associations, suggests a dangerous sequence of cognitive events, especially in situations when adrenaline runs high. But the subconscious link between black faces and crime remains strong even when people have time to think, as other studies have shown.

Black people convicted of capital offenses face the death penalty at a higher rate than white people. (They also tend to face longer prison terms for similar crimes.) To suss out the cognitive component of sentencing, Eberhardt obtained data from hundreds of capital cases in Philadelphia. Without explaining the purpose of the study, she showed photos of the defendants to panels of students and asked them to rate which ones seemed most stereotypically black. In cases when the victim was white, the criminals who appeared the most "black" were more than twice as likely as others to have received a death sentence.

Such work explores "the very soul of our country," Chugh says. In 2016, Eberhardt and colleagues published a study in the *Journal of Experimental Psychology: General* showing that people who saw photos of black families subconsciously associated them with bad neighborhoods, no matter how middle-class those families appeared. Another study of unconscious bias found that teachers were more likely to discipline black students—not on the first offense, but on the second: The teachers apparently were quicker to see "patterns" of bad behavior in black children. And last year, in the *Proceedings of the National Academy of Sciences* (*PNAS*), Eberhardt and colleagues reported that implicit bias affects leaders in the asset allocation industry—a $69.1 trillion business that helps universities, pension funds, governments, and charities decide where to invest. When given virtually identical portfolios of successful investment firms that differed only in the race of the principals, the study indicated, financial managers tended to choose white-managed firms.

SUCH RESULTS MIGHT UPSET a woman whose great-great-grandfather was born into slavery. But Eberhardt says using science to study racial bias drains it of its mystery and power. "As a scientist, I made it my role not to just be a member of a group who could be targeted by bias but to do something about it," she says, "to investigate, understand it, and communicate with others."

One series of studies tested her ability to remain detached. In the 19th century, prominent scientists such as Louis Agassiz and Paul Broca embraced "racial science," which saw black people as an evolutionary step between apes and white people. Long since discredited, such ideas have not disappeared. In the aftermath of the 1991 Rodney King beating and Los Angeles riots, patrol radio chatter revealed officers referring to black people as "gorillas in our midst," among other derogatory descriptions.

Eberhardt wondered about the staying power of those associations. Using the familiar dot-probe technique, she primed a group of students with subliminal images of black or white faces, followed by vague images of various animals, including apes. Students primed with black faces detected ape images more quickly. It didn't seem to be bigotry—the students completed a survey indicating that they did not consciously harbor bias. When she reversed the process, students primed with line drawings of apes directed their attention to black faces more quickly. In a follow-up study, students who viewed a video of police beating a black man after glimpsing an ape were more likely to say the beating was deserved.

The work, Fiske says, is "very disturbing but also spot-on in terms of the science." Eberhardt doesn't know how those ideas made their way into the minds of her study participants, mostly white undergraduates. Few had heard of 19th century race science. And she and her colleagues did the study before the Obama and Trump presidencies, when racist language resurged on the internet and in politics.

Eberhardt admits the findings shook her. "This wasn't just a bias, where you think, 'This group is not as good as my group,'" she says. "This was like placing African Americans outside the human family altogether."

ABOUT A 90-MINUTE DRIVE from Eberhardt's office is a police department with a troubled history, in one of the nation's most violent cities. The Oakland police have a long record of scandals. In the late 1990s, four officers calling themselves the Riders would brutalize and plant evidence on people. In a more recent outrage, a group of officers passed around a 19-year-old prostitute. The department has been the target of lawsuits and sanctions, including a $10.9 million payout in a class action lawsuit resulting from the Riders fiasco. The court-enforced agreement also required the department to reform itself, spelling out 51 tasks. In 2014, Eberhardt's group was enlisted to help with task No. 34—

IMAGES: EBERHARDT *ET AL.*, *JOURNAL OF PERSONALITY AND SOCIAL PSYCHOLOGY*, **87**, (2004) 876

making traffic stops, the most common interactions between civilians and police, less discriminatory and confrontational.

Eberhardt saw a way to bring science to bear. Working with Deputy Chief LeRonne Armstrong, she collected 1 year's worth of "stop data" from forms Oakland police filled out when they pulled someone over. The data included reasons for the stop, the race of the driver, whether the car was searched, and whether the driver was handcuffed or charged with an offense.

After analyzing more than 28,000 traffic stops, Eberhardt and her team found that the data supported the residents' distress. Sixty percent of the stops involved black people, who made up only 28% of the city's population. Oakland police, who were both black and white, searched or handcuffed black drivers at nearly three times the rate for white drivers. Black people were also stopped more often than white drivers for minor violations and indistinct reasons rather than "actionable intelligence" such as a traffic violation or outstanding warrant.

"Before these results, our officers would have told you that close to 90% of those stops were based on intelligence," Armstrong says. "The data said it was actually under 5%." A more recent study by the Computational Policy Lab at Stanford showed the same pattern nationwide.

Equally troubling was the tone of those encounters, as Eberhardt's team documented in unprecedented detail. They collected body camera footage from 1 month's worth of traffic stops in 2014—981 stops by 245 officers—and hired professional transcribers to capture everything police said in those stops, nearly 37,000 utterances. Then the researchers used a combination of human raters and machine learning algorithms to analyze those utterances on scales of respect, formality, impartiality, and politeness.

The results, published in *PNAS* in 2017, confirmed that police routinely used less respectful language when speaking to black people than to white people. The researchers didn't hear ethnic slurs or overt insults. But phrases such as "I'm sorry to have to pull you over, but ..." or "Drive safely, ma'am," were reserved mostly for white people, whereas black motorists more often heard phrases such as "All right, my man. Just keep your hands on the steering wheel real quick."

"You can see how the justice system plays out in day-to-day language and social interaction," says Rob Voigt, a computational linguist at Stanford who took part in the project. Both black and white police officers used similar disrespectful language with black motorists, which tells Eberhardt that although some of that behavior may be racist, most probably arises from unconscious patterns that somehow get transmitted during training or fieldwork. "It's one of the things we want to study more," she says.

Even before knowing the roots of the behavior, Eberhardt's team worked with the police department to change it by creating role-playing exercises to train police to conduct traffic stops more respectfully. Nowadays, Oakland's officers make stops only for documented reasons and ignore minor violations such as double parking. As a result, the number of traffic stops dropped by nearly half from 2016 to 2018, and stops involving black drivers dropped by 43%.

Eberhardt and her team are developing virtual reality programs to train officers in various traffic stop scenarios, and they are expanding their data-gathering and reform work to other urban police departments. The researchers are also looking at how traumatic incidents in one community, such as a police shooting, can affect police and citizen behaviors in another.

Some Oakland activists have questioned the need for the city to fund an ongoing relationship with researchers from Stanford to the tune of hundreds of thousands of dollars. Armstrong disagrees. "We've paid many consultants over the years to come in and do studies, but they'd leave us with their findings and would walk away," he says. "Dr. Eberhardt's team decided to stay on and help us through that process ... and that's why we got so much buy-in from our officers."

THERE'S NO EASY ANTIDOTE for unconscious bias. The legacy of past policies, such as segregated neighborhoods and mass incarceration, creates conditions that trickle down to individual brains. Eberhardt argues that increased diversity in neighborhoods, workplaces, and schools could help, and she calls for studying the effectiveness of the antibias training that some institutions are introducing.

She, like other experts, says one effective countermeasure is to slow down, to move your thinking from the primitive, reactive parts of the brain to more reflective levels. The Oakland police department has tried to buy time for officers by changing its foot pursuit policy. Rather than chase a suspect into a blind alley, officers are encouraged to call for backup, set a perimeter, and make a plan before closing in. As a result, the number of police shootings and officer injuries dramatically dropped.

Another tack is to introduce what Eberhardt calls friction into the system. When the founders of the social networking company Nextdoor saw that too many "suspicious character" postings on its online bulletin boards were based solely on race, they called Eberhardt in to consult. From her advice, they created a checklist so people logging on had to specify suspicious behavior before describing appearance. That friction caused people to evaluate their reasoning before making bias-based assumptions, and the incidence of racial profiling fell by more than 75%.

But dealing with bias is also a personal enterprise of pausing and examining one's assumptions. "We could practice adding friction to our own lives," Eberhardt says, "by interrogating ourselves and slowing ourselves down ... just being aware when we're beginning to make stereotypic associations." As she concludes in her book, "There is hope in the sheer act of reflection. This is where the power lies and how the process starts." ■

Douglas Starr is a journalist in Boston.

Words matter

In recordings of 981 traffic stops by the Oakland, California, police, Jennifer Eberhardt's team found that officers tended to address white drivers respectfully, but more often used informal and brusque language with black drivers.

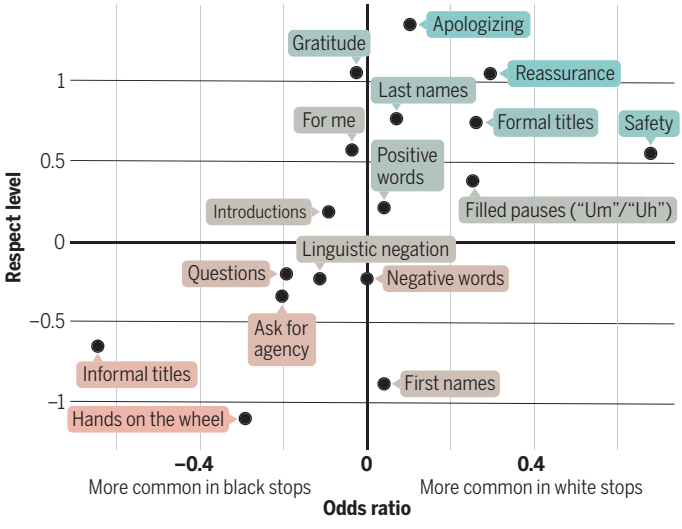

CREDITS: (GRAPHIC) N. DESAI/*SCIENCE*; (DATA) VOIGT *ET AL.*, *PNAS*, **114** (2017) 6521

INSIGHTS

PERSPECTIVES

ANTHROPOLOGY

Neanderthal surf and turf

Did our closest ancestors adapt to the sea in the same way as early *Homo sapiens*?

By **Manuel Will**

Humans share a deep bond with coasts and oceans. More than 500 million people live in coastal communities, and beaches and seafood attract tourists from around the world. Archaeological research in southern Africa revealed early human coastal adaptations that occurred at least as far back as ~160,000 years ago (*1*) in the Middle Stone Age (MSA)—the cultural period of the earliest *Homo sapiens*. Paleolithic sites across Africa and elsewhere support the hypothesis that coastal adaptations have a long and lasting history. Yet, scientists still debate the importance of coastal adaptations for the evolution and dispersal of *H. sapiens* during the Pleistocene (Ice Age) (*2*). On page 1443 of this issue, Zilhão *et al.* (*3*) tackle an even more contentious issue with wide-ranging implications for human evolution: Did Neanderthals share our species' interest in oceans and their inhabitants?

Archaeologists have taken various stances on whether Neanderthals possessed coastal adaptations comparable with those of MSA modern humans. The answers range from emphatic affirmation (*4*, *5*) to outright rejection (*6*), although intermediate positions do exist. The intermediate view grants Neanderthals adaptations to coasts and their resources that differ in some ways from their modern counterparts (*7*, *8*). A brief account of Pleistocene coastal archaeology helps to clarify the importance of the new study.

In the 1920s, archaeologists reported Neanderthal sites with shellfish remains

Department of Early Prehistory and Quaternary Ecology, University of Tübingen, Schloss Hohentübingen, 72070 Tübingen, Germany. Email: manuel.will@uni-tuebingen.de

PHOTOS: (CLOCKWISE FROM TOP) JOSÉ PAULO RUAS; JOÃO ZILHÃO; MARINA DE ARAÚJO IGREJA; MARIANA NABAIS; JOÃO ZILHÃO (2)

Neanderthals left stone tools and the remains of marine and terrestrial animals at Figueira Brava.

on Gibraltar, a narrow peninsula at Spain's southern Mediterranean coast (*9*). Since then, archaeologists have discovered additional European sites containing thin scatters of artefacts, shellfish, and the occasional seal dating from between ~100,000 and 40,000 years ago (*4*, *10*), although these discoveries sometimes lack data to verify their anthropogenic origins. Since the 1990s, excavations from the African MSA uncovered coastal sites of early modern humans dating back to ~160,000 to 50,000 years ago. These sites contain dense accumulations of stone tools and shellfish (*1*, *8*), including spectacular finds such as beads made from shells and shell containers for paint (*11*, *12*). Some of these localities exhibit true shell-midden deposits—sediments almost completely composed of shells—otherwise known only from the Holocene or recent hunter-gatherers. Contrasting this newfound record with the comparatively meager remains from the European Mediterranean coast has raised doubts about Neanderthals' ability to exploit coasts in a similarly efficient and enduring manner (*6*).

The findings of Zilhão *et al.* shed new light on these issues. The authors report on excavations at a cave site, Figueira Brava, along the Atlantic coast of Portugal, where marine productivity is high. Neanderthals left stone tools and the remains of consumed animals within a well-documented stratigraphic sequence dated, by use of various chronometric methods, to ~106,000 to 86,000 years ago. The menu included a variety of surf and turf: shellfish, crabs, and fish from the ocean but also waterfowl, red deer, horse, and even pine nuts. This evidence shows a flexible approach to subsistence that encompassed all surrounding ecosystems.

The authors convincingly demonstrate that Neanderthals collected marine foods, with densities of shellfish and fish falling well into the range of the highest frequencies of rich southern African MSA sites. The variable but consistent signal of these behaviors across multiple archaeological layers at Figueira Brava provides robust evidence of systematic, long-term coastal adaptations by Neanderthals during the Pleistocene. Furthermore, the new findings appear to show the same kinds of interactions with coasts and marine foods as those of early *H. sapiens*. Thus, the current study refutes the theory that Neanderthals were not able to efficiently extract diverse ocean resources in large quantities (*6*). However, one archaeological site does not make a pattern: Figueira Brava constitutes a single high-density example comparable with key MSA sites of southern Africa. Whether this situation resulted from high marine productivity and favorable preservation, as suggested by Zilhão *et al.*, remains a hypothesis in need of further research along the Atlantic coasts of Portugal and Spain.

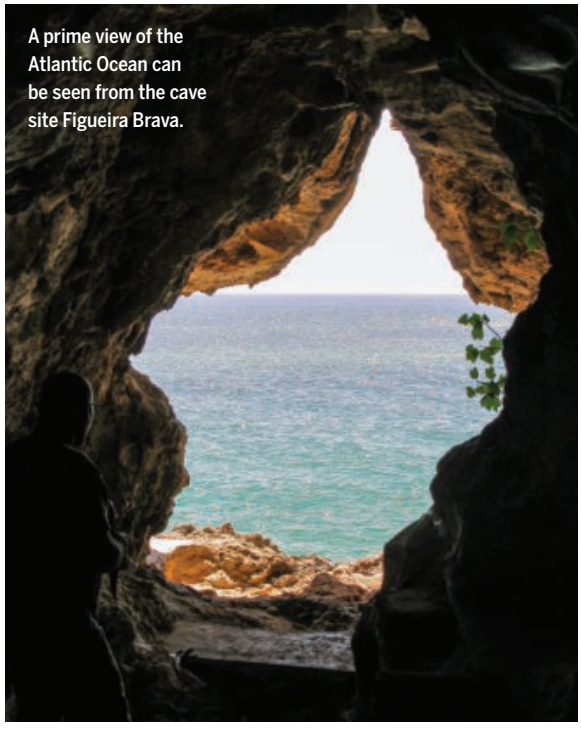

A prime view of the Atlantic Ocean can be seen from the cave site Figueira Brava.

Ultimately, scientists should take a step back and look at the broader picture: Considering the entire archaeological record of coastal adaptations by Neanderthals and MSA modern humans from ~60 sites (*8*), the new study adds important, high-resolution data showing that under some circumstances, the two species shared comparable behaviors. However, taking into account all available evidence from coastal sites, the behavioral records of early *H. sapiens* show more intense occupations of shorelines and use of marine resources compared with Neanderthals'. Furthermore, several MSA sites have yielded shell beads, whereas such ornaments are absent from most coastal Neanderthal sites (*8*), as is the case at Figueira Brava.

After a century of studies in Europe and a much shorter research history in Africa, multifaceted differences in scale and magnitude remain between the two records, and these are hard to explain with preservation and ecology alone. As with many recent archaeological findings in Pleistocene Europe—including rare jewelry made from eagle talons and potential cave art by Neanderthals (*13*), which sparked wide interest and lively debate—the new study narrows the gap between *H. sapiens* and its closest ancestors but does not close it.

Where should the archaeology of early coastal adaptations go from here? The key to expanding our knowledge about the origins, extent, and importance of coastal adaptations across species of *Homo* is to further explore African and Eurasian seashores that escaped Pleistocene sea-level highstands and occur beside productive oceans with narrow continental shelves. This endeavor might require aid from underwater archaeology (*14*). Wider implications of coastal adaptations for human evolution must be reconsidered in an interspecies framework. Marine foods play a crucial role in some scenarios for the evolution of the human brain because they are particularly rich in omega-3 fatty acids and other brain-selective nutrients (*15*). Interdisciplinary studies involving archaeology, biochemistry, and neuroscience could examine the long-term cognitive and health effects of the consumption of variable amounts of seafood, both in *H. sapiens* and in Neanderthals. On the basis of increasing evidence from coastal landscapes, open questions about dispersal corridors and refugia of archaic and modern humans might likewise need a fresh look and renewed fieldwork. Considering current interest, the coast is clear for these lines of research. ■

PHOTO: JOÃO ZILHÃO

REFERENCES AND NOTES

1. C. W. Marean *et al.*, *Nature* **449**, 905 (2007).
2. N. Boivin, D. Q. Fuller, R. Dennell, R. Allaby, M. D. Petraglia, *Quat. Int.* **300**, 32 (2013).
3. J. Zilhão *et al.*, *Science* **367**, eaaz7943 (2019).
4. C. B. Stringer *et al.*, *Proc. Natl. Acad. Sci. U.S.A.* **105**, 14319 (2008).
5. M. Cortés-Sánchez *et al.*, *PLOS ONE* **6**, e24026 (2011).
6. C. W. Marean, *J. Hum. Evol.* **77**, 17 (2014).
7. D. A. Fa *et al.*, *Quat. Int.* **407**, 16 (2016).
8. M. Will, A. W. Kandel, N. J. Conard, *J. World Prehist.* **32**, 33 (2019).
9. D. Garrod *et al.*, *J. R. Anthropologic. I Inst.* **58**, 33 (1928).
10. M. C. Stiner, *Honor Among Thieves: A Zooarchaeological Study of Neandertal Ecology* (Princeton Univ. Press, 1994).
11. C. Henshilwood, F. d'Errico, M. Vanhaeren, K. van Niekerk, Z. Jacobs, *Science* **304**, 404 (2004).
12. C. S. Henshilwood *et al.*, *Science* **334**, 219 (2011).
13. D. L. Hoffmann *et al.*, *Science* **359**, 912 (2018).
14. G. Bailey, J. Harff, D. Sakellariou, Eds., *Under the Sea: Archaeology and Palaeolandscapes of the Continental Shelf* (Springer, 2017).
15. S. C. Cunnane, K. M. Stewart, Eds., *Human Brain Evolution–The Influence of Freshwater and Marine Food Resources* (Wiley-Blackwell, 2010).

10.1126/science.abb3568

CANCER

Deciphering cancer clues from blood

Circulating tumor cells are accessible indicators of real-time cancer biology

By **Ning Ma** and **Stefanie S. Jeffrey**

Cancer is associated with considerable morbidity and mortality, and despite therapeutic advances, it still represents the second leading cause of death worldwide (*1*). As cancers grow, evolve, and spread, they shed circulating tumor cells (CTCs), as well as other tumor-associated cells and products, into the bloodstream. Capturing and analyzing CTCs or other tumor-associated cells and products from a patient's blood sample can provide insight into a particular cancer's biology, response to treatment, and/or potential therapeutic targets (*2*). CTCs are heterogeneous; a pressing question concerns which CTCs represent those directly involved in metastasis, the major cause of cancer-related death. On page 1468 of this issue, Ebright *et al.* (*3*) identify genes in patient-derived CTCs encoding ribosomal proteins (RPs) that were associated with metastatic progression in mouse models, poor outcome in patients, and alterations in global translation. These findings could point to potential biomarkers or targets for future metastatic cancer therapies.

Tumors and their metastases are spatially and temporally heterogeneous, highly influenced by the context of the microenvironment in which they grow and their exposure to immune cells, stromal cells, and cell products (*4*). As tumors evolve according to their intrinsic biology, their environment, and drug selection pressures, genetic, epigenetic, and transcriptional alterations can diverge (*5*). Moreover, biomarker and therapeutic target discordance may occur between the primary tumor and metastases, and even between different metastases, in the same patient. This makes optimal treatment selection a challenge throughout the course of disease.

Because metastases are commonly multifocal, it is impractical, invasive, and potentially dangerous to biopsy each one to identify changing biomarkers that may influence subsequent drug selection. Instead, sampling blood or other bodily fluids such as urine, saliva, or tears—known as "liquid biopsy"—facilitates the analyses of cells or tumor-associated products that may offer a more comprehensive snapshot of tumor burden and its molecular diversity throughout the body at any given time. Liquid biopsy components under investigation include CTCs, either separate or aggregated with immune cells; circulating endothelial, stem, and stromal cells; cell-free components such as DNA and RNAs; and numerous other factors, such as extracellular vesicles (see the figure). Currently approved clinical use of liquid biopsy is limited but expanding, with a few approved tests for cancer screening or for identification of specific actionable mutations that guide cancer drug treatment, especially when tissue biopsy is not possible. Multiple studies are under way for early diagnosis, monitoring of tumor recurrence, evaluation of treatment response, and identification of emerging targets or resistance indicators during disease progression (*6*, *7*).

CTCs are heterogeneous live cells in blood; some retain the capability of seeding or reseeding metastases and thereby contribute to increased metastatic growth. Ebright *et al.* provide a singular approach to determining metastatic CTC subsets: They captured CTCs from patients with hormone receptor–positive (HR^+) metastatic breast cancer, the most common subtype. They cultured the CTCs and transduced them with a library of single guide RNAs to allow genome-wide transcriptional activation (CRISPRa) (*8*). The cells were then injected in mice, and the highly expressed genes that were associated with lung metastases were identified. They found expected genes, such as oncogenes or those involved in transcriptional and translational regulation, cell motility, and cell cycle progression. But they also unexpectedly found that metastatic CTCs expressed genes encoding multiple RPs, which were associated with increased global translation.

Human cells show plasticity. Epithelial-to-mesenchymal transition in cancer is a state whereby epithelial cells lose cell polarity and cell adhesion proteins, becoming more invasive and migratory—an important step in metastasis. Mesenchymal-like cells may revert by mesenchymal-to-epithelial transition, gaining epithelial properties as they integrate and grow in distant organs. CTCs and CTC clusters are heterogeneous even in the same blood sample (*9*) and may show epithelial, mesenchymal, and hybrid phenotypes (*10*, *11*). Ebright *et al.* found that high RP–expressing CTCs captured from the blood of patients with HR^+ breast cancer showed increased expression of epithelial markers and decreased expression of mesenchymal markers, and that these patients had worse overall survival. Their work implies that epithelial cell fate may be associated with higher ribosomal content and a greater propensity for metastasis.

When CTC cell lines were transduced to overexpress specific RPs and then injected into the tail veins of mice, metastases devel-

A snapshot of metastatic cancer biology

Tumor-associated cells and products intravasate into the bloodstream, circulate, extravasate into tissues, and enable metastatic tumor growth in distant organs. Circulating tumor cells (CTCs) captured from a blood sample reflect the diversity of cells from a primay tumor and different metastases.

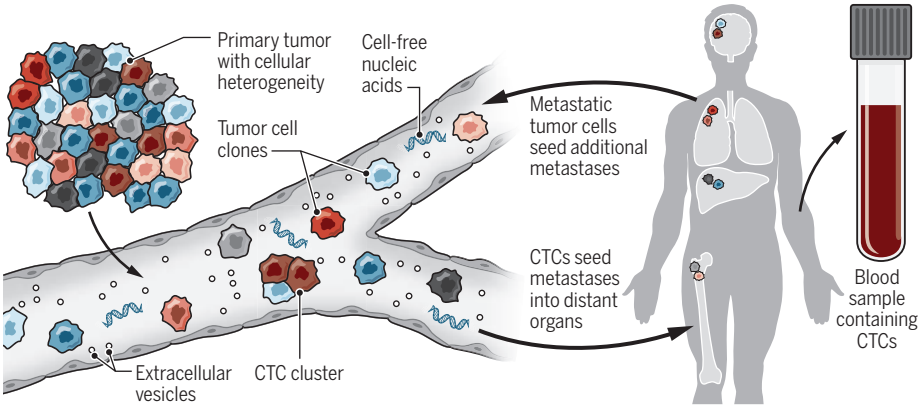

GRAPHIC: KELLIE HOLOSKI/*SCIENCE*

Department of Surgery, Stanford University School of Medicine, Stanford, CA, USA. Email: ssj@stanford.edu

oped that were larger and more numerous than those observed in mice injected with parental CTC cell lines. Metastases were reduced by treating mice with combination therapy whereby one drug inhibited the elongation step of protein synthesis (i.e., inhibiting translation) and another suppressed cell cycle progression. Such therapies might be efficacious in patients whose CTCs show high RP gene expression, although this requires clinical corroboration. The association among epithelial-like CTCs, high RP gene expression, poor clinical outcome, and drugs that inhibit translation would need to be experimentally confirmed in other cancer types to determine whether this can be generalized.

Cellular, cell-free, and particulate components of whole blood provide a dynamic database of functional information. CTCs and circulating tumor DNA (ctDNA) provide evidence of tumor recurrence sooner than radiologic changes, but their utility as clinical assays is limited by factors such as specificity and sensitivity as well as the availability of effective drugs. Although ctDNA may be more easily measured, CTCs are advantageous for elucidating metastatic processes and identifying treatment targets for clinical testing or drug development because they represent cancer cells that survive after drug therapy. Unfortunately, only a fraction of cancer patients will have sufficient numbers of CTCs available to grow, analyze, and therapeutically test using cell culture or mouse models (*12*–*15*). Such models may take months to generate, and patients with advanced cancer may not be able to wait that long. Future research must include the development of new technology platforms to enable real-time drug testing to better understand disease progression. ■

REFERENCES AND NOTES

1. F. Bray *et al.*, *CA Cancer J. Clin.* **68**, 394 (2018).
2. N. Ramalingam, S. S. Jeffrey, *Cancer J.* **24**, 104 (2018).
3. R. Y. Ebright *et al.*, *Science* **367**, 1468 (2020).
4. D. Hanahan, R. A. Weinberg, *Cell* **144**, 646 (2011).
5. N. McGranahan, C. Swanton, *Cell* **168**, 613 (2017).
6. S. S. Jeffrey, M. Toner, *Lab Chip* **19**, 548 (2019).
7. K. Pantel, C. Alix-Panabières, *Nat. Rev. Clin. Oncol.* **16**, 409 (2019).
8. S. Konermann *et al.*, *Nature* **517**, 583 (2015).
9. A. A. Powell *et al.*, *PLOS ONE* **7**, e33788 (2012).
10. M. Yu *et al.*, *Science* **339**, 580 (2013).
11. M. Yu *et al.*, *Science* **345**, 216 (2014).
12. L. Keller, K. Pantel, *Nat. Rev. Cancer* **19**, 553 (2019).
13. A. Soler *et al.*, *Sci. Rep.* **8**, 15931 (2018).
14. A. Lallo, M. W. Schenk, K. K. Frese, F. Blackhall, C. Dive, *Transl. Lung Cancer Res.* **6**, 397 (2017).
15. M. Bleijs, M. van de Wetering, H. Clevers, J. Drost, *EMBO J.* **38**, e101654 (2019).

ACKNOWLEDGMENTS

N.M. is supported by the John and Marva Warnock Research Fund. S.S.J. is supported in part by the Stanford Catalyst for Collaborative Solutions. S.S.J. serves as an expert adviser for Ravel Biotechnology.

10.1126/science.abb0736

GRAPHIC: A. KITTERMAN/*SCIENCE* BASED ON A. KESSLER/UNIVERSITY OF BERGEN

OCEANOGRAPHY

Surprises for climate stability

An ocean sediment record reveals chaotic ocean circulation changes during warm climates

By **Thomas F. Stocker**

Instabilities in Earth's climate system have intrigued scientists ever since analyses from Greenland ice cores revealed climate variations over the last hundred thousand years (*1*, *2*). Abrupt changes were not singular events but a pervasive feature of the last ice age. Studies pointed to the ocean, specifically the Atlantic Meridional Overturning Circulation (AMOC), as a possible origin of these large swings (*3*, *4*). Their occurrence in the distant past of the last ice age and their absence in the past 8000 years suggested that we are living in times of relative climate stability. On page 1485 of this issue, Galaasen *et al.* (*5*) report that over the past 500,000 years, there were disruptions in the formation of the North Atlantic Deep Water mass—an essential driver of the AMOC—during interglacial periods. This suggests that substantial reductions or instabilities of the AMOC could also occur in a future warmer climate.

The AMOC transports warm surface waters from the Southern Hemisphere to the north. When these waters reach the northern North Atlantic, they lose heat, and the increased density causes them to sink, creating the North Atlantic Deep Water mass. Galaasen *et al.* provide a high-resolution sediment record from a core situated in the deep return path of the AMOC. It shows substantial and rapid changes in past warm periods.

The Eirik Drift, located south of Cape Farewell, Greenland, is formed by the North Atlantic deep current. The sedimentation rate at site U1305 in the deep parts of this drift permits an unprecedented view into the dynamics of the deep northern North Atlantic ocean. Galaasen *et al.* discovered large and abrupt water mass changes during each of the warm interglacial periods during the last 500,000 years. At a resolution of better than a century, stable isotope ratios of carbon, measured on the calcareous shells of bottom-dwelling foraminifera, exhibited large and irregular swings of water mass distribution, a frequent push and pull between waters of northern and southern origin.

High values of carbon isotope ratios indicate that the formation of North Atlantic Deep Water is vigorous and associated with strong AMOC. Low values, by contrast, suggest a weak or absent overturning with deep-water mass characteristics suggestive of a southern origin. Transitions between apparently two states occur rapidly, whereas either AMOC state can last for several centuries. This signature, so familiar during the last

Climate and Environmental Physics and Oeschger Centre for Climate Change Research, University of Bern, CH-3012 Bern, Switzerland. Email: stocker@climate.unibe.ch

Ocean circulation growing chaotic

Simulated Atlantic Meridional Overturning Circulation (black) during 10,000 years of the last interglacial warm period about 120,000 years ago. Amplitudes of the AMOC grow and become chaotic within a limited window of the slowly changing solar energy input (blue).

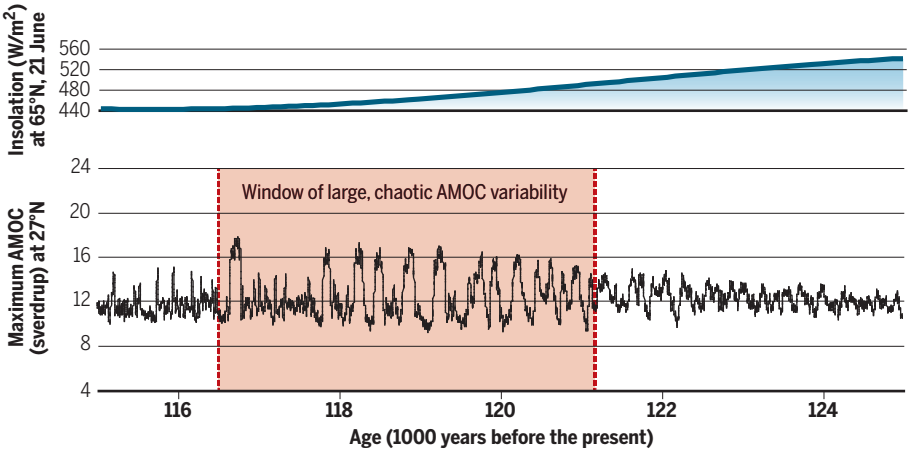

ice age (*6*) and before (*7*), was unexpected in warm climates. That Galaasen *et al.* observed this during the interglacial periods suggests that this ocean circulation system may be much less stable than previously thought.

In the Holocene (the present warm epoch), fluctuations in the carbon isotope ratio in deep-ocean sediments are small, except for a well-documented 8200-year cooling event. But in previous warm periods, most notably during Marine Isotope Stage 11c some 400,000 years ago, many century-scale fluctuations in deep-water mass characteristics are registered at site U1305 of the Eirik Drift. Changes in deep ocean circulation are often associated with ice-rafted debris that originates from large ice sheets surrounding the North Atlantic basin. This debris is found in many sediment cores in the North Atlantic (*8*). However, in the record of Galaasen *et al.* from Eirik Drift, these fluctuations occur primarily in the absence of such debris, which suggests that the deep ocean circulation system may be naturally unstable or sensitive to rather small perturbations.

Galaasen *et al.* underpin their climate reconstruction with simulations over 10,000 years, using a coupled climate model of reduced complexity. Their results show that under the climate conditions of 125,000 years ago (the previous interglacial), the AMOC evolves from small-amplitude centennial variations through a period of nonperiodic self-sustained fluctuations of the AMOC with large amplitudes (see the figure). Fluctuations manifest themselves as two states: a stronger one with an AMOC close to the mean of today and a weaker state. Transitions between these two states are faster than the residence time in either state. This resembles the fingerprint of a nonlinear system with two attractors (*9*). Their model is forced by the Milankovitch cycles (*10*), the slow changes of solar energy input caused by variations in the orientation of Earth's rotation axis with respect to the Sun. This results in small changes of the seasonal distribution of solar irradiation. In a certain window lasting several millennia, the simulated AMOC shows fluctuations with amplitudes larger by as much as a factor of 5. Beyond this window, the variability decreases and the circulation again becomes more stable. In a nonlinear system, unstable chaotic behavior can emerge when a parameter is changed slowly and moves into a critical range of this parameter (*9*). Outside this range, the same nonlinear system may be strictly periodic or even stationary.

Large changes in overturning circulation without an external perturbation were also identified in other coupled ocean-atmosphere models in a specific parameter window (*11*). The largest amplitudes of these self-sustained oscillations are found close to the location of the sediment core that Galaasen *et al.* studied. However, in that study, self-sustained oscillations are periodic and predictable, which is in contrast to the more chaotic fluctuations in the paleoceanographic reconstruction from Eirik Drift and in the model simulation depicted in the figure.

Models show that a reduction of AMOC causes a cooling of the sea surface of the North Atlantic with consequent substantial regional cooling. Galaasen *et al.* do not provide a reconstruction of concurrent surface ocean conditions and their changes on the centennial time scale during the past four interglacials. It would be an important avenue of further research to quantify the climatic impact of these AMOC fluctuations.

Nevertheless, Galaasen *et al.* add to the debate on tipping points in the climate system. So far, climate models seem to agree that the AMOC will gradually decline over the 21st century, owing to the increase in atmospheric CO_2 concentrations and the consequent heating (*12*). This evolution may actually be irreversible. In addition to slow, irreversible, or abrupt transitions of the AMOC, there may also be the possibility that a gradual anthropogenic push of the climate system would move it into a state where variability becomes larger in amplitude and more chaotic. Galaasen *et al.* show that this was a possibility for the AMOC in the past and that such behavior should be factored in when assessing the risk of tipping points in the future.

Much will be learned about tipping points in the climate system through research within the European Commission's Horizon 2020 program, and continued monitoring, which is essential (*13*). But a comprehensive assessment about tipping points, their risks, and their impact is still missing. To provide robust and actionable information to decision-makers and people, this should be a priority for the seventh assessment cycle of the Intergovernmental Panel on Climate Change. ■

REFERENCES AND NOTES

1. W. Dansgaard *et al.*, *Nature* **364**, 218 (1993).
2. W. Dansgaard *et al.*, in *Climate Processes and Climate Sensitivity*, J. E. Hansen, T. Takahashi, Eds. (American Geophysical Union, Washington, DC, 1984), pp. 288–298.
3. H. Oeschger *et al.*, in *Climate Processes and Climate Sensitivity*, J. E. Hansen, T. Takahashi, Eds. (American Geophysical Union, Washington, DC, 1984), pp. 299–306.
4. W. S. Broecker *et al.*, *Nature* **315**, 21 (1985).
5. E. V. Galaasen *et al.*, *Science* **367**, 1485 (2020).
6. N. J. Shackleton *et al.*, *Paleoceanography* **15**, 565 (2000).
7. B. Martrat *et al.*, *Science* **317**, 502 (2007).
8. S. R. Hemming, *Rev. Geophys.* **42**, RG1005 (2004).
9. E. N. Lorenz, *J. Atmos. Sci.* **20**, 130 (1963).
10. J. Laskar *et al.*, *Astron. Astrophys.* **428**, 261 (2004).
11. G. Vettoretti, W. R. Peltier, *Geophys. Res. Lett.* **43**, 5336 (2016).
12. P. Bakker *et al.*, *Geophys. Res. Lett.* **43**, 12252 (2016).
13. E. Frajka-Williams *et al.*, *Front. Mar. Sci.* **6**, 260 (2019).

10.1126/science.abb3569

GENOMICS

Quantifying mutations in healthy blood

Mutated clones in healthy tissues may hold clues for the earlier detection of malignancy

By **Christina Curtis**

Over time, somatic mutations accrue during normal cell division and tissue self-renewal. The patterns of age-associated somatic mutation have been perhaps most extensively characterized in the blood. Although many mutations are functionally benign, a subset represents premalignant initiating events in hematopoietic stem cells that result in clonal expansion. This clonal hematopoiesis confers an increased risk of hematologic malignancy (after the accrual of additional cooperating mutations), as well as cardiovascular disease and overall mortality (*1*). On page 1449 of this issue, Watson *et al.* (*2*) investigate the clonal architecture and evolutionary dynamics of healthy blood by analyzing targeted DNA sequences of ~50,000 blood cancer–free individuals. They find that positive selection for beneficial mutations, rather than neutral genetic drift, dictates the genetic diversity of normal blood. The identification of mutant clones and their associated fitness benefits could improve disease risk stratification.

The high mutational burden in rapidly dividing tissues such as the colonic epithelium was initially described in 2000 (*3*). The application of modern sequencing techniques has since revealed that other healthy tissues, including the blood, are littered with somatic mutations that accrue during normal cell division (*1*, *4*–*6*). However, the relative contributions of random (neutral) genetic drift, arising from fluctuations in allele frequencies in the population, versus positive selection for advantageous mutations on clonal expansions are unknown. Indeed, cancer is thought to arise from a mutated cell that clonally expands while

Departments of Medicine and Genetics, Stanford University School of Medicine, Lorry Lokey Stem Cell Research Building, Stanford, CA 94305, USA.
Email: cncurtis@stanford.edu

continuing to accrue additional mutations that result in diversification, but the dynamics of this process are poorly understood.

Using mathematical modeling, Watson *et al.* show that the genetic diversity of cells in the blood is predominantly determined by positive selection, rather than neutral genetic drift. Further, they quantified the fitness benefit of specific mutations and demonstrate that those that confer high fitness are associated with risk of progression to acute myeloid leukemia (AML) (see the figure). In particular, mutations in epigenetic modifiers, including DNA methyltransferase 3α (*DNMT3A*), tet methylcytosine dioxygenase 2 (*TET2*), additional sex combs–like 1 (*ASXL1*), and the tumor suppressor tumor protein 53 (*TP53*), were estimated to be highly fit, and, consistent with prior studies, the frequency of such mutations in an individual's blood stratifies risk of AML (*7*, *8*). The authors also made the surprising finding that a large number of mutations (~2500) in clonal hematopoiesis genes conferred moderate to high fitness, highlighting a broad and rugged fitness landscape resulting from the potential for interactions between mutations. More generally, application of the approach of Watson *et al.* to broader-coverage sequencing data (that extend beyond known hotspots) has the potential to reveal additional preleukemic drivers and thus has implications for predicting progression to disease. Of note, different mutations in the same gene are not necessarily equivalent, and mutations may confer fitness benefits through different mechanisms or no fitness benefit at all. Functional phenotypic studies will be needed to resolve these differences.

The study of Watson *et al.* demonstrates the value of moving beyond cataloging mutations to modeling genomic data within an evolutionary framework. Previous studies have sought to quantify evolutionary dynamics from genomic sequence data in established cancers (*9*–*11*). For example, the relative fitness of a clone has been inferred from variant allele frequency distributions in solid tumors (*9*) and in chronic lymphocytic leukemia (*10*). Given that tissue architecture is inherent to solid tumors and influences clonal dynamics, other studies have sought to explicitly model tissue spatial constraints when inferring the extent of selection versus neutral drift during tumor growth (*11*). Of note, selection was found to be more stringent in premalignant Barrett's esophagus compared with matched invasive esophageal carcinomas from the same individual (*9*), consistent with the strong selection for specific mutations that occurs before overt hematologic malignancy, as observed by Watson *et al.*

Premalignant tissues such as Barrett's esophagus, colorectal adenomas, and ductal carcinoma in situ in the breast are understudied, but molecular characterization may help to define the earliest alterations in these tissues, features associated with progression to invasion, and patients at risk. In recognition of the need for such studies, the U.S. National Cancer Institute Human Tumor Atlas Network will generate precancer atlases for a variety of tissues—including breast, colon, lung, and skin—with a focus on spatial and temporal molecular profiling (*12*). Clonal evolution in the blood is distinct from that in tissues, both because it is not subject to the same spatial constraints and because of the large number of hematopoietic stem cell progeny in the circulation, and this may potentially explain the widespread clinical consequences of clonal hematopoiesis (*13*).

Clonal hematopoiesis has additional implications for response to therapy, bone marrow transplantation, and noninvasive detection of malignancy based on mutational profiling of circulating cell-free DNA with a reported prevalence of 10 to 20% of individuals over 65 (*13*). However, this is a low estimate owing to the constraints of analytic sensitivity. Error-corrected sequencing methods capable of detecting single-nucleotide variants in the 0.01% frequency range will enable refined estimates of the prevalence of clonal hematopoiesis, which may be pervasive after middle age.

In myeloproliferative diseases and blood cancers, a shift away from reliance on clinical and morphological features toward molecular classification is under way (*14*, *15*). A major objective of research is to develop predictive models that inform patient stratification on the basis of specific mutations and their frequency (*7*, *8*). By demonstrating that the size of clones harboring pathogenic mutations and the distribution of fitness effects influence the pace of progression, Watson *et al.* provide further rationale for such efforts. Critically, however, numerous factors can influence these dynamics—including infection, inflammation, and treatment—making long-term disease forecasting more challenging. Future studies will likely leverage longitudinal cohorts that follow subjects over time. The integration of clinical, demographic, and phenotypic information with detailed genomics will yield insights into clonal dynamics and mutation rates of healthy blood, as well as molecular features associated with prognosis and aging. Such information should also provide clues as to how to better detect and intercept early malignancy, when therapeutic intervention should be most effective. ■

Age-related mutation accumulation in the blood

DNA sequencing of blood cells from ~50,000 individuals and mathematical modeling revealed the accumulation of mutations with age and associated fitness advantages. Positive selection for pathogenic mutations results in clonal hematopoiesis and increased risk of acute myeloid leukemia.

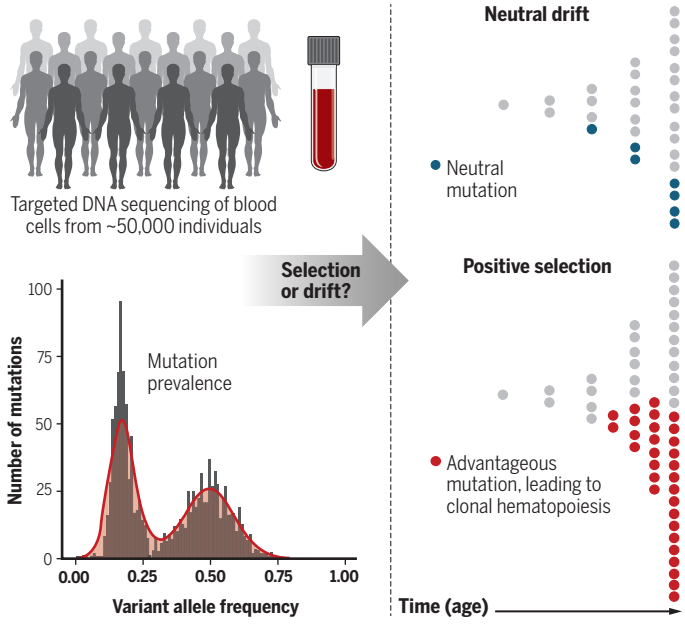

GRAPHIC: KELLIE HOLOSKI/*SCIENCE* BASED ON SOTTORIVA *ET AL.*, *BIOCHIM. BIOPHYS. ACTA* **1867**, 95 (2017) (CC BY-NC)

REFERENCES AND NOTES

1. R. L. Bowman et al., *Cell Stem Cell* **22**, 157 (2018).
2. C. J. Watson *et al.*, *Science* **367**, 1449 (2020).
3. J. L. Tsao *et al.*, *Proc. Natl. Acad. Sci. U.S.A.* **97**, 1236 (2000).
4. I. Martincorena *et al.*, *Science* **362**, 911 (2018).
5. H. Lee-Six *et al.*, *Nature* **561**, 473 (2018).
6. K. Yizhak *et al.*, *Science* **364**, eaaw0726 (2019).
7. S. Abelson *et al.*, *Nature* **559**, 400 (2018).
8. P. Desai *et al.*, *Nat. Med.* **24**, 1015 (2018).
9. M. J. Williams *et al.*, *Nat. Genet.* **50**, 895 (2018).
10. M. Gruber *et al.*, *Nature* **570**, 474 (2019).
11. R. Sun *et al.*, *Nat. Genet.* **49**, 1015 (2017).
12. S. Srivastava *et al.*, *Trends Cancer* **4**, 513 (2018).
13. D. P. Steensma, B. L. Ebert, *Exp. Hematol.* S0301-472X(19)31133-6 10.1016/j.exphem.2019.12.001 (2019).
14. E. Papaemmanuil *et al.*, *N. Engl. J. Med.* **374**, 2209 (2016).
15. J. Grinfeld *et al.*, *N. Engl. J. Med.* **379**, 1416 (2018).

10.1126/science.aba9891

MEDICINE

Antisense oligonucleotides for neurodegeneration

Promising clinical results for Huntington's disease give hope for other diseases

By **Blair R. Leavitt**[1] *and* **Sarah J. Tabrizi**[2]

Antisense oligonucleotides (ASOs) have the potential to reduce, restore, or modify RNA and protein expression. Thus, they can target disease pathogenesis by altering the expression of mutant proteins (*1*). The recent regulatory approval of ASOs for the pediatric motor neuron disease spinal muscular atrophy has provided a regulatory pathway for additional ASO therapies in other central nervous system (CNS) diseases. Developments in ASO chemistry and advances in CNS delivery methods have enabled ASOs to enter clinical trials to treat Huntington's disease (HD). There are currently no available treatments that slow or prevent progression of HD, but two ongoing ASO-based clinical programs have shown promising results. Additionally, clinical trials of ASOs to treat amyotrophic lateral sclerosis (ALS), Parkinson's disease, and Alzheimer's disease are under way, with more in development for other neurodegenerative diseases. It is hoped that ASO-based approaches will provide effective disease-modifying therapies for HD and similar neurodegenerative diseases soon.

ASOs are synthetic single-stranded DNA analogs, generally 16 to 22 bases long, that selectively bind to specific complementary RNA targets. A limitation of the original ASOs developed for clinical use was susceptibility to rapid degradation by cellular nucleases, but chemical modifications have since been introduced to improve their therapeutic utility. For example, substitution of sulfur for oxygen and modification of the 2′-position of the sugar to generate 2′-*O*-methoxyethyl (MOE)–modified ASOs with a phosphorothioate backbone resulted in improved nuclease resistance, potency, and better tolerability in patients. Further modifications of the ribose sugar moiety have led to improved efficacy by improving binding to target RNAs (*2*).

[1]Centre for Molecular Medicine and Therapeutics, and Centre for Huntington's Disease at UBC Hospital, Department of Medical Genetics and Division of Neurology, Department of Medicine, University of British Columbia and BC Children's Hospital, Vancouver, Canada. [2]Huntington's Disease Centre, Department of Neurodegenerative Disease, and UK Dementia Research Institute at UCL, UCL Queen Square Institute of Neurology, University College London, London, UK. Email: s.tabrizi@ucl.ac.uk; bleavitt@cmmt.ubc.ca

ASOs can modulate target gene expression through numerous pathways (*2*). One such pathway is through ribonuclease H1 (RNase H1) recruitment (see the figure). Following selective binding of the ASO to its target RNA, an RNA-DNA hybrid is formed, which induces messenger RNA (mRNA) degradation by RNase H1. Other pathways depend on the specific location of ASO binding to target RNA (*2*). For example, ASOs can target intron-exon junctions in precursor mRNA (pre-mRNA) to modulate RNA splicing. ASO-mediated target suppression can be achieved by modulating splicing to introduce an out-of-frame deletion, which results in reduced protein expression by nonsense-mediated decay of the corresponding transcript. ASOs targeting translation start sites in RNA can block the binding of ribosomes, leading to complete translational inhibition of target protein synthesis.

There are several advantages of ASOs over related RNA interference approaches. Unlike interfering RNAs, ASOs are readily taken up by neurons and have clear dose-dependent and reversible effects. ASOs also have the advantage that they will not saturate endogenous microRNA pathways, a potential cause of toxicity in short inhibitory RNA (siRNA)–based approaches. ASOs are generally highly selective and can target both introns and exons because they bind to pre-mRNA rather than mature mRNAs, allowing selection of specific target sequences for ASOs that do not appear anywhere else in the genome. However, unlike viral-mediated siRNA approaches, repeated administration of ASOs is required to maintain therapeutic effects. This may also be an advantage: If an unwanted outcome occurs from suppression of target RNA (or perhaps off-target RNA), ASOs have an off-switch because their effects are fully reversible.

HD is an inherited autosomal dominant neurodegenerative disorder characterized by a triad of motor, cognitive, and psychiatric features. HD typically arises in midlife, with inexorable progression of disability over 10 to 15 years. HD is caused by an abnormally expanded CAG repeat in one allele of the huntingtin (*HTT*) gene, which is expressed as a long polyglutamine tract in the mutant protein (mHTT) that confers a toxic gain of function (*3*). Proposed pathological mechanisms caused by this alteration include early transcriptional dysregulation, synaptic dysfunction, altered axonal vesicular trafficking, impaired proteostasis, mHTT aggregation, defective nuclear pore complex and nuclear-cytoplasmic transport, oxidative damage, mitochondrial dysfunction, and extrasynaptic excitotoxicity (*3*). ASOs provide a direct approach to reduce mHTT expression by targeting its RNA for destruction, thus preventing translation of mHTT and proximally targeting the primary cause of disease (*1*). Two ASO-based therapeutic programs have recently entered clinical testing for the treatment of HD.

The HTT-targeting ASO RG6042 acts through RNase H1 to target both wild-type and mutant HTT pre-mRNA and results in HTT lowering. Preclinical studies of similar HTT-targeting ASOs in transgenic HD mouse models demonstrated decreased mHTT concentrations in brain tissue, correction of striatal gene transcriptional dysregulation, and phenotypic improvement (*4*). mHTT lowering was prolonged following even a single cerebral spinal fluid (CSF) injection of ASO in these mice, suggesting that the effects of these ASOs will be prolonged in HD patients. Lumbar intrathecal infusion of a similar ASO into nonhuman primates was also shown to effectively lower HTT in many brain regions relevant for HD pathology (*4*).

In the initial phase 1/2a trial of intrathecal RG6042, treatment of 46 patients resulted in a significant dose-dependent reduction in CSF concentrations of mHTT by 40 to 60% (*5*). The CSF concentrations of mHTT continued to decline during this short study, suggesting that maximal reduction was not reached. The amount of CSF mHTT reduction observed in this study is consistent with the reductions in mHTT required for significant phenotypic improvement in transgenic mouse models of HD (*4*). Intrathecal delivery of RG6042 ASO was safe and well tolerated in HD patients, and its potential effects on disease modification and clinical outcomes are being assessed as part of GENERATION HD1, a large phase 3 trial involving more than 800 early-stage HD patients (NCT03761849).

Selective lowering of mHTT is theoretically an attractive approach to HD therapy because it would overcome concerns about the potential loss of wild-type HTT function. Selective mHTT-lowering ASOs that target specific single-nucleotide polymorphisms (SNPs) linked to the CAG expansion show promise in preclinical models of HD (*6*). A chemistry plat-

form has been developed that allows the chirality of the phosphorothioate modification to be controlled during ASO synthesis. It is reported that "stereopure" ASOs have improved activity, stability, and specificity compared with stereoisomer mixtures (*7*). Two clinical trials were initiated in 2017 to assess two different stereopure ASOs targeting specific HD-associated SNPs. These studies require precise genotyping to ensure that the targeted SNP is accurately phased to the *HTT* allele with the CAG expansion. Not all individuals with HD can be treated with this SNP-based approach, and it is estimated that the two ASOs being tested are applicable to ~65% of HD patients from North America or Europe. Each ASO is given as a monthly intrathecal bolus over three consecutive months, and it was recently reported that at the highest dose tested, one of the ASOs caused a modest 12.4% reduction in CSF concentration of mHTT. An additional higher-dose cohort will now be added to this trial (NCT03225833).

It is not known whether HTT lowering or mHTT-selective lowering will be most effective. Both approaches have distinct strengths and limitations, and this question will ultimately be answered empirically in clinical efficacy trials. Preclinical studies in a humanized transgenic HD mouse model found that the benefits of ASO-mediated lowering of total HTT concentrations by 75% were similar to those of ASOs that selectively reduced mHTT. These and other studies have suggested that the degree of mHTT lowering is the most critical parameter for preclinical efficacy (*8*). A substantial advantage of HTT-lowering approaches compared to SNP-based selective mHTT targeting is the potential to develop a single therapeutic agent for the entire HD population.

There is optimism that HTT-targeting ASOs may lead to a viable disease-modifying therapy for HD, as well as the development of ASOs for other neurodegenerative diseases associated with aberrant protein production. Following a substantial preclinical development program, an ASO targeting superoxide dismutase 1 (SOD1) was found to be safe and well tolerated after lumbar intrathecal infusion in a phase 1 trial for the treatment of SOD1 mutated ALS (*9*). A more potent MOE-modified ASO (ISIS-$SOD1_{Rx}$) is being evaluated in a phase 1/2a clinical trial (NCT02623699). Promising preclinical data have also been generated using ASO-based approaches for Parkinson's disease, targeting leucine-rich repeat kinase 2 (*LRRK2*, NCT03976349) and α-synuclein (*10*); for Alzheimer's disease by targeting Tau protein (*11*), which is currently in a phase 1 clinical trial (NCT03186989); and for prion diseases by targeting the prion protein PRP (*12*).

ASO-based therapies are also of interest in diseases whose etiology is similar to that of HD, such as the polyglutamine protein–related forms of spinocerebellar ataxia (*13*) that are caused by polyglutamine inclusions, and in frontotemporal dementia (FTD) with Tau or TAR DNA-binding protein 43 (TDP-43) pathologic inclusions. Indeed, ASOs that lower ataxin 2 expression have shown benefit in mouse models of both spinocerebellar ataxia 2 and TDP-43–related FTD (*14*). The most common genetic cause of ALS and FTD is a GGGGCC repeat expansion in the *C9ORF72* gene that induces RNA-mediated neurotoxicity. ASOs that selectively target these repeat-containing RNAs may be a useful therapeutic approach to this class of diseases (*15*); clinical trials are in development.

ASOs have already changed the landscape of therapeutic development for neurodegenerative diseases. Their advancement in the clinic will require continued development and research, including optimization of target sequence selection, improving biological activity, testing new delivery technologies, and maintaining an appropriate safety profile. Improving the delivery of ASOs to target cells is an important area of future development, including intrathecal pumps and the use of lipid-based and polymer-based nanocarriers. Such delivery systems will potentially improve the controlled release of ASOs and cell and tissue specificity, and may provide additional protection from nuclease degradation. Beyond potency and specificity, another crucial feature of a good candidate molecule is the ability to reach its intracellular target at sufficient concentration. Given the substantially increased potency of MOE-modified ASOs, there are safety concerns regarding excessive on-target lowering of proteins (such as wild-type HTT) and potential off-target effects. It is critical that extensive preclinical assessment of both potency and off-target effects is performed in the development of new ASO therapies.

The ASO RG6042 is the result of more than a decade of extensive preclinical assessment in multiple model systems and is a testament to effective academic and industry collaboration in drug development. With a growing number of ASO therapeutics being tested in clinical trials, this exciting technology holds the potential to change the therapeutic landscape for many neurological and non-neurological conditions (including cancer, and cardiovascular, infectious, and pulmonary diseases) in the near future. ■

Reducing pathological protein expression

Antisense oligonucleotides (ASOs) are small, single-stranded DNAs that can bind specific RNA sequences on precursor messenger RNAs (pre-mRNAs) and mRNAs. The resulting RNA-DNA hybrid can induce ribonuclease H1 (RNase H1) degradation of the targeted RNA, modulation of splicing, or blockade of translation.

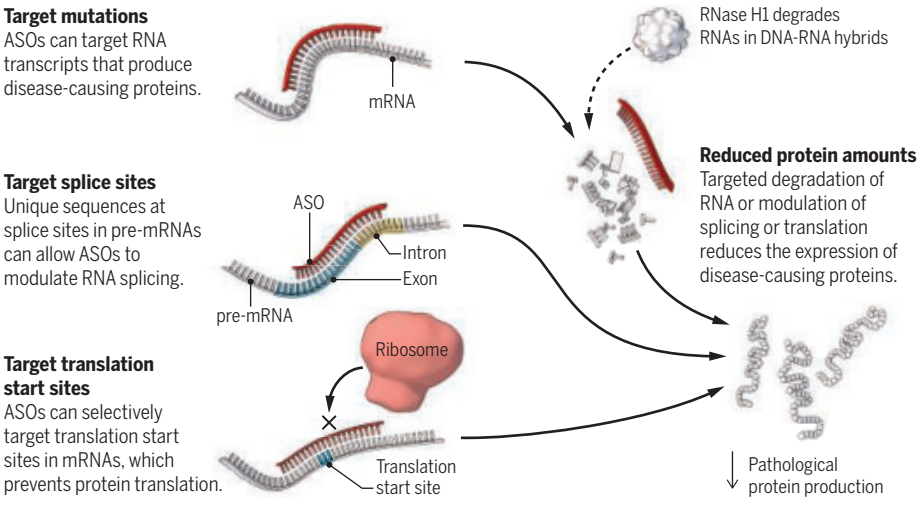

GRAPHIC: C. BICKEL/*SCIENCE*

REFERENCES AND NOTES

1. S. J. Tabrizi, R. Ghosh, B. R. Leavitt, *Neuron* **102**, 899 (2019).
2. C. Rinaldi, M. J. A. Wood, *Nat. Rev. Neurol.* **14**, 9 (2018).
3. G. P. Bates *et al.*, *Nat. Rev. Dis. Primers* **1**, 15005 (2015).
4. H. B. Kordasiewicz *et al.*, *Neuron* **74**, 1031 (2012).
5. S. J. Tabrizi *et al. N Eng. J. Med.* **380**, 2307 (2019).
6. N. H. Skotte *et al.*, *PLOS ONE* **9**, e107434 (2014).
7. N. Iwamoto *et al.*, *Nat. Biotechnol.* **35**, 845 (2017).
8. A. L. Southwell *et al.*, *Sci. Transl. Med.* **10**, eaar3959 (2018).
9. T. M. Miller *et al.*, *Lancet Neurol.* **12**, 435 (2013).
10. H. T. Zhao *et al.*, *Mol. Ther. Nucleic Acids* **8**, 508 (2017).
11. S. L. DeVos *et al.*, *J. Neurosci.* **33**, 12887 (2013).
12. G. J. Raymond *et al.*, *JCI Insight* **5**, 131175 (2019).
13. P. Gonzalez-Alegre, *Hum. Mol. Genet.* **28** (R1), R80 (2019).
14. L. A. Becker *et al.*, *Nature* **544**, 367 (2017).
15. J. Jiang *et al.*, *Neuron* **90**, 535 (2016).

ACKNOWLEDGMENTS

Both authors have undertaken paid consultancy regarding ASOs for Ionis Pharmaceuticals, Takeda Pharmaceuticals, and F. Hoffman-La Roche. B.R.L. is cofounder of Incisive Genetics Inc. and has associated patents pending.

10.1126/science.aba4624

POLICY FORUM

DIVERSITY AND INCLUSION

Leadership to change a culture of sexual harassment

The U.S. National Science Foundation is implementing and refining policies aimed at combatting harassment

By **France Córdova**

When we look at surveys of the scientific community, we see an overall trend: The presence of women, minorities, and other groups that have been historically subject to harassment tapers off in later career stages. This occurs despite those groups' strong interest and proficiency in science and engineering. As a primary public funding resource for science and engineering research and training, the U.S. National Science Foundation (NSF) has a responsibility to address such deficiencies. Shaping the research landscape is a strategic process that normally requires planning on the order of decades, but this is an issue that requires more immediate leadership and action. How, then, does an agency like NSF—which has considerable influence but limited direct authority—work with the community and other institutions to implement change on issues that cannot wait? The case of NSF's work to combat harassment in the science community, a persistent problem for decades that remains shockingly widespread, is illustrative.

A CHALLENGE FOR LEADERSHIP

As a university administrator and president, I encountered the issue of sexual harassment in science, but efforts to address specific cases were overshadowed by pervasive roadblocks to changing a culture that enabled harassment. After my appointment as director of NSF in 2014, I took the opportunity to confront this issue when then–NASA Administrator Charlie Bolden and I simultaneously posted letters to university presidents emphasizing that our agencies had no tolerance for harassment. We reminded universities that they could lose grant funding if they were not compliant with federal Title IX regulations against sex-based discrimination.

In late 2016, a National Academies of Science, Engineering, and Medicine (NASEM) committee convened to begin studying the prevalence, nature, and impact of sexual harassment in science, engineering, and medicine. NSF funded this effort because we needed an accurate accounting of the current scope and scale of the problem. As the NASEM committee worked through 2017, the #MeToo movement brought new light to the problem of sexual harassment. The sustained outcry created a moment where action on NSF's part could draw a greater level of public support than was previously possible. The detailed insights from the NASEM report would be an important factor in how we proceeded once it was released, but we did not need to wait for the committee to complete their work to begin our own. Ample existing data and anecdotal evidence show that harassment deters talent, destroys careers, and impedes the science and engineering enterprise. I decided that NSF needed to act quickly to find a way to give the agency a more operative role in addressing harassment, and that we would not be delayed by calls for more data.

How would our work this time be different, to achieve meaningful change on an issue that had defied correction for decades? To begin, we removed any uncertainty about our commitment to action and progress. I made it clear to NSF's leaders that this was a top priority for our entire organization and that staff were empowered to engage stakeholders, develop ideas, refine proposals, and make progress toward implementation of an antiharassment policy.

Then, we needed to create a robust mechanism to combat harassment. A campaign to simply reiterate our existing policy would be insufficient. We needed a solution that could be integrated into NSF's legal and policy framework without running afoul of other legal structures (including Title IX). Attempting to apply some new regulatory policy could create legal and technical challenges and would take considerable time. Instead, we identified our statutory grant-making authorities as the optimal solution. Adding a new term and condition (TC) directed specifically at harassment to our Proposal and Award Policies and Procedures Guide would place it alongside numerous other requirements that nearly 2000 institutions already agree to every year when they accept NSF funding.

DEVELOPING A COURSE FOR ACTION

The resulting harassment TC draws a connection between researcher behavior and NSF funding. It creates accountability and is auditable. It requires an NSF-supported institution to notify the agency within 10 days of taking any administrative action or making a final determination against a principal investigator (PI) or co-PI related to harassment, including sexual harassment or assault. After consulting with the awardee institution, NSF will determine whether it is taking appropriate action, such as requesting NSF approval to remove a PI and appoint a substitute. This determination would be based on factors that include the need to safeguard students and other researchers. If the institution's work is satisfactory, no further action from NSF is called for. If not, NSF may take action, including reducing or suspending the award. Notifications come to NSF through a secure, electronic system, and the information is sequestered within our Office of Diversity and Inclusion, separate from our other data systems and provided only to staff with a specified need to know.

Describing the TC is straightforward, but the process of crafting it required careful thought about how to create a unified requirement that accounts for gray areas that might arise due to the interplay of existing policies and procedures at institutions we support. Through the TC, NSF sets an expectation for accountability but provides flexibility. Like NSF's other award requirements, institutions have some discretion in how they

Director, National Science Foundation, Alexandria, VA, USA.
Email: programcomplaints@nsf.gov

ILLUSTRATION: DARIA KIRPACH/@SALZMANART

approach the TC. Disclosure to NSF is mandatory, but our hope is that we can approach this issue with the institutions as our partners and that the actions they take in harassment cases will help lead the way.

If there's a defining characteristic of how NSF operates, it's that our policies are shaped with research community input. We are cognizant of the need to avoid unnecessary burdens for proposers and awardees. After NSF leadership developed an initial proposal for the TC, we informed grantee organizations (*1*), then issued a call for public comment (*2*). The public comments were a tremendous help in shaping the final TC. Two examples include changing the reporting time frame from 7 days to 10 and requiring subawardee institutions to report determinations or administrative actions directly to NSF, rather than making the primary award recipient institution responsible.

Some comments raised concerns that institutions might avoid taking administrative action on harassment to get around NSF's reporting requirement. In response, NSF has developed an electronic, secure, anonymous harassment reporting system that can receive complaints directly from individuals. Although that system is new, individuals previously could report sexual harassment to NSF. That commenters were unaware of this indicates that we must communicate better.

NSF began outreach with stakeholder groups to provide assurances on some key issues of concern, such as confidentiality. NSF worked to clearly state what the TC is intended to do (ensure safety and security in NSF-supported projects and that proposed research can be carried out) as well as what it isn't (serve as a second investigation or remove funding that serves many because of the actions of a few).

NSF focused on feedback that helped improve the potential for successful implementation of the TC, not on comments predicated on harassment being overly complex as a basis for recommending inaction or delayed action. We devised what is, in our judgement, the best possible way for NSF to take immediate action when necessary. However, this process is not finished. We are still gathering data to help us refine the TC. We recognize that there are ongoing concerns from some parts of the community, some of which will likely result in modifications to our processes or be addressed through improved communication.

Some officials from the university community have questioned whether reporting is appropriate before their institutional processes to determine guilt or innocence are complete, including all appeals, which often take months if not years. NSF's concern at that stage is not the guilt or innocence of an individual—it's whether publicly funded research can continue under the conditions of the existing award agreement in a manner that ensures the safety of all personnel working on the award. We have heard concerns from those questioning how this TC interacts with Title IX and state laws, and the answer is that it doesn't—institutions are still expected to conform to all applicable laws and codes. And from some focused on specific cases, we have heard calls for NSF to take harsher or more dramatic action. For them, we are committed to explaining how and why we act in these cases and demonstrating that we do so consistently.

RIPPLE EFFECTS BEYOND NSF

Since the implementation of the TC in October 2018, NSF has received 24 harassment action notifications from institutions. The full implications cannot be expressed in a single number; one of our ongoing efforts is to refine metrics that better measure and express progress under the TC. But the impact has gone far beyond those particular cases. NSF has been proactive in our outreach to groups considering action of their own. We've already seen our actions ripple through the community as departments, universities, and scientific associations have set in motion plans to confront harassment in research environments. We have sought to amplify that work, identifying and sharing examples of codes of conduct developed by field sites, facilities, and other infrastructure we support. NSF seeks to build relationships that we can use to address other persistent cultural issues.

When one federal agency works on a culture-change issue, it creates opportunities for others to respond within their own domains. NSF has been in frequent communication with members of Congress and our partner agencies about exploring other possible ways to confront harassment. Shortly after we announced the TC, the National Institutes of Health expressed its commitment to new solutions (*3*). In September 2019, the White House Office of Science and Technology Policy established the Joint Committee on the Research Environment (JCORE) (*4*), with safe and inclusive research as one of its top priorities. JCORE's summary of objectives noted that harassment is "[W]here institutional leadership is extremely important" and called for an approach that addresses "cultural dimensions." Centralized federal leadership on this issue has the potential to spur change at an even greater scale.

NSF leaders have also been meeting with foreign counterparts, exchanging information and discussing how to effect change in legal and ethical frameworks that are often quite different from those of the United States. Camila García, Chile's Science, Innovation, and Technology attaché, indicated that NSF input helped jump-start the process that led to the Chilean government passing a new law to combat harassment in August 2019 (*5*). NSF has engaged with the European Commission, and harassment will be the topic discussed by the Global Research Council's (GRC) Gender Working Group at the 2020 GRC annual meeting, an area of focus NSF suggested.

Lasting change will require sustained involvement, both in terms of maintaining and refining the TC, as well as in helping maximize its benefits. NSF is continuing to assess how the TC is being implemented, identifying potential improvements and ways to streamline processes that have been found to be inefficient.

HOLDING OURSELVES ACCOUNTABLE

Culture change, within and especially across institutions, is never easy. When considering roadblocks, complications, and concerns from different sectors, the easiest option is usually inaction—and some will argue it's the most prudent as well. But we know that harassment is destructive for women and minorities, and for the research community writ large. For those who love science, research is where we can see humanity at its best, and it can be crushing to acknowledge that we often see the worst as well. We have a duty to live up to our ideals and make sure that science and engineering present real opportunities for everyone. We can reach that point by holding ourselves accountable as leaders, committing to taking as much action as quickly as we can within our ability to act. I hope that this serves as an example that others follow to inspire not just change, but change through leadership. ■

REFERENCES AND NOTES

1. NSF, Important notice no. 144: Harassment, 8 February 2018; www.nsf.gov/pubs/issuances/in144.jsp.
2. NSF, *Fed. Regist.* **83**, 47940 (2018); www.federalregister.gov/documents/2018/09/21/2018-20574/notification-requirements-regarding-findings-of-sexual-harassment-other-forms-of-harassment-or.
3. National Institutes of Health, The NIH Director, "Creating meaningful reforms to end sexual harassment in science," 12 December 2019; www.nih.gov/about-nih/who-we-are/nih-director/statements/creating-mean-ingful-reforms-end-sexual-harassment-science.
4. Executive Office of the President, Office of Science and Technology Policy, "Letter to the United States research community," 16 September 2019; www.whitehouse.gov/wp-content/uploads/2019/09/OSTP-letter-to-the-US-research-community-september-2019.pdf.
5. L. Wessel, "Bill to fight sexual harassment in universities approved by Chilean Senate," *Science*, eaaz2340, 22 August 2019; www./news/2019/08/bill-fight-sexual-harassment-universities-approved-chilean-senate .

ACKNOWLEDGMENTS

C. Lohse and R. Margetta contributed to the researching, drafting, and editing of this article. R. Davis, P. Hoyle, B. Cosgrove, J. Feldman, and A. Lupia contributed to review.

10.1126/science.abb5791

BOOKS *et al.*

Hemingway's six-toed "mitten" cats offer clues about how the genome assembles a body.

EVOLUTIONARY BIOLOGY

Evolution gets personal

Engaging anecdotes add intimacy to tales of Earth's 4 billion years of evolution

By **Michael A. Goldman**

Each December for decades now, I've spent a few days in Pacific Grove, California, attending the Asilomar Chromatin, Chromosomes, and Epigenetics Conference. Before reading Neil Shubin's *Some Assembly Required*, however, I never knew that the city's first female mayor, Julia Platt, was also an accomplished embryologist. Having been shut out of academic positions, which were, at the turn of the 20th century, seldom given to women, she pivoted instead to politics, where her legacy includes the establishment of a marine protected area in California's Monterey Bay. This anecdote is one of many intimate and thoughtful stories tucked into the pages of this brief overview of Earth's 4 billion years of evolution.

Shubin, an accomplished paleontologist and evolutionary biologist, begins his history in Victorian England, which, he writes, "was a crucible for enduring ideas and discoveries." "There is something poetic to the notion that knowing how DNA works in the history of life relies on ideas developed during an age when people didn't know that genes even existed," he continues.

Here, he relates the story of St. George Jackson Mivart, apprentice to Thomas Henry Huxley. Mivart, we learn, although initially a supporter of Darwin's theory of evolution, became a vocal critic, focusing on "the incompetency of natural selection to account for the incipient stages of useful structures." Darwin would respond to this criticism in the 1872 edition of *On the Origin of Species*, arguing that "This subject is intimately connected with that of the gradation of the characters, often accompanied *by a change of function*." These words, Shubin writes, "contain the seeds for a new way of seeing major transitions in the history of life."

Among the exciting topics covered in Shubin's sweeping evolutionary history are the transition to land-living animals, the origins of flight, the race for the double helix, and anecdotes from pioneering work in molecular evolution and gene regulation. He recounts the discovery of repetitive DNA sequences and Barbara McClintock's transposable elements, and he explores Richard Goldschmidt's controversial "hopeful monsters" hypothesis of macroevolution. We learn that Lynn Margulis submitted her dogma-defying endosymbiosis work to 15 journals before her insights were recognized—some assembly required, indeed.

Shubin also recounts the charming story of Susumu Ohno, the Japanese American geneticist whose research confirmed that gene duplication played a critical role in molecular evolution. Ohno, we learn, painstakingly weighed paper cutouts of chromosomes from different mammalian species and found that, although the chromosome numbers differed widely, the estimated total amount of DNA was similar in each case. When he moved on to salamanders, however, he was in for a surprise. Some had genomes far larger than those of humans. "With his cardboard cutouts, Ohno discovered something that billions of dollars of genome projects were to confirm decades later," writes Shubin.

Shubin argues that if we were to rerun the course of evolution multiple times, the results would most likely be the same. He refers to this as the inevitability of evolution, which stands in opposition to the theory that evolution is based on chance events, the outcome of which is contingent on specific conditions. But the experimental observations on which Shubin bases his argument—some of which originated in his own research—were made at the microscale. As Blount *et al.* have pointed out, "…repeatability is common when the founding populations are closely related, perhaps resulting from shared genetics and developmental pathways, whereas different outcomes become more likely as historical divergences become greater" (*1*). Furthermore, no experiments have yet accounted for cataclysmic events such as the Cretaceous-Paleogene extinction event.

Some Assembly Required
Neil Shubin
Pantheon, 2020. 288 pp.

One of the book's best features is a 30-page notes section at the end, in which each note could be fodder for an entire volume. These notes are separated by chapter, and many tell a short, engaging story, often accompanied by annotated suggestions for further reading. Readers will want to peruse this section and follow up on some of those readings. ■

The reviewer is at the Department of Biology, San Francisco State University, San Francisco, CA 94132, USA.
Email: goldman@sfsu.edu

REFERENCES AND NOTES

1. Z. D. Blount, R. E. Lenski, J. B. Losos, *Science* **362**, eaam5979 (2018).

10.1126/science.aba6134

ECONOMICS

Reversing the rise in midlife mortality

Stronger safety nets and health care reform could help mitigate "deaths of despair" in America

By **David Canning**

Life expectancy in the United States declined for 3 years in a row between 2014 and 2017. This is surprising in a world where we have grown accustomed to rising life expectancy. Anne Case and Angus Deaton's new book, *Deaths of Despair*, deals with three questions: Who is dying, why are they dying, and what can we do about it?

Case and Deaton have been rightly celebrated for identifying the large rise in U.S. deaths due to suicide, drugs, and alcohol, particularly among white males aged 45 to 54 who have not completed a 4-year degree. Here, they argue that a key social divide exists in America between those who have a bachelor's degree and those who do not and that deaths of despair also occur in white women. Furthermore, they suggest that the problem is more widespread; the stalled decline in heart disease mortality in the United States, against a backdrop of improvements in other countries, may be due, in part, to drugs and alcohol. Such deaths, they argue, are hidden "deaths of despair," and deaths are just the most visible manifestation of a broader crisis of widespread pain, addiction, and misery among the less educated.

Deaths of despair are not an exclusively American phenomenon. Similar deaths occurred in Russia after the fall of communism, and there is evidence that the recent decline in life expectancy in the United Kingdom is attributable to a rise in deaths of despair. Such deaths are the result of a breakdown in social systems that give people a sense of respect and meaning. America, however, may be particularly vulnerable to this phenomenon, because of its emphasis on individualism and its tendency to equate economic success with social value.

The reviewer is at the Department of Global Health and Population, Harvard T.H. Chan School of Public Health, Harvard University, Boston, MA 02115, USA. Email: dcanning@hsph.harvard.edu

When it comes to the factors driving despair, the book rejects a simple economic argument about poverty, jobs, immigration, globalization, automation, and the Great Recession. Case and Deaton note a decline not just in incomes for the less educated in the United States but also in a sense of purpose and a way of life that once included social bonds forged through trade unions, church, and marriage.

American adherence to the idea of meritocracy is, they believe, particularly undermining for the less educated. Despite overwhelming evidence of low intergenerational mobility in education and income levels in the United States, there is a strong cultural belief that poverty reflects personal shortcomings rather than a rigged economic system. Such beliefs may be preposterous, but they have proven difficult to overcome.

Originally documented in white men, deaths of despair occur in white women too.

PHOTO: ISTOCK.COM/VALENTINRUSSANOV

Case and Deaton also offer a scathing indictment of the U.S. health care industry, calling it a cancer at the heart of the economy. They describe the rise of the prescription opioid OxyContin, arguing that pharmaceutical companies put profits above people, leading to widespread addiction.

The authors place the blame squarely on corporations that use political lobbying to create market power and exploit the poor. Case and Deaton's solution for the failures of capitalism, however, is more capitalism,

Deaths of Despair and the Future of Capitalism
Anne Case and Angus Deaton
Princeton University Press, 2020. 324 pp.

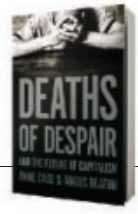

in the form of more-perfect markets. While they are undoubtedly right that it would be possible to reform the U.S. health care industry so that it provides both better and more accessible care at substantially lower costs, the pervasive and perverse role of money and lobbying in this industry makes it hard to see why they are optimistic about such a solution.

Case and Deaton see benefits in globalization and automation, although they recognize the need for policies to ensure that these benefits are equally distributed. They are in favor of a somewhat stronger safety net and modestly higher minimum wages. However, they oppose greater wealth redistribution through taxes as well as more radical ideas such as a universal basic income. Their proposed solutions may be insufficient if the underlying causes are indeed structural.

A criticism that has been leveled against Case and Deaton's work is that their focus on the rise in white midlife mortality downplays the much higher rates of mortality among black Americans. I have sympathy for the position that the scientific analysis of one issue does not imply a disparaging of the importance of other issues, and the book does cover the black-white mortality differential. However, a race-based analysis opens questions not just of science but of justice.

Indeed, the policies that the authors advocate not only would address deaths of despair, they would improve the health and welfare of the American people more generally. A clearer articulation of this point would have helped to assuage the view that the authors are focused only on policies that will improve the health of the white population. ■

10.1126/science.aba3036

Guidance about the effects of ibuprofen and other medications on coronavirus disease 2019 must be based on scientific evidence.

Edited by **Jennifer Sills**

Misguided drug advice for COVID-19

As pandemic coronavirus disease 2019 (COVID-19) continues to accelerate, the French Health Minister, Olivier Véran, has confused matters by claiming on Twitter that anti-inflammatory drugs like ibuprofen or cortisone could aggravate the infection (*1*). However, scientific evidence does not indicate that nonsteroidal anti-inflammatory drug (NSAID) consumption puts patients who otherwise might have mild or asymptomatic infection by severe acute respiratory syndrome–coronavirus 2 (SARS-CoV-2)—the virus that causes COVID-19—at risk of more severe disease. People taking NSAIDs for other reasons should not stop doing so for fear of increasing their COVID-19 risk.

NSAIDs work by suppressing prostaglandin synthases 1 and 2, colloquially known as COX-1 and COX-2. These enzymes produce prostaglandins (PGs), lipids that can trigger pain and fever. COX-2 produces most of the PGs relevant to pain and inflammation. NSAIDs selective for inhibiting COX-2 include celecoxib and diclofenac; ibuprofen is an NSAID that blocks both COXs. Minister Véran advised people to take paracetamol (acetaminophen) instead to treat a fever (*1*), but this guidance only adds to the confusion given that acetaminophen is also an NSAID (*2*).

We don't know with certainty whether NSAIDs could lead to more severe COVID-19 symptoms because PGs, such as PGE_2, PGD_2, and prostacyclin (PGI_2) can both promote and restrain inflammation. For example, the infection of certain immune cells (microglia) with a related coronavirus (not the one that causes COVID-19) activates a proinflammatory response (the inflammasome) to combat the pathogen; however, PGD_2 increases the expression of PYDC3, a putative inflammasome inhibitor, in certain immune cells in mice (*3*). The SARS coronavirus responsible for the 2003 outbreak directly binds to the COX-2 promotor and increases its expression (*4*), boosting PG production capacity, and there is also evidence that PGE_2 inhibits SARS coronavirus replication (*5*). Indomethacin, an NSAID, blocks coronavirus RNA synthesis but independently of COX inhibition (*6*). By contrast, COX-2–dependent PGE_2 attenuates the chronic antiviral lymphocyte response of unresolved viral infection (*7*). Based on these findings, if we see a clinical signal, we can rationalize it, but therein lies the challenge. Many clinical anecdotes remain stalled in biological plausibility.

The prospect of a rapid increase in COVID-19 cases prompts us to seek covariates of disease severity, from the consumption of certain drugs before infection, to human genetic variants (*8*), to demographic factors such as sex and environmental exposures. In the case of NSAIDs, commonly acquired without prescription, such determination requires documentation of drug exposure and evidence of PG suppression.

Considering all of this, should patients with clinically complicated SARS-CoV-2 infections be administered NSAIDs as a treatment? No. There is no evidence of benefit. If such a patient were also to have poor kidney function, maintenance of renal blood flow becomes critically dependent on vasodilator PGs, such as PGE_2 and PGI_2 (*9*). Such a situation might also predispose the patient to the gastrointestinal and cardiovascular complications of NSAIDs. However, until we have robust evidence, patients in chronic pain should continue to take their NSAIDs rather than turn to opiates. Given that the elderly appear to comprise the predominant at-risk group for severe COVID-19 at this time, an association between NSAIDs and the disease may merely reflect reverse causality—that is, infection makes you more susceptible to adverse effects of NSAIDs on the infection.

A similar rationale should be applied to evidence that coronaviruses use the angiotensin converting enzyme (ACE) 2 as a receptor for cellular entry (*10*). There has been speculation, but no clinical evidence, that consumption of ACE inhibitors might worsen the consequences of infection (*11*). Patients on ACE inhibitors should continue to take them rather than risk complications, such as stroke.

Garret A. FitzGerald
Institute for Translational Medicine and Therapeutics, Perelman School of Medicine, University of Pennsylvania, Philadelphia, PA 19104–5158, USA. Email: garret@upenn.edu

REFERENCES AND NOTES

1. K. Willsher, "Anti-inflammatories may aggravate Covid-19, France advises," *The Guardian* (2020).
2. F. Catella-Lawson *et al.*, *N. Engl. J. Med.* **345**, 1809 (2001).
3. R. Vijay *et al.*, *Proc. Natl. Acad. Sci. U.S.A.* **114**, E5444 (2017).
4. W. Yan *et al.*, *Int. J. Biochem. Cell Biol.* **38**, 1417 (2006).
5. C. Amici *et al.*, *Antivir. Ther.* **11**, 1021 (2006).
6. W. J. Sander *et al.*, *Front. Physiol.* **8**, 89 (2017).
7. K. Schaeuble *et al.*, *PLOS Biol.* **17**, e3000072 (2019).
8. Y. Cao *et al.*, *Cell Discov.* **6**, 11 (2020).
9. T. Grosser *et al.*, *J. Clin. Invest.* **116**, 4 (2006).
10. K. Wu, W. Li, G. Peng, F. Li, *Proc. Natl. Acad. Sci. U.S.A.* **106**, 19970 (2009).
11. L. Fang, G. Karakiulakis, M. Roth, *Lancet Resp. Med.* 10.1016/S2213-2600(20)30116-8 (2020).

COMPETING INTERESTS

G.A.F. has NIH support (R01HL141912-01) for atherosclerosis, prostaglandin inhibition, and checkpoint blockade. He is on the board of Kings Health Partners, London, UK; a member of the Governing Authority of the University of Limerick, Ireland; and on the Scientific Advisory Board of the Italian Science Agency. He is a Chief Scientific Advisor for *Science Translational Medicine*.

Published online 20 March 2020
10.1126/science.abb8034

Permanently ban wildlife consumption

Although the origin of severe acute respiratory syndrome–coronavirus 2 (SARS-CoV-2)—the virus that causes coronavirus disease 2019 (COVID-19)—has not been identified, it is clear that China's wildlife

PHOTO: THOMAS J. PETERSON/ALAMY STOCK PHOTO

market played an important role in the early spread of the disease ("Mining coronavirus genomes for clues to the outbreak's origins," J. Cohen, News, 31 January, https://scim.ag/COVID-19genomeclues). On 24 February, China's National People's Congress adopted legislation banning the consumption of any field-harvested or captive-bred wildlife in an effort to prevent further public health threats until a revised wildlife protection law can be introduced (*1*). We argue that China needs to seize this opportunity and permanently ban wildlife consumption.

Since the 2003 outbreak of zoonotic SARS, China has established several management policies and regulations to control wildlife markets (*2*, *3*). However, the vague definition of "wildlife" in the current policies and regulations results in enforcement confusion and loopholes. The current laws protect species of terrestrial and aquatic wildlife that are rare, beneficial, or economically or scientifically valuable (*4*), but they fail to differentiate captive-bred and wild populations. The sika deer (*Cervus nippon*), for instance, is a national, first-class protected species (*5*) and is also on the commercial breeding list (*2*). The indistinguishable differences between wild and captive populations provide opportunities for illegal bushmeat to be blended into exotic livestock and flow into the market (*6*).

Meanwhile, the protected species list has not been updated for nearly 30 years and covers only approximately two-thirds of the native wild species (*2*, *4*, *5*). The critically endangered spoon-billed sandpiper (*Calidris pygmaea*) (*7*) is still listed as a second-class protected animal (*5*). More than 1000 native species are absent from the protected list, including bats, which means that illegal hunting or trading of these species might not be punished and could threaten public health (*4*, *5*).

Furthermore, penalties for illegal wildlife distribution and consumption are not sufficiently severe. Wildlife consumption is not restricted. Therefore, the demand for wildlife products remains high, with high profits and mild punishments driving the dealers (*8*, *9*). In 2018, a man who poached about 8000 birds, including the critically endangered yellow-breasted bunting (*Emberiza aureola*) (*10*), was sentenced to pay only a US$10,000 fine (*11*).

The Chinese legislature should revise the wildlife protection law to ensure the effectiveness of the legislation. The definition of wildlife should be clarified as distinct from captive exotic populations. Meanwhile, a more stringent management plan for exotic livestock should be established, including an individual identification system, to increase the traceability of the exotic livestock products. The ability to technically distinguish captive from wild individuals will strengthen law enforcement. The list of protected species should be updated regularly, and all native wild species should be protected. The penalty for violating behavior should be increased, and wildlife consumption and possession should be treated as criminal offenses. Both the supply and demand sections of the wildlife trading chain should be strictly monitored and contained. China must act to permanently ban wildlife consumption in order to prevent future public health risks.

Nian Yang[1], Peng Liu[1,2], Wenwen Li[1], Li Zhang[1]*
[1]Key Laboratory for Biodiversity and Ecological Engineering of Ministry of Education, College of Life Sciences, Beijing Normal University, Beijing 100875, China. [2]School of Biological Sciences, The University of Hong Kong, Pokfulam, Hong Kong, China.
*Corresponding author.
Email: asterzhang@bnu.edu.cn

REFERENCES AND NOTES

1. CGTN, "China's top legislature approves decision to ban illegal wildlife trade" (2020); https://news.cgtn.com/news/2020-02-24/China-s-top-legislature-approves-to-ban-illegal-wildlife-trade-OIrtorGko0/index.html.
2. National Forestry and Grassland Administration, "Notice on issuing the list of 54 species of terrestrial wildlife such as sika deers with mature domestication and reproduction technologies for commercial operation," (2003); www.forestry.gov.cn/main/4818/20030805/796749.html [in Chinese].
3. National Forestry and Grassland Administration, "Notice on strictly prohibiting illegal hunting, and operating terrestrial wildlife," (2003); [in Chinese]. www.forestry.gov.cn/main/4818/content-796881.html.
4. National People's Congress Standing Committee, "The law of the People's Republic of China on the protection of wildlife" (2017).
5. National Forestry and Grassland Administration, "Lists of wildlife under special national protection" (1989); www.forestry.gov.cn/main/3954/content-1063883.html [in Chinese].
6. B. Gratwicke *et al*., *PLOS One* **3**, e2544 (2008).
7. BirdLife International 2018, *Calidris pygmaea* (The IUCN Red List of Threatened Species, 2018).
8. V. Nijman, M. X. Zhang, C. R. Shepherd, *Glob. Ecol. Conserv.* **5**, 118 (2016).
9. L. Zhang, F. Yin, *Biodivers. Conserv.* **23**, 2371 (2014).
10. BirdLife International 2017, *Emberiza aureola* (The IUCN Red List of Threatened Species, 2017).
11. Anhui Province Wuhe County People's Procuratorate, "Anhui province Wuhe County court verdict" (2018); http://wenshu.court.gov.cn/website/wenshu/181107ANFZ0BXSK4/index.html?docId=f1adbb9b475f404185c1a93801552c64 [in Chinese].

10.1126/science.abb1938

Wildlife consumption ban is insufficient

On 24 February, China's top legislature comprehensively prohibited the consumption of terrestrial wildlife to protect public health (*1*). The ban was enacted in response to the outbreak of coronavirus disease 2019 (COVID-19), which is considered to be linked to wildlife consumption (*2*). However, a total ban on the consumption of terrestrial wildlife alone is not enough to effectively protect public health from wildlife-associated diseases.

China's wildlife farming industry includes 6.3 million direct practitioners and a total output value of $18 billion (*3*). Curtailing this activity in a short period of time will be difficult. Conflicts may occur between the private interests of farmers and public health. It is also unclear how to dispose of the farmed animals. Killing them would be inhumane and could pose new risks to human health. Releasing them into unknown habitats in the wild could threaten ecosystem stability. Furthermore, given that banning the wildlife farming industry would threaten economic growth in many regions, implementation will be challenging.

Meanwhile, myriad traditional Chinese medicines are made from wildlife products, such as pangolin scales (*4*), snake bile (*5*), and bat feces (*6*), yet medicinal use of wildlife is not covered by the ban. Disease transmission risks exist during the process of hunting, storing, and transporting such wildlife for medicinal purposes, activities that will continue (*6*). Even if the ban could be effectively implemented, the traditional medicine industry would continue to threaten wildlife.

In addition to enacting a ban, the Chinese government should manage public health risks caused by wildlife-associated diseases by working together with wildlife protection and animal health agencies and making decisions about wildlife policies based on scientific evidence. Subsidies and financial support should be arranged to facilitate the transformation of the wildlife farming industry required by the ban, as well as made available to help transition away from the production of traditional Chinese medicine. As changes are made, the government should keep information timely and transparent so as to encourage public participation in the reform of the wildlife protection system.

Hongxin Wang[1]*, Junlin Shao[1], Xi Luo[2], Ziang Chuai[1], Shengyue Xu[1], Mingxia Geng[3], Zhouyi Gao[1]
[1]School of Government, Beijing Normal University, Beijing 100875, China. [2]School of Global Affairs, Kings College London, Strand London WC2R 2LS, UK. [3]College of Chinese Language and Literature, Beijing Normal University, Beijing 100875, China.
*Corresponding author.
Email: wanghongxin@bnu.edu.cn

REFERENCES AND NOTES

1. "The Decision of the Standing Committee of the National People's Congress on comprehensively prohibiting the illegal trade of wildlife, eliminating the bad habits of wildlife consumption, and protecting the health and safety of the people," Xinhua.net (2020); www.xinhuanet.com/politics/2020-02/24/c_1125620762.htm [in Chinese].
2. J. Li *et al*., *Lancet Infect. Dis.*, 10.1016/S1473-3099(20)30063-3 (2020).
3. "Report on sustainable development strategy of China's wildlife farming industry" (Consulting Research Project of Chinese Academy of Engineering, 2017) [in Chinese].
4. R. W. Byard, *Forensic Sci. Med. Pathol.* **12**, 125 (2016).
5. J. Still, *Complement Ther. Med.* **11**, 118 (2003).
6. T. M. Wassenaar, Y. Zou, *Lett. Appl. Microbiol.*, 10.1111/lam.13285 (2020).

10.1126/science.abb6463

COVID-19 drives new threat to bats in China

In China, bats are traditionally symbols of good luck and happiness (*1*). There are more than 1400 species of bats worldwide, but more than half of them have unknown or decreasing population trends (*2*). Unfortunately, the suggestion that coronavirus disease 2019 (COVID-19) may have originated in bats (*3*) is putting them at increased risk.

As COVID-19 has spread, people in China have started requesting that hibernating bats in or near their houses be expelled (*4*, *5*). Disturbing hibernating bats causes abnormal arousal patterns (*6*), which could lead to high bat mortality and potentially to the spread of other viruses. Moreover, the captured bats are being released into the wild, which is not their native habitat (*4*), posing further threats to their survival. These decisions are not based in fact; COVID-19 was linked to horseshoe bats (*3*), which do not hibernate in cities in China (*7*). The reputation of bats as virus carriers has even led to extreme suggestions of mass slaughter to protect public health (*8*). The exaggeration of bats' negative traits without regard for their positive ones could ultimately lead to their needless and intentional elimination.

Bats serve many critical roles for the ecosystem. They are biological—and economical—pesticides (*9*), and they contribute to the pollination and seed dispersal for many important plants (*10*). They are also excellent subjects for studies on healthy aging, cancer prevention, disease defense, biomimetic engineering, ecosystem functioning, and adaptive evolution (*11*). The need for public education about bats, including their positive and negative impacts, is urgent and vital to their conservation.

Huabin Zhao
Department of Ecology, Hubei Key Laboratory of Cell Homeostasis, College of Life Sciences, Wuhan University, Wuhan, Hubei 430072, China.
Email: huabinzhao@whu.edu.cn

COVID-19 has been linked to horseshoe bats, putting other bat species at risk.

PHOTO: MERLIN D. TUTTLE/SCIENCE SOURCE

REFERENCES AND NOTES

1. V. Sung, *Five-Fold Happiness: Chinese Concepts of Luck, Prosperity, Longevity, Happiness, and Wealth* (Chronicle Books, 2002).
2. W. F. Frick, T. Kingston, J. Flanders, *Ann. N.Y. Acad. Sci.* 10.1111/nyas.14045 (2019).
3. P. Zhou *et al.*, *Nature* **579**, 270 (2020).
4. "Beijing residents call police to remove bats from their houses" (2020); https://wxn.qq.com/cmsid/20200211A06BJG00 [in Chinese].
5. "Shanghai residents call Wildlife Conservation Department to expel bats around their houses" (2020); https://sh.qq.com/a/20200208/014581.htm [in Chinese].
6. J. R. Speakman *et al.*, *J. Appl. Ecol.* **28**, 1087 (1991).
7. N. M. Furey, P. A. Racey, in *Bats in the Anthropocene: Conservation of Bats in a Changing World*, C. Voigt, T. Kingston, Eds. (Springer, Cham, 2016).
8. "Ecological killing is under heated debate—revision of wildlife protection law must involve experts from all related fields" (2020); https://xw.qq.com/cmsid/20200214A0JB1X00 [in Chinese].
9. J. G. Boyles *et al.*, *Science* **332**, 41 (2011).
10. T. H. Kunz *et al.*, *Ann. N.Y. Acad. Sci.* **1223**, 1 (2011).
11. E. C. Teeling *et al.*, *Annu. Rev. Anim. Biosci.* **6**, 23 (2018).

10.1126/science.abb3088

Travel restrictions violate international law

From China's lockdown of the city of Wuhan (*1*) to U.S. restrictions on travelers from Europe (*2*) to border closures across a widening range of countries (*3*), governments are increasingly seeking to limit freedom of movement in response to the coronavirus disease 2019 (COVID-19). These travel restrictions have slowed, but not halted, the spread of the pandemic ("The effect of travel restrictions on the spread of the 2019 novel coronavirus (COVID-19) outbreak," M. Chinazzi *et al.*, Research Articles, published online 6 March, p. eaba9757). However, the necessity and benefits of this public health response are outweighed by its violation of international law. Under the International Health Regulations (2005) (IHR), binding on all World Health Organization (WHO) member states, health measures "shall not be more restrictive of international traffic and not more invasive or intrusive to persons than reasonably available alternatives" [(*4*), art. 43]. Given the effectiveness of community-based public health measures such as social distancing (*5*) and contact tracing (*6*), the necessity of travel bans must be weighed against less restrictive alternatives, increased global divisions, and violated IHR obligations (*7*).

The IHR seeks to govern how states can come together to address collective public health threats, whereas national travel bans drive nations apart through unnecessary economic isolation and rights violations. Although the IHR demands that health measures be implemented "with full respect for the dignity, human rights, and fundamental freedoms of persons" [(*4*), art. 3], travel restrictions unnecessarily infringe a range of basic rights related to the freedom of movement. In the COVID-19 response, systematic social distancing interventions recommended by WHO were bypassed in the rush toward emergency travel bans, limiting individual freedoms while stoking nationalist responses.

WHO has repeatedly praised the "aggressive" measures taken by governments (*8*), but forced restrictions on travel undercut the global solidarity that WHO seeks in responding to this common threat. Travel bans during past outbreaks have been found to have limited public health effectiveness (*9*), as the prevention of disease is inextricably linked to international cooperation and rights protections (*10*). Rather than implementing coercive travel restrictions, governments should follow WHO recommendations in realizing transparent governance, expanding testing capacity, and implementing social distancing to protect public health. The COVID-19 pandemic will test national systems, but the world is more secure when all national responses comply with both public health necessities and global health law.

Benjamin Mason Meier[1]*, Roojin Habibi[2], Y. Tony Yang[3]
[1]Department of Public Policy, University of North Carolina at Chapel Hill, Chapel Hill, NC 27599, USA. [2]Global Strategy Lab, York University, Toronto, ON M3J 2S5, Canada. [3]Center for Health Policy and Media Engagement, George Washington University, Washington, DC 20006, USA.
*Corresponding author. Email: bmeier@unc.edu

REFERENCES AND NOTES

1. "Report of the WHO-China Joint Mission on Coronavirus Disease 2019 (COVID-19)" (World Health Organization, Geneva, 2020).
2. "Fact sheet: DHS notice of arrival restrictions on China, Iran, and certain countries of Europe" (U.S. Department of Homeland Security, Washington, DC, 2020).
3. "Coronavirus: Travel restrictions, border shutdowns by country" *Al Jazeera* (2020).
4. WHO, "International Health Regulations, WHA 58.3" (World Health Organization, Geneva, ed. 2, 2005).
5. N. M. Ferguson *et al.*, "Report 9: Impact of non-pharmaceutical interventions (NPIs) to reduce COVID-19 mortality and healthcare demand" (Imperial College, London, 2020).
6. J. Hellewell *et al.*, *Lancet Glob. Health* **8**, e488 (2020).
7. R. Habibi *et al.*, *Lancet* **395**, 664 (2020).
8. K. Kupferschmidt, J. Cohen, *Science* **367**, 1061 (2020).
9. N. A. Errett *et al.*, *J. Emerg. Manag.* **8**, 7 (2020).
10. Human Rights Watch, Human Rights Dimensions of COVID-19 Response (2020).

10.1126/science.abb6950

Steps needed to keep immigrant scientists welcome

Experts discuss importance of foreign-born researchers at AAAS Annual Meeting

By **Becky Ham**

Restrictive immigration policies and new protections against foreign government influence on research have American scientists concerned about their ability to attract foreign talent to their laboratories and to collaborate with international colleagues, experts said in sessions throughout the American Association for the Advancement of Science's 2020 Annual Meeting.

At the meeting, held 13–16 February in Seattle, Washington, AAAS launched the Science Beyond Borders program to collect stories of immigrant scientists practicing and studying in the United States, to inform ongoing advocacy with the U.S. government and academic institutions to support foreign researchers.

The program, an initiative of the AAAS Center for Science Diplomacy and Office of Government Relations, grew out of concerns that travel restrictions, shortened visa stays and visa denials, and investigations into foreign researchers were having a negative effect on the U.S. research enterprise, said Joanne Padrón Carney, chief government relations officer at AAAS.

"While many people in government and at high levels at universities were engaged and speaking on the issues, we thought that the individual scientists, especially foreign nationals, did not have a voice," Carney said.

The scientists who have shared their stories with the program so far voice worries about "future collaborative opportunities…and some feel they are being perceived as not a good partner," said Carney. U.S. scientists are also weighing in with concerns about how the restrictions are affecting their workplace.

Foreign researchers benefit the U.S. economy, Chu said at the AAAS meeting.

PHOTO: COHEN PHOTOGRAPHY & VIDEO

Support for the Science Beyond Borders program comes from Jan and Marica Vilcek and the Vilcek Foundation. Jan, a first-generation American microbiologist, wanted to help highlight the contributions of foreign researchers to American science. The funding also allows AAAS to participate in roundtable forums on the issue and share information on current and new policies with stakeholders such as universities. At the AAAS Annual Meeting, the program sponsored a town hall forum on balancing global science pursuits with national security policies.

At the town hall and in similar forums, "we are hearing, increasingly, about this becoming an issue, and how the rhetoric of this administration has departed from the rhetoric of past administrations," said Julia MacKenzie, senior director of international affairs and acting director of the AAAS Center for Science Diplomacy. "All of these feed into each other in a way that we are hearing is very much felt in the lab and at universities."

There is a "cumulative effect of having foreign-born scientists feel unwelcome if they are already here, or feel that they don't want to come, or to seek other options," she added.

Carney said the Science Beyond Borders program will continue as long as needed. "This project needs to have a long shelf life because we don't know what the long-term effect of these policies will be," she said.

The United States could soon feel the strain if international collaborations break down and the flow of immigrant scientists is restricted, said outgoing AAAS President Steven Chu in his plenary address at the start of the meeting.

Chu noted that 34% of all U.S. Nobel laureates have been immigrants to the United States—not to mention the second-generation laureates like himself. Among U.S. Fortune 500 companies, he said, 45% were founded by immigrants or their children, with familiar-sounding names like Jeff Bezos and Elon Musk.

For decades, "graduate students and postdocs from foreign countries came to study in the United States and stayed because we are a free, open, and accepting society," said Chu, the co-recipient of the 1997 Nobel Prize in Physics and U.S. Secretary of Energy from January 2009 to April 2013.

Recent attempts to restrict foreign student visas and efforts to limit collaboration with international scientists could have a chilling effect on future U.S. scientific and economic gains, Chu warned.

Rising concerns about research espionage and conflicts of interest have made some U.S. universities and labs reluctant to open their doors to foreign researchers. Chu and others at the meeting pointed to recent investigations of Chinese national researchers in U.S. institutions by the Federal Bureau of Investigation and the U.S National Institutes of Health, regarding possible intellectual property theft, improper reporting of funders, and biases in the peer review process. Jodi Black, the deputy director of the National Institutes of Health's Office of Extramural Research, said in the town hall event that her office is working on cases involving about 180 individual scientists.

White House Office of Science and Technology Policy Director Kelvin Droegemeier, also speaking at the town hall event, said that new guidelines for auditing federally funded research to address possible research security issues are forthcoming. As chair of the National Science and Technology Council, Droegemeier has been meeting with representatives from academia and industry through the NSTC's Joint Committee on the Research Environment to find ways to strike a balance between open scientific discourse and national security.

"It's not about stigmatizing people from any particular race or country of origin…if you're part of our enterprise, we simply say, play by rules, because scholarly research demands that. It's a code of ethics that we sign up to," Droegemeier said.

In a press breakfast at the meeting, Chu said that "the vast majority of scientists are deeply ethical." But he agreed that work toward establishing a global culture of scientific ethics would be one way to reassure U.S. institutions and to encourage continued international partnerships.

The idea is not to force American scientific culture on other nations, said AAAS CEO Sudip Parikh, who also serves as the publisher of the *Science* family of journals. "I see the creativity and the energy and the vitality that's coming from some of the new nations at the forefront," he said, "but we want to make sure that the data ethics, the scientific conduct, the norms around how to take scientific funding, that those are part of that evolving global scientific culture."

The necessity for international scientific collaboration was laid bare at the meeting in discussions of the expanding threat from the novel coronavirus behind the COVID-19 pandemic. An additional plenary panel session and news briefing were added on-site in Seattle as the scope of the pandemic was coming into view. About 20 to 50 meeting participants from China were unable to attend the meeting, with some reaching out to their colleagues in online sessions.

RESEARCH

IN *SCIENCE* JOURNALS

Edited by **Michael Funk**

CLIMATE FORCING

Not a big deal after all

Do volcanic eruptions affect El Niño–Southern Oscillation (ENSO) variability? Models indicate that sulfate aerosols resulting from large eruptions can initiate an El Niño–like response in the tropical Pacific, but observations have not shown evidence of such behavior. Dee *et al*. present an oxygen-isotope time series of fossil corals from the central tropical Pacific to investigate ENSO's response to large volcanic eruptions during the past millennium. They found a weak tendency for an El Niño–like response in the year after an eruption, but not one that was statistically significant. These results suggest that large volcanic events have not triggered a detectable response in ENSO over the past thousand years and that their impact is small relative to the degree of natural variability. —HJS *Science*, this issue p. 1477

Mount Rinjani on the island of Lombok in Indonesia lies in a crater left behind by the massive eruption of the Samalas volcano in 1257 CE.

PHOTO: PATRICK TR/SHUTTERSTOCK

PLANT SCIENCE

Fruit abscission in response to drought

Plants faced with drought, or simply not quite enough water, may be more likely to drop their fruit prematurely. Reichardt *et al*. found that a small signaling peptide hormone, phytosulfokine, which was previously known for its ability to regulate plant cell growth, also drives fruit abscission. Processed, and thus activated, by a subtilisin-like protease, phytosulfokine in turn drives expression of the hydrolases that degrade the cell walls in the abscission zone, leading to dropped fruit. —PJH

Science, this issue p. 1482

ASTROPARTICLE PHYSICS

X-ray data constrain dark matter decay

Dark matter may consist of previously unknown forms of subatomic particles. An unidentified astronomical x-ray emission line has been interpreted as being caused by the decay of a dark matter particle. If this is correct, then dark matter in the halo of the Milky Way Galaxy should produce a faint emission line across the whole sky. Dessert *et al*. tested this hypothesis using observations by the XMM-Newton (X-ray Multi-Mirror Mission) space telescope. Analyzing blank-sky regions with a total exposure time of about a year, they found no evidence for the predicted line and set upper limits on the decay rate that rule out the previously proposed dark matter interpretation. —KTS

Science, this issue p. 1465

CORONAVIRUS

How SARS-CoV-2 binds to human cells

Scientists are racing to learn the secrets of severe acute respiratory syndrome–coronavirus 2 (SARS-CoV-2), which is the cause of the pandemic disease COVID-19. The first step in viral entry is the binding of the viral trimeric spike protein to the human receptor angiotensin-converting enzyme 2 (ACE2). Yan *et al*. present the structure of human ACE2 in complex with a membrane protein that it chaperones,

B^{0}AT1. In the context of this complex, ACE2 is a dimer. A further structure shows how the receptor binding domain of SARS-CoV-2 interacts with ACE2 and suggests that it is possible that two trimeric spike proteins bind to an ACE2 dimer. The structures provide a basis for the development of therapeutics targeting this crucial interaction. —VV

Science, this issue p. 1444

QUANTUM GASES

Capturing the transformation

Quantum statistics dictates the behavior of identical particles in the quantum world: Bosons like to congregate, whereas fermions avoid one another. However, strong interactions can cause a string of bosons to behave like fermions. This so-called fermionization phenomenon has been studied in equilibrium. Wilson *et al*. instead focused on dynamical fermionization in a nonequilibrium system consisting of tubes of strongly interacting bosonic rubidium atoms. After letting the tubes expand in the axial direction, the researchers monitored the momentum distribution of the atoms and found that it evolved from bosonic-like to fermionic-like. —JS

Science, this issue p. 1461

GLASSES

Glassy metal-organic frameworks

The node-and-linker structure of metal-organic frameworks could enable detailed structural studies of molecular glasses quenched from melts. Zinc-based zeolitic imidazole frameworks exhibit a high propensity for glass formation at conventional cooling rates. Madsen *et al*. used ultrahigh magnetic fields (19.5 and 35.2 tesla) to perform zinc-67 nuclear magnetic resonance of solid samples with magic-angle spinning on three samples with different ratios of imidazole and benzimidazole linkers. The structural disorder of the tetrahedral ligand environment around zinc nodes was higher in the glassy states than in the parent crystals. —PDS

Science, this issue p. 1473

CANCER

Metastasis: A matter of translation?

Solid tumors shed a small number of cancer cells into the bloodstream, some of which are believed to contribute to metastasis. The molecular features that confer these circulating tumor cells (CTCs) with metastatic potential are poorly understood. Ebright *et al*. studied CTCs from breast cancer patients and found that cells with increased expression levels of certain ribosomal proteins and regulators of translation had greater metastatic capacity in a mouse model (see the Perspective by Ma and Jeffrey). Consistent with this finding, patients with higher levels of this subset of CTCs tended to have a poorer prognosis. —PAK

Science, this issue p. 1468; see also p. 1424

IMMUNOTHERAPY

Priming NK cells for tumor destruction

Some tumors can evade CD8$^+$ T cells, which are used in several cancer immunotherapies, but natural killer (NK) cells provide another option to target such tumors for immune elimination. Nicolai *et al*. used several mouse models to investigate how a cyclic dinucleotide (CDN) agonist for an innate immune pathway called STING potentiates the antitumor activity of NK cells. CDN administration induced type I interferons that directly promoted NK cell activation and simultaneously enabled an indirect pathway of activation driven by induction of interleukin-15 signaling in dendritic cells. Amplification of NK-based tumor immunity may offer a valuable adjunct to CD8$^+$ T cell immunotherapy. —IW

Sci. Immunol. **5**, eaaz2738 (2020).

IN OTHER JOURNALS

Edited by **Caroline Ash** *and* **Jesse Smith**

CELL BIOLOGY

A mitotic error code

Mitotic errors leading to chromosome missegregation are a hallmark of human cancers. These errors result from incorrect microtubule attachments to specialized regions on chromosomes called kinetochores. Such errors are normally prevented by the action of a dedicated molecular error correction machinery that promotes microtubule depolymerization and consequent detachment. How does this error correction machinery discriminate correct from incorrect microtubule-kinetochore attachments? Ferreira *et al.* genetically manipulated enzymes that regulate α-tubulin detyrosination, a specific posttranslational modification associated with long-lived microtubules. They found that mitotic error correction in human cells was exquisitely sensitive to the detyrosinated state of kinetochore-attached microtubules. Thus, microtubules encode important signaling cues that allow the discrimination of mitotic errors to promote faithful chromosome segregation. —SMH

J. Cell Biol. **219**, e201910064 (2020).

Immunofluorescence microscopy image of a human cell in anaphase of mitosis with missegregated chromosomes (kinetochore in magenta), highlighting tyrosinated (green) and detyrosinated microtubules (cyan)

PHOTO: LUÍSA FERREIRA AND HELDER MAIATO

REPRODUCTIVE BIOLOGY

In search of a male contraceptive

Although "the pill" has been widely used by women since the 1960s, contraceptive options for men are limited. Gruber *et al.* used an automated robotic screening method that tests candidate molecules for effects on sperm motility and changes in the cap or acrosome of the sperm's head. They identified several compounds from a collection of 12,000 molecules from the ReFRAME (Repurposing, Focused Rescue, and Accelerated

In southern Florida, hurricanes bring pulses of nutrients to mangrove forests.

COASTAL ECOLOGY

A silver lining for hurricanes

Hurricanes are notorious for the havoc that they wreak on coastlines. However, destruction can also be accompanied by an injection of nutrients into ecosystems. Castañeda-Moya *et al.* report a hitherto underappreciated beneficial effect of high-energy disturbances. In the aftermath of Hurricane Irma, which hit the Florida Everglades in 2017, there was a notable fertilization pulse in mangrove forests as far as 10 kilometers inland. Phosphorus-rich sediments deposited by the hurricane boosted the soil nutrient pool and resulted in increased phosphorus uptake by mangrove species. The potential hurricane-enhanced plant productivity may promote soil stabilization and resilience to future disturbances and sea level rise. —AMS

Proc. Natl. Acad. Sci. U.S.A. **117**, 4831 (2020).

Medchem) library, which contains small molecules that have regulatory approval or are in clinical development. Drugs such as KF-4939 (a platelet aggregation factor inhibitor) and Resquimod (a Toll-like receptor 7/8 ligand) were identified. The use of drugs that can be repurposed should assist in speeding translation into the clinic. —BAP

eLife **9**, e51739 (2020).

DOG DOMESTICATION

Feed the dog

Dogs are one of humanity's most frequent companions, but when and how this relationship first began are still open questions. There is considerable evidence for fully domesticated and cohabiting dogs by around 15,000 years ago, but genetic studies and some fossils suggest that the relationship began much earlier, perhaps as long as 40,000 years ago or more. Identifying the first evidence of wolves becoming dogs is challenging, because early domesticating individuals are likely to have looked like wild wolves. Prassack *et al.* studied fossil canid teeth from a Paleolithic site in the Czech Republic from 28,500 years before the present. Using microwear analysis, they found distinct differences between individuals previously classified as "protodogs" or "wolves" based on their jaw structure. They argue that these differences reflect true differences in diet, specifically an increase in bone consumption in the protodogs that could have been due to a shift by early domesticated animals to a diet of human scraps. —SNV

J. Archaeol. Sci. **115**, 105092 (2020).

QUANTUM INFORMATION

Determining odd from even

The parity of a quantum mechanical wave function simply tells you if there is an odd or even number of excitations in the system it describes. Without the need to know the exact number of excitations within a system, being able to measure changes in parity is important and can be exploited in operations such as quantum error correction and stabilizing quantum communication protocols. Besse *et al.* demonstrate a detector that can determine the parity of a propagating microwave field. Using a superconducting phase qubit embedded in a cavity, they show that they can engineer the system such that transmission of the microwaves is conditional on there being an odd or even number of microwave photons in the radiation field. The simplicity of the detector design should have applications across a broad range of setups for quantum information processing. —ISO

Phys. Rev. X **10**, 011046 (2020).

ATMOSPHERIC CHEMISTRY

It's in the air

Dimethyl sulfide, produced by many marine organisms, is the major natural source of natural marine sulfate aerosols, which have an enormous influence on cloud formation and climate. Veres *et al.* report that >30% of oceanic dimethyl sulfide emitted to the atmosphere is oxidized to HPMTF (hydroperoxymethyl thioformate, $HOOCH_2SCHO$), a previously unquantified species. By linking HPMTF concentration to new particle formation and growth, they establish its importance in marine atmospheric chemistry and demonstrate the need to include it in models that describe the links among ocean biogeochemistry, marine aerosol formation, and climate. —HJS

Proc. Natl. Acad. Sci. U.S.A. **117**, 4505 (2020).

PHYSICS

A strange strange metal

The so-called strange metal phase appears in the phase diagrams of many quantum materials, including cuprate high-temperature superconductors and heavy fermion compounds. Strange metals frequently occur in the vicinity of antiferromagnetism, suggesting a connection between the two. Now, Shen *et al.* reveal an unusual strange metal phase near a ferromagnetic quantum critical point in the quasi–one-dimensional material $CeRh_6Ge_4$. The researchers observed anomalous transport and thermodynamics properties typical of strange metals near the critical pressure at which the material becomes ferromagnetic. —JS

Nature **579**, 51 (2020).

PHOTO: RALPH PAGE/MINDEN PICTURES

REVIEW SUMMARY

ECONOMIC HISTORY

The historical roots of economic development

Nathan Nunn

BACKGROUND: Traditionally, research into contemporary economic development has taken a primarily ahistorical approach. The study of the past was relegated to the separate field of economic history, and connections between historical factors and present-day economic outcomes were seldom made. In recent decades, there has been a rapidly growing body of research within economics that takes a historical perspective when attempting to understand contemporary issues related to global poverty and comparative development.

ADVANCES: Typically, studies of this kind begin by collecting new data, often from archival sources, that measure aspects of the historical episode of interest. These data are then connected to contemporary outcomes of interest, matched through populations, societies, or locations, to test whether the historical factor has a causal effect on the contemporary factors being examined. Statistical analysis is undertaken, studying variation across individuals, ethnicities, or countries and using empirical techniques (such as instrumental variables, regression discontinuity, difference-in-difference, or natural experiments) that are aimed at distinguishing causal relationships from mere correlation. Having established the importance of a historical factor or episode for outcomes today, an attempt is then made to understand the exact causal mechanisms that account for the observed relationship. This generally requires the collection of additional data and additional statistical analysis, as well as an integration of the historical literature and descriptive evidence.

A body of empirical research that has emerged over the past two decades has established that a substantial proportion of the variation in economic prosperity that we observe in the world today has its roots in the past. Historical events, such as European expansion across the globe during the 16th century and after, have been shown to have shaped subsequent paths of development. It is now clear that one cannot fully understand contemporary economic development without understanding its historical roots.

OUTLOOK: A common reaction to the finding that history is important for contemporary outcomes is that this leaves little room for policy. If much of the nature of the world today is determined through historical processes, what role is there for policy? I explain how such a view, while natural, is incorrect.

In addition to providing a more complete understanding of the process of economic development, the findings from the literature are also important for thinking about policies that help to address issues related to global development moving forward. This is an important next step for the literature. Recent studies have begun to take on this next challenge.

I illustrate this by providing examples of studies that seek to better understand the origins of mistrust in Western medicine. This mistrust, which is present all over the world, has resulted in underutilization of medical services, resulting in poorer health and higher mortality. Studies have examined the historical roots of such mistrust, showing how it is determined by poor medical practices in the past. I then discuss examples where the insights that are obtained from the historical analyses are used to improve the design, implementation, and effectiveness of policies. These examples illustrate a more general point: There are sizable gains to be realized from research that seeks to better understand how local history and context can be leveraged to inform the design of better policy. ■

ON OUR WEBSITE

Read the full article at http://dx.doi.org/10.1126/science.aaz9986

Harvard University and Canadian Institute for Advanced Research (CIFAR), 1805 Cambridge Street, Cambridge, MA 02139, USA.
Email: nnunn@fas.harvard.edu
Cite this article as N. Nunn, *Science* **367**, eaaz9986 (2020).
DOI: 10.1126/science.aaz9986

IMAGE COURTESY OF UNIVERSITY OF TEXAS LIBRARIES, UNIVERSITY OF TEXAS AT AUSTIN

Map showing the Age of Discovery, the historical period that fostered the origins of the vast differences in economic prosperity that we observe today.

RESEARCH ARTICLE SUMMARY

TOPOLOGICAL MATTER

Flux-induced topological superconductivity in full-shell nanowires

S. Vaitiekėnas, G. W. Winkler, B. van Heck, T. Karzig, M.-T. Deng, K. Flensberg, L. I. Glazman, C. Nayak, P. Krogstrup, R. M. Lutchyn*, C. M. Marcus*

INTRODUCTION: Majorana zero modes (MZMs) localized at the ends of one-dimensional topological superconductors are promising candidates for fault-tolerant quantum computing. One approach among the proposals to realize MZMs—based on semiconducting nanowires with strong spin-orbit coupling subject to a Zeeman field and superconducting proximity effect—has received considerable attention, yielding increasingly compelling experimental results over the past few years. An alternative route to MZMs aims to create vortices in topological superconductors, for instance, by coupling a vortex in a conventional superconductor to a topological insulator.

RATIONALE: We intoduce a conceptually distinct approach to generating MZMs by threading magnetic flux through a superconducting shell fully surrounding a spin-orbit–coupled semiconducting nanowire core; this approach contains elements of both the proximitized-wire and vortex schemes. We show experimentally and theoretically that the winding of the superconducting phase around the shell induced by the applied flux gives rise to MZMs at the ends of the wire. The topological phase sets in at relatively low magnetic fields, is controlled by moving from zero to one phase twist around the superconducting shell, and does not require a large g factor in the semiconductor, which broadens the landscape of candidate materials.

RESULTS: In the destructive Little-Parks regime, the modulation of critical temperature with flux applied along the hybrid nanowire results in a sequence of lobes with reentrant superconductivity. Each lobe is associated with a quantized number of twists of the superconducting phase in the shell, determined by the external field. The result is a series of topologically locked boundary conditions for the proximity effect in the semiconducting core, with a dramatic effect on the subgap density of states.

Tunneling into the core in the zeroth superconducting lobe, around zero flux, we measure a hard proximity-induced gap with no subgap features. In the superconducting regions around one quantum of applied flux, $\Phi_0 = h/2e$, corresponding to phase twists of $\pm 2\pi$ in the shell, tunneling spectra into the core show stable zero-bias peaks, indicating a discrete subgap state fixed at zero energy.

Theoretically, we find that a Rashba field arising from the breaking of local radial inversion symmetry at the semiconductor-superconductor interface, along with 2π-phase twists in the boundary condition, can induce a topological state supporting MZMs. We calculate the topological phase diagram of the system as a function of Rashba spin-orbit coupling, radius of the semiconducting core, and band bending at the superconductor-semiconductor interface. Our analysis shows that topological superconductivity extends in a reasonably large portion of the parameter space. Transport simulations of the tunneling conductance in the presence of MZMs qualitatively reproduce the experimental data in the entire voltage-bias range.

ON OUR WEBSITE

Read the full article at http://dx.doi.org/10.1126/science.aav3392

We obtain further experimental evidence that the zero-energy states are delocalized at wire ends by investigating Coulomb blockade conductance peaks in full-shell wire islands of various lengths. In the zeroth lobe, Coulomb blockade peaks show $2e$ spacing; in the first lobe, peak spacings are roughly $1e$-periodic, with slight even-odd alternation that vanishes exponentially with island length, consistent with overlapping Majorana modes at the two ends of the Coulomb island. The exponential dependence on length, as well as incompatibility with a power-law dependence, provides compelling evidence that MZMs reside at the ends of the hybrid islands.

CONCLUSION: While being of similar simplicity and practical feasibility as the original nanowire proposals with a partial shell coverage, full-shell nanowires provide several key advantages. The modest magnetic field requirements, protection of the semiconducting core from surface defects, and locked phase winding in discrete lobes together suggest a relatively easy route to creating and controlling MZMs in hybrid materials. Our findings open the possibility of studying an interplay of mesoscopic and topological physics in this system. ■

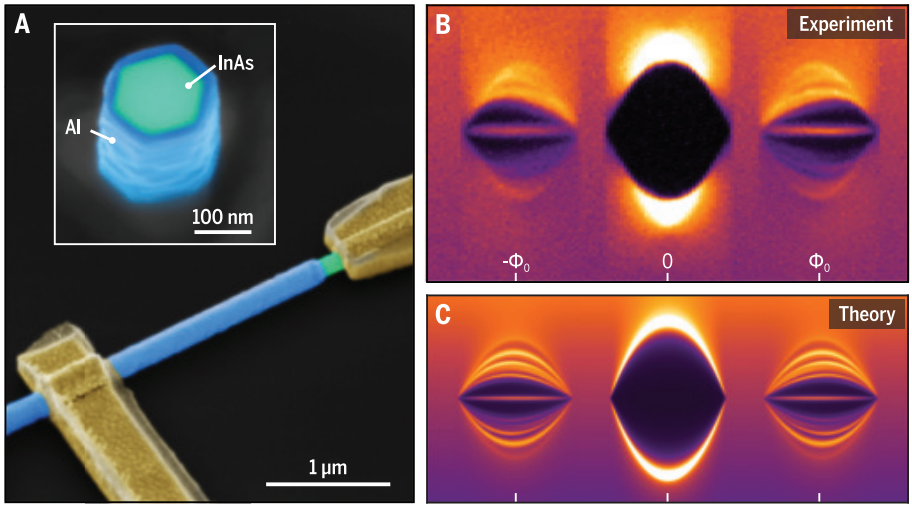

Majorana fingerprints in full-shell nanowires. (**A**) Colorized electron micrograph of a tunneling device composed of a hybrid nanowire with hexagonal semiconducting core and full superconducting shell. (**B**) Tunneling conductance (color) into the core as a function of applied flux (horizontal axis) and source-drain voltage (vertical axis) reveals a hard induced superconducting gap near zero applied flux and a gapped region with a discrete zero-energy state around one applied flux quantum, Φ_0. (**C**) Realistic transport simulations in the presence of MZMs reproduce key features of the experimental data.

The list of author affiliations is available in the full article online.
*Corresponding author. Email: rolutchy@microsoft.com (R.M.L.); chmarcus@microsoft.com (C.M.M.)
Cite this article as S. Vaitiekėnas *et al.*, *Science* **367**, eaav3392 (2020). DOI: 10.1126/science.aav3392

RESEARCH ARTICLE SUMMARY

ARCHAEOLOGY

Last Interglacial Iberian Neandertals as fisher-hunter-gatherers

J. Zilhão*, D. E. Angelucci, M. Araújo Igreja, L. J. Arnold, E. Badal, P. Callapez, J. L. Cardoso, F. d'Errico, J. Daura, M. Demuro, M. Deschamps, C. Dupont, S. Gabriel, D. L. Hoffmann, P. Legoinha, H. Matias, A. M. Monge Soares, M. Nabais, P. Portela, A. Queffelec, F. Rodrigues, P. Souto

INTRODUCTION: A record of the regular exploitation of aquatic foods has been lacking in Neandertal Europe. By contrast, marine resources feature prominently—alongside personal ornaments, body painting, and linear-geometric drawings—in the archeology of Last Interglacial Africa. A competitive advantage scenario of human origins is that the habitual consumption of aquatic foods and the fatty acids they contain, which favor brain development, underpins the acquisition of modernity in cognition and behavior. The resulting innovations in technology, demographic growth, and enhanced prosociality would therefore explain modern humans' out-of-Africa expansion with regard to both dispersal process (along coastal routes and to southern Asia first) and outcome (the demise of coeval non-modern Eurasians). A corollary of this view is that the paucity of marine foods at Neandertal coastal sites is a genuine reflection of their subsistence behavior.

RATIONALE: Europe's Atlantic façade boasts resource-rich coastal waters comparable to those of South Africa. From Scandinavia to France, however, any evidence for the Last Interglacial exploitation of marine resources would have been lost to subsequent icecap advances and postglacial submersion of the wide continental platform. Conversely, the very steep shelf off Arrábida, a littoral mountain range 30 km south of Lisbon, Portugal, has enabled extant and submerged shorelines to be preserved short distances apart. Gruta da Figueira Brava, one of Arrábida's erosion-protected, seaside cave sites, provides a singular opportunity to investigate whether any considerable Last Interglacial accumulations of marine food debris ever existed in Europe.

RESULTS: The Figueira Brava archeological sequence dates to ~86 to 106 thousand years ago (kya). Throughout, there is evidence of a settlement-subsistence system based on regular exploitation of all animal resources offered by the coastal environment: large crabs, marine mollusks, fish, marine birds and mammals, tortoise, waterfowl, and hoofed game. The composition of the food basket and the structure of the deposit vary as a function of the following: (i) sea-level oscillation, with implications for the ecosystems that were preferentially targeted; (ii) frequency of human occupation; (iii) site-formation process; and (iv) position of the archeological trenches relative to the changing configuration of the inhabited space. The initial occupations (phases FB1 and FB2), when the sea was closer to the cave (~750 m), include shell-supported accumulations. These occupations were followed by a period of infrequent use (phase FB3) and a final phase (FB4), when the shoreline was ~2000 m away but shellfish were again discarded at the site in substantial amounts. The density of marine food remains compares well to that seen in the regional Mesolithic and the Last Interglacial of South Africa and the Maghreb and exceeds the latter two in the case of crabs and fish. Figueira Brava also documents a stone pine economy featuring seasonal harvesting and on-site storage of the cones for deferred consumption of the nuts. The stability of this subsistence system suggests successful long-term adaptation.

ON OUR WEBSITE

Read the full article at http://dx.doi.org/10.1126/science.aaz7943

CONCLUSION: Figueira Brava provides the first record of significant marine resource consumption among Europe's Neandertals. Taphonomic and site-preservation biases explain why this kind of record has not been previously found in Europe on the scale seen among coeval African populations. Consistent with rapidly accumulating evidence that Neandertals possessed a fully symbolic material culture, the subsistence evidence reported here further questions the behavioral gap once thought to separate them from modern humans. ■

PHOTOS: PEDRO SOUTO/JOÃO ZILHÃO.

Gruta da Figueira Brava, Arrábida, Portugal. Note the Mediterranean vegetation, like at the time of the Last Interglacial occupation, the MIS 5e marine abrasion terrace, and, under the overhang, the brecciated remnant dated to ~86 to 106 kya. Neandertal use of this cave space, which is currently unroofed due to Holocene erosion, has left an archeological record rich in fish, shellfish, and other coastal resources.

The list of author affiliations is available in the full article online.
*Corresponding author. Email: joao.zilhao@ub.edu
Cite this article as J. Zilhão *et al.*, *Science* **367**, eaaz7943 (2020). DOI: 10.1126/science.aaz7943

RESEARCH ARTICLES

CORONAVIRUS

Structural basis for the recognition of SARS-CoV-2 by full-length human ACE2

Renhong Yan[1,2], Yuanyuan Zhang[1,2]*, Yaning Li[3]*, Lu Xia[1,2], Yingying Guo[1,2], Qiang Zhou[1,2]†

Angiotensin-converting enzyme 2 (ACE2) is the cellular receptor for severe acute respiratory syndrome–coronavirus (SARS-CoV) and the new coronavirus (SARS-CoV-2) that is causing the serious coronavirus disease 2019 (COVID-19) epidemic. Here, we present cryo–electron microscopy structures of full-length human ACE2 in the presence of the neutral amino acid transporter B^0AT1 with or without the receptor binding domain (RBD) of the surface spike glycoprotein (S protein) of SARS-CoV-2, both at an overall resolution of 2.9 angstroms, with a local resolution of 3.5 angstroms at the ACE2-RBD interface. The ACE2-B^0AT1 complex is assembled as a dimer of heterodimers, with the collectrin-like domain of ACE2 mediating homodimerization. The RBD is recognized by the extracellular peptidase domain of ACE2 mainly through polar residues. These findings provide important insights into the molecular basis for coronavirus recognition and infection.

Severe acute respiratory syndrome–coronavirus 2 (SARS-CoV-2) is a positive-strand RNA virus that causes severe respiratory syndrome in humans. The resulting outbreak of coronavirus disease 2019 (COVID-19) has emerged as a severe epidemic, claiming more than 2000 lives worldwide between December 2019 and February 2020 (*1*, *2*). The genome of SARS-CoV-2 shares about 80% identity with that of SARS-CoV and is about 96% identical to the bat coronavirus BatCoV RaTG13 (*2*).

In the case of SARS-CoV, the spike glycoprotein (S protein) on the virion surface mediates receptor recognition and membrane fusion (*3*, *4*). During viral infection, the trimeric S protein is cleaved into S1 and S2 subunits and S1 subunits are released in the transition to the postfusion conformation (*4*–*7*). S1 contains the receptor binding domain (RBD), which directly binds to the peptidase domain (PD) of angiotensin-converting enzyme 2 (ACE2) (*8*), whereas S2 is responsible for membrane fusion. When S1 binds to the host receptor ACE2, another cleavage site on S2 is exposed and is cleaved by host proteases, a process that is critical for viral infection (*5*, *9*, *10*). The S protein of SARS-CoV-2 may also exploit ACE2 for host infection (*2*, *11*–*13*). A recent publication reported the structure of the S protein of SARS-CoV-2 and showed that the ectodomain of the SARS-CoV-2 S protein binds to the PD of ACE2 with a dissociation constant (K_d) of ~15 nM (*14*).

Although ACE2 is hijacked by some coronaviruses, its primary physiological role is in the maturation of angiotensin (Ang), a peptide hormone that controls vasoconstriction and blood pressure. ACE2 is a type I membrane protein expressed in lungs, heart, kidneys, and intestine (*15*–*17*). Decreased expression of ACE2 is associated with cardiovascular diseases (*18*–*20*). Full-length ACE2 consists of an N-terminal PD and a C-terminal collectrin-like domain (CLD) that ends with a single transmembrane helix and a ~40-residue intracellular segment (*15*, *21*). The PD of ACE2 cleaves Ang I to produce Ang-(1-9), which is then processed by other enzymes to become Ang-(1-7). ACE2 can also directly process Ang II to give Ang-(1-7) (*15*, *22*).

Structures of the claw-like ACE2-PD alone and in complex with the RBD or the S protein of SARS-CoV have revealed the molecular details of the interaction between the RBD of the S protein and PD of ACE2 (*7*, *8*, *23*, *24*). Structural information on ACE2 is limited to the PD domain. The single transmembrane (TM) helix of ACE2 makes it challenging to determine the structure of the full-length protein.

ACE2 also functions as the chaperone for membrane trafficking of the amino acid transporter B^0AT1, also known as SLC6A19 (*25*), which mediates uptake of neutral amino acids into intestinal cells in a sodium-dependent manner. Mutations in B^0AT1 may cause Hartnup disorder, an inherited disease with symptoms such as pellagra, cerebellar ataxia, and psychosis (*26*–*28*). Structures have been determined for the SLC6 family members *d*DAT (*Drosophila* dopamine transporter) and human SERT (serotonin transporter, SLC6A4) (*29*, *30*). It is unclear how ACE2 interacts with B^0AT1. The membrane trafficking mechanism for ACE2 and B^0AT1 is similar to that of the LAT1-4F2hc complex, a large neutral–amino acid transporter complex that requires 4F2hc for its plasma membrane localization (*31*). Our structure of LAT1-4F2hc shows that the cargo LAT1 and chaperone 4F2hc interact through both extracellular and transmembrane domains (*32*). We reasoned that the structure of full-length ACE2 may be revealed in the presence of B^0AT1.

Here, we report cryo–electron microscopy (cryo-EM) structures of the full-length human ACE2-B^0AT1 complex at an overall resolution of 2.9 Å and a complex between the RBD of SARS-CoV-2 and the ACE2-B^0AT1 complex, also with an overall resolution of 2.9 Å and with 3.5-Å local resolution at the ACE2-RBD interface. The ACE2-B^0AT1 complex exists as a dimer of heterodimers. Structural alignment of the RBD-ACE2-B^0AT1 ternary complex with the S protein of SARS-CoV-2 suggests that two S protein trimers can simultaneously bind to an ACE2 homodimer.

Structural determination of the ACE2-B^0AT1 complex

Full-length human ACE2 and B^0AT1, with Strep and FLAG tags on their respective N termini, were coexpressed in human embryonic kidney (HEK) 293F cells and purified through tandem affinity resin and size exclusion chromatography. The complex was eluted in a single monodisperse peak, indicating high homogeneity (Fig. 1A). Details of cryo-sample preparation, data acquisition, and structural determination are given in the materials and methods section of the supplementary materials. A three-dimensional (3D) reconstruction was obtained at an overall resolution of 2.9 Å from 418,140 selected particles. This immediately revealed the dimer of heterodimers' architecture (Fig. 1B). After applying focused refinement and C2 symmetry expansion, the resolution of the extracellular domains improved to 2.7 Å, whereas the TM domain remained at 2.9-Å resolution (Fig. 1B, figs. S1 to S3, and table S1).

The high resolution supported reliable model building. For ACE2, side chains could be assigned to residues 19 to 768, which contain the PD (residues 19 to 615) and the CLD (residues 616 to 768), which consists of a small extracellular domain, a long linker, and the single TM helix (Fig. 1C). Between the PD and TM helix is a ferredoxin-like fold domain; we refer to this as the neck domain (residues 616 to 726) (Fig. 1C and fig. S4). Homodimerization is entirely mediated by ACE2, which is sandwiched by B^0AT1. Both the PD and neck domains contribute to dimerization, whereas each B^0AT1 interacts with the neck and TM helix in the adjacent ACE2 (Fig. 1C). The extracellular region is highly glycosylated, with seven and five glycosylation sites on each ACE2 and B^0AT1 monomer, respectively.

[1]Key Laboratory of Structural Biology of Zhejiang Province, Institute of Biology, Westlake Institute for Advanced Study, 18 Shilongshan Road, Hangzhou 310024, Zhejiang Province, China. [2]School of Life Sciences, Westlake University, 18 Shilongshan Road, Hangzhou 310024, Zhejiang Province, China. [3]Beijing Advanced Innovation Center for Structural Biology, Tsinghua-Peking Joint Center for Life Sciences, School of Life Sciences, Tsinghua University, Beijing 100084, China.
*These authors contributed equally to this work.
†Corresponding author. Email: zhouqiang@westlake.edu.cn

During classification, another subset with 143,857 particles was processed to an overall resolution of 4.5 Å. Whereas the neck domain still dimerizes, the PDs are separated from each other in this reconstruction (Fig. 1D and fig. S1, H to K). We therefore define the two classes as the open and closed conformations. Structural comparison shows that the conformational changes are achieved through rotation of the PD domains, with the rest of the complex left nearly unchanged (movie S1).

Homodimer interface of ACE2

Dimerization of ACE2 is mainly mediated by the neck domain, with the PD contributing a minor interface (Fig. 2A). The two ACE2 protomers are hereafter referred to as A and B, with residues in protomer B followed by a prime symbol. Extensive polar interactions are mapped to the interface between the second (residues 636 to 658) and fourth (residues 708 to 717) helices of the neck domain (Fig. 2B). Arg^{652} and Arg^{710} in ACE2-A form cation-π interactions with $Tyr^{641'}$ and $Tyr^{633'}$ in ACE2-B. Meanwhile, Arg^{652} and Arg^{710} are respectively hydrogen-bonded (H-bonded) to $Asn^{638'}$ and $Glu^{639'}$, which also interact with Gln^{653}, as does $Asn^{636'}$. Ser^{709} and Asp^{713} from ACE2-A are H-bonded to $Arg^{716'}$. This extensive network of polar interactions indicates stable dimer formation.

The PD dimer interface appears much weaker, with only one pair of interactions between Gln^{139} and $Gln^{175'}$ (Fig. 2C). Gln^{139} is in a loop that is stabilized by a disulfide bond between Cys^{133} and Cys^{141} as well as multiple intraloop polar interactions (Fig. 2C). The weak interaction is consistent with the ability to transition to the open conformation, in which the interface between the neck domains remains the same while the PDs are separated from each other by ~25 Å (Fig. 2D and movie S1).

Overall structure of the RBD-ACE2-B^{0}AT1 complex

To gain insight into the interaction between ACE2 and SARS-CoV-2, we purchased 0.2 mg of recombinantly expressed and purified RBD-mFc of SARS-CoV-2 (for simplicity, hereafter referred to as RBD; mFc, mouse Fc tag) from Sino Biological Inc., mixed it with our purified ACE2-B^{0}AT1 complex at a stoichiometric ratio of ~1.1 to 1, and proceeded with cryo-grid preparation and imaging. Finally, a 3D EM reconstruction of the ternary complex was obtained.

In contrast to the ACE2-B^{0}AT1 complex—which has two conformations, open and closed—only the closed state of ACE2 was observed in the dataset for the RBD-ACE2-B^{0}AT1 ternary complex. The structure of the ternary complex was determined to an overall resolution of 2.9 Å from 527,017 selected particles. However, the resolution for the ACE2-B^{0}AT1 complex was substantially higher than that for the RBDs, which are at the periphery of the complex (Fig. 3A). To improve the local resolution, focused refinement was applied; this allowed us to reach a resolution of 3.5 Å for the RBD, supporting reliable modeling and analysis of the interface (Fig. 3, figs. S5 to S7, and table S1).

Interface between the RBD and ACE2

As expected, each PD accommodates one RBD (Fig. 3B). The overall interface is similar to that between SARS-CoV and ACE2 (*7*, *8*), mediated mainly through polar interactions (Fig. 4A). An extended loop region of the RBD spans the arch-shaped α1 helix of the ACE2-PD like a bridge. The α2 helix and a loop that connects the β3 and β4 antiparallel strands, referred

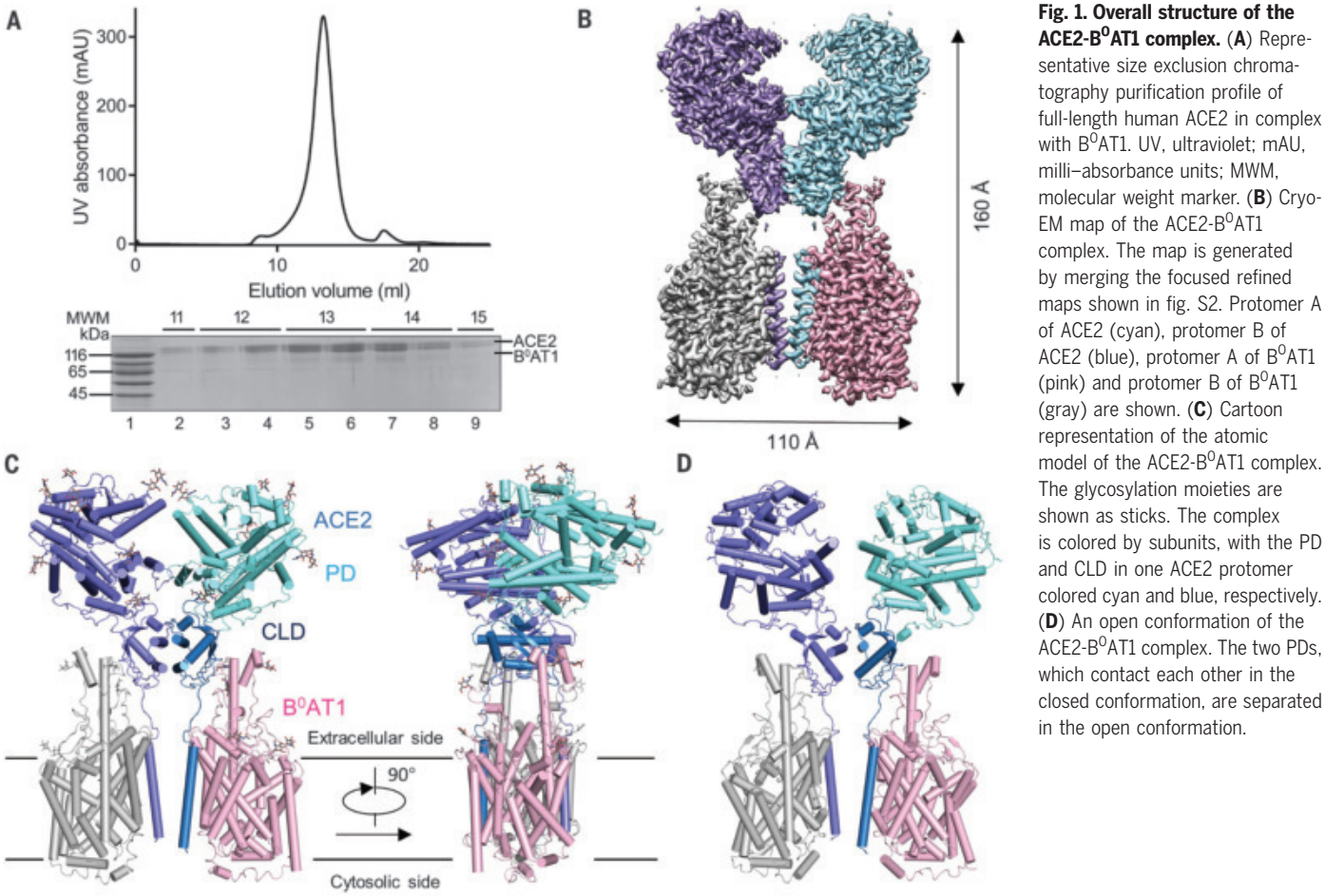

Fig. 1. Overall structure of the ACE2-B^{0}AT1 complex. (**A**) Representative size exclusion chromatography purification profile of full-length human ACE2 in complex with B^{0}AT1. UV, ultraviolet; mAU, milli–absorbance units; MWM, molecular weight marker. (**B**) Cryo-EM map of the ACE2-B^{0}AT1 complex. The map is generated by merging the focused refined maps shown in fig. S2. Protomer A of ACE2 (cyan), protomer B of ACE2 (blue), protomer A of B^{0}AT1 (pink) and protomer B of B^{0}AT1 (gray) are shown. (**C**) Cartoon representation of the atomic model of the ACE2-B^{0}AT1 complex. The glycosylation moieties are shown as sticks. The complex is colored by subunits, with the PD and CLD in one ACE2 protomer colored cyan and blue, respectively. (**D**) An open conformation of the ACE2-B^{0}AT1 complex. The two PDs, which contact each other in the closed conformation, are separated in the open conformation.

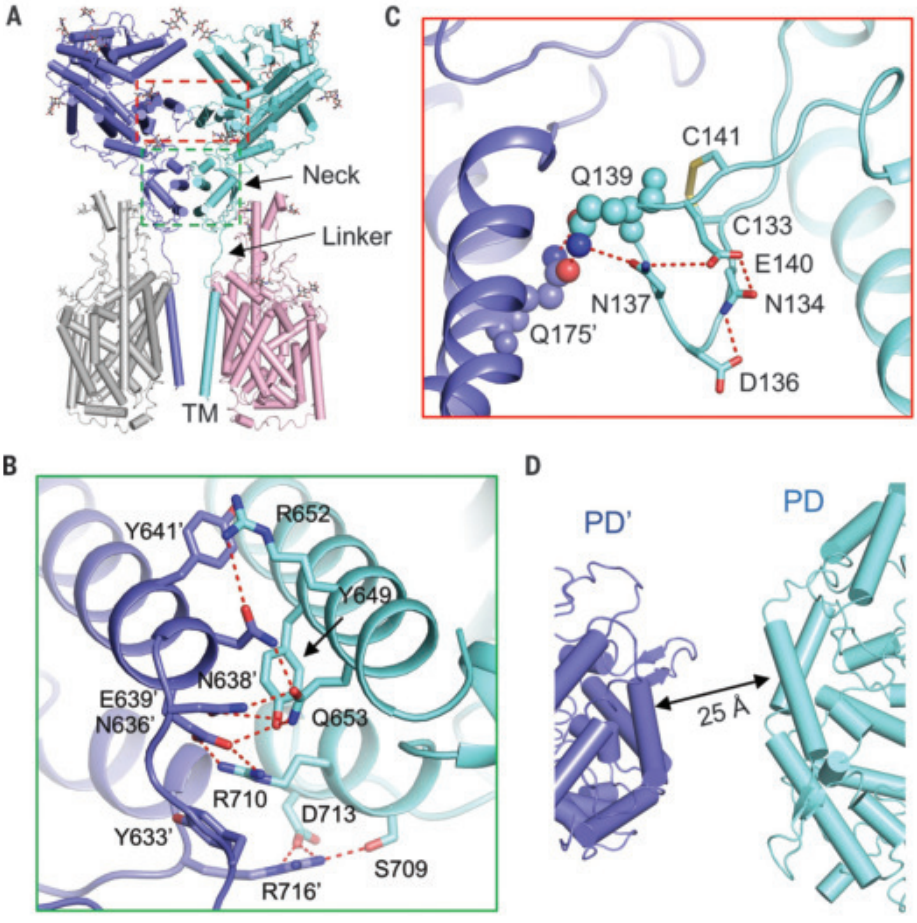

Fig. 2. Dimerization interface of ACE2. (**A**) ACE2 dimerizes through two interfaces, the PD and the neck domain. The regions enclosed by the cyan and red dashed lines are illustrated in detail in (B) and (C), respectively. (**B**) The primary dimeric interface is through the neck domain in ACE2. Polar interactions are represented by red dashed lines. (**C**) A weaker interface between PDs of ACE2. The only interaction is between Gln^{139} and $Gln^{175'}$, which are highlighted as spheres. The polar residues that may contribute to the stabilization of Gln^{139} are shown as sticks. (**D**) The PDs no longer contact each other in the open state. Single-letter abbreviations for the amino acid residues used in the figures are as follows: C, Cys; D, Asp; E, Glu; F, Phe; H, His; K, Lys; L, Leu; M, Met; N, Asn; Q, Gln; R, Arg; S, Ser; T, Thr; V, Val; and Y, Tyr.

to as loop 3-4, of the PD also make limited contributions to the coordination of the RBD.

The contact can be divided into three clusters. The two ends of the bridge interact with the N and C termini of the α1 helix as well as small areas on the α2 helix and loop 3-4. The middle segment of α1 reinforces the interaction by engaging two polar residues (Fig. 4A). At the N terminus of α1, Gln^{498}, Thr^{500}, and Asn^{501} of the RBD form a network of H-bonds with Tyr^{41}, Gln^{42}, Lys^{353}, and Arg^{357} from ACE2 (Fig. 4B). In the middle of the bridge, Lys^{417} and Tyr^{453} of the RBD interact with Asp^{30} and His^{34} of ACE2, respectively (Fig. 4C). At the C terminus of α1, Gln^{474} of the RBD is H-bonded to Gln^{24} of ACE2, whereas Phe^{486} of the RBD interacts with Met^{82} of ACE2 through van der Waals forces (Fig. 4D).

Comparing the SARS-CoV-2 and SARS-CoV interfaces with ACE2

Superimposition of the RBD in the complex of SARS-CoV (SARS-CoV-RBD) and ACE2-PD [Protein Data Bank (PDB) 2AJF] with the RBD in our ternary complex shows that the SARS-CoV-2 RBD (SARS-CoV-2-RBD) is similar to SARS-CoV-RBD with a root mean square deviation (RMSD) of 0.68 Å over 139 pairs of Cα atoms (Fig. 5A) (*8*). Despite the overall similarity, a number of sequence variations and conformational deviations are found in their respective interfaces with ACE2 (Fig. 5 and fig. S8). At the N terminus of α1, the variations Arg^{426}→Asn^{439}, Tyr^{484}→Gln^{498}, and Thr^{487}→Asn^{501} at equivalent positions are observed between SARS-CoV-RBD and SARS-CoV-2-RBD (Fig. 5B). More variations are observed in the middle of the bridge. The most prominent alteration is the substitution of Val^{404} in the SARS-CoV-RBD with Lys^{417} in the SARS-CoV-2-RBD. In addition, from SARS-CoV-RBD to SARS-CoV-2-RBD, the substitution of interface residues Tyr^{442}→Leu^{455}, Leu^{443}→Phe^{456}, Phe^{460}→Tyr^{473}, and Asn^{479}→Gln^{493} may also change the affinity

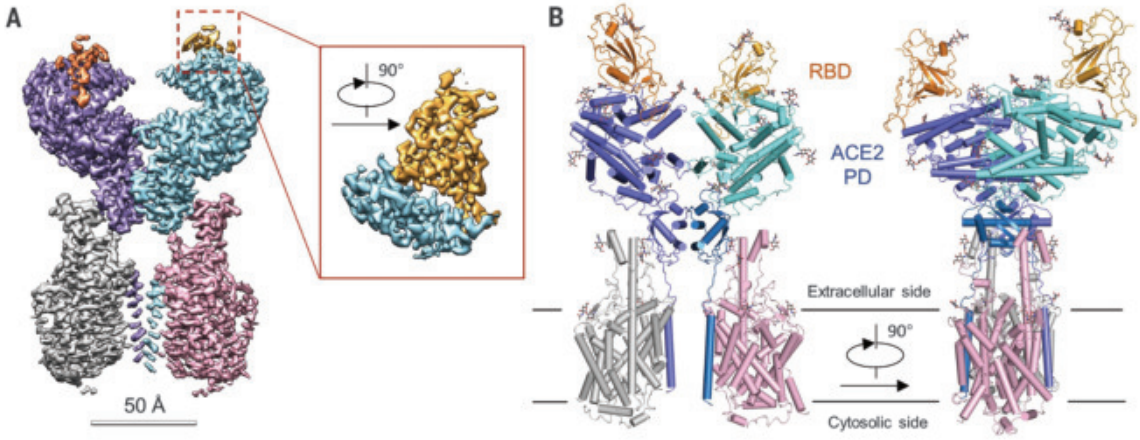

Fig. 3. Overall structure of the RBD-ACE2-B^0AT1 complex. (**A**) Cryo-EM map of the RBD-ACE2-B^0AT1 complex. The overall reconstruction of the ternary complex at 2.9 Å is shown on the left. The inset shows the focused refined map of RBD. The color scheme is the same as that in Fig. 1B, with the addition of red and gold, which represent RBD protomers. (**B**) Overall structure of the RBD-ACE2-B^0AT1 complex. The color scheme is the same as that in Fig. 1C. The glycosylation moieties are shown as sticks.

for ACE2 (Fig. 5C). At the C terminus of α1, Leu^{472} in the SARS-CoV-RBD is replaced by Phe^{486} in the SARS-CoV-2-RBD (Fig. 5D).

Discussion

Although ACE2 is a chaperone for B^{0}AT1, our focus is on ACE2 in this study. With the stabilization by B^{0}AT1, we elucidated the structure of full-length ACE2. B^{0}AT1 is not involved in dimerization, suggesting that ACE2 may be a homodimer even in the absence of B^{0}AT1. Further examination suggests that a dimeric ACE2 can accommodate two S protein trimers, each through a monomer of ACE2 (fig. S9). The trimeric structure of the S protein of SARS-CoV-2 was recently reported, with one RBD in an up conformation and two in down conformations (PDB 6VSB) (*14*). The PD clashes with the rest of the S protein when the ternary complex is aligned to the RBD of the down conformation. There is no clash when the complex is superimposed on RDB in the up conformation, with a RMSD of 0.98 Å over 126 pairs of C_α atoms, confirming that an up conformation of RDB is required to bind to the receptor (fig. S9) (*14*).

Cleavage of the S protein of SARS-CoV is facilitated by cathepsin L in endosomes, indicating a mechanism of receptor-mediated endocytosis (*10*). Further characterization is required to examine the interactions between ACE2 and the viral particle as well as the effect of cofactors on this process (*25*, *33*). It remains to be investigated whether there is clustering between the dimeric ACE2 and trimeric S proteins, which may be important for invagination of the membrane and endocytosis of the viral particle, a process similar to other types of receptor-mediated endocytosis.

Cleavage of the C-terminal segment, especially residues 697 to 716 (fig. S4), of ACE2 by proteases, such as transmembrane protease serine 2 (TMPRSS2), enhances the S protein–driven viral entry (*34*, *35*). Residues 697 to 716 form the third and fourth helices in the neck domain and map to the dimeric interface of ACE2. The presence of B^{0}AT1 may block the access of TMPRSS2 to the cutting site on ACE2. The expression distribution of ACE2 is broader than that of B^{0}AT1. In addition to kidneys and intestine, where B^{0}AT1 is mainly expressed, ACE2 is also expressed in lungs and heart (*27*). It remains to be tested whether B^{0}AT1 can suppress SARS-CoV-2 infection by blocking ACE2 cleavage. Enteric infections have been reported for SARS-CoV, and possibly also for SARS-CoV-2 (*36*, *37*). B^{0}AT1 has also been shown to interact with another coronavirus receptor, aminopeptidase N (APN or CD13) (*38*). These findings suggest that B^{0}AT1 may play a regulatory role for the enteric infections of some coronaviruses.

Comparing the interaction interfaces of SARS-CoV-2-RBD and SARS-CoV-RBD with ACE2

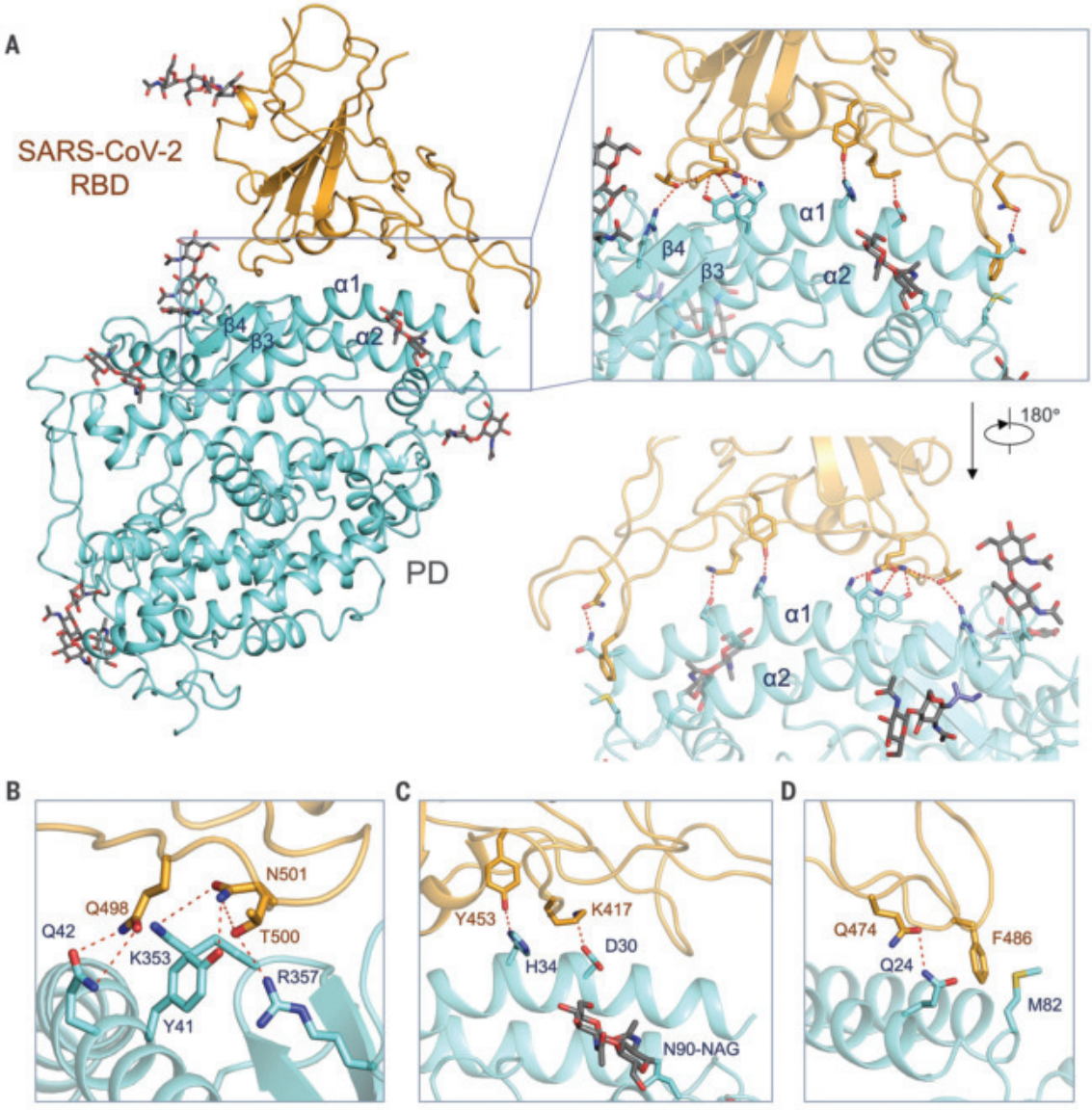

Fig. 4. Interactions between SARS-CoV-2-RBD and ACE2. (**A**) The PD of ACE2 mainly engages the α1 helix in the recognition of the RBD. The α2 helix and the linker between β3 and β4 also contribute to the interaction. Only one RBD-ACE2 is shown. (**B** to **D**) Detailed analysis of the interface between SARS-CoV-2-RBD and ACE2. Polar interactions are indicated by red dashed lines. NAG, *N*-acetylglucosamine.

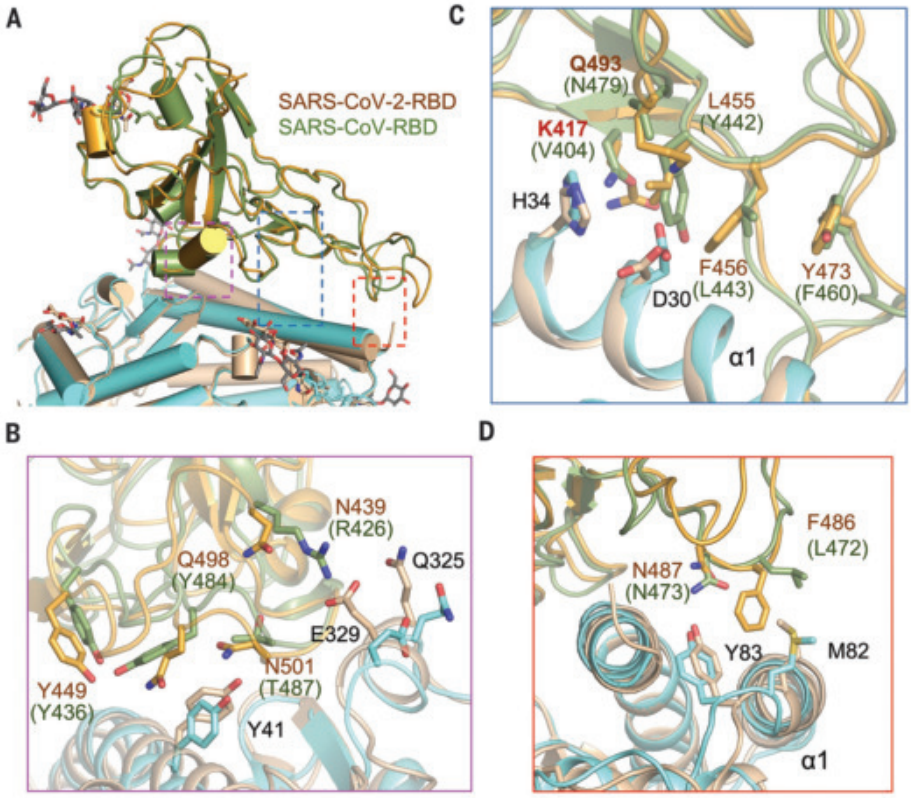

Fig. 5. Interface comparison between SARS-CoV-2-RBD and SARS-CoV-RBD with ACE2. (**A**) Structural alignment for the SARS-CoV-2-RBD and SARS-CoV-RBD. The structure of the ACE2-PD and the SARS-CoV-RBD complex (PDB 2AJF) is superimposed on our cryo-EM structure of the ternary complex relative to the RBDs. The regions enclosed by the purple, blue, and red dashed lines are illustrated in detail in (B) to (D), respectively. SARS-CoV-2-RBD and the PD in our cryo-EM structure are colored orange and cyan, respectively; SARS-CoV-RBD and its complexed PD are colored green and gold, respectively. (**B** to **D**) Variation of the interface residues between SARS-CoV-2-RBD (labeled in brown) and SARS-CoV-RBD (labeled in green).

reveals some variations that may strengthen the interactions between SARS-CoV-2-RBD and ACE2 and other variations that are likely to reduce the affinity compared with SARS-CoV-RBD and ACE2. For instance, the change from Val^{404} to Lys^{317} may result in a tighter association because of the salt bridge formation between Lys^{317} and Asp^{30} of ACE2 (Figs. 4C and 5C). The change from Leu^{472} to Phe^{486} may also result in a stronger van der Waals contact with Met^{82} (Fig. 5D). However, replacement of Arg^{426} with Asn^{439} appears to weaken the interaction by eliminating one important salt bridge with Asp^{329} on ACE2 (Fig. 5B).

Our structural work reveals the high-resolution structure of full-length ACE2 in a dimeric assembly. Docking the S protein trimer onto the structure of the ACE2 dimer with the RBD of the S protein bound suggests simultaneous binding of two S protein trimers to an ACE2 dimer. Structure-based rational design of binders with enhanced affinities to either ACE2 or the S protein of the coronaviruses may facilitate development of decoy ligands or neutralizing antibodies for suppression of viral infection.

REFERENCES AND NOTES

1. N. Zhu *et al*., *N. Engl. J. Med.* **382**, 727–733 (2020).
2. P. Zhou *et al*., *Nature* (2020).
3. T. M. Gallagher, M. J. Buchmeier, *Virology* **279**, 371–374 (2001).
4. G. Simmons, P. Zmora, S. Gierer, A. Heurich, S. Pöhlmann, *Antiviral Res.* **100**, 605–614 (2013).
5. S. Belouzard, V. C. Chu, G. R. Whittaker, *Proc. Natl. Acad. Sci. U.S.A.* **106**, 5871–5876 (2009).
6. G. Simmons *et al*., *Proc. Natl. Acad. Sci. U.S.A.* **101**, 4240–4245 (2004).
7. W. Song, M. Gui, X. Wang, Y. Xiang, *PLOS Pathog.* **14**, e1007236 (2018).
8. F. Li, W. Li, M. Farzan, S. C. Harrison, *Science* **309**, 1864–1868 (2005).
9. J. K. Millet, G. R. Whittaker, *Virus Res.* **202**, 120–134 (2015).
10. G. Simmons *et al*., *Proc. Natl. Acad. Sci. U.S.A.* **102**, 11876–11881 (2005).
11. M. Hoffmann *et al*., bioRxiv 2020.01.31.929042 [Preprint]. 31 January 2020. https://doi.org/10.1101/2020.01.31.929042.
12. W. Li *et al*., *Nature* **426**, 450–454 (2003).
13. K. Kuba *et al*., *Nat. Med.* **11**, 875–879 (2005).
14. D. Wrapp *et al*., *Science* eabb2507 (2020).
15. M. Donoghue *et al*., *Circ. Res.* **87**, E1–E9 (2000).
16. H. Zhang *et al*., bioRxiv 2020.01.30.927806 [Preprint]. 31 January 2020. https://doi.org/10.1101/2020.01.30.927806.
17. Y. Zhao *et al*., bioRxiv 2020.01.26.919985 [Preprint]. 26 January 2020. https://doi.org/10.1101/2020.01.26.919985.
18. M. A. Crackower *et al*., *Nature* **417**, 822–828 (2002).
19. L. S. Zisman *et al*., *Circulation* **108**, 1707–1712 (2003).
20. M. K. Raizada, A. J. Ferreira, *J. Cardiovasc. Pharmacol.* **50**, 112–119 (2007).
21. H. Zhang *et al*., *J. Biol. Chem.* **276**, 17132–17139 (2001).
22. I. Hamming *et al*., *J. Pathol.* **212**, 1–11 (2007).
23. R. N. Kirchdoerfer *et al*., *Sci. Rep.* **8**, 15701 (2018).
24. P. Towler *et al*., *J. Biol. Chem.* **279**, 17996–18007 (2004).
25. S. Kowalczuk *et al*., *FASEB J.* **22**, 2880–2887 (2008).
26. H. F. Seow *et al*., *Nat. Genet.* **36**, 1003–1007 (2004).
27. R. Kleta *et al*., *Nat. Genet.* **36**, 999–1002 (2004).
28. A. Bröer *et al*., *J. Biol. Chem.* **279**, 24467–24476 (2004).
29. A. Penmatsa, K. H. Wang, E. Gouaux, *Nature* **503**, 85–90 (2013).
30. J. A. Coleman, E. M. Green, E. Gouaux, *Nature* **532**, 334–339 (2016).
31. L. Mastroberardino *et al*., *Nature* **395**, 288–291 (1998).
32. R. Yan, X. Zhao, J. Lei, Q. Zhou, *Nature* **568**, 127–130 (2019).
33. Q. Lin, R. S. Keller, B. Weaver, L. S. Zisman, *Biochim. Biophys. Acta* **1689**, 175–178 (2004).
34. A. Shulla *et al*., *J. Virol.* **85**, 873–882 (2011).
35. A. Heurich *et al*., *J. Virol.* **88**, 1293–1307 (2014).
36. C. Drosten *et al*., *N. Engl. J. Med.* **348**, 1967–1976 (2003).
37. C. Yeo, S. Kaushal, D. Yeo, *Lancet Gastroenterol. Hepatol.* S2468-1253(20)30048-0 (2020).
38. J. Jando, S. M. R. Camargo, B. Herzog, F. Verrey, *PLOS ONE* **12**, e0184845 (2017).

ACKNOWLEDGMENTS

We thank the Cryo-EM Facility and Supercomputer Center of Westlake University for providing cryo-EM and computation support, respectively. This work was funded by the National Natural Science Foundation of China (projects 31971123, 81920108015, and 31930059), the Key R&D Program of Zhejiang Province (2020C04001), and the SARS-CoV-2 emergency project of the Science and Technology Department of Zhejiang Province (2020C03129). **Author contributions:** Q.Z. and R.Y. conceived the project. Q.Z. and R.Y. designed the experiments. All authors performed the experiments. Q.Z., R.Y., Y.Z., and Y.L. contributed to data analysis. Q.Z. and R.Y. wrote the manuscript. **Competing interests:** The authors declare no competing interests. **Data and materials availability:** Atomic coordinates and cryo EM maps for the ACE2-B^0AT1 complex of closed conformation (whole structure and map, PDB 6M18 and EMD-30040; extracellular region map, EMD-30044; and TM region map, EMD-30045), the ACE2-B^0AT1 complex of open conformation (PDB 6M1D and EMD-30041), and the complex of the RBD of SARS-CoV-2 with the ACE2-B^0AT1 complex (whole structure and map, PDB 6M17 and EMD-30039; extracellular region map, EMD-30042; TM region map, EMD-30043; and ACE2-RBD interface map, EMD-30046) have been deposited in the Protein Data Bank (www.rcsb.org) and the Electron Microscopy Data Bank (www.ebi.ac.uk/pdbe/emdb/). Correspondence and requests for materials should be addressed to corresponding author Q.Z.

SUPPLEMENTARY MATERIALS

science. /content/367/6485/1444/suppl/DC1 Materials and Methods
Figs. S1 to S9
Table S1
References (*39*–*52*)
MDAR Reproducibility Checklist
Movie S1

12 February 2020; accepted 3 March 2020
Published online 4 March 2020
10.1126/science.abb2762

CLONAL EXPANSION

The evolutionary dynamics and fitness landscape of clonal hematopoiesis

Caroline J. Watson[1,2]*, A. L. Papula[3], Gladys Y. P. Poon[1,2], Wing H. Wong[4], Andrew L. Young[4], Todd E. Druley[4], Daniel S. Fisher[3], Jamie R. Blundell[1,2]*

Somatic mutations acquired in healthy tissues as we age are major determinants of cancer risk. Whether variants confer a fitness advantage or rise to detectable frequencies by chance remains largely unknown. Blood sequencing data from ~50,000 individuals reveal how mutation, genetic drift, and fitness shape the genetic diversity of healthy blood (clonal hematopoiesis). We show that positive selection, not drift, is the major force shaping clonal hematopoiesis, provide bounds on the number of hematopoietic stem cells, and quantify the fitness advantages of key pathogenic variants, at single-nucleotide resolution, as well as the distribution of fitness effects (fitness landscape) within commonly mutated driver genes. These data are consistent with clonal hematopoiesis being driven by a continuing risk of mutations and clonal expansions that become increasingly detectable with age.

As we age, physiologically healthy tissues such as skin (*1*, *2*), colon (*3*, *4*), esophagus (*5*, *6*), and blood (*7*–*18*) acquire mutations in cancer-associated genes. In blood, this phenomenon, termed clonal hematopoiesis (CH), increases in prevalence with age (*7*–*18*), becoming almost ubiquitous in those over the age of 65 (*10*, *15*). The majority of CH mutations are thought to arise in hematopoietic stem cells (HSCs) (*10*, *19*) and typically fall within the genes *DNMT3A*, *TET2*, *ASXL1*, *JAK2*, and *TP53* and spliceosome genes, although chromosomal alterations are also observed (*17*). Because CH is associated with an increased risk of blood cancers (*7*, *8*, *19*) and the genes affected are commonly mutated in preleukemic stem cells (*20*–*24*), CH has emerged as an important precancerous state, for which a quantitative understanding would accelerate risk stratification and improve our understanding of normal hematopoiesis.

The risk of progressing to a blood cancer depends on the gene in which a variant falls (*14*, *18*). However, our ability to stratify specific variants and their relative risk remains crude. If variants confer a fitness advantage to HSCs, they are more likely to expand over time. Furthermore, higher variant allele frequencies (VAFs) are predictors of acute myeloid leukemia (AML) development (*14*, *18*). It stands to reason, therefore, that by analyzing the spectrum of VAFs, one might be able to infer the fitness advantage conferred by specific variants from a static "snapshot." This would enable us to generate a comprehensive map between specific variants and their fitness consequences, allowing risk to be stratified with greater resolution.

A major challenge to using VAFs to risk stratify variants is that the spectrum of VAFs, even at the level of a specific variant, is considerably broad (*10*). Whether these differences in VAFs are a result of cell-intrinsic fitness advantages (*25*), cell-extrinsic perturbations (*26*), or sheer chance (*13*) remains unclear. To identify the most highly fit variants, we first need to understand how mutation, genetic drift, and differences in fitness (selection) combine to produce the spectrum of VAFs observed in CH.

Results

The VAF distribution from ~50,000 individuals

Insights from evolutionary theory were applied to the VAF spectra of somatic mutations detected in the blood from ~50,000 blood cancer–free individuals from nine publicly available blood sequencing datasets (*7*–*15*) [see (*27*)] to tease apart the effects of mutation, drift, and selection. Using single blood sample snapshots, we quantified the fitness advantages of key pathogenic single-nucleotide variants (SNVs) as well as the spectrum of fitness effects (fitness landscape) of the most commonly mutated driver genes. VAF measurements in bone marrow and peripheral blood show good concordance (*28*), so peripheral blood VAF measurements are used as a proxy to reflect clonal composition at the level of the bone marrow HSCs. The nine studies we analyzed varied in their number of participants and sequencing depth (Fig. 1A). Most large-scale studies were limited by standard sequencing error rates and were only able to detect VAFs >3% (*7*, *8*), whereas smaller studies, which used error-correcting techniques, were able to detect VAFs as low as 0.03% (*10*, *12*, *15*). VAFs varied by more than three orders of magnitude across individuals even within the same gene, as exemplified by *DNMT3A*, the most commonly mutated CH gene (Fig. 1B). The distribution of variants was strongly skewed to low VAFs. Variants were observed far more frequently at certain sites [e.g., *DNMT3A* R882 (Arg^{882}) hotspot codon; red data in Fig. 1B] and were almost exclusively putatively functional (nonsynonymous and frameshifts); synonymous variants were rare and restricted to low VAFs.

A branching model of stem cell dynamics

To reveal the relative contributions of genetic drift, mutation rate differences, and cell-intrinsic fitness effects on the observed variation in VAFs, we considered a simple stochastic branching model of HSC dynamics built on classic population genetic models (*29*–*33*), adapted to include a spectrum of ages and fitness effects [see (*27*)]. The model is of an HSC population of N diploid cells that stochastically self-renew or differentiate symmetrically or asymmetrically (Fig. 1C) and describes a variety of biologically plausible scenarios, including HSCs occupying a fixed number of spatially constrained niches [see (*27*)]. Mutations are acquired stochastically at a constant rate μ per year. The fate of a new mutation depends on its influence on stochastic cell fate decisions through a fitness effect, s, which is the average growth rate per year of that variant relative to the average growth rate of normal HSCs. Neutral mutations ($s = 0$) do not alter the balance between self-renewal and differentiation, which both occur at rate $1/\tau$. Thus, neutral mutations usually rapidly go extinct or, owing to random fluctuations, grow slowly and remain at low VAFs (orange trajectories in Fig. 1D). Beneficial mutations ($s > 0$) increase the rate of self-renewal relative to symmetric differentiation and, provided they escape stochastic extinction, eventually grow exponentially at rate s per year (red and blue trajectories in Fig. 1D). This relative increase in the rate of self-renewal can be achieved by biasing cell fates alone [increasing the probability of self-renewal (*34*) (red plus sign in Fig. 1C) or decreasing differentiation or apoptosis (*35*) (red minus sign in Fig. 1C)] or by a combination of cell fate bias and an increase in division rate.

Variants with a high fitness effect or those acquired early in life are expected to reach high VAFs (trajectories labeled 1 and 2 in Fig. 1D), whereas variants with a low fitness effect or those acquired late in life are restricted to low VAFs (trajectories labeled 3 and 4 in Fig. 1D). This variation in both the age acquired and fitness effect of variants produces a characteristic spectrum of VAFs that can be measured in a single blood sample (insets of Fig. 1D). How these distributions change with age (t) is determined by the fitness effect of variants (s), their mutation rate

[1]Department of Oncology, University of Cambridge, Cambridge, UK. [2]Early Detection Programme, CRUK Cambridge Cancer Centre, University of Cambridge, Cambridge, UK. [3]Department of Applied Physics, Stanford University, Stanford, CA, USA. [4]Department of Pediatrics, Division of Hematology and Oncology, Washington University School of Medicine, St. Louis, MO, USA.
*Corresponding author. Email: cw672@cam.ac.uk (C.J.W.); jrb75@cam.ac.uk (J.R.B.)

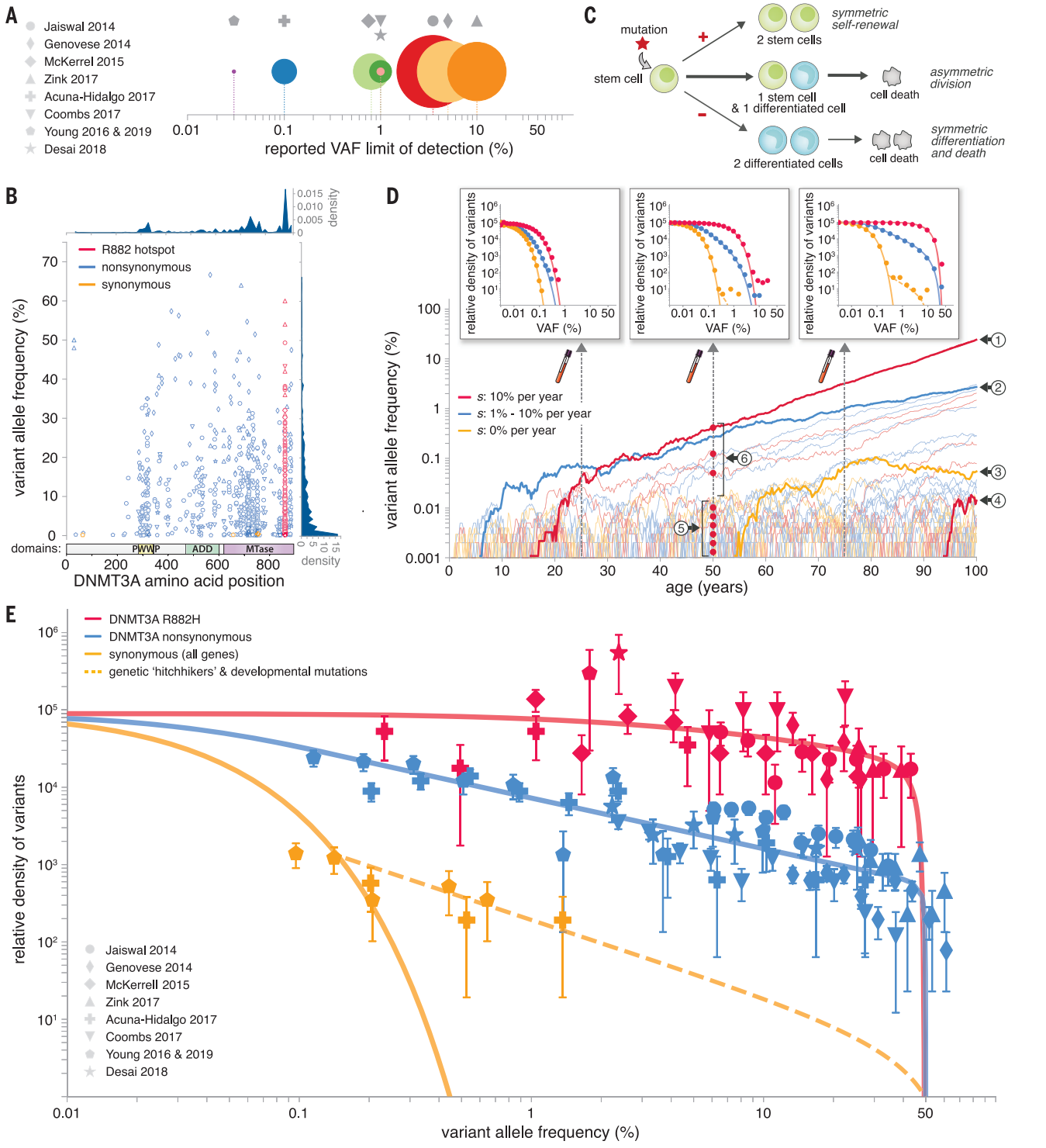

Fig. 1. A branching model of HSC dynamics explains the observed VAF distribution for variants in healthy blood. (**A**) Studies used in this analysis varied in the number of participants (indicated by relative circle size) and reported VAF detection thresholds. (**B**) The density of variants in *DNMT3A* varies widely by VAF (>3 logs) and position in the gene. (**C**) A branching model of HSC dynamics. Mutations with a positive fitness effect (red star) cause an imbalance in stochastic cell fates toward self-renewal. This can be an increase in the rate of self-renewal (red plus sign), a decrease in differentiation or apoptosis (red minus sign), or a combination of the two, resulting in clonal expansions. (**D**) Simulations of HSC populations under a branching model show how differences in fitness effect and age produce VAF spectra (insets) in close agreement with observed data [shown in (E)]. The vertical dashed lines indicate the timings of the blood samples that produce the VAF spectra shown in the insets. The numbered features are explained in the main text. The red dots labeled 5 and 6 highlight where the red trajectories cross the vertical dashed line. (**E**) Plotting all VAF measurements of *DNMT3A* variants as log-binned histograms normalized by mutation rates (data points) demonstrates the consistency with the theoretical predictions of the branching model (lines). The theoretical predictions account for a distribution of ages in the studies. The density of high-frequency synonymous variants is consistent with the predicted density of genetic hitchhikers and early developmental mutations [dashed orange line; see (*27*)]. Error bars represent sampling noise.

(μ), the population size of HSCs (N), and the time (τ) in years between successive symmetric cell differentiation divisions according to the following expression for the probability density as a function of l = log(VAF) [full derivation in (*27*)]:

$$\rho(l) = \theta \exp\left(-\frac{e^l}{\phi}\right) \quad (1)$$

where l = log(VAF), $\theta = 2N\tau\mu$, and $\phi = \frac{e^{st}-1}{2N\tau s}$.

To develop an intuition for the two key features of this distribution, consider variants with a fitness advantage entering the HSC population uniformly at a rate θ/τ per year and growing exponentially. The exponential growth means that variant trajectories, plotted on a log-VAF scale, are uniformly spaced straight lines (red dots labeled 5 in Fig. 1D), producing a flat density with y intercept of θ. Dividing the density of variants by the mutation rate (measured per year), the y intercept therefore provides an estimate for $N\tau$ [insets of Fig. 1D, (*27*)]. Because the age of the oldest surviving variant cannot exceed the age of the individual, there is a characteristic maximum VAF, ϕ, a variant can reach, which increases with fitness effect, s, and age, t. To reach VAFs >ϕ requires a variant to both occur early in life and stochastically drift to high frequencies, which is unlikely. Therefore, the density falls off exponentially for VAFs >ϕ (red dots labeled 6 in Fig. 1D). The sharp density falloff at 50% VAF occurs because even a variant that is present in a very large proportion of total HSCs will tend toward 50% VAF because the cells are diploid.

HSC numbers and division times

To infer HSC numbers and test the predictions of our model, we plotted log-VAF distributions for SNVs from all the studies (*7*–*15*) [see (*27*)]. Studies differed in their number of participants as well as their panel size, both of which affect the number of variants detected. Therefore, to combine the data from all the studies, we normalized the number of observed variants by their study size and total study-specific mutation rate (for variant or gene of interest), controlling for trinucleotide contexts of mutations [see (*27*)]. For a given specific position in the genome, mutation rates are low enough that, over a human life span, clones acquiring multiple driver mutations are rare and thus variants can uniquely mark clones [see (*27*)].

We first focused on mutations in the gene *DNMT3A* (Fig. 1E). The most commonly observed variant in *DNMT3A* is the missense variant R882H (Arg^{882}→His; red data in Fig. 1E). Because fitness effects are expected to be variant-specific (*36*), all R882H variants should confer the same fitness effect and so serve as a useful check on the model. Consistent with our predictions, the density of R882H variants is flat over almost the entire frequency range (VAFs <15%) with a y intercept of $N\tau \approx$ 100,000 ± 30,000 years (figs. S9 and S11). Encouragingly, this number is in agreement with that inferred from single HSC phylogenies (*37*). It is important to note that population genetic analyses can only reliably infer the combination $N\tau$ and not N or τ separately. Early developmental mutations indicate that HSCs accrue ≈1.2 mutations per cell division (*37*), which, combined with an HSC mutation rate in adulthood of ≈16 per cell per year (*37*), suggests that HSCs divide ≈13 times per year. Although symmetric divisions are harder to estimate, this provides an upper bound on the number of HSCs, suggesting that <1.3 million HSCs maintain the peripheral blood. Because $\tau < 1/s_{max}$ [see (*27*)], the maximum inferred $s \approx 25\%$ suggests that $\tau < 4$ years, providing a lower bound of 25,000 on the number of HSCs.

To validate our estimates for $N\tau$, we turned to the distribution of all synonymous variants (orange data in Fig. 1E). Because synonymous variants are generally expected to be functionally neutral, the characteristic VAF of the biggest synonymous variants (ϕ) increases only linearly with age because it is driven by drift alone (see Eq. 1), and $N\tau$ is the time it would take for a neutral mutation to drift to fixation

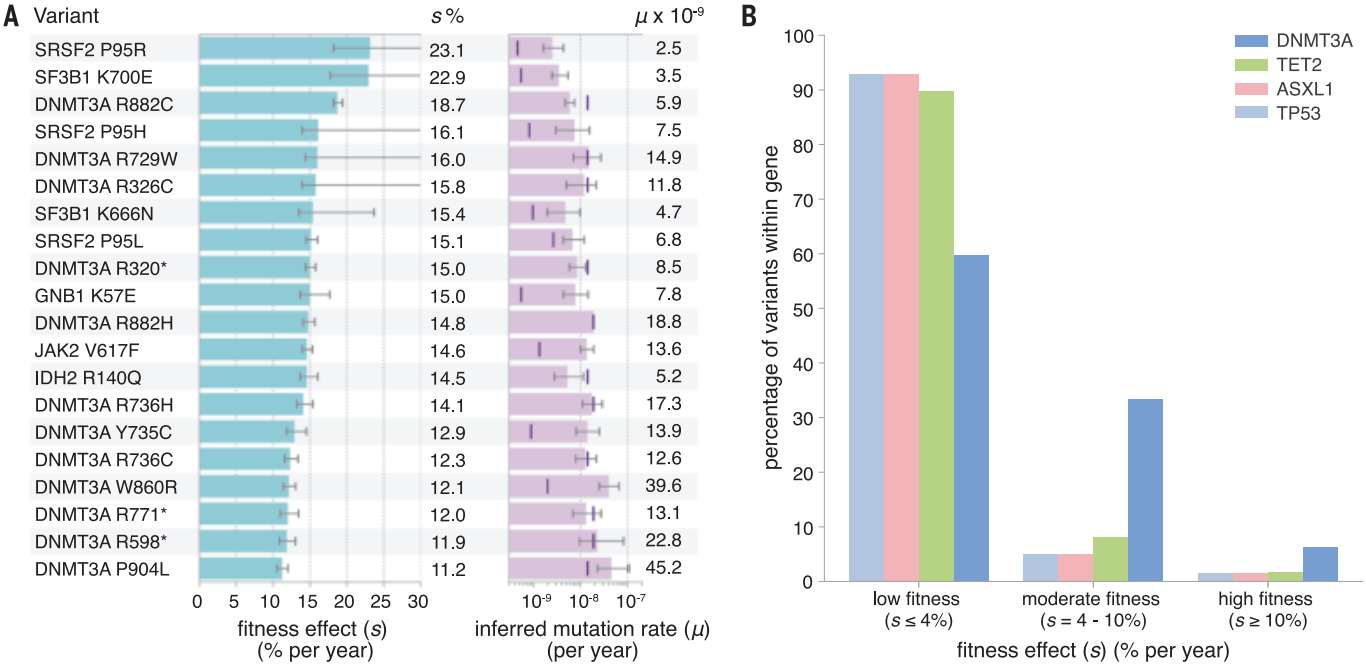

Fig. 2. The fitness landscape of CH variants and genes. (**A**) Inferred fitness effects and mutation rates for the top 20 most commonly observed CH variants. Error bars represent 95% confidence intervals. Purple vertical lines indicate site-specific mutation rates inferred from trinucleotide context [see (*27*)]. (**B**) The distribution of fitness effects of nonsynonymous variants in key CH driver genes, inferred by fitting a stretched exponential distribution and dividing this into three fitness classes (low, moderate, and high) [see (*27*)]. These distributions reveal many low-fitness and few high-fitness variants. Over a human life span, variants with fitness effects <4% expand only a modest factor more than a neutral variant (low fitness), variants with fitness effects of 4 to 10% per year expand by substantial factors (moderate fitness), and variants with fitness effects >10% per year can expand enough to overwhelm the marrow (high fitness).

by chance. The synonymous variants provide a crucial validation of the model because it predicts that the majority of synonymous variants should be found at very low VAFs. Quantitatively, if our inferred value of $N\tau \approx 100{,}000$ years from DNMT3A R882H variants is correct, it would predict that the majority of synonymous mutations should be restricted to VAFs below $\phi = t/2N\tau \approx 0.025\%$ at age 50. This prediction broadly agrees with the data, where the maximum likelihood inferred $\phi \approx 0.03 \pm 0.005\%$ [see (*27*)]. This internal consistency check indicates that both synonymous and *DNMT3A* R882H variants point toward similar values of $N\tau$. Synonymous variants with VAFs $>>\phi$ are rare (orange dashed line in Fig. 1E) and are consistent with having hitchhiked to high frequencies on the back of an expanding clone that had already acquired a fit variant [see (*27*)], although it is also possible that a handful are developmental in origin; have a functional consequence themselves, for example, owing to codon usage bias; or are in fact nonsynonymous in an alternatively spliced transcript.

The fitness landscape of CH

Because the characteristic maximum VAF, ϕ, depends on the fitness effect, s, by estimating ϕ from the VAF spectrum, we can infer a variant's fitness. We illustrate this approach using *DNMT3A* R882H variants. As predicted by the model, the density of R882H variants does indeed begin to fall off exponentially for VAFs >12% [red data in Fig. 1E; see (*27*)]. This suggests that R882H variants provide HSCs with a large selective advantage ($s \approx 15 \pm 1\%$ per year) because, over the course of ≈55 years (mean age across all studies), they have expanded to VAFs ≈12%, although some have reached VAFs as high as 50%.

To reveal the fitness landscape of other highly fit and possibly pathogenic variants, we applied this analysis to each of the 20 most commonly observed variants across all studies (Fig. 2A). Variants in the spliceosome genes *SF3B1* and *SRSF2* are some of the fittest in CH, with fitness effects as high as $s \approx 23\%$ per year, but are relatively rare owing to low mutation rates. *DNMT3A* R882H is the most common CH variant, because it is both highly fit and has a high mutation rate owing to its CpG context. The *DNMT3A* R882C ($Arg^{882} \rightarrow Cys$) variant is notably fitter than R882H ($s \approx 19 \pm 1\%$ versus $s \approx 15 \pm 1\%$ per year) but is observed less frequently because of its lower mutation rate [see (*27*)]. The potential of our analyses is underscored by the *GNB1* K57E ($Lys^{57} \rightarrow Glu$) variant. Although this variant has received little attention in CH, it is highly fit and strongly associated with myeloid cancers and represents a potentially targetable variant (*38*).

To reveal the overall fitness landscapes of key CH driver genes, we considered the VAF distribution of all nonsynonymous variants in each of the genes *DNMT3A*, *TET2*, *ASXL1*, and *TP53* (Fig. 2B). For *DNMT3A*, the density of nonsynonymous variants at low VAFs is broadly consistent with the same $N\tau \approx 100{,}000$ years inferred from R882H variants (blue data in Fig. 1E). However, with increasing VAF, the density of variants declines, consistent with a spectrum of ϕ and thus a spectrum of fitness effects. Performing a maximum likelihood fit to a family of stretched exponential distributions, we found that the spectrum of fitness effects for nonsynonymous variants in *DNMT3A* is very broad, with ≈40% of variants conferring moderate to high fitness effects [$s > 4\%$ per year, Fig. 2B; see (*27*)]. By contrast, the genes *TET2*, *ASXL1*, and *TP53* have a spectrum that is more skewed toward low fitness effects, with only ≈7 to 10% of all possible nonsynonymous variants in these genes conferring moderate or high fitness effects. These distributions highlight that, in these CH genes, most nonsynonymous variants have a low enough fitness that they are effectively neutral, whereas an important minority expand fast enough to become pathogenic and overwhelm the marrow over a human life span.

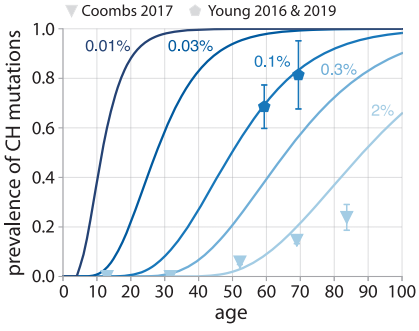

Fig. 3. Predicted prevalence of CH mutations as a function of age for different detection thresholds. Prevalence is predicted for individuals to have acquired at least one variant within 10 of the most commonly mutated CH genes (*DNMT3A*, *TET2*, *ASXL1*, *JAK2*, *TP53*, *CBL*, *SF3B1*, *SRSF2*, *IDH2*, and *KRAS*), taking into account the distribution of fitness effects across these genes [see (*27*)]. The actual prevalence of variants within these genes, as a function of age, is shown for (*10*, *15*) (pentagons, VAF limit of detection ≈ 0.1%) and (*11*) (triangles, VAF limit of detection ≈ 2%). Error bars represent sampling noise.

Highly fit variants confer an increased risk of AML

We next asked whether high-fitness variants confer an increased risk of AML development. By considering the pre-AML and control samples from three studies (*14*, *15*, *18*), we found that individuals harboring one or more of the 20 highly fit variants we identified (Fig. 2A) are ≈4-fold more likely to develop AML compared with those harboring lower-fitness variants [one-sided Fisher's exact test, $p < 10^{-5}$; see (*27*)].

Age dependence of CH

A key prediction of the model is that, because variants enter the HSC population at a constant rate, the apparent prevalence of a specific variant, at a defined sequencing sensitivity, is predicted to increase roughly linearly with age at rate $2N\tau\mu s$ [see (*27*)]. We confirmed this prediction using *DNMT3A* R882H and R882C variants, which, when combined, had enough data to be broken down by age group (fig. S18). In agreement with predictions, the age prevalence of these variants does increase linearly with age, consistent with the age dependence of CH being driven by the expansion of clones that become more detectable in individuals of older ages. The rate of this increase provides an independent way to validate estimates of fitness effects and, in this case, the rate of increase is consistent with a fitness effect of $s \approx 14\%$ per year, which is in agreement with estimates inferred from the VAF distribution (Fig. 2A).

By inferring the spectrum of fitness effects across 10 of the most commonly mutated CH genes, we can predict how common CH will be as a function of both age and sequencing sensitivity [Fig. 3 and (*27*)]. With sensitive-enough sequencing (VAFs ≥0.01%), CH variants will be detectable even in young adults and almost ubiquitous in people aged over 50 years. Our framework also enables us to predict the emergence of clones harboring multiple driver mutations. Although this depends on the cooperativity between mutations, under the assumption of additive fitness effects, we predict that, at a VAF detection limit of 0.01%, <15% of individuals aged 80 years will harbor clones with two or more mutations within the same cell [see (*27*)].

Discussion

A simple framework explains CH

Analyzing the VAF spectra from nine publicly available clonal hematopoiesis datasets in light of evolutionary theory points to a simple and consistent picture of how HSC population dynamics shape the genetic diversity of blood. The very wide variation in VAFs observed among people can be largely explained by the combined effects of chance (when a mutation arises) and fitness differences (how fast they expand). Our framework produces quantitative predictions for the number of HSCs, the prevalence of CH across ages, and how the number of somatic variants scale with VAF. These predictions are in agreement with available data and, in the case of HSC numbers, have been independently validated by an orthogonal method (*37*).

Implicit to our analysis is the assumption that many of the CH mutations drive cell-intrinsic increases in fitness. However, fitness is always context dependent, and therefore, cell-extrinsic effects are likely crucial in some

cases. It is also possible that the fitness effect of variants themselves changes over time, for example, owing to a slow but steady loss or gain of epigenetic marks due to mutations in epigenetic regulators (*39*, *40*). Changes in bone marrow environment driven by aging (*41*, *42*), chemotherapy (*11*, *26*, *35*, *43*), acute infection (*44*, *45*), and inflammation (*46*) could all shape the fitness effects of some variants. Indeed, specific variants (e.g., *PPM1D*, *TP53*, *CHEK2*, and *ASXL1*) are known to be strongly influenced by external factors (*26*, *35*, *47*). Taken together, however, the data from healthy individuals over a broad range of ages are quantitatively consistent with cell-intrinsic fitness differences playing a major role in shaping the variation in HSC clone sizes.

Although it might seem surprising that a simple model captures many quantitative aspects of CH data, more complex scenarios, including spatially partitioned niches, yield the same effective model for the multiyear development of CH; although in these scenarios, N and τ have more complex meanings [see (*27*)]. These include models with HSCs switching between active and quiescent states and models with progenitors occasionally reverting to HSCs. But there are important observations that the model cannot fully explain, including a considerably broader than expected distribution in the number of variants observed in different individuals, although this could be attributed to variations in mutation rates across individuals or environment-specific effects. Distinguishing between these scenarios and teasing apart the relative contributions of cell-intrinsic versus cell-extrinsic influences on cellular fitness will likely require longitudinal data and is an important area for future work.

In HSCs, fitness dominates drift

The relative roles of mutation, drift, and selection in shaping the somatic mutational diversity observed in human tissues has been the subject of much recent debate, especially regarding the conflicting interpretations from the ratio of nonsynonymous to synonymous mutations (dN/dS) (*1*, *5*, *48*) and clone size statistics (*32*, *49*, *50*). In blood, the two measures are in quantitative agreement; nonsynonymous variants are under strong positive selection, and most synonymous variants fluctuate by means of neutral drift.

Our inference of the large HSC population size ($N\tau \approx 100{,}000$ years) has an important interpretation: On average, it would take 100,000 years for a variant to reach VAFs of 50% by drift alone and >2000 years to be detectable by standard sequencing (VAF > 1%). Therefore, the vast majority of CH variants reaching VAFs >0.1% over a human life span likely do so because of positive selection. However, this is not to say that variants with VAFs <0.1% are not potentially pathogenic. Indeed, most highly fit variants exist at low VAFs simply because not enough time has yet passed for them to expand, although they are less likely to acquire subsequent driver mutations while they are at low VAFs.

More than 2500 variants confer moderate to high fitness

By considering the VAF spectrum across 10 of the most commonly mutated CH genes, we have inferred that mutations conferring fitness effects $s > 4\%$ per year occur at a rate of $\approx 4 \times 10^{-6}$ per year [see (*27*)]. Given that the average site-specific mutation rate in HSCs is 1.6×10^{-9} per year [see (*27*)], this implies that there are ≥2500 variants within these genes conferring moderate to high selective advantages. Our framework, in combination with broader coverage sequencing outside of known hotspot regions, could facilitate the discovery of these preleukemic drivers. However, targeting specific preleukemic clones may be clinically challenging, especially because the targeted therapy may alter the clonal dynamics of other variants. Although there is direct evidence from longitudinal data (*18*) and indirect evidence from age-prevalence patterns [see (*27*)] that variants at many of these moderate- and high-fitness sites expand at a roughly constant rate, other variants, notably *JAK2* V617F ($Val^{617} \rightarrow$ Phe), might exhibit more complex dynamics given the small exponential growth rates observed in longitudinal data (*51*). It is likely that specific mutations achieve their selective advantages in different ways. Some will simply cause a bias toward self-renewal (*34*, *52*), whereas others may cause a bias as well as an increase in the intrinsic cell division rate. Distinguishing between these scenarios will require important future functional studies.

The variants commonly observed in CH are not necessarily the most fit but are both sufficiently fit and sufficiently frequently mutated. To reveal variants that are infrequently mutated yet potentially highly fit, we considered all variants in *DNMT3A*, *TET2*, *ASXL1*, and *TP53* that were detected at least twice across all nine studies and estimated their fitness effects by determining what fitness effect would be needed to produce the number of observed variants [see (*27*)]. Although the lack of data at infrequently mutated sites and the crudeness of this counting method necessarily lead to large uncertainties, there appear to be at least some highly fit yet infrequently mutated variants which, although individually rare, could be collectively common [see (*27*)]. We note that the high-fitness variants identified in *TP53* are strongly enriched for missense variants in the DNA binding domain (figs. S24 and S25), in agreement with recent functional and clinical data (*53*).

Given the average site-specific mutation rate of 1.6×10^{-9} per year (table S4), a comprehensive map between variant and fitness effect for all sites that confer a selective advantage large enough to expand substantially over a human life span ($s > 4\%$) could be achieved with the current sample size by increasing sequencing sensitivity to detect variants at VAFs >0.04% (fig. S26B). However, because sites can mutate at rates as low as $\mu \sim 10^{-10}$ per year (table S4), to quantify all variants, even rare ones, would require both a 6-fold increase in sample size as well as sequencing sensitivities as low as 0.01% VAF [see (*27*)]. Nonetheless, even with small study sizes, there are major advantages to being sensitive to very low VAFs (*10*, *12*, *15*), particularly in relation to synonymous variants, which, when grouped together, provide important information on $N\tau$ and genetic hitchhikers (Fig. 1E).

The near absence of variants in known AML drivers, such as *FLT3* and *NPM1*, across the nine studies suggests that mutations in these genes do not confer an unconditional selective advantage to HSCs, consistent with studies in mice and humans showing that they are late occurring and possibly cooperating mutations necessary for transformation to AML (*20*, *23*).

Future directions

CH has associated risks with cardiovascular disease (*7*, *54*) and progression to blood cancers (*7*, *8*, *14*, *18*) and consequences in the study of circulating tumor DNA (*55*, *56*), aplastic anemia (*57*), response to chemotherapies (*58*, *59*), and bone marrow transplant (*43*, *60*, *61*). A major challenge is to develop a predictive understanding of how variants and their VAFs affect disease risk. Recent studies show that both gene identity and VAF are predictive of progression to AML (*14*, *18*). The framework presented here provides a rational basis for quantifying the fitness effects of these variants and understanding VAF variations. Using this framework, we demonstrate that fitness estimates can be used to stratify AML risk. Because higher VAFs are strong predictors of AML development (*14*, *18*) and fitter variants are more likely to reach higher VAFs, it is perhaps not surprising that high-fitness variants are able to stratify AML risk. However, fitness predicts which variants are likely to reach high VAF and thus ought to have increased predictive power. Combining this framework with studies that longitudinally track individuals over time will shed light on how these initiating mutations acquire further mutations that drive overt disease. More sensitive sequencing techniques, broader sampling of the genome (e.g., regulatory regions), and the study of environmental factors that alter the fitness of mutations will improve our quantitative understanding of native human hematopoiesis and accelerate the development of risk predictors.

REFERENCES AND NOTES

1. I. Martincorena *et al.*, *Science* **348**, 880–886 (2015).
2. A. S. Jonason *et al.*, *Proc. Natl. Acad. Sci. U.S.A.* **93**, 14025–14029 (1996).
3. F. Blokzijl *et al.*, *Nature* **538**, 260–264 (2016).
4. H. Lee-Six *et al.*, *Nature* **574**, 532–537 (2019).
5. I. Martincorena *et al.*, *Science* **362**, 911–917 (2018).
6. A. Yokoyama *et al.*, *Nature* **565**, 312–317 (2019).
7. S. Jaiswal *et al.*, *N. Engl. J. Med.* **371**, 2488–2498 (2014).
8. G. Genovese *et al.*, *N. Engl. J. Med.* **371**, 2477–2487 (2014).
9. T. McKerrell *et al.*, *Cell Rep.* **10**, 1239–1245 (2015).
10. A. L. Young, G. A. Challen, B. M. Birmann, T. E. Druley, *Nat. Commun.* **7**, 12484 (2016).
11. C. C. Coombs *et al.*, *Cell Stem Cell* **21**, 374–382.e4 (2017).
12. R. Acuna-Hidalgo *et al.*, *Am. J. Hum. Genet.* **101**, 50–64 (2017).
13. F. Zink *et al.*, *Blood* **130**, 742–752 (2017).
14. P. Desai *et al.*, *Nat. Med.* **24**, 1015–1023 (2018).
15. A. L. Young, R. S. Tong, B. M. Birmann, T. E. Druley, *Haematologica* **104**, 2410–2417 (2019).
16. M. Xie *et al.*, *Nat. Med.* **20**, 1472–1478 (2014).
17. P.-R. Loh *et al.*, *Nature* **559**, 350–355 (2018).
18. S. Abelson *et al.*, *Nature* **559**, 400–404 (2018).
19. D. P. Steensma *et al.*, *Blood* **126**, 9–16 (2015).
20. M. Jan *et al.*, *Sci. Transl. Med.* **4**, 149ra118 (2012).
21. L. I. Shlush *et al.*, *Blood* **122**, 487 (2013).
22. M. R. Corces-Zimmerman, R. Majeti, *Leukemia* **28**, 2276–2282 (2014).
23. L. I. Shlush *et al.*, *Nature* **506**, 328–333 (2014).
24. L. I. Shlush *et al.*, *Nature* **547**, 104–108 (2017).
25. L. I. Zon, *Nature* **453**, 306–313 (2008).
26. K. L. Bolton *et al.*, bioRxiv 848739 [Preprint]. 20 November 2019.
27. See supplementary methods.
28. S. M. Hwang *et al.*, *Leuk. Res.* **71**, 92–94 (2018).
29. E. Clayton *et al.*, *Nature* **446**, 185–189 (2007).
30. A. M. Klein, D. P. Doupé, P. H. Jones, B. D. Simons, *Phys. Rev. E Stat. Nonlin. Soft Matter Phys.* **76**, 021910 (2007).
31. M. M. Desai, D. S. Fisher, *Genetics* **176**, 1759–1798 (2007).
32. B. D. Simons, *Proc. Natl. Acad. Sci. U.S.A.* **113**, 128–133 (2016).
33. J. R. Blundell *et al.*, *Nat. Ecol. Evol.* **3**, 293–301 (2019).
34. M. Jeong *et al.*, *Cell Rep.* **23**, 1–10 (2018).
35. J. I. Hsu *et al.*, *Cell Stem Cell* **23**, 700–713.e6 (2018).
36. S. Venkataram *et al.*, *Cell* **166**, 1585–1596.e22 (2016).
37. H. Lee-Six *et al.*, *Nature* **561**, 473–478 (2018).
38. A. Yoda *et al.*, *Blood* **124**, 3567 (2014).
39. G. A. Challen *et al.*, *Nat. Genet.* **44**, 23–31 (2011).
40. N. A. Robertson *et al.*, *Curr. Biol.* **29**, R786–R787 (2019).
41. A. I. Rozhok, J. DeGregori, *Proc. Natl. Acad. Sci. U.S.A.* **112**, 8914–8921 (2015).
42. T. McKerrell, G. S. Vassiliou, *Sci. Transl. Med.* **7**, 306fs38 (2015).
43. T. N. Wong *et al.*, *Nature* **518**, 552–555 (2015).
44. H. Takizawa, S. Boettcher, M. G. Manz, *Blood* **119**, 2991–3002 (2012).
45. M. Meisel *et al.*, *Nature* **557**, 580–584 (2018).
46. K. Y. King, M. A. Goodell, *Nat. Rev. Immunol.* **11**, 685–692 (2011).
47. K. Murai *et al.*, *Cell Stem Cell* **23**, 687–699.e8 (2018).
48. I. Martincorena *et al.*, *Cell* **171**, 1029–1041.e21 (2017).
49. M. J. Williams, B. Werner, C. P. Barnes, T. A. Graham, A. Sottoriva, *Nat. Genet.* **48**, 238–244 (2016).
50. M. J. Williams *et al.*, *Nat. Genet.* **50**, 895–903 (2018).
51. C. Nielsen, S. E. Bojesen, B. G. Nordestgaard, K. F. Kofoed, H. S. Birgens, *Haematologica* **99**, 1448–1455 (2014).
52. S. M. Chan, R. Majeti, *Int. J. Hematol.* **98**, 648–657 (2013).
53. S. Boettcher *et al.*, *Science* **365**, 599–604 (2019).
54. S. Jaiswal *et al.*, *N. Engl. J. Med.* **377**, 111–121 (2017).
55. J. Liu *et al.*, *Ann. Oncol.* **30**, 464–470 (2019).
56. C. Swanton *et al.*, *J. Clin. Oncol.* **36**, 12003–12003 (2018).
57. T. Yoshizato *et al.*, *N. Engl. J. Med.* **373**, 35–47 (2015).
58. K. Takahashi *et al.*, . *Lancet Oncol.* **18**, 100–111 (2017).
59. K. L. Bolton *et al.*, *J. Clin. Oncol.* **37**, 7–11 (2019).
60. T. N. Wong *et al.*, *Nat. Commun.* **9**, 455 (2018).
61. R. C. Lindsley *et al.*, *N. Engl. J. Med.* **376**, 536–547 (2017).
62. C. J. Watson, blundelllab/ClonalHematopoiesis: The evolutionary dynamics and fitness landscape of clonal hematopoiesis. Zenodo (2020); doi:10.5281/zenodo.3706791.
63. C. J. Watson, The evolutionary dynamics and fitness landscape of clonal hematopoiesis. Dryad (2020); https://doi.org/10.5061/dryad.83bk3j9mw.

ACKNOWLEDGMENTS

We thank all members of the Blundell, Fisher, and Druley labs. We thank S. Levy, I. Cvijovic, D. Petrov, B. Simons, M. Gerstung, B. Huntly, I. Martincorena, R. Levine, A. Levine, S. Jaiswal, and R. Majeti for helpful comments. **Funding:** C.J.W. is funded by a CRUK Cambridge Centre Clinical Research Fellowship. A.L.P. is supported by the National Science Foundation GRFP. G.Y.P.P. is funded by the CRUK Cambridge Centre Early Detection Programme and the Bei Shan Tang Foundation. W.H.W., A.L.Y., and T.E.D. are supported by NIH/NCI 1R01CA211711. D.S.F. and J.R.B. are supported by the Stand Up to Cancer Foundation and the National Science Foundation through PHY-1545840. J.R.B. is funded by the CRUK Cambridge Centre Early Detection Programme and by a UKRI Future Leaders Fellowship. **Author contributions:** J.R.B. and D.S.F. conceived the project. C.J.W., J.R.B., D.S.F., and A.L.P. developed the theory. C.J.W. and J.R.B. developed the data analysis methods and performed the data analysis and numerical simulations with input from D.S.F., A.L.P., and G.Y.P.P. D.S.F. and A.L.P. developed and analyzed the alternative models. G.Y.P.P. developed and analyzed the hitchhiking and multiple-mutant model and performed its data analysis. W.H.W., A.L.Y., and T.E.D. provided data. C.J.W. and J.R.B. wrote the manuscript. All authors provided comments and edits on the manuscript. **Competing interests:** C.J.W., A.L.P., G.Y.P.P., W.H.W., D.S.F., and J.R.B. have no competing interests. T.E.D. is the Chief Medical Officer for ArcherDX, Inc. As such, he holds ownership and receives salary. T.E.D. and A.L.Y. are co-inventors on patent application no. 62/106,967 submitted by Washington University School of Medicine in St. Louis, MO, USA, that covers an error-corrected sequencing method. This patent has been licensed by Canopy Biosciences, who were not involved in any data generation within this manuscript. **Data and materials availability:** All code used in this study is available at Zenodo (*62*) and accompanying data are available on Dryad (*63*).

SUPPLEMENTARY MATERIALS

science. /content/367/6485/1449/suppl/DC1 Supplementary Methods
Figs. S1 to S26
Tables S1 to S11
References (*64*–*69*)

31 July 2019; accepted 24 January 2020
10.1126/science.aay9333

REPORTS

SUPERCONDUCTIVITY

Type-II Ising pairing in few-layer stanene

Joseph Falson[1]*, Yong Xu[2,3,4], Menghan Liao[2], Yunyi Zang[2], Kejing Zhu[2], Chong Wang[2], Zetao Zhang[2], Hongchao Liu[5], Wenhui Duan[2,4,6], Ke He[2,4,7], Haiwen Liu[8]†, Jurgen H. Smet[1]†, Ding Zhang[2,4,7]†, Qi-Kun Xue[2,4,7]

Spin-orbit coupling has proven indispensable in the realization of topological materials and, more recently, Ising pairing in two-dimensional superconductors. This pairing mechanism relies on inversion symmetry–breaking and sustains anomalously large in-plane polarizing magnetic fields whose upper limit is predicted to diverge at low temperatures. Here, we show that the recently discovered superconductor few-layer stanene, epitaxially strained gray tin (α-Sn), exhibits a distinct type of Ising pairing between carriers residing in bands with different orbital indices near the Γ-point. The bands are split as a result of spin-orbit locking without the participation of inversion symmetry–breaking. The in-plane upper critical field is strongly enhanced at ultralow temperature and reveals the predicted upturn.

The realization of superconducting materials that are resilient to strong external magnetic fields remains an important pursuit for both applied and fundamental research (*1*–*7*). One recent breakthrough has been the identification of "Ising pairing" in two-dimensional (2D) crystalline superconductors (*2*). This pairing mechanism can apparently boost the in-plane upper critical field, $B_{c2,//}$. For example, molybdenum disulfide (MoS_2) (*3*, *4*), populated with charge carriers through ionic liquid gating, exhibits a $B_{c2,//}$ exceeding 52 T at a temperature T equal to ~20% of the zero-field superconducting transition temperature $T_{c,0}$. In atomically thin niobium diselenide ($NbSe_2$), $B_{c2,//}$ was reported to be 31.5 T at 10% $T_{c,0}$ (*5*), even though an isotropic bulk superconductor with the same $T_{c,0}$ would only sustain a field of up to 5.6 T, as set by the Chandrasekhar-Clogston or Pauli limit (*8*, *9*): $B_p = 1.86T_{c,0}$. In amorphous superconducting films, spin-orbit scattering (Fig. 1A) (*10*) has been attributed a key role in enhancing $B_{c2,//}$. However, in high-mobility crystalline samples, spin-orbit scattering can be safely discarded as the origin of the enhancement because it would imply unphysically short scattering times (*3*–*5*). Theory has therefore pointed to properties inherent to the band structure of these 2D materials to account for the anomalous robustness. As a result of broken inversion symmetry, opposing valleys in k-space host states of opposite spin orientation (Fig. 1C); strong spin-orbit coupling (SOC) induces substantial spin splitting

between these valleys. Consequently, Cooper pairs formed from carriers in opposing valleys possess locked opposite spins and become resilient to an in-plane pair-breaking field. This physical framework inaugurated the search for ever increasing $B_{c2,//}$ almost exclusively in transition-metal dichalcogenides because their crystal structure may naturally break in-plane inversion symmetry. Single layers of tungsten disulfide (WS_2) and tantalum disulfide (TaS_2)—both hosting heavier elements than those in MoS_2 and $NbSe_2$—were recently shown to support an even larger enhancement of $B_{c2,//}$ (*6*, *7*).

One key theoretical prediction for Ising superconductivity remains to be verified experimentally: $B_{c2,//}$ is expected to diverge and deviate from the 2D Ginzburg-Landau (G-L) formula at low temperatures, even if a moderate amount of disorder is present (*11*–*13*). Such behavior is reminiscent of the Fulde-Ferrell-Larkin-Ovchinnikov (FFLO) state (Fig. 1B) (*14*–*19*), an epitome of robust pairing against spin-polarizing fields in clean superconductors. There, macroscopic coherence gets replaced by a spatially ordered phase in the presence of a partial spin polarization at low temperatures, $T < 0.5T_{c,0}$. The experimental observation of a rapidly increasing $B_{c2,//}$ at low temperature provides strong support to the existence of the FFLO state in organic superconductors (*19*). In Ising superconductors, however, it is the spin split band structure that imposes a similar renormalization to the G-L formula at $T \ll T_{c,0}$. Unfortunately, the relevant magnetic field regime in the phase diagram as $T \to 0$ is difficult to access for established Ising superconductors owing to technical limitations in the attainable magnetic fields.

We identified a divergence of $B_{c2,//}$ at low temperature and breakdown of the G-L formula in epitaxial thin films of α-Sn(111), also referred to as few-layer stanene (*20*, *21*). This material has recently emerged as a 2D superconductor (*21*). By cooling the sample down to as low as 2% of $T_{c,0}$, we observed an anomalous increase of $B_{c2,//}$ by 30% over the conventional behavior in a temperature window as narrow as 200 mK.

The atomic structure of trilayer stanene grown on PbTe substrates with low-temperature molecular beam epitaxy is illustrated in Fig. 2A (*20*). The 3D rendering of the band structure of the trilayer based on angle-resolved photoemission spectroscopy (ARPES) data as well as first-principles calculations (*21*) is shown in Fig. 2B. In the vicinity of the Fermi level, a linearly dispersing hole band surrounds a small electron pocket at the Γ-point, giving rise to two-band superconductivity (*21*). We show in Fig. 2C the temperature dependence of the sheet resistance of a sample consisting of trilayer stanene that has been grown on a 12-layer-thick lead telluride (PbTe) buffer (3-Sn/12-PbTe) down to 250 mK (details of the sample preparation and measurement techniques are provided in the supplementary materials, materials and methods and supplementary text, note I); we observed a superconducting transition at the temperature of 1.1 K. Displayed in Fig. 2, D and E, are color renditions of the sample resistance in the parameter space spanned by the temperature and either the perpendicular (Fig. 2D) or the in-plane (Fig. 2E) magnetic field. They reflect the phase diagram of the superconducting ground state. The white color in Fig. 2, D and E, corresponds to approximately half of the normal state resistance (R_n) and hence demarcates the superconducting transition from the normal state; it also traces the temperature dependence of the upper critical magnetic fields indicated with open circles [setting the boundary at 1%R_n yields qualitatively the same results (figs. S3 to S7)]. Close to $T_{c,0}$, both $B_{c2,\perp}(T)$ and $B_{c2,//}(T)$ follow the 2D G-L formula (*21*), and deviations only become apparent at lower temperatures. The out-of-plane upper critical field $B_{c2,\perp}(T)$ exhibits an upturn, which is properly captured by the formula of a two-band superconductor (Fig. 2D, solid black curve) (*22*) that considers the orbital effect of the perpendicular magnetic field. However, when the magnetic field is applied parallel to an ultrathin superconductor, superconductivity is primarily suppressed by the paramagnetic effect, and the two-band formula reduces to a simple square root dependence on T (*22*), indistinguishable from that of the 2D G-L formula (Fig. 2E, pink curve). Clearly, such a two-band treatment fails to describe the enhancement in the in-plane upper critical field observed in experiment, which amounts to 1 T by cooling below $T = 0.2$ K. The in-plane upper critical field exceeds the Pauli limit by a factor of 2, assuming the common estimate of $B_p = 1.86T_{c,0}$ for an isotropic bulk superconductor (we discuss the possible anisotropy in the supplementary text, note IV).

We next turned to elucidating the mechanism of the upper critical field enhancement in our samples. The upper critical fields of two trilayer stanene samples with differing PbTe buffer layer thicknesses are compared in Fig. 3A. The position of the Fermi level is known to decrease as the thickness of the buffer layer is decreased because of the reduced donation of carriers from PbTe (*21*). This results in a lower $T_{c,0}$ for trilayer stanene on six-layer PbTe. Nevertheless, this sample also exhibits a $B_{c2,//}(T)$ that clearly departs from that of the 2D G-L formula (fig. S4). It possesses a higher $B_{c2,//}/B_p$ at $T \to 0$ as compared with the 3-Sn/12-PbTe sample (Fig. 3A), although the divergence is less prominent. These results indicate that an unusual mechanism renders the Cooper pairs robust against in-plane fields. The spin-orbit scattering mechanism (*10*) can be readily ruled out because it disagrees with the experimental data (Fig. 2E, light blue curve marked "KLB"). The up-turn bears a striking resemblance to that observed in superconductors hosting the FFLO state. However, the mean free path (l) of our superconductor is ~10 nm (supplementary text, note II), which is much smaller than the coherence length $\xi \sim 50$ nm extracted from a linear fitting of $B_{c2,\perp}(T)$ close to $T_{c,0}$. We define

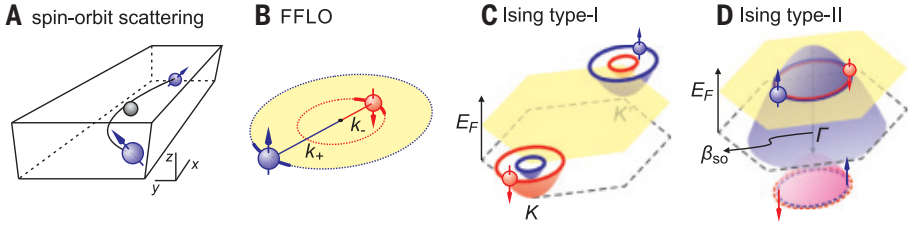

Fig. 1. Mechanisms for an enhanced in-plane upper critical field. (**A**) Spin-orbit scattering. Electronic spins get randomized through scattering off impurities. (**B**) FFLO state. Cooper pairs form with a finite momentum q. Only a small section of the Fermi surface can host pairs (solid curves). Owing to this finite momentum q, the order parameter is spatially modulated along the same direction, $\Delta = \Delta_0 e^{iqr}$. (**C**) Type-I Ising superconductivity, pairing of electrons in opposite spin split valleys. Only one pair of electron pockets centered on K and K' points are highlighted. (**D**) Type-II Ising superconductivity, pairing of charge carriers on orbits around the Γ-point with their spins aligned in the out-of-plane orientation. β_{SO} represents the SOC-induced splitting. Hole bands are illustrated as an example. Electron bands or bands with a more complicated dispersion are also allowed as long as the spin splitting is caused by the same SOC. The red and blue circles indicate two energetically degenerate bands with opposite spin orientations, each of which has a spin split counterpart below the Fermi level (indicated with the dashed circles).

[1]Max Planck Institute for Solid State Research, Stuttgart 70569, Germany. [2]State Key Laboratory of Low-Dimensional Quantum Physics, Department of Physics, Tsinghua University, Beijing 100084, China. [3]RIKEN Center for Emergent Matter Science (CEMS), Wako, Saitama 351-0198, Japan. [4]Frontier Science Center for Quantum Information, Beijing 100084, China. [5]International Center for Quantum Materials, Peking University, Beijing 100871, China. [6]Institute for Advanced Study, Tsinghua University, Beijing 100084, China. [7]Beijing Academy of Quantum Information Sciences, Beijing 100193, China. [8]Center for Advanced Quantum Studies, Department of Physics, Beijing Normal University, Beijing 100875, China.
*Present address: Department of Applied Physics and Materials Science, California Institute of Technology, Pasadena, CA, USA.
†Corresponding author. Email: haiwen.liu@bnu.edu.cn (H.L.); j.smet@fkf.mpg.de (J.H.S.); dingzhang@mail.tsinghua.edu.cn (D.Z.)

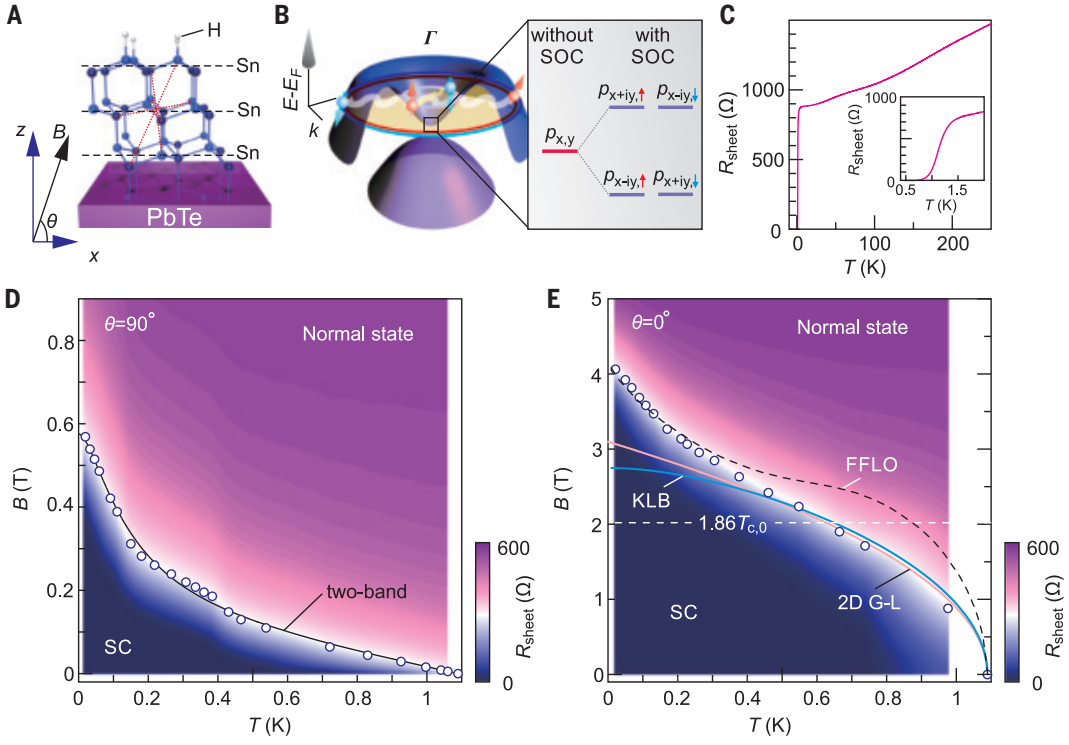

Fig. 2. Superconducting properties of trilayer stanene. (**A**) Atomic structure of hydrogen-decorated trilayer stanene on a PbTe substrate. Dashed lines indicate the three layers of Sn atoms. Red dotted lines indicate the inversion symmetry. (**B**) 3D schematic of the band structure of trilayer stanene. Blue and red circles reflect the hole-electron bands intersecting with the Fermi level. (Right) The band splitting around the Γ point owing to SOC. (**C**) Temperature-dependent sheet resistance of trilayer stanene grown on 12 layers of PbTe. (**D** and **E**) Color-coded resistance of the trilayer stanene on 12-PbTe as a function of (D) perpendicular and (E) in-plane magnetic field at a set of temperature points. The white stripe indicates the boundary between the superconducting (SC) and normal state. Circles represent the magnetic fields where the resistance becomes 50%R_n at a fixed T. Because of the smooth nature of this transition, determining B_{c2} by using another definition, such as 1%R_n or 10%R_n, would not change the general temperature-dependent behavior obtained. Solid and dashed curves are theoretical fits. The solid curve in (D) is based on the formula derived for a two-band superconductor (*23*). The blue curve in (E) was obtained by using the formula that takes into account the spin-orbit scattering as derived by Klemm, Luther, and Beasley (KLB) (*10*). The pink curve in (E) is based on the 2D G-L formula (*21*). The black dashed curve in (E) is based on the formula for a superconductor in the FFLO state (*16*). The white dashed line marks the Pauli limit using the standard Bardeen-Cooper-Schrieffer (BCS) ratio (*3*) as well as a g-factor of 2.

$B_{c2,\perp}$ as the position at which the resistance drops to 50%R_n. Using the criterion of 1%R_n yields an even larger ξ (supplementary text, note II). By contrast, the FFLO state requires a clean superconductor with $l > \xi$ (*17*). Furthermore, the temperature dependence expected from a superconductor in the FFLO state (*16*) is different (Fig. 2E). Ising superconductivity also predicts an up-turn when temperature drops; however, few-layer stanene itself has no M_z mirror symmetry and is centrosymmetric in the free-standing case (*23*, *24*). The films under study have surface decoration and sit on a substrate (Fig. 2A), but this type of inversion symmetry–breaking induces only the Rashba effect, which is detrimental to Ising pairing. Moreover, stanene hosts bands around Γ-point, in contrast to MoS_2 or $NbSe_2$, whose spin-split bands are around K and K' points. Apart from these differences in atomic and electronic structure, the experimentally observed thickness dependence of $B_{c2,//}(T)$ also distinguishes few-layer stanene from the established Ising superconductors. Instead of a fast diminishing effect of Ising pairing in thicker films of transition-metal dichalcogenides (*7*), the up-turn stays prominent even in pentalayer stanene but is smeared out when the thickness is reduced down to a bilayer (Fig. 3B).

The distinct difference between stanene and the widely studied transition-metal dichalcogenides necessitates an alternative mechanism in stanene to produce the out-of-plane spin orientations. It should not rely on inversion symmetry–breaking and in addition be applicable for spin-degenerate Fermi pockets near time-reversal invariant momenta. We formulated our model by focusing on the bands that involve the p_x- and p_y-orbitals of Sn because they are the most relevant for electronic conduction according to previous ARPES results and first-principles calculations. The SOC lifts the fourfold degeneracy at the Γ-point (Fig. 2B) and results in two sets of spin-degenerate bands mainly composed of $(|+\uparrow\rangle, |-\downarrow\rangle)$ (Fig. 1D, solid circles) and $(|+\downarrow\rangle, |-\uparrow\rangle)$ (Fig. 1D, dashed circles), respectively, where + and – refer to the $p_x + ip_y$ and $p_x - ip_y$ orbitals, respectively (*23*). Thanks to spin-orbit locking (Fig. 1D), bands with different orbital indices experience an opposite out-of-plane effective Zeeman field. This Zeeman splitting is parametrized as $\beta_{SO}(k)$ and is strongly k-dependent. $\beta_{SO}(k)$ is extraordinarily large at the Γ-point, where a splitting of ~0.5 eV in monolayer stanene—equivalent to a field of ~10^3 T—can occur. However, it substantially weakens at larger k because of interorbital mixing, given that an in-plane magnetic field contributes a perturbation term to the Hamiltonian proportional to $\langle +\uparrow, -\downarrow|\sigma_x|+\uparrow, -\downarrow\rangle$, where σ_x is the Pauli matrix. This term is zero for k = 0 and exerts increasing influence at larger k. Even though $\beta_{SO}(k)$ decreases moderately with film thickness in few-layer stanene as a consequence of reduced band splitting in a quantum well setting, Ising-like pairing between $|+\uparrow\rangle$ and $|-\downarrow\rangle$ within the Fermi pockets near the Γ-point is expected to persist, and this pairing is anticipated to be robust against in-plane magnetic fields. Hence, we have termed this mechanism type-II Ising superconductivity in order to distinguish it from previous instances of Ising superconductivity.

A full theoretical derivation of the temperature dependence of $B_{c2,//}$ using the Gor'kov Green function is presented in the supplementary text, note V. We used the Bernevig-Hughes-Zhang Hamiltonian based on atomic orbitals of stanene (*23*) and took into account the spin-dependent scattering and Rashba effect. The solid and dashed curves in Fig. 3 are theoretical fits to the data by using the equations we derived from this model (eqs. S3 and S2, respectively). The temperature dependence is essentially governed by two fit parameters—the disorder renormalized SOC strength β_{SO}^{*} and the Rashba SOC strength αk_F—whereas the theoretically chosen $T_{c,0}$ is slightly adjusted within 5% of the experimental values to obtain the best fit (the values are listed in Fig. 3 and compared with experimental values in table S1). The model agrees well with experimental data

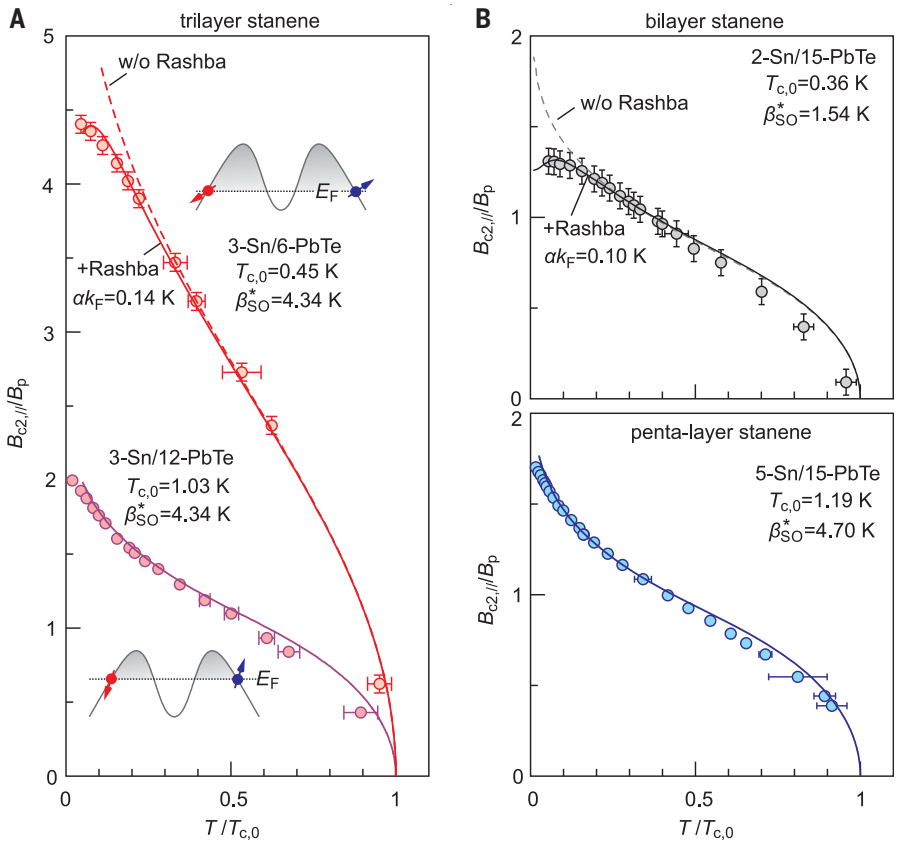

Fig. 3. Temperature dependence of the in-plane upper critical fields in few-layer stanene samples. (**A** and **B**) Data obtained from four samples with different stanene and PbTe substrate thicknesses. For example, 3-Sn/6-PbTe refers to a trilayer stanene grown on top of six layers of PbTe. The ratio of the in-plane upper critical fields—the magnetic fields at which the sample resistance becomes 50% of the normal state resistance at a given temperature—to the Pauli limit field $B_p = 1.86T_{c,0}$ are plotted as circular symbols. Vertical error bars arise from the step size of the magnetic field in obtaining the resistance data (fig. S2). Horizontal error bars stem from the temperature variation during each scan of the resistance data. Errors are smaller than the symbols for those data points without apparent error bars. Solid and dashed curves are theoretical fits by using the formula derived for a type-II Ising superconductor (supplementary text, note V). $T_{c,0}$ is the zero-field transition temperature. β^*_{SO} is the intrinsic SOC strength renormalized by disorder. αk_F denotes the renormalized Rashba SOC strength.

and captures the prominent up-turn feature in the low-temperature regime. Within this framework, the physical origin of this up-turn can be traced back to the peculiar spin split bands associated with different orbitals (Fig. 1D), which are protected by the crystal structure. At T close to $T_{c,0}$, thermal activation results in a partial population of the upper two orbitals, suppressing the contribution of the spin-orbit–induced spin split effect on $B_{c2,//}$. Data in this regime therefore overlap with the 2D G-L formula. As T approaches zero, however, the charge carriers are polarized into the lower orbitals and cause the up-turn of $B_{c2,//}$. Quantitatively, the dimensionless parameter $\frac{\beta^*_{SO}}{T_{c,0}}$ controls the deviation point between the enhancement behavior characteristic for "Ising" superconductivity and the behavior governed by the G-L formula. Typically, $\beta^*_{SO}/T_{c,0} \approx 4$ in our samples (3-Sn/12-PbTe, for example), and a clear up-turn appears at $T_c/T_{c,0} \approx 0.6$.

On the basis of the theoretical model, we can understand qualitatively the substrate- and layer thickness–dependence of $B_{c2,//}$. The smoothening in 3-Sn/6-PbTe in comparison with 3-Sn/12-PbTe can be attributed to the variation of the spin-locking strength as one moves away from the Γ-point along the inverted Mexican hat band shape (Fig. 3A, inset). Spins of the $|+\rangle$ and $|-\rangle$ orbitals are strongly locked out of plane at the Γ-point. This Ising-like orientation becomes, however, less favorable at larger momenta. Lowering the Fermi level therefore suppresses the spin polarization of the outer hole band, which can be simulated by an effective Rashba term in the Hamiltonian. The experimental data can be fitted well by taking into account this effect. The modified formula also nicely describes the upper critical fields of bilayer stanene (Fig. 3B). We attribute the missing up-turn feature to stronger inversion symmetry–breaking because the top Sn layer is decorated by hydrogen atoms, whereas the bottom Sn layer sits on the Te atoms of PbTe (we compare the band structures obtained from first-principles calculations in fig. S8). Following this line of reasoning, a pentalayer stanene should experience a weaker Rashba effect, giving rise to an apparent enhancement of $B_{c2,//}$ at low T (Fig. 3B, bottom). Our work points to a broader range of materials hosting such pairing mechanisms without the participation of inversion symmetry–breaking (*25*).

Note added in proof: After we submitted this report, similar observations were reported (*26*, *27*).

REFERENCES AND NOTES

1. A. Gurevich, *Nat. Mater.* **10**, 255–259 (2011).
2. Y. Saito, T. Nojima, Y. Iwasa, *Nat. Rev. Mater.* **2**, 16094 (2017).
3. J. M. Lu *et al.*, *Science* **350**, 1353–1357 (2015).
4. Y. Saito *et al.*, *Nat. Phys.* **12**, 144–149 (2015).
5. X. Xi *et al.*, *Nat. Phys.* **12**, 139–143 (2016).
6. J. Lu *et al.*, *Proc. Natl. Acad. Sci. U.S.A.* **115**, 3551–3556 (2018).
7. S. C. de la Barrera *et al.*, *Nat. Commun.* **9**, 1427 (2018).
8. A. M. Clogston, *Phys. Rev. Lett.* **9**, 266–267 (1962).
9. B. S. Chandrasekhar, *Appl. Phys. Lett.* **1**, 7–8 (1962).
10. R. A. Klemm, A. Luther, M. R. Beasley, *Phys. Rev. B* **12**, 877–891 (1975).
11. S. Ilić, J. S. Meyer, M. Houzet, *Phys. Rev. Lett.* **119**, 117001 (2017).
12. Y. Liu *et al.*, *Phys. Rev. X* **8**, 021002 (2018).
13. R. Wakatsuki, K. T. Law, Proximity effect and Ising superconductivity in superconductor/transition metal dichalcogenide heterostructures. arXiv:1604.04898 [cond-mat.supr-con] (2016).
14. P. Fulde, R. A. Ferrell, *Phys. Rev.* **135** (3A), A550–A563 (1964).
15. A. I. Larkin, Yu. N. Ovchinnikov, *Sov. Phys. JETP* **20**, 762 (1965).
16. H. Shimahara, *Phys. Rev. B Condens. Matter* **50**, 12760–12765 (1994).
17. Y. Matsuda, H. Shimahara, *J. Phys. Soc. Jpn.* **76**, 051005 (2007).
18. G. Zwicknagl, S. Jahns, P. Fulde, *J. Phys. Soc. Jpn.* **86**, 083701 (2017).
19. J. Wosnitza, *Ann. Phys.* **530**, 1700282 (2018).
20. Y. Zang *et al.*, *Adv. Funct. Mater.* **28**, 1802723 (2018).
21. M. Liao *et al.*, *Nat. Phys.* **14**, 344–348 (2018).
22. A. Gurevich, *Physica C* **456**, 160–169 (2007).
23. Y. Xu *et al.*, *Phys. Rev. Lett.* **111**, 136804 (2013).
24. Y. Xu, Z. Gan, S.-C. Zhang, *Phys. Rev. Lett.* **112**, 226801 (2014).
25. C. Wang *et al.*, *Phys. Rev. Lett.* **123**, 126402 (2019).
26. Y. Liu *et al.*, arXiv:1904.12719 [cond-mat.supr-con] (2019).
27. A. Devarakonda *et al.*, arXiv:1906.02065 [cond-mat.supr-con] (2019).
28. D. Zhang, Data for "Type-II Ising superconductivity in few-layer stanene". Harvard Dataverse (2020);

ACKNOWLEDGMENTS

We thank B. Friess for technical assistance and Y. Zhang for fruitful discussions. **Funding:** This work is financially supported by the National Natural Science Foundation of China (grants 11790311, 11922409, 11674028, and 51788104); the Ministry of Science and Technology of China (2017YFA0304600, 2017YFA0302902, 2017YFA0303301, 2018YFA0307100, 2018YFA0305603, and 2016YFA0301001); and the Beijing Advanced Innovation Center for Future Chip (ICFC). **Author contributions:** D.Z. conceived the project. J.F., D.Z., and M.L. performed the low-temperature electrical measurements. Y.Z., K.Z., and K.H. grew the samples. Y.X., C.W., Z.Z., and W.D. carried out first-principles calculations and theoretical analysis. Ha.L. derived the microscopic model of superconductivity with Ho.L.'s assistance. D.Z., J.F., Y.X., Ha.L., and J.H.S. analyzed the data and wrote the paper with input from Q.-K.X. All authors discussed the results and commented on the manuscript. **Competing interests:** The authors declare no competing interests; **Data and materials availability:** All data are available in (*26*).

SUPPLEMENTARY MATERIALS

science. /content/367/6485/1454/suppl/DC1 Materials and Methods
Supplementary Text
Figs. S1 to S8
Table S1
References (*29*–*42*)

19 March 2019; accepted 27 February 2020
Published online 12 March 2020
10.1126/science.aax3873

SPECTROSCOPY

Frequency-comb spectroscopy on pure quantum states of a single molecular ion

C. W. Chou[1]*, A. L. Collopy[1], C. Kurz[1], Y. Lin[2,1,3,4], M. E. Harding[5], P. N. Plessow[6], T. Fortier[1,7], S. Diddams[1,7], D. Leibfried[1,7], D. R. Leibrandt[1,7]

Spectroscopy is a powerful tool for studying molecules and is commonly performed on large thermal molecular ensembles that are perturbed by motional shifts and interactions with the environment and one another, resulting in convoluted spectra and limited resolution. Here, we use quantum-logic techniques to prepare a trapped molecular ion in a single quantum state, drive terahertz rotational transitions with an optical frequency comb, and read out the final state nondestructively, leaving the molecule ready for further manipulation. We can resolve rotational transitions to 11 significant digits and derive the rotational constant of $^{40}CaH^+$ to be B_R = 142 501 777.9(1.7) kilohertz. Our approach is suited for a wide range of molecular ions, including polyatomics and species relevant for tests of fundamental physics, chemistry, and astrophysics.

Molecular spectroscopy is essential to understand molecular properties, which underpin chemistry and biology. Improved spectroscopic precision and state control can uncover obfuscated molecular properties and enable direct manipulation of molecular quantum states. However, because numerous effects crowd and blur molecular spectra, spectroscopic experiments often fail to resolve the natural linewidth of the transitions. Some of these effects can be ameliorated by using cold trapped molecules. Laser cooling and trapping (*1*) have enabled molecule formation from cold atoms (*2*) and precision molecular spectroscopy (*3*). Direct laser cooling shows promise for molecular species with advantageous level structures (*4*, *5*). Long interrogation times and low translational temperature yield high resolution (*6*), which has enabled, for example, the most stringent test of fundamental theory carried out by molecular ions (*7*). Yet, even with trapped and cooled molecules (*8*), commonly used detection methods, such as state-dependent photodissociation or ionization, are destructive, preventing further manipulation. For larger molecules with more hyperfine and spin-rotation couplings, spectra typically become more complex and assignment of features more difficult.

We perform high-resolution rotational spectroscopy of a single $^{40}CaH^+$ molecular ion using methods applicable to a broad range of molecular ion species. We coherently drive stimulated terahertz Raman rotational transitions using an optical frequency comb (OFC) (*9*–*12*) with a spectrum far off-resonant from most vibrational and all electronic transitions (*10*). We demonstrate <1-kHz spectral linewidth and determine the transition centroid frequencies with ~1 part per billion (ppb) accuracy. Using OFCs with broader spectra, we could interrogate molecular transitions up to optical frequencies in a similar way (*13*) for applications such as testing fundamental physics, benchmarking molecular theories, and assigning spectral lines observed in the interstellar medium (*14*). In this direction, we determine the frequency differences between rotational centroids from measured transition frequencies (*13*) to derive precise $^{40}CaH^+$ rotational constants up to fourth order. We detect both the initial and final states of the attempted rotational transition, demonstrating a capability that simplifies the spectra and facilitates line assignment. We independently confirm our assignments by comparison with quantum-chemical calculations (*15*).

In our experiments (Fig. 1), a $^{40}Ca^+$–$^{40}CaH^+$ ion pair, trapped in a linear Paul trap in ultrahigh vacuum, is studied with quantum-logic spectroscopy (*16*–*19*). At room temperature, the $^{40}CaH^+$ is in its $^1\Sigma$ vibronic ground state, but its rotation is thermalized with the environment. Blackbody radiation continuously perturbs the molecule, causing rotational state jumps on a time scale of tens of milliseconds to seconds for the states that we study.

We label the molecular eigenstates in a static external magnetic field **B** as $|\mathcal{J}\rangle = |J, m, \xi\rangle$, where J is the rotational quantum number, m is the projection quantum number of the total (rotational and proton nuclear spin) angular momentum on the **B** direction, and $\xi \in \{+,-\}$ labels the two eigenstates that share the same J and m, or is the sign of m for the case $m = -J - 1/2$ or $J + 1/2$ (*17*). For $1 \le J \le 6$ and our ~0.357-mT quantization field, each

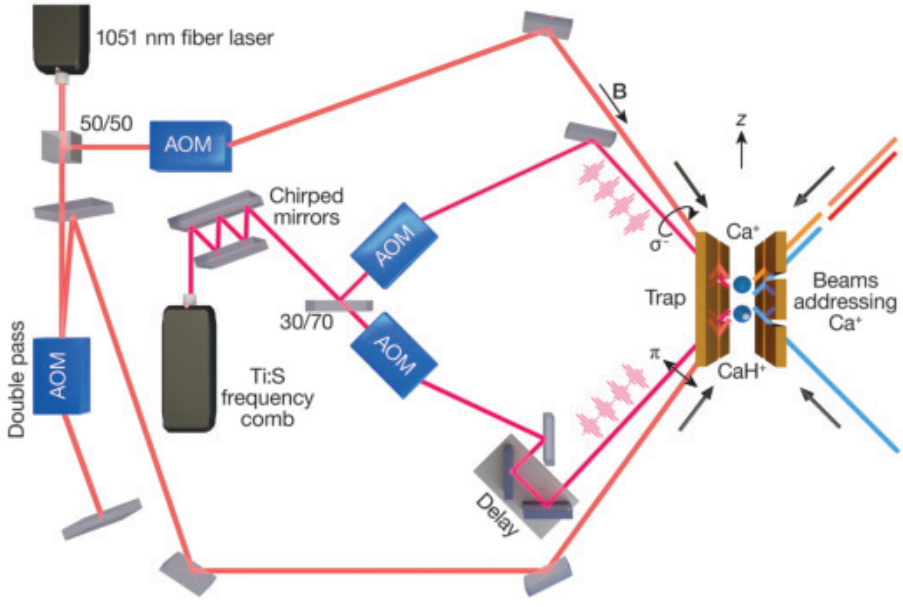

Fig. 1. Experimental setup. A $^{40}CaH^+$–$^{40}Ca^+$ ion pair is held in a linear Paul trap. The $^{40}CaH^+$ is projectively prepared using Raman beams from a 1051-nm fiber laser (red) (*17*). A Ti:S OFC is divided into two Raman beams (pink). The frequencies and powers of the beams are controlled by AOMs. The normal mode of motion used for quantum-logic operations is along the z axis. The two pairs of Raman beams have π and σ^- polarizations relative to the quantization axis defined by the static magnetic field **B**. They drive two-photon SRTs in the molecule, for which selection rules ΔJ = 0, ±2 and Δm = ±1 apply. Group delay dispersion introduced by optical elements is precompensated with chirped mirrors, and a tunable delay stage ensures that the pulses from both arms temporally overlap on the molecular ion.

[1]Time and Frequency Division, National Institute of Standards and Technology, Boulder, CO 80305, USA. [2]CAS Key Laboratory of Microscale Magnetic Resonance and Department of Modern Physics, University of Science and Technology of China, Hefei 230026, China. [3]Hefei National Laboratory for Physical Sciences at the Microscale, University of Science and Technology of China, Hefei 230026, China. [4]Synergetic Innovation Center of Quantum Information and Quantum Physics, University of Science and Technology of China, Hefei 230026, China. [5]Institute of Nanotechnology, Karlsruhe Institute of Technology (KIT), 76021 Karlsruhe, Germany. [6]Institute of Catalysis Research and Technology, Karlsruhe Institute of Technology (KIT), 76021 Karlsruhe, Germany. [7]Department of Physics, University of Colorado, Boulder, CO 80309, USA.
*Corresponding author. Email: chin-wen.chou@nist.gov

rotational manifold contains a signature transition (Fig. 2) with a unique frequency (*13*). Two states connected by such a signature transition can be used for high-fidelity state preparation and detection for the corresponding manifold (*13*, *17*).

Our spectroscopy starts with heralded projective molecular state preparation (*17*). First, the molecular population is pumped toward a state connected by a signature transition. Then, one normal mode of the coupled harmonic motion of the atomic and molecular ions in the external potential of the trap is initialized in the ground $|n=0\rangle$ or first excited $|n=1\rangle$ state by manipulation of the atom (*20*, *21*). We subsequently attempt to drive the signature transition with a π pulse on a sideband of the shared motion $|J,m=-J+1/2,-\rangle|n=0\rangle \leftrightarrow |J,-J-1/2,-\rangle|n=1\rangle$ using a pair of Raman beams derived from a 1051-nm continuous-wave (CW) fiber laser (*17*). With finite probability, successful state preparation is heralded by a motional state change, detected with operations on the atom (*13*, *17*). The sequence is repeated to suppress molecular preparation errors. The CW Raman beams can prepare and read out the $|\mathcal{J}''=\{J,-J-1/2,-\}\rangle$ and $|\mathcal{J}'=\{J+2,-J-3/2,-\}\rangle$ states [$J \in \{1,2,3,4\}$ in this work], each connected by the signature transition in the respective manifold.

We then probe a rotational transition and detect the molecular state. We coherently excite the rotational transitions $|\mathcal{J}'\rangle \leftrightarrow |\mathcal{J}''\rangle$ with Raman beams derived from a titanium:sapphire (Ti:S) femtosecond laser OFC with a repetition rate f_{rep} ~80 MHz and 800- to 850-nm center wavelength (Fig. 2). The frequencies of the Raman beams are shifted oppositely by f_{AOM} with acousto-optic modulators (AOMs) (Figs. 1 and 2). The comb teeth in one beam together with the corresponding ones in the other beam collectively drive a stimulated Raman transition (SRT) of frequency $f_{Raman} = |Nf_{rep} - 2f_{AOM}|$ (N is an integer) (*9*–*13*) (Fig. 2). By sequentially detecting the $|\mathcal{J}''\rangle$ and $|\mathcal{J}'\rangle$ states, we confirm excitation of the attempted transition. With the molecule prepared in a known state, the ~10-THz bandwidth OFC can probe all allowed transitions up to several terahertz by scanning f_{AOM} over $f_{rep}/2$. This facilitates the search for transitions when knowledge of the molecular constants is limited.

Figure 3A shows the spectra of a transition between the J = 2 and J = 4 rotational manifolds. When f_{Raman} of the comb Raman pulse train (CRPT) is tuned near the ~2-THz resonance frequency, the molecular population is transferred from the prepared state $|\mathcal{J}''=\{2,-5/2,-\}\rangle$ to the final state $|\mathcal{J}'=\{4,-7/2,-\}\rangle$.

Rabi flopping between $|\mathcal{J}''\rangle$ and $|\mathcal{J}'\rangle$ is driven by setting f_{Raman} on resonance with a transition and varying the duration of the CRPT. This puts the molecular ion into superpositions of the form $\alpha|\mathcal{J}''\rangle + \beta|\mathcal{J}'\rangle$, $|\alpha|^2 + |\beta|^2 = 1$, as shown for J″ = 2 to J′ = 4 in Fig. 3B. Any set of two states can implement a qubit that can, in principle, be coherently rotated or entangled with atomic ions or other molecular ions using standard quantum information-processing techniques (*22*), potentially enabling precision measurements with quantum advantages on molecular ions.

The measured frequencies of transitions with J between 1 and 6 are presented in Table 1. With <1 kHz full width at half-maximum (FWHM) Fourier-limited spectroscopic line shapes, we reach statistical uncertainties in the line centers below 100 Hz, but uncertainty

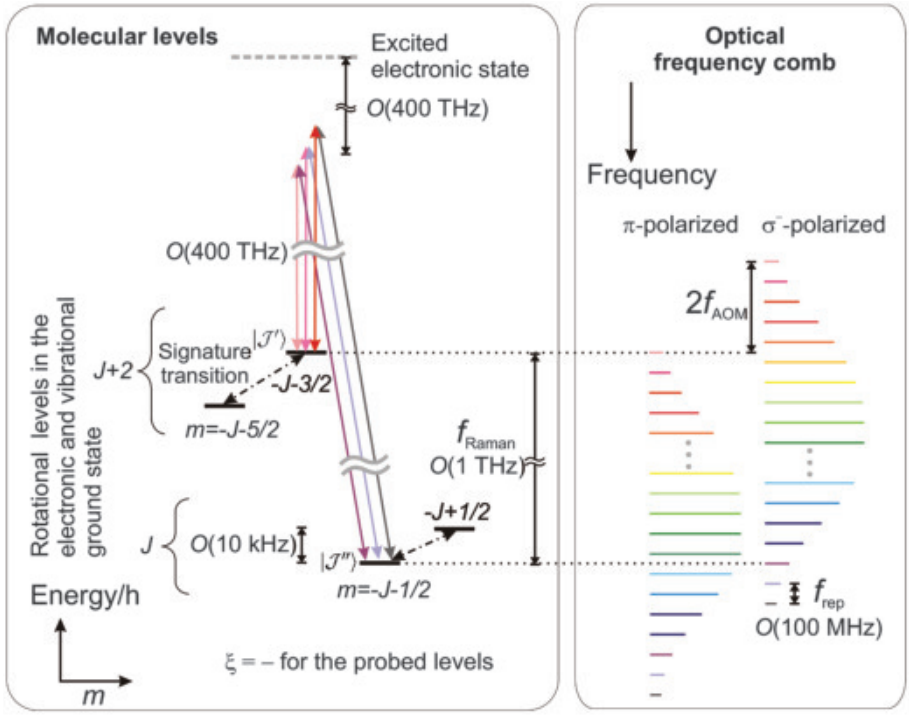

Fig. 2. Molecular levels probed with comb Raman beams. Within the Jth manifold, either of the $|J,-J-1/2,-\rangle$ and $|J,-J+1/2,-\rangle$ states connected by the signature transition (dot-dash arrow) can be nondestructively detected and prepared with the CW Raman beams. The comb teeth in each comb Raman beam are spaced in frequency by f_{rep}. Within the limit of the comb spectrum, any comb tooth from one beam (e.g., the tooth in red from the π-polarized beam) can have a target difference frequency f_{Raman} with a corresponding comb tooth from the other beam (the tooth in dark gray from the σ^--polarized beam). The $\Delta J = \pm 2$ transition $|\mathcal{J}'=\{J+2,-J-3/2,-\}\rangle \leftrightarrow |\mathcal{J}''=\{J,-J-1/2,-\}\rangle$, $J \in \{1,2,3,4\}$ is interrogated by a CRPT. The gray dashed line indicates off-resonant excited electronic states of the molecule. *O*(...) indicates "on the order of."

Table 1. Measured and inferred rotational transition frequencies. The transition frequencies $f_{\mathcal{J}'',\mathcal{J}'}$ were determined at a magnetic field of 0.357(1) mT with statistical uncertainties $\delta f_{\mathcal{J}'',\mathcal{J}'}$ representing 95% confidence intervals of the line centers. The centroid frequencies $cf_{J'',J'}$ are calculated from measured frequencies by subtracting shifts due to finite magnetic field and spin-rotation coupling. The uncertainties in these corrections and the systematic uncertainty due to the trap radio-frequency electric field at the molecule are included in the 95%-confidence systematic uncertainties $\delta cf_{J'',J'}$ of the centroid that are substantially larger than the statistical uncertainties of the measured resonances.

J''	J'	$f_{\mathcal{J}'',\mathcal{J}'}$ (THz)	Statistical uncertainty $\delta f_{\mathcal{J}'',\mathcal{J}'}$ (Hz)	$cf_{J'',J'}$ (THz)	$\delta cf_{J'',J'}$ (kHz)
1	3	1.424 204 460 565	14	1.424 204 457 7	2.4
2	4	1.992 911 000 121	16	1.992 910 990 8	3.3
3	5	2.560 643 630 446	20	2.560 643 614 2	3.7
4	6	3.127 125 998 610	63	3.127 125 974 8	4.5

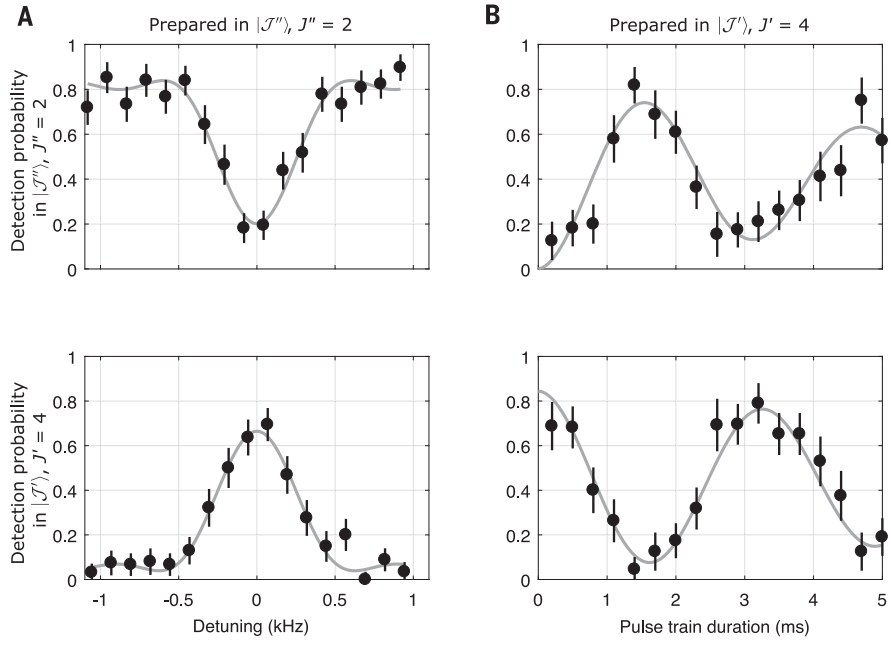

Fig. 3. Spectra and Rabi flopping for a frequency-comb driven $\Delta J = 2$ transition. (**A**) Spectra. $^{40}CaH^+$ is prepared in $|\mathcal{J}'' = \{2, -5/2, -\}\rangle$, followed by a CRPT probing the $|\mathcal{J}' = \{4, -7/2, -\}\rangle \leftarrow |\mathcal{J}''\rangle$ transition. After excitation, we determine the probabilities of the molecule being in either state. The horizontal axis shows the offset of the Raman difference frequency from the resonant value. The solid lines are fits to line shapes corresponding to a ~1.6-ms square pulse excitation. (**B**) Rabi flopping. Starting in $|\mathcal{J}'\rangle$, the state of the $^{40}CaH^+$ ion is driven on resonance coherently to and from $|\mathcal{J}''\rangle$ by a CRPT of variable duration. The solid curves are fits to decaying sinusoidal functions. The error bars indicate ±1 SD derived from Bayesian inference.

Table 2. Experimental values of the molecular constants in Eq. 1 inferred from measured rotational transition frequencies and ab initio values.

k	Experimental C_k (Hz)	Ab initio C_k (Hz)	Comments
1	1.42 501 777 9 (17) ×10^{11}	1.427 (11) ×10^{11}	B_R (rotational constant)
2	−5.81217 (19) ×10^6	−5.831 (19) ×10^6	$-D_R$ (centrifugal correction)
3	222.9 (7.2)	222.6 (0.6)	H_R (second centrifugal correction)
4	−0.021 (88)	−0.0158 (4)	Third centrifugal correction

in the trap radio-frequency electric field in our current setup limits uncertainties in extrapolation (*13*) of line centers to zero electric field to hundreds of hertz. A more detailed study of these effects is ongoing, and we expect that they can be better controlled in future experiments.

We derive precise values for the rotational constants from the unperturbed rotational transition frequencies. The centroid energy E_J of the Jth manifold can be parametrized:

$$E_J = h\sum C_k J^k (J+1)^k \quad k = 1, 2, 3, \ldots \qquad (1)$$

where h is the Planck constant and the coefficients C_k are the rotational constants. The inferred frequencies corresponding to the energy differences between the centroids of the rotational manifolds, obtained by subtracting the energy arising from the interactions of the proton and the rotational magnetic moment with the external magnetic field and among themselves (*17*), are also listed in Table 1 (*13*). The rotational constants derived from our measured transition frequencies are shown in Table 2.

We compare the experimentally determined rotational constants to ones obtained from ab initio calculations. To compute the rotational constants of $^{40}CaH^+$, complete basis set extrapolated coupled-cluster calculations at the CCSD(T) level (*23*) were used in conjunction with incremental corrections for electron correlation up to the CCSDTQ level (*24*, *25*), with relativistic and diagonal Born-Oppenheimer corrections. The computed rotational constants (Table 2) are in good agreement with experiment. The 1.2×10^{-8} relative precision of our $^{40}CaH^+$ rotational constant B_R determination is orders of magnitude higher than achievable from ab initio molecular structure calculations. For $^{40}CaH^+$, the accuracy of the computed constants is mainly limited by the one-electron basis sets. The comparison between calculated and experimental results clearly shows that the relative accuracy of computational methods sensitively depends on the computed property.

Our resolution is currently limited by the coherence of the microwave-referenced OFC and can be further improved to the sub-hertz level (*26*). The measurement accuracy could be improved to the sub-hertz (<1 part per trillion) level with improvements of the apparatus or for molecules that are less sensitive to the trap field. This may enable tests of fundamental physics on a much larger variety of molecular species than currently considered. They may include searches for electron-to-proton mass ratio variations (*27*, *28*) and measurements of isomer transition frequency differences, including those for chiral molecules (*29*, *30*). When extended to excited vibrational levels, the full ro-vibrational energy-level structure of molecules can be probed for information that can benchmark accurate theoretical models of the potential energy surfaces of molecular ground states. Combined with frequency-comb–enabled coherent manipulation, the current protocol could elucidate molecular dynamics and complement studies based on ultrafast laser techniques. Moreover, coherent manipulation of molecular states may enable precise alignment and orientation of molecules, preparation of squeezed or Schrödinger cat–type states of rotation, and precisely state-controlled dissociation.

REFERENCES AND NOTES

1. W. D. Phillips, *Rev. Mod. Phys.* **70**, 721–741 (1998).
2. K. K. Ni *et al.*, *Science* **322**, 231–235 (2008).
3. S. S. Kondov *et al.*, *Nat. Phys.* **15**, 1118–1122 (2019).
4. E. S. Shuman, J. F. Barry, D. Demille, *Nature* **467**, 820–823 (2010).
5. D. McCarron, *J. Phys. B* **51**, 212001 (2018).
6. S. Alighanbari, M. G. Hansen, V. I. Korobov, S. Schiller, *Nat. Phys.* **14**, 555–559 (2018).
7. W. B. Cairncross *et al.*, *Phys. Rev. Lett.* **119**, 153001 (2017).
8. M. Zeppenfeld *et al.*, *Nature* **491**, 570–573 (2012).
9. D. Hayes *et al.*, *Phys. Rev. Lett.* **104**, 140501 (2010).
10. D. Leibfried, *New J. Phys.* **14**, 023029 (2012).
11. S. Ding, D. N. Matsukevich, *New J. Phys.* **14**, 023028 (2012).
12. C. Solaro, S. Meyer, K. Fisher, M. V. DePalatis, M. Drewsen, *Phys. Rev. Lett.* **120**, 253601 (2018).

13. See supplementary materials.
14. B. A. McGuire, Census of interstellar, circumstellar, extragalactic, protoplanetary disk, and exoplanetary molecules. arXiv:1809.09132v1 [astro-ph.GA] (2018).
15. C. Puzzarini, J. F. Stanton, J. Gauss, *Int. Rev. Phys. Chem.* **29**, 273–367 (2010).
16. F. Wolf *et al.*, *Nature* **530**, 457–460 (2016).
17. C. W. Chou *et al.*, *Nature* **545**, 203–207 (2017).
18. M. Sinhal, Z. Meir, K. Najafian, G. Hegi, S. Willitsch, *Science* **367**, 1213–1218 (2020).
19. P. O. Schmidt *et al.*, *Science* **309**, 749–752 (2005).
20. Ch. Roos *et al.*, *Phys. Rev. Lett.* **83**, 4713–4716 (1999).
21. R. Rungango *et al.*, *New J. Phys.* **17**, 035009 (2015).
22. R. Blatt, D. Wineland, *Nature* **453**, 1008–1015 (2008).
23. K. Raghavachari, G. W. Trucks, J. A. Pople, M. Head-Gordon, *Chem. Phys. Lett.* **157**, 479–483 (1989).
24. S. A. Kucharski, R. J. Bartlett, *Theor. Chim. Acta* **80**, 387–405 (1991).
25. N. Oliphant, L. Adamowicz, *J. Chem. Phys.* **95**, 6645–6651 (1991).
26. A. Bartels, C. W. Oates, L. Hollberg, S. A. Diddams, *Opt. Lett.* **29**, 1081–1083 (2004).
27. S. Schiller, V. Korobov, *Phys. Rev. A* **71**, 032505 (2005).
28. V. V. Flambaum, M. G. Kozlov, *Phys. Rev. Lett.* **99**, 150801 (2007).
29. M. Quack, J. Stohner, *Phys. Rev. Lett.* **84**, 3807–3810 (2000).
30. R. Berger, M. Quack, J. Stohner, *Angew. Chem. Int. Ed.* **40**, 1667–1670 (2001).
31. C. W. Chou *et al.*, Data for "Frequency-comb spectroscopy on pure quantum states of a single molecular ion," NIST Public Data Repository (2020).

ACKNOWLEDGMENTS

We thank F. C. Cruz and A. Kazakov for careful reading of this manuscript. **Funding:** This work was supported by the U.S. Army Research Office (grant no. W911NF-19-1-0172). A.L.C. is supported by a National Research Council postdoctoral fellowship. Y.L. acknowledges support from the National Key R&D Program of China (grant no. 2018YFA0306600), the National Natural Science Foundation of China (grant no. 11974330), and the Anhui Initiative in Quantum Information Technologies (grant no. AHY050000). C.K. acknowledges support from the Alexander von Humboldt foundation. P.N.P. acknowledges support by the state of Baden-Wurttemberg through bwHPC (bwUnicluster and JUSTUS, RV bw17D01). **Author contributions:** C.W.C., A.L.C., C.K., T.F., S.D., D.L., and D.R.L. developed components of the experimental apparatus. C.W.C., A.L.C., and C.K. collected and analyzed data. C.W.C., Y.L., D.L., and D.R.L. designed the experimental methods and pulse sequences. M.E.H. and P.N.P. computed rotational transition frequencies and constants. All authors provided experimental suggestions, discussed the results, and contributed to writing the manuscript. **Competing interests:** The authors declare no competing interests. **Data and materials availability:** The data from the main text and supplementary materials are available from the NIST Public Data Repository (*31*). This is a contribution of the National Institute of Standards and Technology, not subject to U.S. copyright.

SUPPLEMENTARY MATERIALS

science. /content/367/6485/1458/suppl/DC1 Supplementary Text
Fig. S1
Tables S1 to S5
References (*32*–*45*)

27 November 2019; accepted 4 March 2020
10.1126/science.aba3628

QUANTUM GASES

Observation of dynamical fermionization

Joshua M. Wilson, Neel Malvania, Yuan Le, Yicheng Zhang, Marcos Rigol, David S. Weiss*

The wave function of a Tonks-Girardeau (T-G) gas of strongly interacting bosons in one dimension maps onto the absolute value of the wave function of a noninteracting Fermi gas. Although this fermionization makes many aspects of the two gases identical, their equilibrium momentum distributions are quite different. We observed dynamical fermionization, where the momentum distribution of a T-G gas evolves from bosonic to fermionic after its axial confinement is removed. The asymptotic momentum distribution after expansion in one dimension is the distribution of rapidities, which are the conserved quantities associated with many-body integrable systems. Our measurements agree well with T-G gas theory. We also studied momentum evolution after the trap depth is suddenly changed to a new nonzero value, and we observed the theoretically predicted bosonic-fermionic oscillations.

Integrable many-body quantum systems have been extensively studied theoretically since 1931, when Bethe solved the one-dimensional (1D) Heisenberg model (*1*). The theoretical appeal of these systems stems from the deep symmetries they exhibit and the fact that it is possible to exactly solve for their many-body wave functions (*2*). Over the past 20 years, there have been more than a dozen experimental implementations of very nearly integrable models. Systems of bosons (*3*), spins (*3*), and fermions (*4*) have been realized, using a range of ultracold atom, trapped ion, and condensed matter techniques. Each of these integrable many-body systems has a set of conserved quantities, the distribution of rapidities, which fully characterizes the many-body state. The rapidities embody what makes integrable systems special, including the fact that integrable systems do not reliably thermalize under unitary dynamics [see (*5*) for a recent set of reviews on this topic]. The rapidities depend on complicated interactions among many particles, which makes it difficult if not impossible to extract their distribution directly from equilibrium measurements. However, when the particles in an integrable system are allowed to expand in one dimension, the interparticle interactions vanish asymptotically and the momentum distribution of the system approaches the distribution of rapidities (*6*–*11*).

Here, we report such an expansion measurement with a Lieb-Liniger gas (*12*), an integrable system of 1D bosons with contact interactions. We operate in the Tonks-Girardeau (T-G) gas limit (*13*–*15*), where the interactions are very strong. The many-body wave function of the T-G gas is the same as that of a noninteracting Fermi (NIF) gas, to within an absolute value (*13*). All properties that depend on the square of the wave function, such as total energy (*14*) and local pair correlations (*16*), are the same for the two types of gases. Other properties, such as momentum distributions, are typically different. One central property shared by the two gases is the rapidity distribution (*3*). In the absence of a confining potential, the momentum distribution of a NIF gas is its rapidity distribution. Therefore, the T-G gas rapidity distribution is the same as the momentum distribution of a NIF gas. Hence, as interactions become negligible upon expansion in a flat potential, the T-G momentum distribution transforms into a NIF gas momentum distribution (*7*). The observation of this "dynamical fermionization" constitutes a direct measurement of the distribution of rapidities in this many-body interacting quantum system, thus bringing these theoretical constructs into the realm of experiment. Our experimental results for time-of-flight (TOF) measurements are in almost complete agreement with exact theoretical calculations. We have also measured momentum distribution dynamics after quenches to different nonvanishing trap strengths (*8*).

The momentum distributions of equilibrium 1D Bose gases have been measured with TOF, Bragg spectroscopy, observation of phase fluctuations, and momentum focusing techniques (*3*, *17*). These measurements have all been initiated by shutting off both axial and transverse trapping simultaneously, which precludes the expansion in one dimension that is required for a rapidity measurement. In our experimental setup, we can remove the axial potential without affecting the transverse trapping that makes the system 1D, thus allowing for free expansion in one dimension. We initiate the momentum measurement at controllable times, t_{ev}, during the 1D expansion by suddenly shutting off the transverse trapping (Fig. 1A). The wave functions rapidly expand transversely, which markedly decreases their interaction energy before the axial wave function appreciably changes. After a long TOF, the spatial distribution approaches the momentum distribution at t_{ev} (Fig. 1B).

The experiment starts with a Bose-Einstein condensate of 10^5 ^{87}Rb atoms in the $F = 1$, $m_F =$

Department of Physics, Pennsylvania State University, University Park, PA 16802, USA.
*Corresponding author. Email: dsweiss@psu.edu

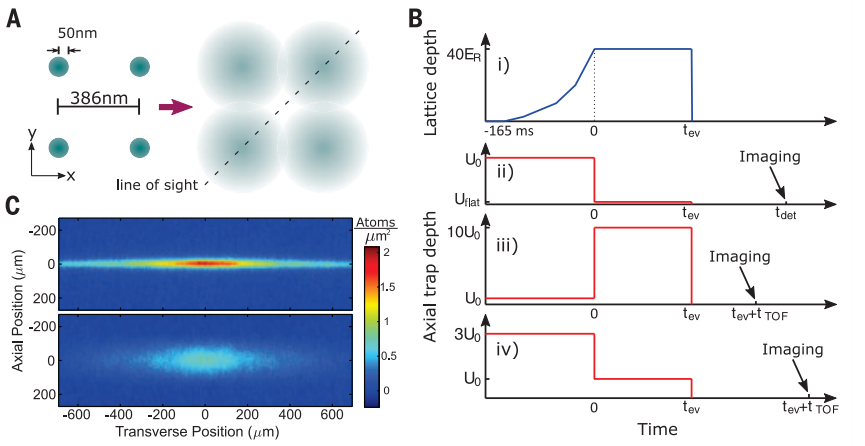

Fig. 1. Timing and measurement. (**A**) Rapid removal of interaction energy. Atoms are initially confined in a 2D optical lattice of 1D tubes (left). When the 2D lattice is shut off, rapid transverse expansion reduces the density, taking away interaction energy and allowing a good momentum measurement after TOF. The drawing at right illustrates the moment when the density has dropped by a factor of 20, before atoms in adjacent tubes start to overlap. Absorption imaging is done along the line of sight. (**B**) Timing diagram (not to scale horizontally). (i) Lattice depth as a function of time. (ii) Axial trap depth as a function of time for the dynamical fermionization measurement. $U_0 = 0.628E_R$ is the initial trap depth and $U_{flat} = 0.068E_R$ is the depth required to yield an approximately flat potential. At $t = 0$, the depth is suddenly lowered to cancel out the residual anti-trap due to the lattice beams. All traps are shut off at a variable t_{ev}, and imaging occurs at a fixed t_{det} (relative to $t = 0$). (iii and iv) Axial trap depth as a function of time for the Bose-Fermi oscillation experiments. The axial trap depth is suddenly changed at $t = 0$, and the atoms evolve in the new trap for a variable t_{ev}. The absorption image is taken at $t = t_{ev} + t_{TOF}$. (**C**) Absorption images for $t_{ev} = 0$ (top) and $t_{ev} = 15$ ms (bottom) after quenching to a flat potential. The images are averages over 30 shots. Sudden lattice shutoff makes the atoms expand rapidly transversely. The 1D TOF distributions (in the z direction, vertical in the images) are obtained by integrating the images transversely.

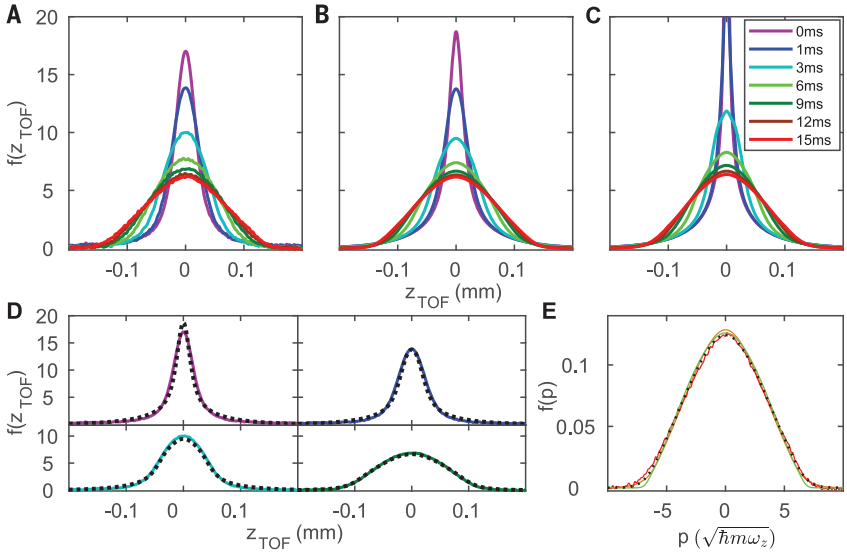

Fig. 2. Dynamical fermionization. (**A**) Normalized experimental axial TOF distributions for a range of t_{ev} values. Each profile is an average of 30 implementations. By 15 ms, an asymptotic shape has been reached. z_{TOF} denotes spatial positions after the time of flight. (**B**) Theoretical simulation of the experiment in the T-G limit, with no free parameters (*18*). (**C**) The corresponding theoretical momentum distributions (rescaled by t_{det}). (**D**) Experimental distributions for four of the t_{ev} values (0, 1, 3, and 9 ms) shown in (A) (colored curves), separately compared to the corresponding theoretical curves from (B) (dotted black lines). (**E**) Comparison of curves at $t_{ev} = 15$ ms. The experimental (red) and theoretical (dotted black) TOF curves are rescaled by t_{det} so that they can be compared to the theoretical T-G gas (orange) and NIF gas (green) momentum distributions. The agreement between the two TOF curves shows that the experiment is well described by the T-G limit. That the T-G gas momentum distribution overlaps with the TOF curves shows that finite size and resolution effects cease to be appreciable. Overlap with the NIF gas momentum distribution shows that t_{ev} is long enough that the momentum distribution has largely evolved into its asymptotic shape, which is the distribution of rapidities.

1 state trapped in a crossed dipole trap, around which we slowly turn on a blue-detuned 2D optical lattice to a depth of $40E_R$, where $E_R = \hbar k^2/2m$ is the recoil energy, $\hbar$ is the reduced Planck constant, m is the Rb atom mass, and $k = 2\pi/772$ nm is the lattice wave vector (*14*, *16*, *18*). The atoms end up trapped in a 2D array of nearly identical "tubes" with negligible tunneling among them. The number of particles per tube varies from 26 to 0 (*18*). The axial trapping frequency is approximately the same in all the occupied tubes, $\omega_z/2\pi = 18.1 \pm 0.36$ Hz. The Lieb-Liniger model that describes these 1D gases is characterized by the dimensionless coupling strength γ (*3*). For large values of γ, there are strong correlations among the single-particle wave functions because it is too energetically costly for them to appreciably overlap. In our tubes, $\gamma = 4.44/n_{1D}$, where n_{1D} is the local 1D density in μm^{-1} (*19*). With our initial trapping parameters, the weighted average γ is 8.5, and the smallest γ is 4.2 at the center of the central tube. Our theoretical analysis assumes the T-G gas limit of $\gamma \to \infty$.

To demonstrate dynamical fermionization, we suddenly reduce the depth of the crossed dipole trap at $t = 0$ so that, when combined with the weak axial anti-trap due to the blue-detuned 2D lattice, there is an approximately flat potential over an axial range of ~40 μm (fig. S1A). After a variable t_{ev}, we turn off the 2D lattice. We use a non-sudden turnoff (32 μs), which allows for a longer TOF expansion in the axial direction before the atoms spread transversely to a region where gravity is not well canceled by our magnetic field gradient (fig. S2A). This turnoff still removes interactions fast enough that the TOF distribution is barely distinguishable from what is obtained after a sudden shutoff (fig. S2B). At time $t_{det} = 70$ ms, we take absorption images of the atoms (Fig. 1C) and integrate over the transverse direction to obtain the TOF 1D distributions (*18*). The results are shown in Fig. 2A. The initially peaked "bosonic" TOF distribution smoothly deforms and approaches a rounded "fermionic" TOF distribution over the first 12 ms [see also fig. S1B, which shows the full width at half maximum (FWHM) of the TOF distributions]. In the 12 ms over which the distribution has mostly fermionized, the FWHM of the axial spatial extent of the atoms (before TOF) grows from 22 μm to 42 μm. When $t_{ev} >$ 15 ms, the atoms have expanded to where the axial potential is insufficiently flat and starts to affect the TOF distribution.

We theoretically simulated our experiment using the continuum limit of a lattice hard-core boson model (*20*), which incorporates all the experimental details, including the initial size, the evolution up to t_{ev}, the TOF, the instrumental resolution (4.8 μm), and the sum over tubes (*18*). The results are shown in Fig.

2B. Shown in Fig. 2, D and E, are direct comparisons between individual experimental curves (solid lines) and their theoretical counterparts (black dotted lines). With no free parameters, the simulations match the experimental results well, particularly in the asymptotic limit (Fig. 2E). The agreement at long times suggests that the T-G gas model is sufficient for our finite-γ system. The small discrepancies at earlier times are probably caused by the nonzero initial temperatures in the experiments, which are known to strongly affect the height of the zero-momentum peak in the T-G limit (*21*).

In Fig. 2C, we show the evolution of the theoretical momentum distributions, which do not have the complications of initial size, instrumental resolution, and finite t_{det}. Those curves can be compared to the full simulations of the experiment in Fig. 2B, which contain those complications. At small values of t_{ev},

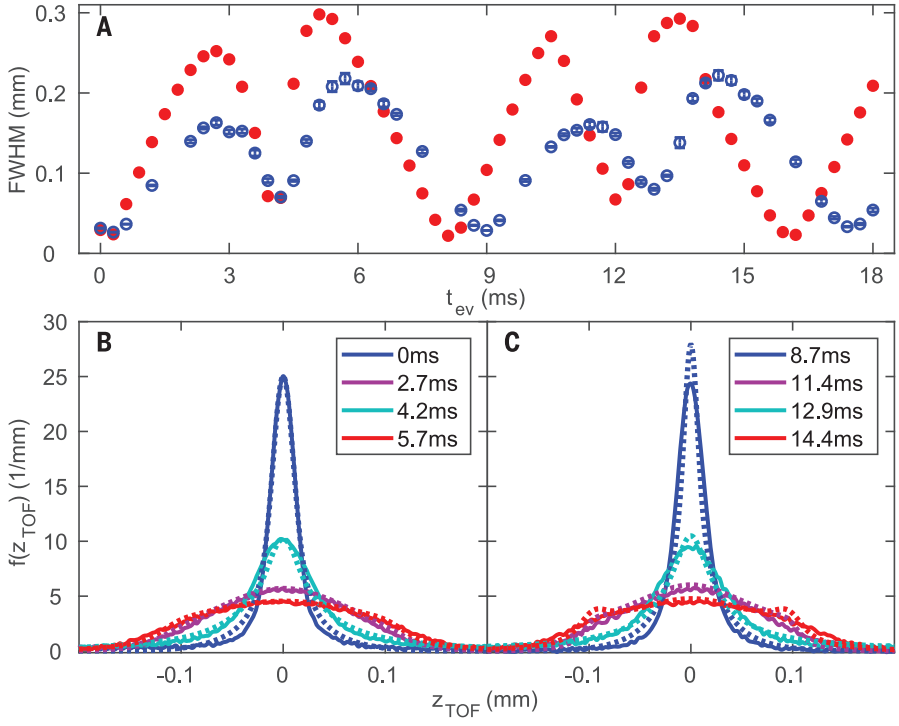

Fig. 3. Bose-Fermi oscillations (quench from low to high ω_z). (**A**) FWHM as a function of time after the quench to an axial trap that is deeper by a factor of 10 (see Fig. 1B). The blue points are from the experiment, with standard error bars from an average of 5 to 14 shots (*18*). The red points are from the T-G gas theory (*18*). For a few points in the second period, the center of the distribution is not the maximum (see fig. S3); in those cases, we still define the half maximum relative to the center point. We attribute the difference in oscillation period to finite γ in the experiment. (**B**) TOF distributions associated with the extrema of the first oscillation cycle. The experimental curves are solid; the corresponding theoretical curves are dotted. The shapes at the minima (blue and teal) are bosonic, with small differences between them associated with finite initial sizes. The shapes at the maxima (purple and red) are fermionic, like the asymptotic dynamical fermionization distribution. The theoretical curves have been rescaled to better compare the shapes to the experimental curves. (**C**) TOF distributions associated with the extrema of the second oscillation cycle. The shapes at the minima (blue and teal) are bosonic. The experimental curves at the maxima (purple and red) are fermionic, but the theoretical curves have small side lobes that are associated with the axial trap anharmonicity. We suspect that their absence in the experiment is a consequence of the smaller γ (see text).

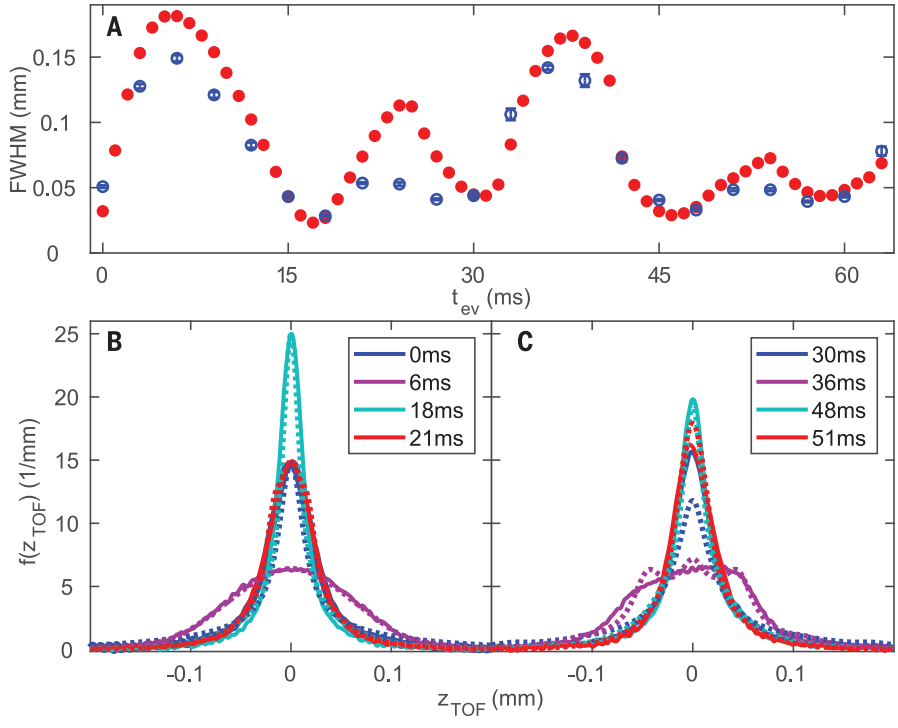

Fig. 4. Bose-Fermi oscillations (quench from high to low ω_z). (**A**) FWHM as a function of time after the quench to an axial trap that is shallower by a factor of 3 (see Fig. 1B). The blue points are from the experiment, with standard error bars from an average of 10 shots. The red points are from the T-G gas theory (*18*). (**B**) TOF distributions associated with the extrema of the first oscillation cycle. The experimental curves are solid; the corresponding theoretical curves are dotted. The shapes at the minima (blue and teal) are bosonic, with small differences between them associated with finite initial sizes. The shapes at the maxima (purple and red) are fermionic, like the asymptotic dynamical fermionization distribution. The theoretical curves have been rescaled to better compare the shapes to the experimental curves. (**C**) TOF distributions associated with the extrema of the second oscillation cycle. The shapes at the minima (blue and teal) are bosonic. The experimental curves at the maxima (purple and red) are fermionic. Both theoretical and experimental curves have distorted shapes associated with the axial trap anharmonicity.

these factors broaden the measured widths, but by t_{ev} = 15 ms, the TOF distributions are nearly identical to the theoretical momentum distribution, as shown by direct comparison in Fig. 2E. Also shown in Fig. 2E is the theoretical momentum distribution of an identically trapped NIF gas, which is the rapidity distribution of the measured T-G gas. Its good overlap with the other curves confirms that we have measured the distribution of rapidities; previously, such distributions were not experimentally accessible in any many-body quantum system.

We also studied the dynamics after suddenly changing the depth of the axial trap. Related quenches have previously been studied in the weakly interacting regime (*22*). A theoretical simulation in the T-G limit has shown that for harmonic traps, a sudden factor of 10 reduction in axial trapping frequency leads to the surprising behavior that the momentum distribution oscillates between bosonic and fermionic shapes (*8*, *23*). The initial change to a fermionic shape is easily understood as approximately dynamical fermionization. What is more remarkable and counterintuitive is the return at $T/2$ (where T is the breathing oscillation period) to a bosonic distribution with a height and width changed by a factor of the ratio of the oscillation frequencies, $r = \omega_{z_f}/\omega_{z_0}$, $f(p, T/2) = rf(rp, 0)$. In the second half of the period, the distribution evolves through the fermionized distribution back to the original bosonic one.

We experimentally performed quenches to axial traps that were deeper by a factor of 10 and shallower by a factor of 3. The former makes initial size effects less important, so that the TOF distributions better approximate the momentum distributions. However, quenching to a deeper trap decreases γ to an average of near 2 at $T/2$ (*18*), which worsens the T-G gas approximation. Higher densities require that we shut off the lattice as fast as possible to prevent axial evolution while the interaction energy is being removed, which in turn limits the available TOF time t_{TOF} to 40 ms (*18*). We first characterize the TOF distributions of the evolving gas in a shape-agnostic way by plotting the FWHM versus time over the first two periods, as shown by the blue points in Fig. 3A. The corresponding T-G gas theory curves are shown by the red points. The theoretical period is ~9% shorter than in the experiment. The longer experimental period is expected, according to the known functional dependence of the ratio of breathing to dipole oscillation frequencies, which varies from 2 to $\sqrt{3}$ when γ goes from ∞ to 0 (*18*, *24*, *25*).

The solid lines in Fig. 3, B and C, show the experimental TOF distributions near the peaks and valleys from Fig. 3A (see fig. S3 for the shapes at other times). The dotted lines in Fig. 3, B and C, are from corresponding theory curves, with the heights and widths rescaled for easier comparison of the shapes (*18*). Focusing on the first period, the salient point is that the theory and experimental shapes evolve in the same way. They are bosonic at 0 and $T/2$, with experimental and theoretical widths that are within 6% of each other (*8*). They are fermionic at the FWHM peaks and at the surrounding points (fig. S3). The asymmetry in Fig. 3A about $T/2$ is a finite size effect. The fact that the fermionic FWHMs are smaller in the experiment than the theory is a consequence of finite γ in the former.

The experimental shapes are almost identical between the first and second periods, highlighting the lack of damping in this integrable evolution. The theoretical shapes, however, are slightly different near the FWHM peaks in the second period, showing flattening at the top and side peaks. We use the width and amplitude rescaling from the first cycle on the second-cycle theory curves. The new features in the theory curves result from the Gaussian trap's small deviation from harmonicity; they are absent when we use a harmonic trap for the calculation (see fig. S4). We suspect that the absence of these features in the experiment results from the reduced γ. A similar discrepancy between experiments and $\gamma \to \infty$ theory was seen in (*26*).

In the quench to a shallower trap, γ increases from 4.4 to ~6.7 during the oscillation. The observed period matches that of the T-G gas theory (Fig. 4A), possibly because two small frequency shifts cancel (*18*). The first-cycle shapes (Fig. 4B and fig. S5) are similar to those in the other quench (Fig. 3B and fig. S3). In the second cycle, we observe a flattening in the experimental distribution near the FWHM peaks in both the experiment and theory (Fig. 4C and fig. S5). The value of γ is apparently large enough that this effect of anharmonicity is not completely smoothed out, but is still far enough from ∞ to suppress the FWHM peaks.

The technique presented here can also be used to measure rapidity distributions, and to explore the expansion dynamics of density and momentum distributions, in intermediate-γ 1D Bose gases. This is complementary to what is accessible in atom-chip experiments (*27*) and provides a broad testing ground for the recently developed generalized hydrodynamics theory (*28*, *29*). Our technique can also be applied to the measurement of rapidity distributions and momentum dynamics after more complex quenches, like those in quantum Newton's cradles (*30*, *31*), recently studied theoretically using generalized hydrodynamics (*32*). It can be applied to 1D lattice models such as the 1D Fermi-Hubbard model (*9*, *11*). Knowledge of the rapidity distributions, together with the theoretical tools that have been developed in the field of integrable quantum systems, allows predictions of all aspects of integrable quantum systems, including correlation functions and dynamics.

REFERENCES AND NOTES

1. H. Bethe, *Z. Phys.* **71**, 205–226 (1931).
2. B. Sutherland, *Beautiful Models* (World Scientific, Singapore, 2004).
3. M. A. Cazalilla, R. Citro, T. Giamarchi, E. Orignac, M. Rigol, *Rev. Mod. Phys.* **83**, 1405–1466 (2011).
4. X.-W. Guan, M. T. Batchelor, C. Lee, *Rev. Mod. Phys.* **85**, 1633–1691 (2013).
5. P. Calabrese, F. H. L. Essler, G. Mussardo, *J. Stat. Mech.* **2016**, 064001 (2016).
6. B. Sutherland, *Phys. Rev. Lett.* **80**, 3678–3681 (1998).
7. M. Rigol, A. Muramatsu, *Phys. Rev. Lett.* **94**, 240403 (2005).
8. A. Minguzzi, D. M. Gangardt, *Phys. Rev. Lett.* **94**, 240404 (2005).
9. C. J. Bolech *et al*., *Phys. Rev. Lett.* **109**, 110602 (2012).
10. A. S. Campbell, D. M. Gangardt, K. V. Kheruntsyan, *Phys. Rev. Lett.* **114**, 125302 (2015).
11. Z. Mei, L. Vidmar, F. Heidrich-Meisner, C. J. Bolech, *Phys. Rev. A* **93**, 021607 (2016).
12. E. H. Lieb, W. Liniger, *Phys. Rev.* **130**, 1605–1616 (1963).
13. M. Girardeau, *J. Math. Phys.* **1**, 516–523 (1960).
14. T. Kinoshita, T. Wenger, D. S. Weiss, *Science* **305**, 1125–1128 (2004).
15. B. Paredes *et al*., *Nature* **429**, 277–281 (2004).
16. T. Kinoshita, T. Wenger, D. S. Weiss, *Phys. Rev. Lett.* **95**, 190406 (2005).
17. I. Bloch, J. Dalibard, W. Zwerger, *Rev. Mod. Phys.* **80**, 885–964 (2008).
18. See supplementary materials.
19. M. Olshanii, *Phys. Rev. Lett.* **81**, 938–941 (1998).
20. W. Xu, M. Rigol, *Phys. Rev. A* **92**, 063623 (2015).
21. M. Rigol, *Phys. Rev. A* **72**, 063607 (2005).
22. B. Fang, G. Carleo, A. Johnson, I. Bouchoule, *Phys. Rev. Lett.* **113**, 035301 (2014).
23. Y. Y. Atas, I. Bouchoule, D. M. Gangardt, K. V. Kheruntsyan, *Phys. Rev. A* **96**, 041605 (2017).
24. C. Menotti, S. Stringari, *Phys. Rev. A* **66**, 043610 (2002).
25. H. Moritz, T. Stöferle, M. Köhl, T. Esslinger, *Phys. Rev. Lett.* **91**, 250402 (2003).
26. L. Vidmar *et al*., *Phys. Rev. Lett.* **115**, 175301 (2015).
27. M. Schemmer, I. Bouchoule, B. Doyon, J. Dubail, *Phys. Rev. Lett.* **122**, 090601 (2019).
28. B. Bertini, M. Collura, J. De Nardis, M. Fagotti, *Phys. Rev. Lett.* **117**, 207201 (2016).
29. O. A. Castro-Alvaredo, B. Doyon, T. Yoshimura, *Phys. Rev. X* **6**, 041065 (2016).
30. T. Kinoshita, T. Wenger, D. S. Weiss, *Nature* **440**, 900–903 (2006).
31. Y. Tang *et al*., *Phys. Rev. X* **8**, 021030 (2018).
32. J.-S. Caux, B. Doyon, J. Dubail, R. Konik, T. Yoshimura, *SciPost Phys.* **6**, 70 (2019).
33. D. S. Weiss, *Harvard Dataverse*, doi: 10.7910/DVN/7H7GRO.

ACKNOWLEDGMENTS

Funding: Supported by NSF grants PHY-1707482 (Y.Z. and M.R.) and PHY-1707576 (D.S.W., J.M.W., N.M., and Y.L.) and by U.S. Army Research Office grant W911NF-16-0031-P00005 (D.S.W., J.M.W., N.M., and Y.L.). The computations were carried out at the Institute for CyberScience at Penn State. **Author contributions:** J.M.W., N.M., and Y.L. carried out the experiments; Y.Z. carried out the theoretical calculations; and M.R. and D.S.W. oversaw the theoretical and experimental work. All authors were involved in the analysis of the results, and all contributed to writing the paper. **Competing interests:** The authors declare no competing interests. **Data and materials availability:** All experimental and theoretical data required to draw the conclusions from this paper are included in the text and supplementary materials. Tables of the data in the figures can be found at (*33*). Reasonable requests or additional information should be addressed to the corresponding author.

SUPPLEMENTARY MATERIALS

science. /content/367/6485/1461/suppl/DC1 Materials and Methods
Supplementary Text
Figs. S1 to S5
References (*34*–*40*)

14 August 2019; accepted 27 February 2020
10.1126/science.aaz0242

ASTROPARTICLE PHYSICS

The dark matter interpretation of the 3.5-keV line is inconsistent with blank-sky observations

Christopher Dessert[1], Nicholas L. Rodd[2,3], Benjamin R. Safdi[1]*

Observations of nearby galaxies and galaxy clusters have reported an unexpected x-ray emission line around 3.5 kilo–electron volts (keV). Proposals to explain this line include decaying dark matter—in particular, that the decay of sterile neutrinos with a mass around 7 keV could match the available data. If this interpretation is correct, the 3.5-keV line should also be emitted by dark matter in the halo of the Milky Way. We used more than 30 megaseconds of XMM-Newton (X-ray Multi-Mirror Mission) blank-sky observations to test this hypothesis, finding no evidence of the 3.5-keV line emission from the Milky Way halo. We set an upper limit on the decay rate of dark matter in this mass range, which is inconsistent with the possibility that the 3.5-keV line originates from dark matter decay.

A plethora of cosmological and astrophysical measurements indicate that dark matter (DM) exists and makes up ~80% of the matter in the Universe, but its microscopic nature is unknown. If DM consists of particles that can decay into ordinary matter, the decay process may produce photons that are detectable with x-ray telescopes. Some DM models, such as sterile neutrino DM, predict such x-ray emission lines (*1*). If sterile neutrinos exist with a mass energy of a few kilo–electron volts, they may explain the observed abundance of DM (*2*–*4*). The detection of an unidentified x-ray line (UXL) around 3.5 keV in a stacked sample of nearby galaxy clusters (*5*), and an independent detection in one of those clusters and a galaxy (*6*), have been interpreted as evidence for DM decay (*7*). Other less-exotic explanations have also been proposed, such as emission lines of potassium or argon from hot gas within the clusters (*8*) or charge-exchange lines from interactions of the hot intracluster plasmas and cold gas clouds (*9*, *10*).

The 3.5-keV UXL (hereafter just UXL) has been confirmed by several groups using different astrophysical targets and telescopes. These include observations of the Perseus cluster using the Chandra (*5*) and Suzaku (*11*) x-ray space telescopes, observations of the Galactic Center of the Milky Way with XMM-Newton (X-ray Multi-Mirror Mission) (*12*), and observations of the diffuse Milky Way halo with Chandra deep-field data (*13*). Several nondetections of the UXL have also been reported (*14*–*18*). It is possible for a decaying DM model to be consistent with both the positive detections and negative results. Figure 1 shows the existing detections and upper limits for the UXL, in the plane of sterile neutrino DM mass m_s and sterile-active mixing parameter $\sin^2(2\theta)$, which characterizes (and linearly scales with) the decay rate of the sterile neutrino DM state (*19*).

We seek to constrain the DM decay rate in the mass range relevant for the UXL by using XMM-Newton blank-sky observations (BSOs). Our analysis utilizes ~10^3 BSOs, which we define as observations away from large x-ray emitting regions, for a total of 30.6 Ms of exposure time. We focus on the line signal predicted from DM decay within the Milky Way, which should be present at every point in the sky. The sensitivity of this technique can be estimated in the limit of large counts, in other words, detected photons. The test statistic (TS) in favor of detection of DM decay (related to the significance $\sigma \sim \sqrt{\mathrm{TS}}$), scales as $\mathrm{TS} \sim S^2/B$, where S is the number of signal photons from DM decay and B is the number of background photons. The number of signal photons expected from a given location in the sky is proportional to the product of the decay rate of DM and the integrated column density of DM along the line of sight, which is quantified by the D factor, $D = \int ds \rho_{\mathrm{DM}}(s)$, where ρ_{DM} is the DM density and s is the line-of-sight distance.

We use these scalings to estimate the expected sensitivity of a BSO analysis, given the previous UXL observations. For example, the UXL has been detected with a 320-ks observation of the Perseus cluster using the XMM-Newton Metal Oxide Semiconductor (MOS) camera at roughly the 4σ level (TS ~ 16) (*5*). The background x-ray flux from Perseus is much higher than that for the BSOs, typically by a factor of 50. Averaged over the field of view of XMM-Newton, the D factor of the Perseus cluster is $D_{\mathrm{Pers}} \sim 3 \times 10^{28}$ keV cm^{-2}, which is approximately the same as D_{BSO}, the D factor within the Milky Way halo for observations ~45° away from the Galactic Center. We calculated both D factors assuming a Navarro-Frenk-White (NFW) DM profile (*20*). Although the signal power should therefore be the same between Perseus and the BSO, we expect the same sensitivity to the UXL with a 6-ks BSO observation—assuming a DM origin—because the BSO background is expected to be lower than that of Perseus. Our analysis below uses ~30 Ms of BSO exposure time, which implies that the UXL would be seen with a TS ~ 10^5, corresponding to a detection significance of >100σ, if it is caused by decaying DM with the same properties as that in the Perseus cluster.

We analyzed all publicly available archival XMM-Newton observations that pass a set of quality cuts. For our fiducial analysis, we first

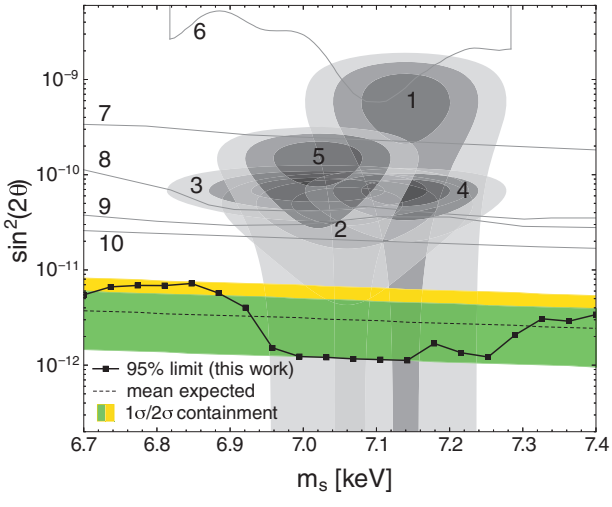

Fig. 1. Our upper limits on sterile neutrino decay. The one-sided 95% upper limit on the sterile neutrino DM mixing parameter $\sin^2(2\theta)$ as a function of the DM mass m_s from our analysis of XMM-Newton BSOs (black squares). We compare this with the expected sensitivity from the Asimov procedure (1σ shown in green and 2σ in yellow), and previous constraints (gray lines) and parameters required for DM decay explanations of previous UXL detections (3σ in dark gray, 2σ in gray, and 1σ in light gray). We also show several existing detections (labeled 1 to 5) and constraints (6 to 10) (*7*).

[1]Leinweber Center for Theoretical Physics, Department of Physics, University of Michigan, Ann Arbor, MI 48109, USA. [2]Berkeley Center for Theoretical Physics, University of California, Berkeley, CA 94720, USA. [3]Theoretical Physics Group, Lawrence Berkeley National Laboratory, Berkeley, CA 94720, USA.
*Corresponding author. Email: bsafdi@umich.edu

restrict the observations used to those between 5° and 45° of the Galactic Center. Within this region, there are 1492 observations, with 4303 total exposures, for ~86 Ms of exposure time. These observations are distributed quite uniformly through our fiducial region, although there is a bias toward the Galactic plane. There are more exposures than observations because each of the charge-coupled devices (CCDs) in the European Photon Imaging Cameras on XMM-Newton [two MOSs and one positive-negative (PN)] (*21*, *22*) record a separate exposure, and each camera may have multiple exposures in a single observation if the data taking was interrupted. For each observation, we process and reduce the data using the standard tools for extended emission (*19*). In addition to the photon-count data, we also extract the quiescent particle background (QPB). The QPB is an instrumental background caused by high-energy particles interacting with the detector, rather than true photon counts. The magnitude of the QPB contribution is estimated from parts of the instrument that are shielded from incident x-rays; we refer to this as the QPB data.

We then perform a background-only analysis of each of the exposures to determine properties that are used for further selection. We calculate the QPB contribution and the astrophysical flux over the energy range of 2.85 to 4.2 keV. The QPB rate is estimated from the QPB data, whereas the astrophysical flux is measured using the likelihood analysis described below. We rescale the astrophysical flux measured in the restricted energy range to a wider energy range of 2 to 10 keV by assuming a power-law spectrum of $dN/dE \sim E^{-1.5}$, where N is the photon flux and E is energy. The cosmic x-ray background has a 2 to 10 keV intensity of $I_{2\text{–}10} \approx 2 \times 10^{-11}$ erg cm^{-2} s^{-1} deg^{-2} (*23*, *24*). In our fiducial analysis, we remove exposures with $I_{2\text{–}10} > 10^{-10}$ erg cm^{-2} s^{-1} deg^{-2} to avoid including exposures with either extended emission or flux from unresolved point sources. Approximately 58% of the exposures pass this cut, whereas ~13% of the exposures have $I_{2\text{–}10} < 3 \times 10^{-11}$ erg cm^{-2} s^{-1} deg^{-2}. Because the individual exposures are in the background-dominated regime and the signal we are searching for is restricted to a narrow energy range, even a clearly detectable DM line would have no effect on this selection criterion. We further remove exposures with anomalously high QPB rates; for our fiducial analysis, we keep the 68% of exposures with the lowest QPB rates. We apply this criterion separately to the MOS and PN exposures. Lastly, we remove exposures with <1 ks of exposure time, because these exposures do not substantially improve our sensitivity and the associated low photon counts reduce the reliability of the background estimates. After these cuts, we are left with ~30.6 Ms of exposure time, distributed between 1397 exposures and 752 distinct observations.

We analyze the ensemble of exposures for evidence of the UXL by using a joint-likelihood procedure. Individual exposures are not stacked. To evaluate the UXL hypothesis for a given m_s, we first construct profile likelihoods for the individual exposures as functions of the DM-induced line flux F. The x-ray counts are analyzed with a Poisson likelihood, from the number of counts in each energy channel. The associated model is a combination of the DM-induced flux, represented by an x-ray line broadened by the detector response, and two independent power laws for the background astrophysical emission and the instrumental QPB, where the normalization and spectral indices of each power law are free parameters. This same QPB power-law contribution is also fitted to the estimated QPB data using a Gaussian likelihood. Both datasets are restricted to the energy range $m_s/2 \pm 0.25$ keV, which was chosen to be wider than the energy resolution of the detector (~0.1 keV) but small enough that our power-law background models are valid over the whole energy range.

The two likelihoods for the x-ray counts and the QPB estimate are then combined, providing a likelihood that, for a given m_s, is a function of five parameters: F, the two normalization factors, and the two spectral indices of the astrophysical and QPB power laws. The last four of these are treated as nuisance parameters; that is, we maximize the individual likelihoods over the valid ranges of these parameters. Each dataset was therefore reduced to a profile likelihood as a function of F. This flux can be converted to a lifetime and, hence, $\sin^2(2\theta)$ (*1*, *19*) once the D factor for this region of the sky is known. In our fiducial analysis, we compute the D factors by assuming that the DM density profile of the Milky Way is an NFW profile with a 20-kpc scale radius. We normalize the density profile, assuming a local DM density of 0.4 GeV cm^{-3} (*25*), and take the distance between the Sun and the Galactic Center to be 8.13 kpc (*26*).

Joining the resulting likelihoods associated with each exposure yields the final joint likelihood, which is a function of only $\sin^2(2\theta)$ for a given m_s. This likelihood is then used to calculate the one-sided 95% confidence limit on the mixing angle and to search for evidence for the UXL using the discovery TS, which is defined as twice the log-likelihood difference between the maximum likelihood and the likelihood at the null hypothesis [this assumes the likelihood is maximized at a positive value of $\sin^2(2\theta)$]. For statistical consistency, we include negative values of $\sin^2(2\theta)$ in the profile likelihood, which correspond to underfluctuations of the data.

To calibrate our expectation for the sensitivity under the null hypothesis, we construct the 68 and 95% expectations for the limit using the Asimov procedure (*27*). The Asimov procedure requires a model for the data under the null hypothesis; we compute this model by performing the likelihood fits described above under the null hypothesis [$\sin^2(2\theta) = 0$]. We use this to set one-sided power-constrained limits (*28*). The measured limit is not allowed to go below the 68% containment region for the expected limit, so as to prevent setting tighter limits than expected because of downward statistical fluctuations.

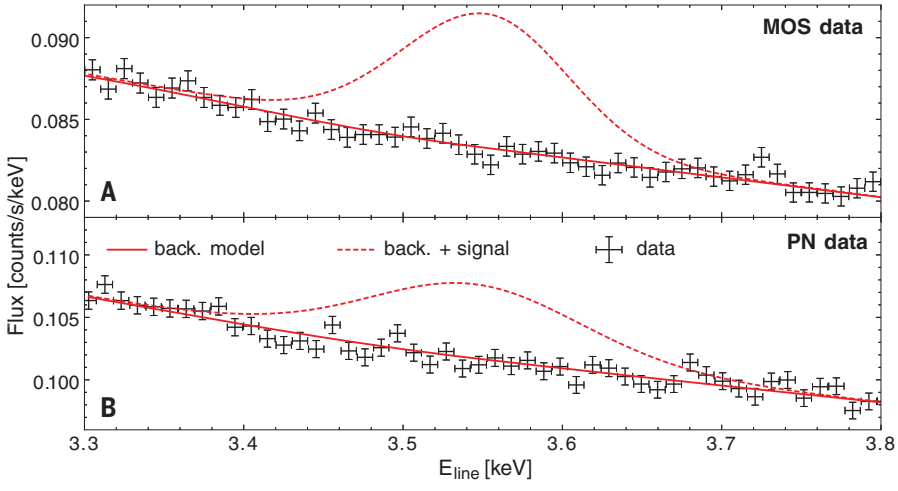

Fig. 2. The summed spectra. (**A** and **B**) The summed MOS (A) and PN (B) spectra (black data points) for the exposures used in our fiducial analysis. We also show the summed best-fitting background (back.) models (red solid line) and an example signal contribution with m_s = 7.105 keV and $\sin^2(2\theta) = 10^{-10}$ (red dashed line).

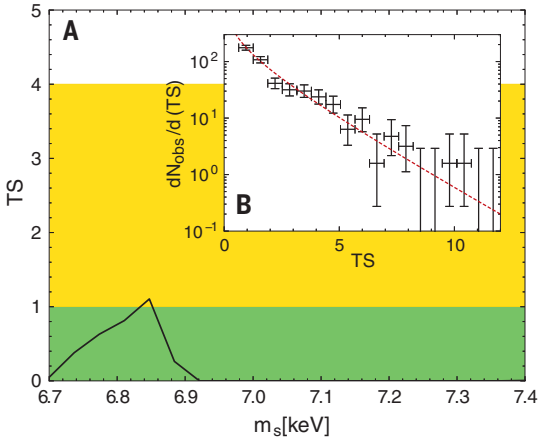

Fig. 3. No evidence for the decaying DM interpretation of the UXL. (**A**) The TS for the UXL as a function of the DM mass m_s from the joint-likelihood analysis. The black curve shows the result from the data analysis, whereas the green and yellow shaded regions indicate the 1σ and 2σ expectations, respectively, under the null hypothesis. (**B**) A histogram of the TSs from the individual exposures, with vertical error bars from Poisson counting statistics and horizontal error bars bracketing the histogram bin ranges.

In Fig. 2, we show the summed spectra over all exposures included in the analysis for the MOS and PN data separately. We emphasize that we do not use the summed spectra for our fiducial data analysis; instead, we use the joint likelihood procedure described above. However, the summed spectra are shown for illustrative purposes. We also show the summed best-fitting background models. Because our full model has independent astrophysical and QPB power-law models for each exposure, these curves are not single power laws but sums over 2794 independent power laws. The summed data closely match the summed background models. Figure 2 also shows the expected signal for m_s = 7.105 keV and $\sin^2(2\theta) = 10^{-10}$, which are values we chose to be in the middle of the parameter space for explaining the observed UXL (Fig. 1). Figure 2 shows that this model is inconsistent with the data.

Our fiducial one-sided power-constrained 95% upper limit is shown in Fig. 1 along with mean, 1σ, and 2σ expectations under the null hypothesis. The upper limit is consistent with the expectation values and strongly disfavors the decaying DM explanation of the UXL. Our results disagree with the parameters required to explain the previous UXL observations as decaying DM by over an order of magnitude in $\sin^2(2\theta)$. In Fig. 3, we show the TS for decaying DM as a function of DM mass, with the 1σ and 2σ expectations under the null hypothesis; we find no evidence for decaying DM.

Figure 3 shows the TS for the joint-likelihood analysis over the ensemble of exposures. However, we can also calculate a TS for decaying DM from each individual exposure. Under the null hypothesis, Wilks' theorem states that the distribution of TSs from the individual exposures should asymptotically follow a χ^2 distribution. In the inset of Fig. 3, we show the histogram of the number of exposures that are found for a given TS, for our reference mass of m_s = 7.105 keV. The distribution matches the expectation under the null hypothesis. We also performed a Kolmogorov-Smirnov test comparing the observed TSs with the expected one-sided χ^2 distribution and found a P value of 0.77, which indicates that the TS data are consistent with the null hypothesis.

Although Fig. 3 shows that our results appear to be consistent with the expected statistical variability, there remains the possibility that systematic effects such as unmodeled instrumental lines could conspire to hide a real line. We performed tests for such systematics (*19*), which are illustrated in fig. S9 for analysis of the data from the individual cameras separately, in fig. S14 for explicitly allowing extra possible instrumental lines in the background model, and in figs. S16 and S17 for looking at the data in subregions increasingly far away from the Galactic Center. Accounting for these possible systematics in a data-driven way (*19*) can weaken our limits to $\sin^2(2\theta) < 2 \times 10^{-11}$ (fig. S17, region 4), which still strongly rules out the decaying DM interpretation of the UXL. We also analyzed the summed x-ray count data shown in Fig. 2 directly (*19*), and found, again, that the decaying DM interpretation of the UXL was excluded (fig. S18).

We have analyzed ~30 Ms of XMM-Newton BSOs for evidence of DM decay in the energy range of 3.35 to 3.7 keV. We found no evidence for DM decay. Our analysis rules out the decaying DM interpretation of the previously observed 3.5-keV UXL because our results exclude the required decay rate by more than an order of magnitude.

REFERENCES AND NOTES

1. P. B. Pal, L. Wolfenstein, *Phys. Rev. D* **25**, 766–773 (1982).
2. S. Dodelson, L. M. Widrow, *Phys. Rev. Lett.* **72**, 17–20 (1994).
3. X.-D. Shi, G. M. Fuller, *Phys. Rev. Lett.* **82**, 2832–2835 (1999).
4. A. Kusenko, *Phys. Rev. Lett.* **97**, 241301 (2006).
5. E. Bulbul *et al.*, *Astrophys. J.* **789**, 13 (2014).
6. A. Boyarsky, O. Ruchayskiy, D. Iakubovskyi, J. Franse, *Phys. Rev. Lett.* **113**, 251301 (2014).
7. K. N. Abazajian, *Phys. Rep.* **711-712**, 1–28 (2017).
8. T. Jeltema, S. Profumo, *Mon. Not. R. Astron. Soc.* **450**, 2143–2152 (2015).
9. L. Gu *et al.*, *Astron. Astrophys.* **584**, L11 (2015).
10. C. Shah *et al.*, *Astrophys. J.* **833**, 52 (2016).
11. O. Urban *et al.*, *Mon. Not. R. Astron. Soc.* **451**, 2447–2461 (2015).
12. A. Boyarsky, J. Franse, D. Iakubovskyi, O. Ruchayskiy, *Phys. Rev. Lett.* **115**, 161301 (2015).
13. N. Cappelluti *et al.*, *Astrophys. J.* **854**, 179 (2018).
14. S. Horiuchi *et al.*, *Phys. Rev. D* **89**, 025017 (2014).
15. D. Malyshev, A. Neronov, D. Eckert, *Phys. Rev. D* **90**, 103506 (2014).
16. M. E. Anderson, E. Churazov, J. N. Bregman, *Mon. Not. R. Astron. Soc.* **452**, 3905–3923 (2015).
17. T. Tamura, R. Iizuka, Y. Maeda, K. Mitsuda, N. Y. Yamasaki, *Publ. Astron. Soc. Jpn.* **67**, 23 (2015).
18. F. A. Aharonian *et al.*, *Astrophys. J.* **837**, L15 (2017).
19. Materials and methods are available as supplementary materials.
20. J. F. Navarro, C. S. Frenk, S. D. M. White, *Astrophys. J.* **462**, 563 (1996).
21. M. J. L. Turner *et al.*, *Astron. Astrophys.* **365**, L27–L35 (2001).
22. L. Strüder *et al.*, *Astron. Astrophys.* **365**, L18–L26 (2001).
23. D. H. Lumb, R. S. Warwick, M. Page, A. De Luca, *Astron. Astrophys.* **389**, 93–105 (2002).
24. A. Moretti, *AIP Conf. Proc.* **1126**, 223–226 (2009).
25. R. Catena, P. Ullio, *J. Cosmol. Astropart. Phys.* **08**, 004 (2010).
26. R. Abuter *et al.*, *Astron. Astrophys.* **615**, L15 (2018).
27. G. Cowan, K. Cranmer, E. Gross, O. Vitells, *Eur. Phys. J. C* **71**, 1554 (2011).
28. G. Cowan, K. Cranmer, E. Gross, O. Vitells, Power-Constrained Limits. arXiv:1105.3166 [physics.data-an] (16 May 2011).
29. N. Rodd, C. Dessert, nickrodd/XMM-DM: XMM-DM, version v1.0, Zenodo (2020); http://doi.org/10.5281/zenodo.3669387.

ACKNOWLEDGMENTS

We thank S. Mishra-Sharma for collaboration in the early stages of this work and K. Abazajian, J. Beacom, A. Boyarsky, E. Bulbul, D. Finkbeiner, J. Kopp, K. Perez, S. Profumo, J. Thaler, and C. Weniger for useful discussions and comments on the draft. We further thank K. Abazajian for preliminary discussions of this topic and the members of the XMM-Newton Helpdesk for assistance with the data-reduction process. **Funding:** C.D. and B.R.S. were supported by the Department of Energy Early Career Grant DE-SC0019225. N.L.R. is supported by the Miller Institute for Basic Research in Science at the University of California, Berkeley. Computational resources and services were provided by Advanced Research Computing at the University of Michigan, Ann Arbor. **Author contributions:** C.D. and N.L.R. wrote the data-reduction code. B.R.S. wrote the analysis code. All authors contributed to the writing of the manuscript. **Competing interests:** The authors declare no competing interests. **Data and material availability:** The observations used in this work were downloaded from the XMM archive http://nxsa.esac.esa.int/nxsa-web/#home. The full list of exposures used in our fiducial analysis, our data-reduction software, our analysis code, and the numerical data plotted in the figures are provided at (*29*).

SUPPLEMENTARY MATERIALS

science. /content/367/6485/1465/suppl/DC1 Materials and Methods
Supplementary Text
Figs. S1 to S18
Tables S1 and S2
References (*30–43*)

15 December 2018; accepted 4 March 2020
10.1126/science.aaw3772

CANCER

Deregulation of ribosomal protein expression and translation promotes breast cancer metastasis

Richard Y. Ebright[1], Soocheol Lee[1], Ben S. Wittner[1], Kira L. Niederhoffer[1], Benjamin T. Nicholson[1], Aditya Bardia[1,2], Samuel Truesdell[1], Devon F. Wiley[1], Benjamin Wesley[1], Selena Li[1], Andy Mai[1], Nicola Aceto[1]*, Nicole Vincent-Jordan[1]†, Annamaria Szabolcs[1], Brian Chirn[1], Johannes Kreuzer[1], Valentine Comaills[1], Mark Kalinich[1], Wilhelm Haas[1,2], David T. Ting[1,2], Mehmet Toner[3,4,5], Shobha Vasudevan[1,2], Daniel A. Haber[1,2,6]‡, Shyamala Maheswaran[1,5]‡, Douglas S. Micalizzi[1,2]

Circulating tumor cells (CTCs) are shed into the bloodstream from primary tumors, but only a small subset of these cells generates metastases. We conducted an in vivo genome-wide CRISPR activation screen in CTCs from breast cancer patients to identify genes that promote distant metastasis in mice. Genes coding for ribosomal proteins and regulators of translation were enriched in this screen. Overexpression of *RPL15*, which encodes a component of the large ribosomal subunit, increased metastatic growth in multiple organs and selectively enhanced translation of other ribosomal proteins and cell cycle regulators. RNA sequencing of freshly isolated CTCs from breast cancer patients revealed a subset with strong ribosome and protein synthesis signatures; these CTCs expressed proliferation and epithelial markers and correlated with poor clinical outcome. Therapies targeting this aggressive subset of CTCs may merit exploration as potential suppressors of metastatic progression.

Circulating tumor cells (CTCs) shed into the bloodstream from primary tumors sustain physical, oxidative, and other environmental stresses before disseminating to distant organs, where only a small subset of these cells may be competent to generate metastatic tumors (*1*, *2*). For hormone receptor–positive (HR+) breast cancer, which may recur at distant sites many years after tumor resection and adjuvant therapy (*3*), defining the mechanisms that regulate survival and proliferation of CTCs presents an opportunity to suppress such delayed metastatic recurrence. Using a microfluidic platform to enrich viable CTCs from the blood of patients with HR+ metastatic breast cancer, we generated a panel of ex vivo CTC cultures that are highly tumorigenic when injected into the mammary fat pad of immunodeficient NSG mice (*4*–*7*). After direct intravenous tail vein injection, however, CTCs that are trapped in the lung fail to generate metastatic tumors for up to 6 months, in contrast to standard human breast cancer cell lines such as MDA-MB-231-LM2 (Fig. 1A).

The absence of blood-borne lung metastasis by patient-derived, tumorigenic breast cancer cells provides an experimental system by which to identify genes in CTCs that promote metastases. We therefore conducted a genome-wide CRISPR activation (CRISPRa) screen using the synergistic activation mediator system; this system combines modified single guide RNAs (sgRNAs) and a catalytically inactive Cas9 (dCas9) to localize protein transactivators to the promoter of a target gene, resulting in gene-specific transcriptional activation (*8*). The screen included 70,290 sgRNAs, covering all 23,430 human coding isoforms in the RefSeq database. Two different patient-derived breast cancer CTC lines (Brx-82 and Brx-142) were each infected with the lentiviral library of sgRNAs and injected into mice via the tail vein (Fig. 1B). Two months after tail vein injection, the mice were euthanized, and, because of the low background of metastatic burden in the lungs in this model, bulk lung tissue from each mouse was sequenced

[1]Massachusetts General Hospital Cancer Center, Harvard Medical School, Charlestown, MA 02129, USA. [2]Department of Medicine, Massachusetts General Hospital, Harvard Medical School, Boston, MA 02114, USA. [3]Center for Bioengineering in Medicine, Massachusetts General Hospital, Harvard Medical School, Boston, MA 02114, USA. [4]Shriners Hospital for Children, Boston, MA 02114, USA. [5]Department of Surgery, Massachusetts General Hospital, Harvard Medical School, Boston, MA 02114, USA. [6]Howard Hughes Medical Institute, Harvard Medical School, Boston, MA 02114, USA. *Present address: Department of Biomedicine, Cancer Metastasis Lab, University of Basel and University Hospital Basel, Basel, Switzerland. †Present address: Oncology Biotherapeutics at Novartis Institutes for BioMedical Research, Cambridge, MA 02139, USA. **‡Corresponding author. Email: dhaber@mgh.harvard.edu (D.A.H.); maheswaran@helix.mgh.harvard.edu (S.M.)**

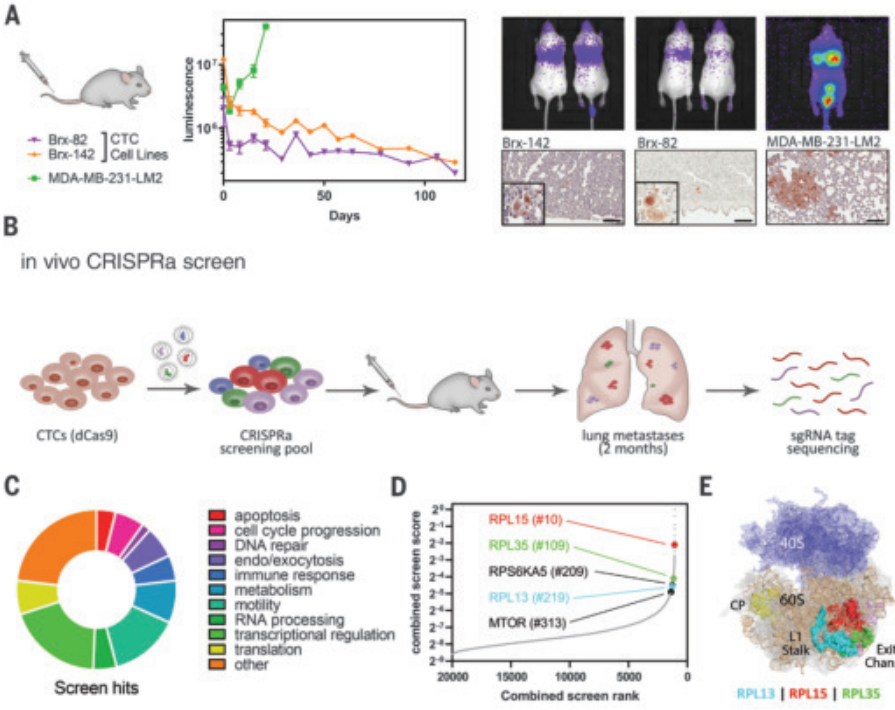

Fig. 1. In vivo genome-wide CRISPR activation screen. (**A**) (Left) Whole-body bioluminescence monitoring of NSG mice injected via tail vein with green fluorescent protein (GFP)–luciferase tagged CTC lines or MDA-MB-231-LM2 cells (n = 3 mice per cell line). (Right) Representative images of the bioluminescent signal at day 22 and corresponding lung histologic sections stained with anti-GFP to identify tumor cells. Insets indicate micrometastases. Scale bars, 100 μm. (**B**) Diagram of in vivo CRISPR activation (CRISPRa) screening in CTCs. (**C**) Classification of known functions of the top 250 genes identified in the combined screen ranking. (**D**) Distribution of combined screen scores, demonstrating that only the top few hundred genes are enriched. The top genes related to translation are indicated. (**E**) Crystal structure of the large and small subunits of the eukaryotic ribosome (*11*), highlighting the locations of RPL13, RPL15, and RPL35, as well as direct RPL13:RPL35 and RPL15:RPL35 interactions. Ribosome structural features indicated include the central protuberance (CP), exit channel, and L1 stalk.

to identify enriched sgRNAs. Most sgRNAs exhibited reduced or no representation, whereas a small set showed significant enrichment compared with the input baseline (data S1). Genes were scored using an algorithm to calculate the level of enrichment of corresponding sgRNAs in the two independent breast CTC lines, allowing for the identification of genes that are broadly capable of enhancing metastatic potential.

Many of the highest-scoring genes were established oncogenes or genes involved in processes critical to cancer progression—including transcriptional and translational regulation, cellular motility, and cell cycle progression (Fig. 1C)—thus supporting the validity of the screen. Among the protein synthesis–related hits were *MTOR* and *RPS6KA5* and several structural components of the large subunit of the ribosome—*RPL15* (*eL15*), *RPL35* (*uL29*), and *RPL13* (*eL13*) [revised ribosomal protein nomenclature (*9*)]—with *RPL15* ranking 10th across the entire genome (Fig. 1D). These three structural ribosomal proteins (RPs) cluster on the solvent-exposed surface near the exit tunnel on the back of the 60*S* ribosome, and they physically interact with each other (*10*, *11*) (Fig. 1E and fig. S1). Given their unexpected link to metastasis, we chose these RPs for further study.

To exclude sgRNA- or CRISPR-specific effects, we first validated the effects of RP expression on metastasis using a cytomegalovirus promoter–driven, lentiviral-encoded vector to ectopically express these proteins in CTCs, followed by tail vein injection of the cells (fig. S2). Threefold ectopic expression of RPL15 in a cultured CTC line (RPL15-CTCs) markedly increased metastatic burden in mice, as determined by total body bioluminescence (Fig. 2A). Consistent with its lower sgRNA enrichment, RPL35 also increased metastatic burden, but to a lesser extent than RPL15. By contrast, RPL8 (uL2), which was not a top hit in our screen, did not increase metastatic burden, indicating that the prometastatic phenotype is not a general property of all RPs. Histological analysis of the lungs from RPL15-CTC–inoculated mice showed an increase in the number of metastatic lesions, with a strong shift from single cells to multicellular foci (P = 0.0299) (Fig. 2, B and C). Mice injected with RPL15-CTCs also developed massive ovarian metastases, compared with small nodular ovarian lesions in control animals (Fig. 2B). A similar increase in the number and size of metastatic lesions was observed in mice injected with RPL35-CTCs (fig. S3). The increased tumor burden correlated with increased proliferation (as indicated by the presence of Ki-67) rather than reduced apoptosis (as denoted by cleaved caspase-3) (Fig. 2D and fig. S4). To extend these observations beyond direct intravascular inoculation of CTCs, we tested the effect of RPL15 overexpression after orthotopic tumor formation in the mammary fat pad. RPL15-CTCs generated primary tumors of similar size to control lesions, but their spontaneous lung metastases were markedly increased in number (average 8.2-fold increase in the number of metastatic foci, P = 0.0088), consistent with strongly enhanced metastatic potential (Fig. 2, E and F). Together, these findings establish RPL15 as a potent positive regulator of in vivo metastatic potential in breast cancer CTCs.

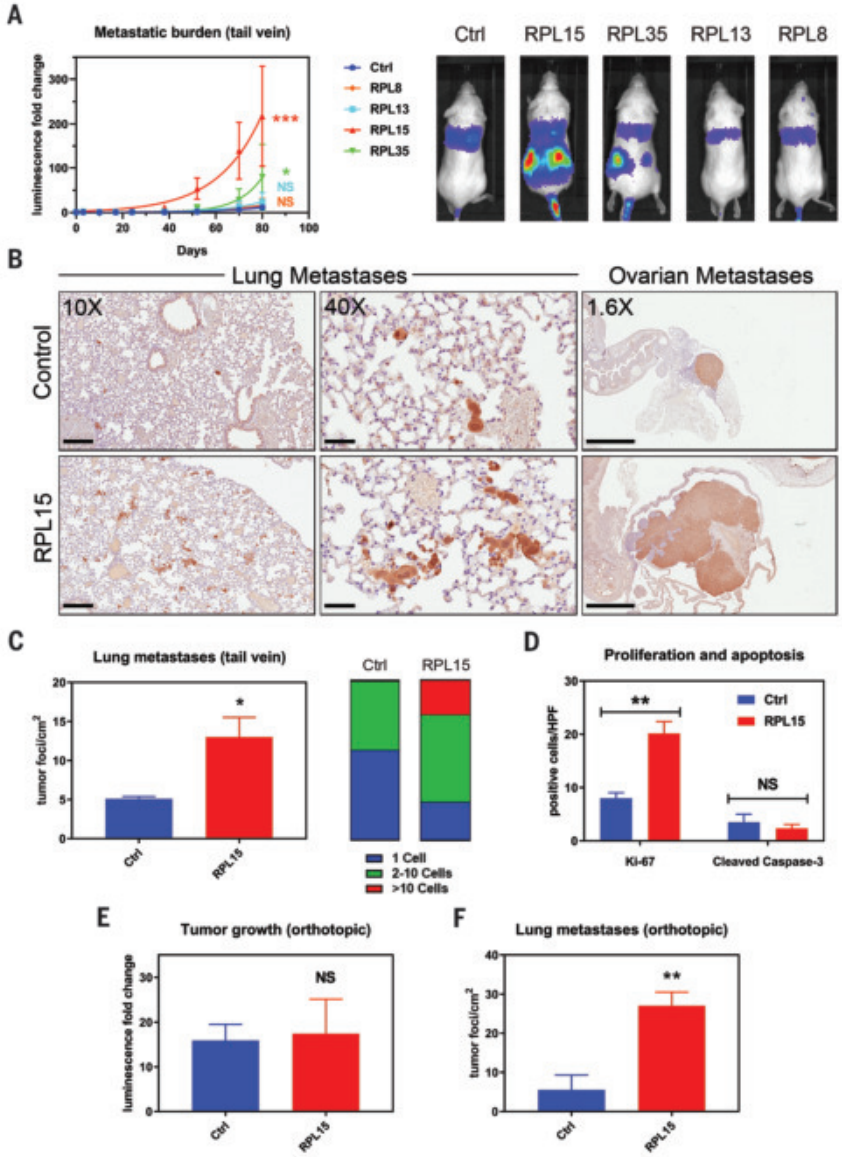

Fig. 2. Validation of prometastatic effect of RPL15 overexpression. (**A**) (Left) Whole-body luminescence monitoring of NSG mice injected via tail vein with CTCs overexpressing RPL8, RPL13, RPL15, or RPL35 (n = 4 mice per group). Curve was fit by the least squares method. P values were calculated by the extra sum-of-squares F test. (Right) Representative images of the bioluminescent signal 1 month after injection. (**B**) Representative sections of lung (left and middle) and ovarian (right) histology after staining with anti-GFP (brown) and counterstaining with hematoxylin. Average long-axis diameter of ovarian metastases in mice injected with RPL15-CTCs versus control: 9.1 mm versus 2.4 mm. Scale bars, 200 μm (left); 50 μm (middle); 2 mm (right). (**C**) Quantitation of the number and size of tumor foci per square centimeter identified by anti-GFP staining of lung histologic sections from mice injected with RPL15-CTCs or control. (**D**) Quantitation of the number of cells positive for Ki-67 or cleaved caspase-3 per high-powered field (HPF) by immunohistochemical staining of ovarian histologic sections. (**E**) Fold change in tumor bioluminescence after mammary fat pad injections of RPL15-CTCs or control at the terminal time point of day 78 (n = 4 mice per group, 2 tumors per mouse). (**F**) Quantitation of the number of tumor foci per square centimeter identified by anti-GFP staining of lung histologic sections from mice after orthotopic injection of RPL15-CTCs or control. Error bars represent SEM. P values were calculated by two-tailed unpaired Student's t test. ***P < 0.001; **P < 0.01; *P < 0.05; NS: P > 0.05.

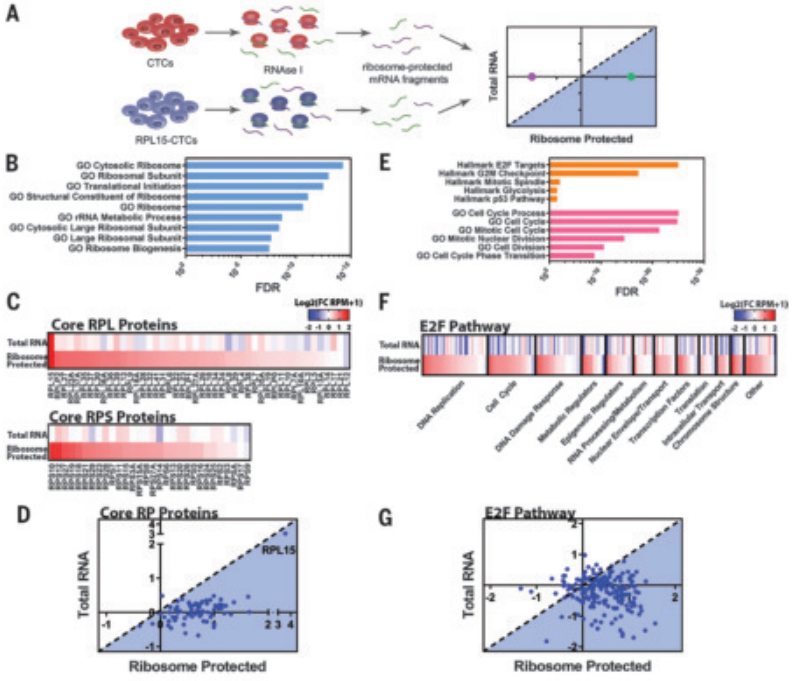

Fig. 3. RPL15 overexpression promotes translation of core RPs and E2F pathway proteins. (**A**) Schema illustrating ribosome profiling of control CTCs or RPL15-CTCs. (**B**) GSEA of transcripts preferentially bound by ribosomes in RPL15-CTCs. The most-enriched ribosomal and translational GO gene sets and associated FDR values are shown. (**C**) Heat map representing the fold change of RPL15-CTCs relative to control for each RP gene for total RNA-seq and ribosome profiling. (**D**) Scatter plot representing the translational efficiency of individual RP gene transcripts. The *y* axis represents the $\log_2$(fold change in RNA-seq), and the *x* axis represents the $\log_2$(fold change in ribosome profiling). The shaded region represents transcripts that have increased translational efficiency relative to the level of the transcript. (**E**) GSEA of transcripts preferentially bound by ribosomes in RPL15-CTCs. The most-enriched "hallmarks of cancer" gene sets from the Broad Molecular Signatures Database, the most-enriched cell cycle–related Gene Ontology (GO) gene sets, and the associated FDR values are shown. (**F**) Heat map representing fold change of RPL15-CTCs relative to control for each gene within the Hallmark_E2F_Targets gene set for total RNA-seq and ribosome profiling. Genes were categorized according to their function and ordered on the basis of fold change in the ribosome profiling. (**G**) Scatter plot representing the translational efficiency of individual transcripts within the Hallmark_E2F_Targets gene set. The *y* axis represents the $\log_2$(fold change in RNA-seq), and the *x* axis represents the $\log_2$(fold change in ribosome profiling). The shaded region represents transcripts that have increased translational efficiency relative to the level of the transcript. Ribosome profiling was performed in duplicate.

As components of large and complex structures, RPs are reported to have highly coordinated expression to ensure the fidelity of ribosome subunit biogenesis and assembly (*12*). Altered expression of an individual component, such as RPL15, may alter ribosome translational efficiency, either globally or for specific subsets of mRNAs (*13*). We performed ribosomal profiling in control and RPL15-CTCs to determine the global ribosome occupancy of mRNA transcripts, identify changes in translational preference, and calculate the translational efficiency for any given transcript (ratio of ribosome-bound mRNA to total mRNA) (*14*) (Fig. 3A and fig. S5). Consistent with ectopic expression, RPL15-CTCs showed an 8-fold increase in total *RPL15* transcripts and a 12-fold increase in ribosome-protected *RPL15* transcripts. In total, 183 genes were significantly enriched for ribosome-protected fragments in RPL15-CTCs, whereas 250 genes were significantly depleted [fold change > 2.0; false discovery rate (FDR) < 0.05]. Gene set enrichment analysis (GSEA) of these ribosome-protected transcripts identified other RP genes and regulators of translation as the most highly enriched ribosome-protected signatures in RPL15-CTCs (Fig. 3B). Virtually all 76 core RPs, from both the large and small subunits, were markedly increased (mean 1.6-fold) among the ribosome-protected transcripts (Fig. 3C), suggesting that overexpression of RPL15 leads to coordinated translational up-regulation of the core RPs (Fig. 3D). Although a conserved 5′ untranslated region element in the RP genes is known to drive the stoichiometric coordination of RPs (*15*, *16*), the ability of a single RP to drive translation of all other RPs is unexpected. To validate these ribosome-protection experiments, we conducted polysome profiling and found that, compared with control CTCs, RPL15-CTCs had an increased proportion of RP transcripts within the polysome fractions (fig. S6A). Polysome profiling also identified a significant increase in the global polysome-to-monosome ratio in RPL15-CTCs (fig. S6, B and C), indicating a global enhancement in the proportion of ribosomes found within polysomes, in addition to the specific enrichment for RP transcripts. Indeed, RPL15-CTCs had increased total RNA, a reflection of increased ribosomal RNA (rRNA) content, which accounts for the majority of cellular RNA (*17*) (fig. S7A). Finally, RPL15-CTCs had increased global translational activity, as measured by *O*-propargyl-puromycin and L-azidohomoalanine incorporation, two orthogonal measures of total cellular translation (fig. S7, B and C).

In addition to the RP genes, GSEA of ribosome-protected transcripts from RPL15-CTCs identified cell proliferation pathways, including downstream targets of the transcription factor E2F, as highly enriched among ribosome-protected signatures (Fig. 3E). The absence of E2F pathway enrichment by total cellular RNA sequencing (RNA-seq) confirmed that up-regulation of this proliferative program represents increased translational efficiency (Fig. 3, F to G). Quantitative proteomic analysis of E2F targets identified a positive correlation between ribosomal occupancy of E2F target mRNAs and protein level, confirming a functional effect of increased translational efficiency induced by RPL15 (fig. S8). The RPL15-induced proliferative signature is not correlated with increased *ERBB2* expression and therefore is independent of the previously reported heterogeneity of HER2 protein expression in breast CTCs (*7*). Together, these findings demonstrate that overexpression of the ribosomal structural protein RPL15 augments global protein translation, with a selectively enhanced impact on translation of transcripts encoding other RPs and proliferation programs.

The CTC-iChip microfluidic device (*4*) enables isolation of rare, viable CTCs directly from whole-blood specimens of patients with cancer, with RNA quality compatible with single-cell RNA-seq (*18*–*20*). We examined RNA-seq profiles of 135 freshly isolated single CTCs or CTC clusters from 45 patients with HR+ metastatic breast cancer: Unsupervised clustering based on the 2000 most variant genes revealed a subset of CTCs with substantially increased expression of multiple RP genes (Fig. 4A). GSEA of the genes driving this subset clustering demonstrated highly significant enrichment for RP genes and genes involved with translational regulation (FDR from 10^{-25} to 10^{-35}) (Fig. 4A). Supervised clustering of CTCs

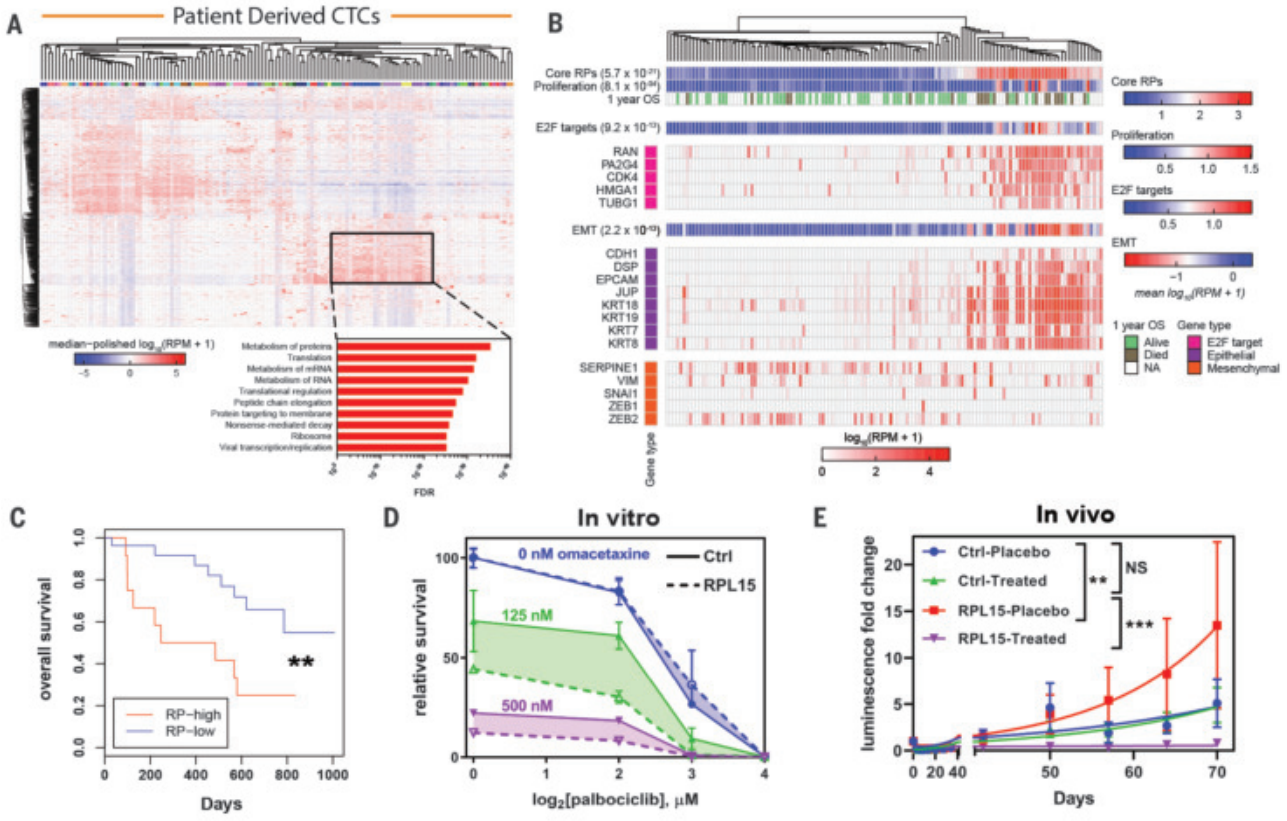

Fig. 4. Heterogeneity of RP expression in primary patient CTCs correlates with worse clinical outcome and sensitivity to translational and cell cycle inhibition. (**A**) (Top) RNA-seq from CTCs enriched from whole blood with the iChip microfluidic device and isolated as single cells or clusters. Expression values represent $\log_{10}$(RPM+1), and the dataset was median polished. RPM, reads per million. The dendrogram represents unsupervised clustering of the 2000 most-variant genes within the dataset. The color bar identifies individual patients. The highlighted box represents a subset of CTCs with coordinately expressed RP genes. (Bottom) GSEA for KEGG (Kyoto Encyclopedia of Genes and Genomes) and Reactome gene sets of the genes found in the highlighted box. (**B**) Heat map of the expression level of selected E2F target genes, epithelial markers, and mesenchymal markers. The dendrogram represents supervised clustering of the CTC samples on the basis of RP gene expression. The OS bar indicates whether patients were alive 1 year after CTC sample collection. The color bar illustrates metagene analysis of core RPs, a proliferation signature, E2F targets, and an EMT signature and associated *P* values. (**C**) Kaplan-Meier analysis of the overall survival for patients with high average RP gene expression versus those with low average RP gene expression. The RP-high and RP-low subgroups were determined on the basis of average RP gene expression for each patient blood draw. The *P* value was calculated by the log rank test. (**D**) Dose–response curves for RPL15-CTCs and control treated with increasing doses of palbociclib and omacetaxine. Shaded regions represent the difference between RPL15-CTCs and control across tested concentrations of palbociclib. (**E**) Whole-body luminescence monitoring of NSG mice after intracardiac injection with RPL15-CTCs or control and treatment with placebo or a combination of palbociclib and omacetaxine (n = 4 or 5 mice per condition). Error bars represent SEM. Curves were fit by the least squares method. *P* values were calculated by the extra sum-of-squares *F* test. ***$P < 0.001$; **$P < 0.01$; NS: $P > 0.05$.

based on expression of RP genes confirmed coordinate expression of the core RPs, allowing division of the clinical dataset into CTCs with RP-high (33% of all patient-derived CTCs) and RP-low gene expression (67%) (fig. S9). RP-high versus RP-low expression in patient-derived CTCs was again highly correlated with expression of E2F targets ($P = 9.2 \times 10^{-13}$) and a proliferation signature ($P = 8.1 \times 10^{-4}$) (*21*) (Fig. 4B and fig. S10). To validate these findings, we investigated a second, independent cohort of single-cell RNA-seq data that we had previously derived from 109 CTCs individually isolated from 33 patients with metastatic breast cancer (*7*). As in our first cohort, expression of RP genes clearly identified a distinct RP-high CTC subset (44% of all CTCs) and an RP-low CTC subset (56%), with high RP expression again correlated with E2F target gene expression ($P = 9.4 \times 10^{-13}$) (figs. S11 and S12).

Primary CTCs exhibit heterogeneous expression of epithelial and mesenchymal markers (*22*); among these cells, the RP-high subset had significantly increased epithelial markers and decreased mesenchymal markers (Fig. 4B). To explore the link between epithelial-to-mesenchymal transition (EMT) and protein translation, we assessed translational changes in the canonical EMT model of transforming growth factor–β (TGF-β) treatment in MCF10A breast epithelial cells (*23*). EMT induction by TGF-β in these cells suppressed global translational activity and rRNA expression (fig. S13, A to B). Polysome profiling revealed depletion in gene sets related to RPs and translation (fig. S13C). The coordinated and pronounced suppression in translation of RP transcripts (89% of RPs translationally down-regulated, median down-regulation of 1.25-fold) was accompanied by a smaller decrease in total RP mRNA content (76% of RPs transcriptionally down-regulated, median down-regulation of 1.06-fold), suggesting that EMT primarily mediates translational down-regulation of RPs (fig. S13, D to E). Thus, in cancer cells circulating in the blood, persistent epithelial cell fate is associated with higher protein translation and proliferative potential.

Clinical outcome data were available for the first cohort of patients, making it possible to investigate CTC single-cell RNA-seq data for markers correlated with patient survival (data S2). Using a Cox proportional hazards model, we identified 765 genes associated with worse

overall survival (OS) [hazard ratio (HR): 1.25, FDR: 0.25] (fig. S14A). These genes overlapped significantly with genes associated with adverse outcomes in multiple published datasets (table S1). GSEA of these adverse outcome genes revealed highly significant enrichment of protein synthesis pathways and of the RPs themselves (e.g., FDR = 3.98×10^{-72} for Reactome: Translation) (fig. S14, B and C). High mean expression of all RP genes was associated with significantly worse OS (HR: 3.4, $P = 0.0078$) (Fig. 4C), as was elevated expression of *RPL15* itself (HR: 3.4, $P = 0.011$) (fig. S15). Consistent with the contribution of RPL15 to cellular heterogeneity in advanced metastatic phenotypes, this correlation was less evident within bulk primary breast cancer tissues, although in one dataset (*24*), high RP expression was correlated with reduced progression-free survival [RPL (large subunit): HR: 1.34, $P = 0.00023$; RPS (small subunit): HR: 1.34, $P = 0.00057$] (fig. S16).

The enhancement of tumorigenesis by eukaryotic initiation factors (eIFs) and other functional regulators of translation (*12*, *25*–*28*) has led to the suggestion that targeting the translational machinery may be selectively toxic to malignant cells (*29*, *30*). The translational inhibitor omacetaxine, approved by the U.S. Food and Drug Administration, prevents the initial elongation step of protein synthesis by occupying the A-site cleft and preventing proper aminoacyl-tRNA positioning (*31*, *32*). We found that omacetaxine inhibited global translation in breast cancer CTCs (fig. S17A). In combination with the CDK4/6 inhibitor palbociclib, which suppresses cell cycle progression and is used in breast cancer treatment (*33*), omacetaxine showed significantly increased efficacy against RPL15-CTCs compared with parental CTCs in vitro (Fig. 4D and fig. S17B). To extend these results to an in vivo mouse model, we used intracardiac injections to maximize mouse metastatic burden. In this model, omacetaxine-palbociclib treatment showed markedly increased efficacy against metastases derived from RPL15-CTCs compared with those from parental CTCs (Fig. 4E). These early results suggest that simultaneous therapeutic targeting of the cell translational machinery and cell proliferation pathways may merit investigation as a method to suppress an aggressive subset of CTCs that are characterized by high expression of RP genes.

On the basis of two convergent lines of evidence—an in vivo CRISPRa screen for prometastatic genes in a mouse model and unsupervised clustering of single-cell RNA-seq from human breast cancer CTCs—we propose a model whereby the epithelial state mediates translational up-regulation of RPs and regulators of cellular proliferation, thus contributing to the metastatic propensity of CTCs. The direct role of structural RPs in this phenotype extends the previously established contributions of mTOR and MAPK oncogenic signaling pathways (*34*, *35*); translation initiation factors eIF4A, eIF4E, and eIF4G (*26*, *27*, *36*, *37*); and specific tRNA pools (*38*). In vivo genome-wide CRISPRa screening for a complex phenotype is unlikely to be saturating for all genes that modulate protein translation, but the identification of hits in structural RP genes points to a previously unappreciated regulatory role of these genes.

Enlarged nucleoli, resulting from aberrant ribosomal biosynthesis, were first observed in cancer cells more than 100 years ago (*39*), and germline mutations in RP genes, including *RPL15*, cause the cancer-associated ribosomopathy Diamond-Blackfan anemia (DBA) (*40*). Increased expression of some RPs has been reported in tumor specimens (*41*–*43*), although its importance has been unclear. In addition to demonstrating the functional effects of RP expression on metastasis, our observation that RPL15 overexpression increases ribosomal content and global translation has mechanistic implications. Ribosome biogenesis is a highly coordinated process between rRNAs, RPs, and assembly factors, with RPs implicated as critical platforms for ribosome assembly (*44*). In yeast, both Rpl15 and Rpl35 are recruited by ribosome assembly factors (including Nop4, Nop7, and Erb1) to establish a large-subunit assembly platform, and both also bind rRNA at key domain interfaces during pre-60*S* assembly (*45*, *46*), suggesting that Rpl15 and Rpl35 may be rate limiting for large-subunit formation. Notably, in both yeast and a model of DBA, altered ribosome concentrations lead to transcript-specific differences in translational efficiency (*13*, *47*). Although our data point to a RPL15-dependent increase in total ribosomal content, we cannot exclude the possibility of RPL15-specific effects leading to altered ribosome composition or extraribosomal RP functions (*48*, *49*).

Finally, although mesenchymal cell states are associated with cancer cell migration, proliferative potential is correlated with epithelial phenotypes and the mesenchymal-to-epithelial transition (MET) (*50*). Our work suggests that the increased ribosomal content in epithelial cell fates may contribute to their enhanced metastatic potential. The identification of a well-demarcated subset of breast cancer CTCs defined by high ribosomal content and conferring an adverse prognosis raises the possibility of pharmacologic targeting of metastatic-competent cancer cells.

REFERENCES AND NOTES

1. R. R. Gomis, S. Gawrzak, *Mol. Oncol.* **11**, 62–78 (2017).
2. D. S. Micalizzi, S. Maheswaran, D. A. Haber, *Genes Dev.* **31**, 1827–1840 (2017).
3. H. Pan *et al.*, *N. Engl. J. Med.* **377**, 1836–1846 (2017).
4. E. Ozkumur *et al.*, *Sci. Transl. Med.* **5**, 179ra47 (2013).
5. N. M. Karabacak *et al.*, *Nat. Protoc.* **9**, 694–710 (2014).
6. M. Yu *et al.*, *Science* **345**, 216–220 (2014).
7. N. V. Jordan *et al.*, *Nature* **537**, 102–106 (2016).
8. S. Konermann *et al.*, *Nature* **517**, 583–588 (2015).
9. N. Ban *et al.*, *Curr. Opin. Struct. Biol.* **24**, 165–169 (2014).
10. S. Klinge, F. Voigts-Hoffmann, M. Leibundgut, N. Ban, *Trends Biochem. Sci.* **37**, 189–198 (2012).
11. A. Ben-Shem *et al.*, *Science* **334**, 1524–1529 (2011).
12. J. Pelletier, G. Thomas, S. Volarević, *Nat. Rev. Cancer* **18**, 51–63 (2018).
13. Z. Cheng *et al.*, *Mol. Cell* **73**, 36–47.e10 (2019).
14. N. T. Ingolia, G. A. Brar, S. Rouskin, A. M. McGeachy, J. S. Weissman, *Nat. Protoc.* **7**, 1534–1550 (2012).
15. S. Robledo *et al.*, *RNA* **14**, 1918–1929 (2008).
16. R. Yamashita *et al.*, *Nucleic Acids Res.* **36**, 3707–3715 (2008).
17. M. Scott, C. W. Gunderson, E. M. Mateescu, Z. Zhang, T. Hwa, *Science* **330**, 1099–1102 (2010).
18. D. T. Ting *et al.*, *Cell Rep.* **8**, 1905–1918 (2014).
19. N. Aceto *et al.*, *Cell* **158**, 1110–1122 (2014).
20. D. T. Miyamoto *et al.*, *Science* **349**, 1351–1356 (2015).
21. M. L. Whitfield *et al.*, *Mol. Biol. Cell* **13**, 1977–2000 (2002).
22. M. Yu *et al.*, *Science* **339**, 580–584 (2013).
23. Y. Arima *et al.*, *Cancer Res.* **68**, 5104–5112 (2008).
24. Z. Mihály *et al.*, *Breast Cancer Res. Treat.* **140**, 219–232 (2013).
25. N. Robichaud, N. Sonenberg, D. Ruggero, R. J. Schneider, *Cold Spring Harb. Perspect. Biol.* **11**, a032896 (2019).
26. N. Robichaud *et al.*, *Oncogene* **34**, 2032–2042 (2015).
27. N. Robichaud *et al.*, *Proc. Natl. Acad. Sci. U.S.A.* **115**, E2202–E2209 (2018).
28. E. Petroulakis *et al.*, *Cancer Cell* **16**, 439–446 (2009).
29. M. Bhat *et al.*, *Nat. Rev. Drug Discov.* **14**, 261–278 (2015).
30. J. R. Devlin *et al.*, *Cancer Discov.* **6**, 59–70 (2016).
31. Y. Rosshandler, A. Q. Shen, J. Cortes, H. J. Khoury, *Expert Rev. Hematol.* **9**, 419–424 (2016).
32. G. Gürel, G. Blaha, P. B. Moore, T. A. Steitz, *J. Mol. Biol.* **389**, 146–156 (2009).
33. N. C. Turner *et al.*, *N. Engl. J. Med.* **373**, 209–219 (2015).
34. Y. Mamane, E. Petroulakis, O. LeBacquer, N. Sonenberg, *Oncogene* **25**, 6416–6422 (2006).
35. I. Topisirovic, N. Sonenberg, *Cold Spring Harb. Symp. Quant. Biol.* **76**, 355–367 (2011).
36. A. Lazaris-Karatzas, K. S. Montine, N. Sonenberg, *Nature* **345**, 544–547 (1990).
37. S. Avdulov *et al.*, *Cancer Cell* **5**, 553–563 (2004).
38. H. Gingold *et al.*, *Cell* **158**, 1281–1292 (2014).
39. G. Pianese, *Beitr. Pathol. Anat. Allgem. Pathol.* **142**, 1–193 (1896).
40. E. W. Mills, R. Green, *Science* **358**, eaan2755 (2017).
41. A. de Las Heras-Rubio, L. Perucho, R. Paciucci, J. Vilardell, M. E. Lleonart, *Cancer Metastasis Rev.* **33**, 115–141 (2014).
42. H. Wang *et al.*, *BMC Cancer* **6**, 91 (2006).
43. Q. Wang *et al.*, *Gene* **263**, 205–209 (2001).
44. C. Peña, E. Hurt, V. G. Panse, *Nat. Struct. Mol. Biol.* **24**, 689–699 (2017).
45. S. Granneman, E. Petfalski, D. Tollervey, *EMBO J.* **30**, 4006–4019 (2011).
46. Z. A. Sanghai *et al.*, *Nature* **556**, 126–129 (2018).
47. R. K. Khajuria *et al.*, *Cell* **173**, 90–103.e19 (2018).
48. Z. Shi *et al.*, *Mol. Cell* **67**, 71–83.e7 (2017).
49. J. R. Warner, K. B. McIntosh, *Mol. Cell* **34**, 3–11 (2009).
50. N. P. Gunasinghe, A. Wells, E. W. Thompson, H. J. Hugo, *Cancer Metastasis Rev.* **31**, 469–478 (2012).

ACKNOWLEDGMENTS

We are grateful to all of the patients who participated in this study. We thank W. Wu for artistic support in the creation of figures; L. Libby for technical support; and C. Van Rechem for technical assistance. **Funding:** This work was supported by NIH grant 2R01CA129933, the Breast Cancer Research Foundation, the Howard Hughes Medical Institute, and the National Foundation for Cancer Research (D.A.H.); NIH Quantum Grant 2U01EB012493 (M.T. and D.A.H.); NIH grant U01CA214297 (M.T., D.A.H., and S.M.); ESSCO Breast Cancer Research (S.M.); NCI grant K12CA087723 and Susan G. Komen Foundation grant CCR15224703 (A.B.); NIH grant T32GM007753 (R.Y.E. and M.K.); NIH grant 1F30CA232407-01 (R.Y.E.); NIH grant 1F30CA224588-01 (M.K.); NIGMS grant R01GM100202 (S.V.); NIH grant T32CA009361 and Susan G. Komen Foundation grant PDF16376429 (N.V.-J.); and American Cancer Society grant 132140-PF-18-127-01-CSM and an ASCO Young Investigator Award (D.S.M.).

Author contributions: R.Y.E., D.S.M., D.A.H., and S.M. conceived the project and provided project leadership. S.Lee, S.T., and S.V. provided ribosome and polysome profiling support. B.S.W., B.C., B.W., and M.K. performed bioinformatics analyses. K.L.N., B.T.N., D.F.W., S.Li, A.M., and V.C. assisted with molecular biology and animal experiments. A.B. enrolled patients and provided clinical guidance. N.A. and N.V.-J. collected and processed clinical samples. A.S. and D.T.T. provided RNA-seq support. J.K. and W.H. provided proteomics support. M.T. collaboratively developed the CTC-iChip isolation of viable CTCs. **Competing interests:** D.T.T., M.T., D.A.H., and S.M. are founders of and own equity in TellBio, Inc., which is involved with CTC therapeutics and diagnostics. At this time, there has been no funding received or license given to TellBio, Inc., for this work. D.T.T. is also a founder of and owns equity in ROME Therapeutics and PanTher Therapeutics, which are not related to this work. D.T.T. has received consulting fees from Merrimack Pharmaceuticals; Ventana Roche; Foundation Medicine, Inc.; and EMD Millipore Sigma, which are not related to this work. D.T.T.'s interests were reviewed and are managed by Massachusetts General Hospital and Partners HealthCare in accordance with their conflict-of-interest policies. A.B. is a paid consultant and/or serves on the scientific advisory boards of Diiachi/Astra Zeneca, Eli Lilly, Genentech/Roche, Immunomedics, Merck, Novartis, Pfizer, Phillips, PUMA, Radius Health, Sanofi, and Takeda. The other authors declare no competing interests. **Data and materials availability:** Raw data from RNA-seq of primary human breast cancer CTCs and ribosome profiling of RPL15-CTCs and microarray data from polysome profiling of TGF-β–treated MCF10A cells have been deposited in the Gene Expression Omnibus (GEO) database under accession number GSE143626. All other data and materials are available from the corresponding author upon request.

SUPPLEMENTARY MATERIALS

science. /content/367/6485/1468/suppl/DC1 Materials and Methods
Figs. S1 to S17
Table S1
References (*51*–*63*)
Data S1 and S2

21 May 2019; resubmitted 1 December 2019
Accepted 26 January 2020
Published online 6 February 2020
10.1126/science.aay0939

GLASSES

Ultrahigh-field ^{67}Zn NMR reveals short-range disorder in zeolitic imidazolate framework glasses

Rasmus S. K. Madsen[1]*, Ang Qiao[1]*, Jishnu Sen[2], Ivan Hung[3], Kuizhi Chen[3], Zhehong Gan[3], Sabyasachi Sen[2]†, Yuanzheng Yue[1,4,5]†

The structure of melt-quenched zeolitic imidazole framework (ZIF) glasses can provide insights into their glass-formation mechanism. We directly detected short-range disorder in ZIF glasses using ultrahigh-field zinc-67 solid-state nuclear magnetic resonance spectroscopy. Two distinct Zn sites characteristic of the parent crystals transformed upon melting into a single tetrahedral site with a broad distribution of structural parameters. Moreover, the ligand chemistry in ZIFs appeared to have no controlling effect on the short-range disorder, although the former affected their phase-transition behavior. These findings reveal structure-property relations and could help design metal-organic framework glasses.

Glasses can be obtained through a variety of synthesis and processing routes (*1*, *2*), but rapid cooling of the liquids remains the predominant approach. Melt-quenched (MQ) glasses can be broadly classified as inorganic, organic, and metallic and containing ionic-covalent, covalent, and metallic bonds, respectively. Recently, a fourth family of MQ glasses based on metal-organic frameworks (MOFs) have been reported that have coordination bonds (*3*–*7*). The MQ-MOF glasses are primarily represented by the subset of MOFs called the zeolitic imidazolate frameworks (ZIFs). Their extended tetrahedral network is analogous to silica and zeolites (*8*): Metal ion nodes (such as Zn^{2+} and Co^{2+}) substitute for silicon, and imidazole ($C_3N_2H_3$)–based ligands substitute for oxygen as the bridging unit. A number of ZIF glasses have porosity, which has potential applications in gas capture and storage, and ZIF-62 glass exhibits high transparency and broad mid-infrared luminescence, which have potential photonic applications (*7*, *9*–*13*).

Recent studies have found ZIF-4 ($Zn[Im]_2$) and ZIF-62 ($Zn[Im_{2-x}bIm_x]$)—where Im and bIm are imidazole and benzimidazole, respectively—to be rather stable against crystallization during heat treatment, and that the parent liquids have a higher glass-forming ability compared with most of the network glass-forming liquids (*14*, *15*). The glass-forming ability of ZIF-62 is greater than that of ZIF-4 because its mixed linkers, consisting of imidazole and benzimidazole in some tetrahedra, create greater steric hindrance (*14*). Previous studies explored the structural origin of this high glass-forming ability in both ZIF systems using systematic heat treatments, differential scanning calorimetry (DSC), and x-ray pair distribution function (PDF) analyses (*3*, *14*, *15*). The PDF analyses provided no clear evidence of the appearance of any medium- or long-range order in these glasses after a calorimetric scan, despite the appearance of an exothermic peak immediately before melting (*15*). The enthalpy release was attributed to the densification of the structural network, but the nature and the length scale of the structural changes associated with the decrease of the potential energy remain unclear to date. In addition, although ZIF-4 is chemically simpler than ZIF-62, the former exhibits several features in its temperature-induced phase transitions, including the transition from a low-density amorphous phase (LDA) to a high-density amorphous phase (HDA),

Table 1. ^{67}Zn NMR parameters. ^{67}Zn MAS NMR line shape simulation parameters for crystalline and glassy MOFs.

MOF	Lattice site*	δ_{iso} (ppm)	C_Q (±0.2 MHz)	η_Q (±0.05)	Relative fraction (±5%)
ZIF-4 crystal	Zn1	296	5.1	0.6	46
	Zn2	295	3.7	0.6	54
ZIF-62 crystal	Zn1	297	5.8	0.5	48
	Zn2	296	4.0	0.4	52
ZIF-zni crystal	Zn1	288	6.0	0.6	46
	Zn2	290	4.0	0.5	54
ZIF-4 glass	Zn	277	6.9†	N/A	100
ZIF-62 glass	Zn	278	6.5†	N/A	100
ZIF-62b glass	Zn	277	6.8†	N/A	100

*Lattice sites correspond to those designated in structural refinements of ZIF-4, ZIF-62, and ZIF-zni, as reported in (*8*, *28*, *29*). †These values represent the root mean square quadrupolar product $\sqrt{\langle C^2_{Qn}\rangle}$.

[1]Department of Chemistry and Bioscience, Aalborg University, 9220 Aalborg, Denmark. [2]Department of Materials Science and Engineering, University of California at Davis, Davis, CA 95616, USA. [3]National High Magnetic Field Laboratory, 1800 E. Paul Dirac Drive Tallahassee, FL 32310, USA. [4]State Key Laboratory of Silicate Materials for Architectures, Wuhan University of Technology, Wuhan 430070, China. [5]School of Materials Science and Engineering, Qilu University of Technology, Jinan 250353, China.
*These authors equally contributed equally to this work.
†Corresponding author. Email: yy@bio.aau.dk (Y.Y.); sbsen@ucdavis.edu (S.S.)

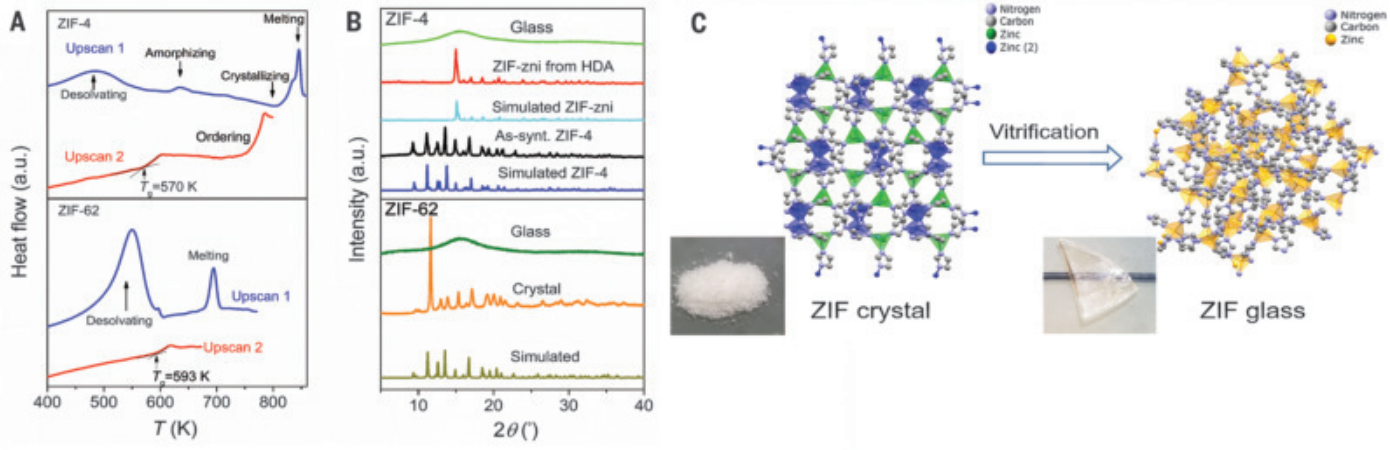

Fig. 1. Phase transitions, glass formation, and glass transition for ZIFs. (**A**) First and second DSC upscans for both (top) ZIF-4 and (bottom) ZIF-62. (**B**) XRD patterns of as-prepared ZIF-4 crystals, ZIF-zni crystals, ZIF-4 glass, ZIF-62 crystals, and ZIF-62 glass. (**C**) Schematic representation of the structural change from crystalline ZIF (powder sample) to its glassy state (transparent bulk sample) during melt-quenching.

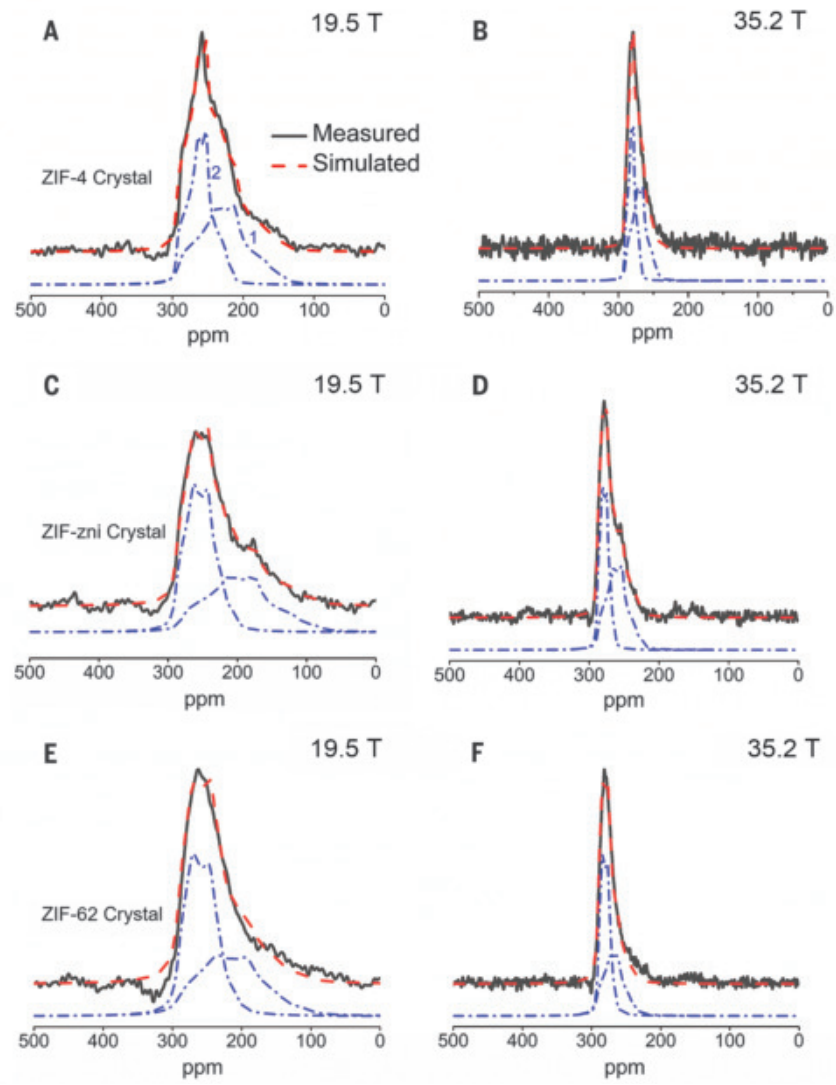

Fig. 2. Short-range order of crystalline ZIFs. (**A** to **F**) Experimental (solid black line) and simulated (dashed red line) ^{67}Zn MAS NMR spectra of [(A) and (B)] crystalline ZIF-4, [(C) and (D)] ZIF-zni, and [(E) and (F)] ZIF-62 collected at 19.5 and 35.2 T. Individual simulation components (dot-dashed blue lines) are vertically offset for clarity.

as well as the formation and melting of ZIF-zni (which is denser than ZIF-4).

The origin of these multiple transitions remains elusive given the limitations of the analytical techniques available for determining short- and intermediate-range structure in glasses. Raman spectroscopy, $^{13}C/^{1}H$ nuclear magnetic resonance (NMR) spectroscopy, along with x-ray PDFs have been used in the past to study the short-range and medium-range structure of ZIF glasses. Although these studies provided some structural information, no substantial structural difference in the short-range order between the ZIF crystals and corresponding glasses could be identified (*14*). Previous studies showed that the organic ligands in ZIFs remained intact during melt-quenching, implying that the chemical integrity was retained after glass formation (*3*, *5*, *14*). Molecular dynamics simulations indicated that upon melting, the imidazolate-based linkers dissociate and reassociate with Zn atoms through the scission and renewal of Zn–N coordination bonds (*14*, *16*). The Zn[ligand]$_4$ tetrahedral units remain intact in the ZIF glass state after the melt is quenched, and long-range structural disorder is believed to be primarily induced by the distortion of the Zn[ligand]$_4$ intertetrahedral connections (*14*, *16*).

By contrast, the short-range structural order at the scale of the Zn[ligand]$_4$ tetrahedra in MOF glasses remains unknown. Because ^{67}Zn is a quadrupolar nuclide, its NMR spectra can provide not only the information on the chemical shift that is characteristic of the tetrahedral environment of Zn in the ZIFs but also on the electric-field gradient (EFG) at the site of this nuclide in the structure, as encoded in its quadrupolar coupling constant C_Q and asymmetry parameter η_Q. The EFG is a second-rank tensor quantity sensitive to the degree of positional and orientational order at length scales corresponding to the nearest and next-nearest neighbor distances, and possibly to even longer distances (*17*).

Only a few ^{67}Zn NMR spectroscopic studies have been reported that analyzed crystalline structures in zinc-based compounds, including Zn-based crystalline MOFs (*18*–*23*), because the ^{67}Zn nuclide has a low gyromagnetic ratio, large quadrupole moment Q, as well as a low natural abundance (*18*). These issues, in combination with the low atomic density of MOFs, necessitated ^{67}Zn NMR spectral data collection at ultrahigh magnetic fields that are ~20 T or higher. We report a comparative structural study of select crystalline ZIFs and their glassy counterparts derived by means of melt-quenching, using ultrahigh-field ^{67}Zn magic-angle-spinning (MAS) NMR spectroscopy at 19.5 and 35.2 T at the National High Magnetic Field Laboratory.

The DSC traces of ZIF-4 and ZIF-62 samples (Fig. 1A) measured the temperature-driven enthalpic responses to the chemical reactions and phase transitions. During the first upscan (from 323 to 863 K), the as-synthesized ZIF-4 crystal underwent solvent release, amorphization, polymorphic transformation to ZIF-zni crystal, and last, melting. Subsequent quenching of the ZIF-zni melt resulted in the formation of a ZIF-4 glass with a glass transition temperature (T_g) of 570 K during the second upscan. By contrast, during upscan 1, the as-synthesized standard ZIF-62 crystal displays the enthalpy responses only to the solvent release and the subsequent melting. After melt-quenching, the second upscan of ZIF-62 glass showed a glass transition with a T_g of 593 K.

To explore the effect of the linker chemistry (the Im/bIm ratio) on the short-range structure, we prepared a ZIF-62 crystal with a higher bIm content (denoted as ZIF-62b) (table S1). Its x-ray diffraction (XRD) patterns confirmed that ZIF-62 and ZIF-62b had the same crystalline structure (fig. S2). The final chemical compositions of ZIF-62 and ZIF-62b were $Zn(Im)_{1.75}(bIm)_{0.25}$ and $Zn(Im)_{1.68}(bIm)_{0.32}$, as determined from ^{1}H liquid NMR measurements (fig. S3). Additionally, we prepared a ZIF-62b glass sample by melt-quenching, which was also subjected to two DSC scans. The increase of bIm in ZIF-62 framework led to an increase of both melting temperature (T_m) and T_g (fig. S4), which is consistent with a previous study (*14*). The XRD patterns of

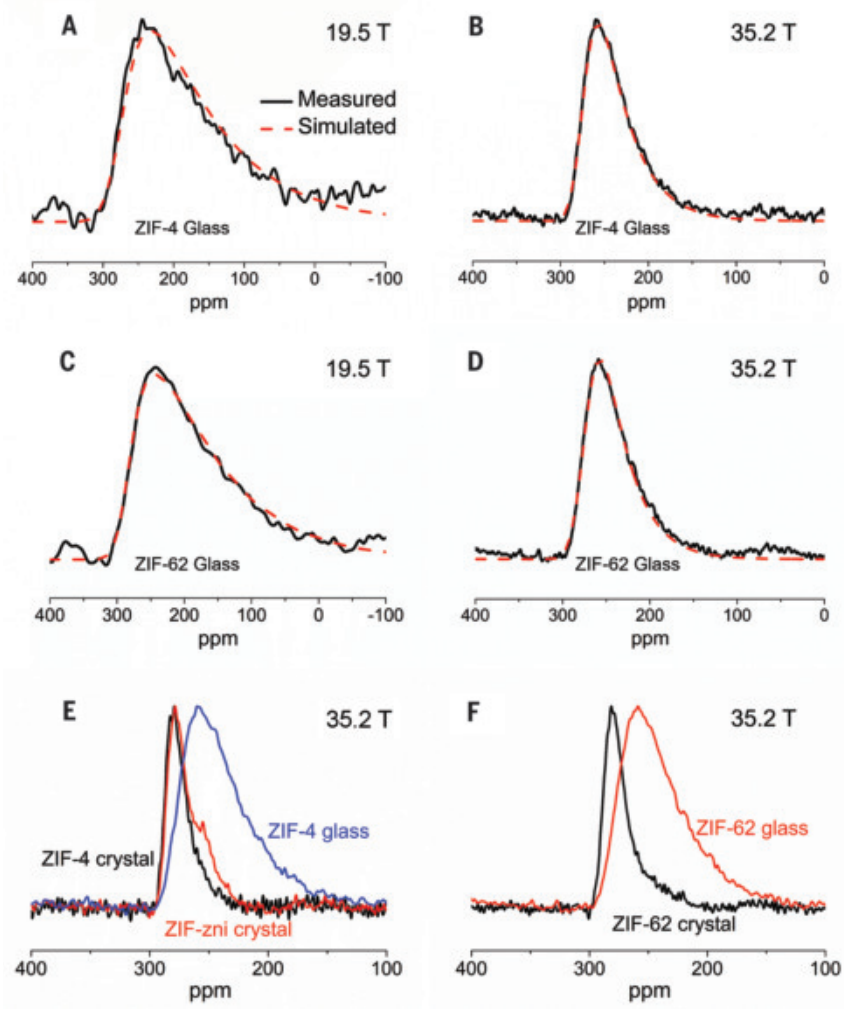

Fig. 3. Comparison of short-range structure between ZIF glasses and crystals. (**A** to **D**) Experimental (solid black line) and simulated (dashed red line) ^{67}Zn MAS NMR spectra for [(A) and (B)] ZIF-4 glass and [(C) and (D)] the standard ZIF-62 glass at different magnetic fields. (**E**) Direct comparison of ^{67}Zn MAS NMR spectra collected at 35.2 T between ZIF-4 crystal, ZIF-zni crystal, and ZIF-4 glass. (**F**) Direct comparison of spectra collected at 35.2 T of ZIF-62 crystal and glass.

both crystal and glass samples for ZIF-4, -zni, and -62 (Fig. 1B) show the presence of long-range order in crystalline ZIFs and its absence in their glassy counterparts. The vitrification of these ZIF crystals is schematically demonstrated in Fig. 1C.

The ^{67}Zn MAS NMR spectra of the three crystalline ZIFs (ZIF-4, ZIF-62, and ZIF-zni) were obtained at two different magnetic fields, 19.5 and 35.2 T (Fig. 2). Each of these crystals contained two crystallographically distinct Zn sites at a 1:1 ratio, one of which is a more distorted Zn[ligand]$_4$ tetrahedron (*18*). The ^{67}Zn MAS NMR line shapes also necessitated simulation with at least two sites with subequal (within ±5%) relative fractions (Fig. 2); we used the software Dmfit (*24*). For each composition, the spectra collected at both magnetic fields were fitted simultaneously with the same set of NMR parameters: isotropic chemical shift δ_{iso}, the quadrupolar coupling constant C_Q, and asymmetry parameter η_Q. These parameters are listed in Table 1, and the C_Q values for ZIF-4 are in good agreement with those reported in a recent study (*18*).

The data in Table 1 indicated that the δ_{iso} for all Zn sites in all materials varied over a rather narrow range, from ~277 to 297 parts per million (ppm). However, for each crystalline ZIF, the less distorted Zn sites (Zn2) had a smaller C_Q of ~4.0 MHz compared with the more distorted ones (Zn1) characterized by a larger C_Q of ~5 to 6 MHz. These assignments followed the density functional theory–based calculations by Sutrisno *et al.* (*18*). Intriguingly, in spite of having the same composition, the ^{67}Zn C_Q values of the two Zn sites in ZIF-4 crystal are substantially different from those in ZIF-zni crystal. This result may be indicative of the corresponding difference in the topology between these two crystals; ZIF-4 has a *cag* topology and the ZIF-zni has a *zni* topology (*5*). The higher C_Q values of the Zn sites in the ZIF-zni crystal compared with those for the ZIF-4 crystal are also consistent with ZIF-zni possessing a greater variance in the bond angles and lengths for the Zn sites compared with ZIF-4 (tables S2 and S3).

The ^{67}Zn MAS-NMR spectra of the ZIF-4 and ZIF-62 glasses were obtained at both 19.5 and 35.2 T (Fig. 3, A to D). These spectra had asymmetric line shapes with low-frequency tails that we attributed to a continuous distribution of C_Q characteristic of structural disorder in the glassy state. These ^{67}Zn MAS NMR line shapes were well simulated with δ_{iso} (277 to 278 ppm) similar to that observed in corresponding crystals (288 to 297 ppm) (Table 1) and with a Czjzek distribution of the C_Q parameter (*25*), which yields a root-mean-square quadrupolar product $\sqrt{\langle C^2_{Q\eta}\rangle}$ of ~6.9 MHz for the ZIF-4 glass and ~6.5 to 6.8 MHz for the two ZIF-62 glasses. When taken together, the results in Table 1 indicate that as the ZIF crystals were melt-quenched into glass, the C_Q values increased and displayed a broader distribution, indicating that the structural disorder of the Zn[ligand]$_4$ tetrahedral environment in the glassy state was higher than that in the parent crystals. The ^{67}Zn NMR parameters for all three ZIF glasses were similar (Table 1), implying a similar degree of short-range disorder, despite their differences in the Im/bIm ratio in the ligands.

The disappearance of the two distinct Zn sites characteristic of the ZIF crystals upon melting and vitrification indicates that the scission and renewal of the Zn–N bonds upon melting resulted in structural reconstruction (Fig. 1C and fig. S1). With their three-dimensional network of corner-sharing Zn[ligand]$_4$ tetrahedral units, ZIF glasses are structurally analogous to vitreous silica, but the coordination bonds in ZIF glasses were considerably weaker than the covalent-ionic bonds in silica. (*26*, *27*). The silica glass network would be more rigid than ZIF glasses, and the local structure of the former would be more ordered than that of ZIF glasses. The bulky nature of the organic linkers in ZIF glasses could also cause steric hindrance, thus limiting the ability of the linker to return to its equilibrium position—to the ordered structural state with lower potential energy—upon melt-quenching. The comparison in NMR spectra among ZIF-4 and -zni crystals and ZIF-4 glass (Fig. 3E), and between ZIF-62 crystal and glass (Fig. 3F), shows broadening of the glasses compared with the crystals, and the resonance peaks moved to somewhat lower isotropic chemical shift from crystal to glass. Although the increased broadening corresponds to a high degree of structural disorder in glasses at the short-range scale, the lowering of the isotropic chemical shift is suggestive of a more specific change in the local coordination environment of Zn atoms upon vitrification. Previous Zn K-edge x-ray absorption fine structure and PDF measurements (*5*) indicated that Zn is in tetrahedral coordination with N in both glassy and crystalline ZIFs, and that the Zn–N distance did not change considerably upon vitrification. However, ^{67}Zn solid-state NMR results of Sutrisno *et al.* (*18*) showed that the ^{67}Zn NMR isotropic chemical shift of ZIF-14 (260 ppm) with longer Zn–N distances (2.00 to 2.02 Å) was significantly lower than that of ZIF-8 or ZIF-4 (300 to 315 ppm) characterized by shorter Zn–N distances (1.98 to 1.99 Å). Although further systematic studies are needed to establish this trend, the lower ^{67}Zn NMR isotropic chemical shift of ZIF glasses compared with their crystalline counterparts as observed in the present study could be an indication of an increase in the average Zn–N distance in the former, which is consistent with the corresponding increase in the molar volume upon vitrification.

REFERENCES AND NOTES

1. C. A. Angell, *Science* **267**, 1924–1935 (1995).
2. G. N. Greaves, S. Sen, *Adv. Phys.* **56**, 1–166 (2007).
3. T. D. Bennett *et al.*, *Nat. Commun.* **6**, 8079 (2015).
4. D. Umeyama *et al.*, *Chem. Commun.* **51**, 12728–12731 (2015).
5. T. D. Bennett *et al.*, *J. Am. Chem. Soc.* **138**, 3484–3492 (2016).
6. D. Umeyama, S. Horike, M. Inukai, T. Itakura, S. Kitagawa, *J. Am. Chem. Soc.* **137**, 864–870 (2015).
7. Y. Zhao, S. Y. Lee, N. Becknell, O. M. Yaghi, C. A. Angell, *J. Am. Chem. Soc.* **138**, 10818–10821 (2016).
8. K. S. Park *et al.*, *Proc. Natl. Acad. Sci. U.S.A.* **103**, 10186–10191 (2006).
9. C. Zhou *et al.*, *Nat. Commun.* **9**, 5042 (2018).
10. L. Frentzel-Beyme *et al.*, *J. Mater. Chem. A Mater. Energy Sustain.* **7**, 985–990 (2019).
11. L. Frentzel-Beyme, M. Kloß, P. Kolodzeiski, R. Pallach, S. Henke, *J. Am. Chem. Soc.* **141**, 12362–12371 (2019).
12. M. A. Ali *et al.*, *ACS Omega* **4**, 12081–12087 (2019).
13. A. Qiao *et al.*, *Opt. Lett.* **44**, 1623–1625 (2019).
14. A. Qiao *et al.*, *Sci. Adv.* **4**, eaao6827 (2018).
15. J. Zhang *et al.*, *Chem. Commun.* **55**, 2521–2524 (2019).
16. R. Gaillac *et al.*, *Nat. Mater.* **16**, 1149–1154 (2017).
17. A. P. M. Kentgens, *Geoderma* **80**, 271–306 (1997).
18. A. Sutrisno *et al.*, *Chemistry* **18**, 12251–12259 (2012).
19. K. H. Mroué, W. P. Power, *J. Phys. Chem. A* **114**, 324–335 (2010).
20. T. Bastow, *J. Phys. Condens. Matter* **8**, 11309–11315 (1996).
21. G. Wu, S. Kroeker, R. E. Wasylishen, *Inorg. Chem.* **34**, 1595–1598 (1995).
22. F. H. Larsen, A. S. Lipton, H. J. Jakobsen, N. C. Nielsen, P. D. Ellis, *J. Am. Chem. Soc.* **121**, 3783–3784 (1999).
23. A. S. Lipton, R. W. Heck, P. D. Ellis, *J. Am. Chem. Soc.* **126**, 4735–4739 (2004).
24. D. Massiot *et al.*, *Magn. Reson. Chem.* **40**, 70–76 (2002).
25. J.-B. d'Espinose de Lacaillerie, C. Fretigny, D. Massiot, *J. Magn. Reson.* **192**, 244–251 (2008).
26. R. Gaillac, P. Pullumbi, F.-X. Coudert, *J. Phys. Chem. C* **122**, 6730–6736 (2018).
27. D. C. Clupper, L. L. Hench, *J. Non-Cryst. Solids* **318**, 43–48 (2003).
28. P. Z. Moghadam *et al.*, *Chem. Mater.* **29**, 2618–2625 (2017).
29. R. Banerjee *et al.*, *Science* **319**, 939–943 (2008).

ACKNOWLEDGMENTS

Funding: The authors thank the VILLUM FONDEN (13253) and the NSFC (51802263), China, for financial support. S.S. acknowledges support from the National Science Foundation grant NSF-DMR 1855176. The National High Magnetic Field Laboratory (NHMFL) is supported by the National Science Foundation through NSF/DMR-1644779 and the state of Florida. Development of the 36-T series connected hybrid magnet and NMR instrumentation was supported by NSF (DMR-1039938 and DMR-0603042) and NIH (BTRR 1P41 GM122698). **Author contributions:** Y.Y. and S.S. conceived the project; Y.Y., S.S., R.S.K.M., and A.Q. made the outline of the project. I.H., K.C., and Z.G. performed NMR measurements at NHMFL. J.S. performed all NMR spectral data processing and simulation. A.Q., R.S.K.M., and Y.Y. synthesized the samples and conducted DSC and XRD measurements. Y.Y., S.S., R.S.M., and A.Q. wrote the manuscript, with inputs from I.H., K.C., Z.G., and J.S. **Competing interests:** The authors declare that they have no competing interests. **Data and materials availability:** All data needed to evaluate the conclusions in the paper are present in the paper and/or the supplementary materials. Additional data related to this paper may be requested from the authors.

SUPPLEMENTARY MATERIALS

science. /content/367/6485/1473/suppl/DC1 Materials and Methods
Figs. S1 to S5
Table S1 to S3
References (*30*–*34*)

6 August 2019; resubmitted 22 January 2020
Accepted 5 March 2020
10.1126/science.aaz0251

CLIMATE FORCING

No consistent ENSO response to volcanic forcing over the last millennium

Sylvia G. Dee[1]*, Kim M. Cobb[2], Julien Emile-Geay[3], Toby R. Ault[4], R. Lawrence Edwards[5], Hai Cheng[6,5], Christopher D. Charles[7]

The El Niño–Southern Oscillation (ENSO) shapes global climate patterns yet its sensitivity to external climate forcing remains uncertain. Modeling studies suggest that ENSO is sensitive to sulfate aerosol forcing associated with explosive volcanism but observational support for this effect remains ambiguous. Here, we used absolutely dated fossil corals from the central tropical Pacific to gauge ENSO's response to large volcanic eruptions of the last millennium. Superposed epoch analysis reveals a weak tendency for an El Niño–like response in the year after an eruption, but this response is not statistically significant, nor does it appear after the outsized 1257 Samalas eruption. Our results suggest that those models showing a strong ENSO response to volcanic forcing may overestimate the size of the forced response relative to natural ENSO variability.

Detecting forced changes in El Niño–Southern Oscillation (ENSO) variability is a formidable challenge, requiring centuries of data beyond the range of the instrumental record (*1*, *2*). Indeed, tropical Pacific variability documented by instrumental and satellite observations spans only a century and a half at the very most, but it can be extended using paleoclimate archives from the relatively data-rich last millennium (hereafter LM). Recent work using both paleoclimate data and climate models has searched for forced changes to ENSO over the LM, evaluating the response of the tropical Pacific to external forcing over longer time scales. In particular, a large body of recent modeling studies suggest that global cooling associated with explosive volcanism can initiate an El Niño–like response in the tropical Pacific up to 2 years after the eruption. In models, this response is linked to basin-scale cooling patterns that drive an equatorward shift of the Intertropical Convergence Zone, which favors weaker trade winds in the western and central tropical Pacific (*2*–*4*), changes in the zonal sea surface temperature (SST) gradients with cooling in the west and a reduction in mean upwelling typically associated with an El Niño event [consistent with a dynamical thermostat mechanism (*5*–*7*)]. Still other studies invoke substantial cooling over tropical Africa (*8*) as a means for initiating a tropical warming response through perturbations to the Walker circulation. In all cases, the modeled response additionally depends on the background ENSO state during the time of the eruption and the eruption size (*6*, *9*), with a potential influence from the season in which the eruption occurs (*10*). In general, these massive volcanic eruptions provide an opportunity to test climate system and model sensitivity to sulfate aerosol forcing, offered as a possible geoengineering strategy for offsetting greenhouse warming (*11*).

The response to LM external forcing as recorded by paleoclimate data is documented in previous work (*2*, *12*–*16*), but most such studies rely on teleconnected responses outside the core ENSO region. Coral oxygen isotopic records from the northern Line Islands have yielded monthly resolved, high-fidelity records of past ENSO variability (*17*–*20*), recording SST variability in the heart of the central tropical Pacific. Correlation coefficients for Christmas, Fanning, and Palmyra island coral records and the NINO3.4 SST index are –0.92, –0.85, and –0.82, respectively, on interannual time scales (*19*), demonstrating high sensitivity to ENSO (*17*, *18*).

Here, we present measurements of oxygen isotopes in two fossil coral segments that bridge previously published Palmyra coral reconstructions (*18*) to constitute 319 years of absolutely dated, continuous, submonthly resolved coral $\delta^{18}O$ data extending from 1146 to 1465 CE (Fig. 1). The full record is composed of eight overlapping corals, with 75% of the time series generated from measurements of more than

[1]Rice University, Department of Earth, Environmental, and Planetary Sciences, Houston, TX 77005, USA. [2]School of Earth and Atmospheric Sciences, Georgia Institute of Technology, Atlanta, GA 30332, USA. [3]Department of Earth Sciences, University of Southern California, Los Angeles, CA 90089, USA. [4]Department of Earth and Atmospheric Sciences, Cornell University, Ithaca, NY 14853, USA. [5]Department of Earth Sciences, University of Minnesota, Minneapolis, MN 55455, USA. [6]Institute of Global Environmental Change, Xi'an Jiaotong University, Xi'an 710054, China. [7]Scripps Institution of Oceanography, San Diego, CA 92037, USA.
*Corresponding author. Email: sylvia.dee@rice.edu

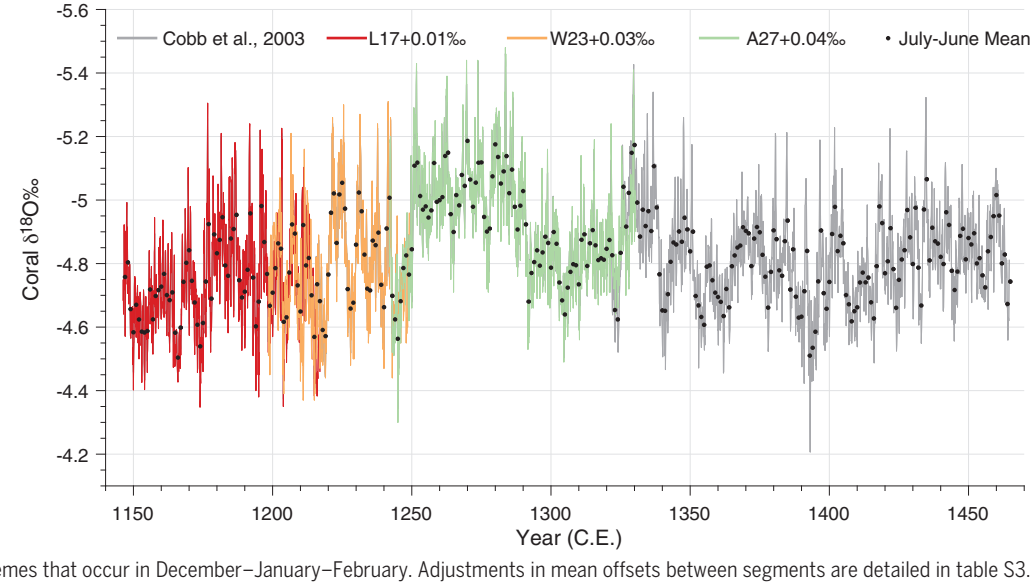

Fig. 1. Coral oxygen isotopes from Palmyra island. Shown are monthly resolved fossil coral oxygen isotopes measured in the multisegment Palmyra corals spanning the LM. This work highlights three new segments added to a monthly resolved, continuous eight-coral splice spanning three centuries of tropical Pacific oxygen isotope variability. The *y*-axis is inverted given that El Niño events drive negative $\delta^{18}O$ excursions in the coral data. U-Th dating places a bottom date in the coral segment of 1147 CE, and residual errors compound exponentially before and after this date horizon (see materials and methods section S1 and fig. S1). Annual means (black) are calculated as 1 July to 30 June averages to center coral annual averages on peak ENSO extremes that occur in December–January–February. Adjustments in mean offsets between segments are detailed in table S3.

one coral segment. The high reproducibility of overlapping segments bolsters our confidence in both the fidelity of the climate signal embedded in these records, as well as the accuracy of the individual coral uranium-thorium (U-Th) age models (see materials and methods sections S1.1 and S1.2). Eleven new high-precision U-Th dates yield age control for the bridging segments such that, in combination with the previously published dates (*18*), chronological errors are reduced to σ = ±1 year, rivaling the precision of the most well-replicated ice-core and tree-ring chronologies (*21*) (see materials and methods sections S1.1 and S1.2, tables S1 and S2, and figs. S1 and S2). Note that offsets in the mean values of coral $\delta^{18}O$ are reported in both Fig. 1 and section S1.2, but are not relevant to the analyses presented herein, which rely on interannual changes in coral $\delta^{18}O$, not the absolute value of a given sequence. The new composite coral $\delta^{18}O$ record represents the longest, best replicated, highest-resolution, and most proximal record to the center of ENSO variability currently available and presents a window into the effects of large volcanic eruptions on tropical Pacific climate.

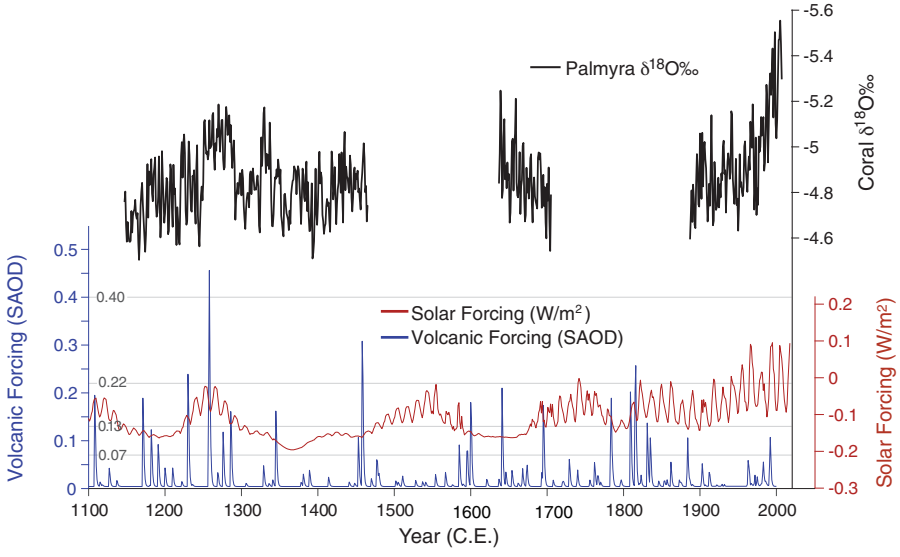

Fig. 2. External forcing and the Palmyra coral record over the LM. Reconstructed volcanic eruption dates reconstructed through SAOD (unitless) from (*22*) (blue), as well as the average LM solar-forcing reconstruction (red) (*36*) plotted with the full Palmyra $\delta^{18}O$ record (black), with individual segments spanning 1147 to 1998 CE. The modern coral piece spans 1887 to 1998 CE; earlier segments are measurements from fossil corals. The *y*-axis is inverted given that El Niño events drive negative $\delta^{18}O$ excursions in the coral data. Coral annual means (black) are calculated as 1 July to 30 June averages to center data across the largest ENSO anomalies. Volcanic-forcing thresholds are marked corresponding to SAOD exceeding 0.07, 0.13, 0.22, and 0.40 (gray lines).

Table 1. Ten largest volcanic eruptions intersecting coral data. Scaling from SAOD to radiative forcing (RF, in W/m^2) differs between reconstructions (*21*, *22*). Both are scaled as a function of sulfate measurements from ice cores. Shown are eruptions that occur in the tropics (latitude within [20°S;20°N], if known) and that intersect coral data over the LM. The top six largest eruption years intersecting the coral data are shown in Fig. 3. For reference, an AOD of 0.01 represents a clear atmosphere and 0.4 is extremely hazy.

Year (CE)	eVolv2ke		Sigl *et al.* (2015)
	SAOD	RF (W/m^2)	RF (W/m^2)
1258	0.46	−11.39	−32.8
1458	0.31	−7.7	−20.6
1230	0.24	−5.97	−15.9
1641	0.21	−5.24	−11.8
1171	0.19	−4.73	−11.3
1695	0.17	−4.35	−10.2
1345	0.16	−4.05	−9.4
1286	0.16	−4.03	−9.7
1182	0.12	−3.09	−5.6
1276	0.12	−2.94	−7.7

This work tests the hypothesis that volcanic-induced cooling may initiate a dynamical response leading to an "El Niño–like" tropical Pacific anomaly (*2*–*4*, *6*–*8*). The newly generated multicentury coral splice spanning the 12th to the 15th century improves our ability to diagnose the role of volcanic activity in shaping tropical Pacific climate during the LM and allows us to reevaluate the response of the tropical Pacific to external forcing using the latest reconstructions of volcanic forcing (*21*, *22*) (Fig. 2 and fig. S7). In particular, the corals span several of the largest tropical eruptions of the LM (Table 1), including the 1257 CE Samalas eruption (*23*). Samalas was the largest and most sulfurous eruption of the LM, with about twice the sulfate aerosol emissions as the 1815 CE eruption of Mt. Tambora (*16*). The full record, composited from multiple cores, covers 564 years of the period 1150 to 1998 CE (Figs. 1 and 2) and samples 26 tropical volcanic eruptions. ENSO variability at Palmyra is captured as low-$\delta^{18}O$ anomalies corresponding to warm, wet, El Niño–like conditions and high-$\delta^{18}O$ anomalies corresponding to cool, dry, La Niña–like conditions; thus, the hypothesis as posed tests for lower $\delta^{18}O$ in the 1- to 3-year period after tropical volcanic eruptions. In combination with the longevity and central Pacific location of the Palmyra Island corals, the data offer a good opportunity for independent analysis of the model results.

Coral sensitivity to tropical volcanic forcing over the past ~900 years is examined using the evolv2k volcanic aerosol reconstruction (Fig. 2) (*21*, *22*). Using sulfate aerosols in laminated ice cores, the reconstruction yields improved estimates of eruption date and forcing magnitude using multiparameter measurements (*21*). These enable reconstructions of stratospheric aerosol optical depth (SAOD), a dimensionless measure of the extinction of downwelling sunlight by aerosol particles in a given vertical column of the atmosphere. Volcanic reconstructions differ in their scaling parameterization of SAOD to estimate radiative forcing (see materials and methods section S1.5 and fig. S6). Furthermore, uncertainties remain as to the amount of sulfate aerosols present in ice cores that actually penetrates the stratosphere (*24*). Thus,

we circumvent these uncertainties by focusing solely on eruption timing as derived from ice-core chemistry. Volcanic eruptions are defined as local maxima across SAOD values reported in the ice-core reconstructions. The top 10 eruptions of the LM in terms of SAOD and estimated radiative forcing are given in Table 1.

Of the six largest eruptions of the LM intersecting the coral data (Fig. 3), four show a shift toward more negative (thus, El Niño–like) anomalies in the year after the eruption. To isolate the coral response to all tropical eruptions, we used superposed epoch analysis (SEA) (see materials and methods section S1.4). Previous work using intermediate complexity models of ENSO indicate that only large eruptions with forcing less than –3.7 W/m^2 increase the likelihood of initiating an El Niño response (*6*). To assess the sensitivity of our findings to the eruption magnitude and reconstruction uncertainties, the volcanic radiative-forcing threshold was systematically varied (SAOD > 0.07, 0.13, 0.22, and 0.43), testing the assumption that eruption size affects the detection of a significant response in the corals (see materials and methods section S1.4 and Fig. 4). For reference, the 1991 eruption of Mt. Pinatubo resulted in an estimated SAOD of 0.11. These thresholds scale to a radiative forcing of approximately –1.5, –3, –5, and –10 W/m^2, respectively, using the SAOD conversion reported in (*22*). As forcing threshold increases, the number of eruptions of sufficient magnitude intersecting the coral data sharply decreases from 26 to 1 (the 1257 CE eruption only) (Fig. 4), which complicates evaluation of statistical significance. In particular, the small sample size affects the probability of incorrect retention of the null hypothesis, a "type II error." This issue was circumvented by applying a block bootstrap resampling of the coral data in the SEA composite matrix, drawing only from no-eruption years (see materials and methods sections S1.3 and S1.4). This assesses volcanic responses against the null hypothesis of a stationary stochastic process in which no eruption occurs.

For the SEA composite across eruptions exceeding an AOD of 0.13 (1230, 1257, 1458, and 1641 CE), we observe El Niño–like anomalies in the year after the eruption, close to, but under, the 95% confidence level (Fig. 4C). As a result, we cannot confirm or deny the presence of a post-eruption warming at this level; there may be a response for sufficiently large eruptions but large internal variability obscures detection of a significant signal. Although a single composite response (Fig. 4C) grazes the uncertainty bounds, across all eruption thresholds, none of the coral responses was significant at the 95% confidence level. Thus, whereas SEA composite means of the post-eruption δ^{18}O anomalies (Fig. 4, C and D) do show an El Niño–like shift in coral δ^{18}O values after large volcanic eruptions, the response is indistinguishable from unforced (endogenous) variability. The coral data neither confirm nor refute a shift in the occurrence of ENSO anomalies after volcanic eruptions, even for the largest events. This result was replicated and confirmed using three additional volcanic reconstructions (*21*, *25*, *26*) (see materials and methods section S1.5 and fig. S7).

This analysis suggests that the influence of external forcing on ENSO is either absent or difficult to detect over the past millennium. The impacts of external forcing (and the reconstructions of these forcings) on ENSO in climate models are still uncertain, but paleoclimate archives from Palmyra island provide independent validation for model simulations. Despite the fossil corals' demonstrated high sensitivity to ENSO variability and mean state (*15*, *18*), the record shows no significant sensitivity to volcanic forcing on interannual to decadal time scales. Our result holds for the largest known volcanic events of the LM, including those in 1230, 1257, 1458, and 1641 CE; all of these eruptions have an SAOD >0.22, twice as large as the 1991 Pinatubo eruption. The Palmyra data do shift toward warmer temperatures in the eruption year and the following 2 years, with coral δ^{18}O anomalies consistent with an El Niño–like response to sufficiently explosive volcanism. However, uncertainty quantification suggests that the data do not support the hypothesis that large volcanic events trigger a detectable response in central Pacific climate.

To directly compare available model simulations of ENSO's response to volcanic forcing to the fossil corals, Fig. 4 shows the same analysis for the Paleoclimate Modeling Intercomparison Project (PMIP3) and Community Earth

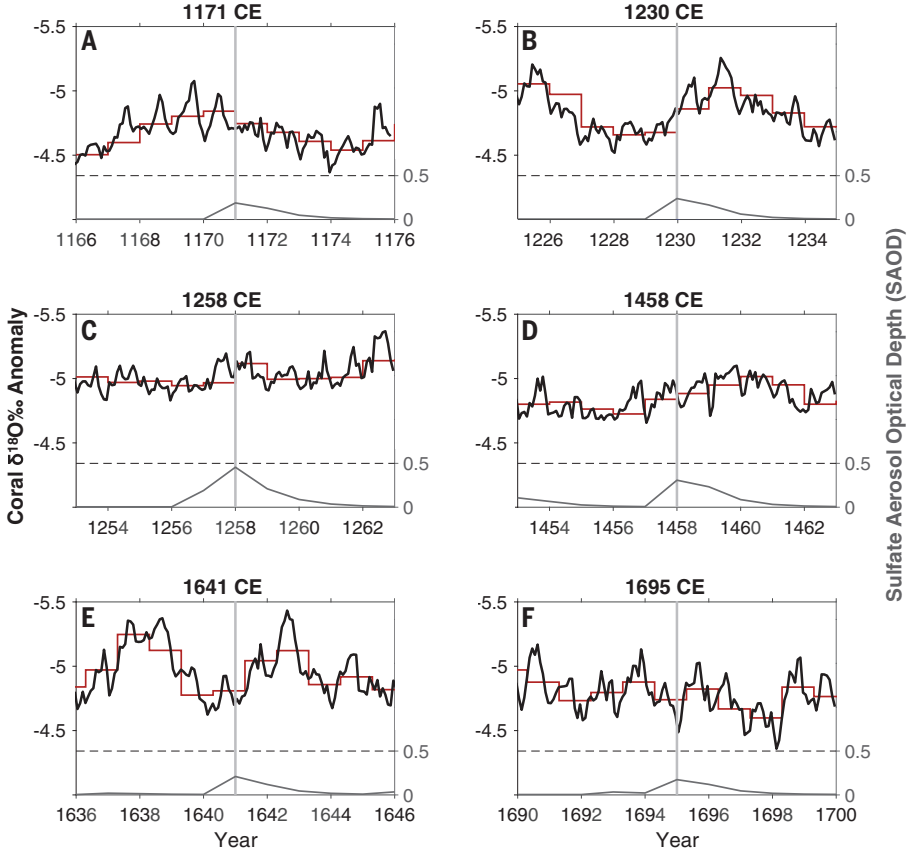

Fig. 3. Coral δ^{18}O monthly measured values across the largest eruptions of the LM (forcing < –10 W/m^2: 1171, 1230, 1258, 1458, 1641, and 1695). (**A**) to (**F**) show the Palmyra record coral annual average (dark red) and monthly values (black) plotted across each eruption. The *y*-axis is inverted such that warm events (which drive negative δ^{18}O) are above zero in the figure. Annual means (dark red) are calculated as 1 July to 30 June averages to center coral annual averages on peak ENSO extremes that occur in December–January–February. Gray lines show the respective SAOD forcing for each eruption, as well as the timing of the SAOD maxima (vertical gray lines intersecting coral time series).

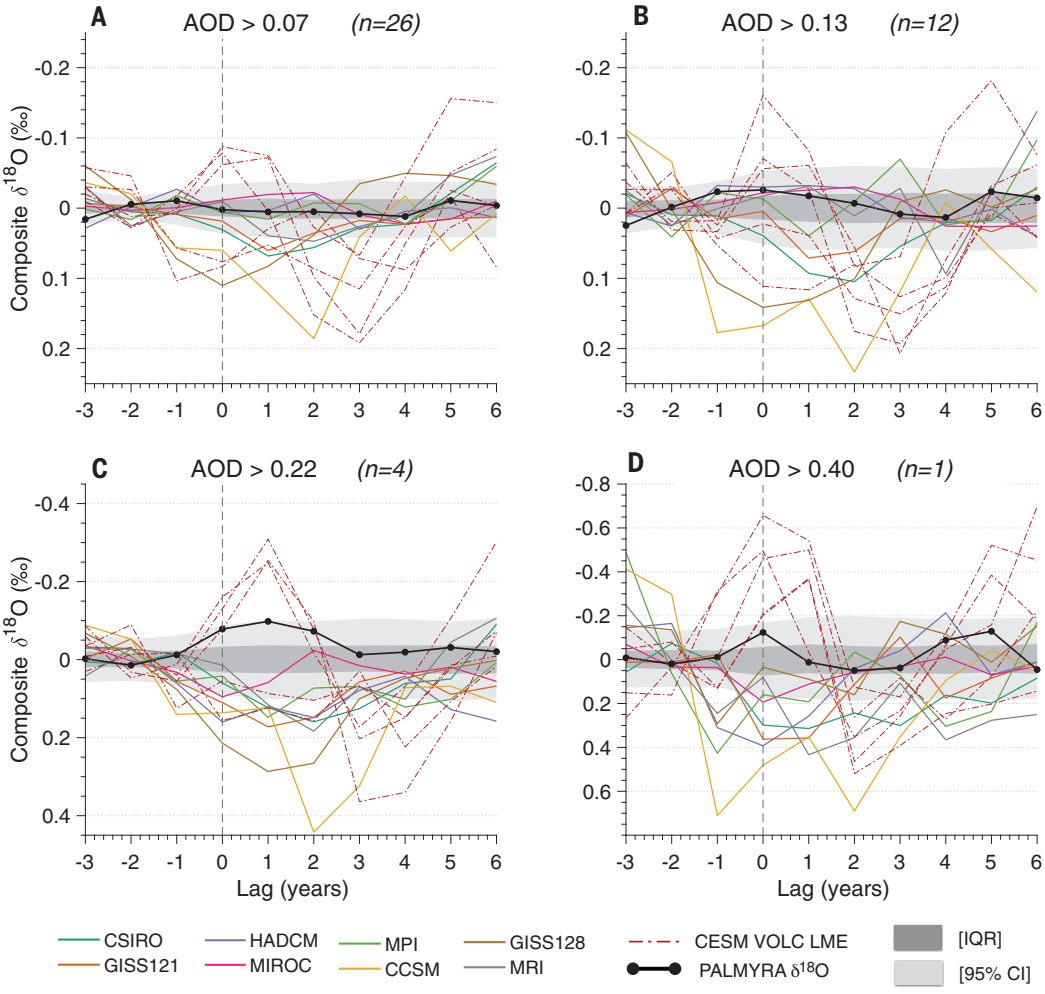

Fig. 4. Superposed epoch analysis for coral data intersecting with eruptions as defined in the Toohey *et al.* (2017) volcanic-forcing reconstruction. Composite $\delta^{18}O$ response for the 3 years before and 6 years after all eruptions exceeding a given forcing threshold (see materials and methods). The *y*-axis is inverted such that El Niño events (which drive negative $\delta^{18}O$ at Palmyra) correspond to upward excursions. (**A**) AOD > 0.07 (26 eruptions), (**B**) AOD > 0.12 (12 eruptions), (**C**) AOD > 0.22 (1230, 1257, 1458, and 1641 CE), (**D**) AOD > 0.43 (1257 CE; Samalas only); note the different *y*-axis for (C) and (D) because of the large model response curve. SEA averages over the *n* events that exceed the specified AOD threshold for each case [(D); AOD > 0.40] includes only the 1257 CE Samalas eruption. Light gray–shaded areas show the 50% and 95% highest-density regions from block bootstrap resampling of noneruption years (for comparison). Only excursions falling outside these intervals may be deemed significant at the 95% confidence level. Dark gray shading indicates middle 50% [0.25–0.75] interquartile range of the block bootstrap ensemble (IQR). Before evaluating the coral response to volcanic events, a 2- to 7-year bandpass filter was applied to emphasize canonical ENSO variability. Also plotted are the PMIP3 (solid colors) and CESM-LME volcanic forcing (dashed red lines) simulations for the same eruption thresholds, mapped to $\delta^{18}O$ space through the forward model of (*28*, *37*) (see materials and methods). Note that various simulations used different volcanic-forcing reconstructions (*25*, *26*) (see table S5), contributing to differences in their composite response.

System Model Last Millennium Ensemble [CESM-LME (*27*)] volcanic-forcing ensemble members. (For clarity, we note that this analysis is specific to this study and is independent of literature cited in this work evaluating model responses to volcanism.) The climate model simulations were processed identically to the coral data by extracting monthly Niño 3.4 region SST anomalies, computing anomalies relative to the monthly mean seasonal cycle, and applying the SST-scaling conversion for Porites corals (Fig. 4 caption, materials and methods section S1.6, and fig. S8). For completeness, the model conversion was repeated using a full proxy system model for coral $\delta^{18}O$, which considers the joint impacts of temperature and hydroclimate (*28*) (see materials and methods section S1.6 and fig S9). The model simulations generally exhibit a stronger, though highly variable, response to volcanism. The PMIP3 ensemble responses are inconsistent in that many models exhibit a muted response to volcanism, whereas others exhibit large post-eruption cooling in years 2 to 3 (*7*). By contrast, the mean of the CESM-LME ensemble members indicates substantial warming in years 0 to 1, as described in (*2*). For AOD thresholds >0.13 (corresponding to forcing ≤−3: −5 W/m^2), most models' temperature response to volcanic eruptions is characterized by a larger post-eruption variability than that of the corals. For CESM, the warming response is larger than the coral response for all eruption magnitude thresholds (Fig. 4). This result is robust to multiple SST-coral conversions (see materials and methods section S1.6 and figs. S8 and S9) (*29*).

Taken together, our results show that tropical Pacific SSTs as recorded by $\delta^{18}O$ of Palmyra corals are broadly insensitive to changes in radiative forcing given SEA across several AOD thresholds. There is a coral $\delta^{18}O$ response consistent with El Niño–like conditions detected below the 95% confidence level for large eruptions, but it is absent for the 1257 CE eruption of Samalas, the largest of the LM. These results imply that if the dynamical links between LM volcanism and tropical Pacific state suggested by climate models (*2*–*4*, *7*) do exist in the real world, their impact is small relative to natural variability, and potentially overestimated in some models. This is consistent with the claim that most, if not all, of the variability exhibited by ENSO over the preindustrial portion of the LM is linked to endogenous climate variability.

Volcanism's impact in the tropical Pacific in climate models is characterized by a high variance response and, in some cases, a strong warming or cooling in the central tropical

Pacific (Fig. 4). The Palmyra data, which show no significant change in the frequency, occurrence, or magnitude of El Niño events nor a significant change in central tropical Pacific $\delta^{18}O$, thus highlight an important data-model discrepancy surrounding the sensitivity of the tropical Pacific to external forcing. The broad range of model responses shown in Fig. 4 underscores structural uncertainties in model forcing and/or physics. Directly addressing uncertainties surrounding the size and partitioning between tropospheric and stratospheric aerosols during volcanic events, new high-resolution sulfur isotope measurements that differentiate between sulfate aerosols derived from stratospheric intrusions are poised to refine forcing estimates from ice cores spanning the LM (*24*). Additionally, mounting evidence suggests that volcanic forcing used to drive current-generation climate models is up to 67% too large because of structural uncertainties in stratospheric aerosol physics (*30*). This results in overestimated responses to volcanism in terms of intensity and longevity (*31*). Forthcoming improvements to the volcanic forcing applied in models may result in a weaker climatic response to a given aerosol loading (*30*).

Furthermore, recent work has shown that eruption season may prove as important as eruption magnitude in shaping the response of tropical Pacific climate to volcanic forcing (*10*), complicating data-model comparison. Many model simulations assume that all eruptions occur in a single month [e.g., January (*21*, *22*) or April (*25*)], which introduces uncertainties in the response with respect to proxy signatures of real-world eruptions. As highlighted in (*10*), multiproxy tropical temperature reconstructions lend some support for a warming response in the year after a tropical eruption, but data from moisture-sensitive trees in ENSO-teleconnected regions yield evidence of tropical Pacific cooling. In assessing these lines of evidence, we note that the volcanic response of extratropical tree ring width reflects two or more confounding sources: (i) local changes in precipitation caused by the direct radiative cooling from volcanic events (*32*) and (ii) changes in ENSO state, whether they be endogenous to the tropical Pacific or induced by volcanism. Moreover, a modeling study suggests that these two responses bear a close resemblance to each other (*2*). Such studies highlight the importance of using proximal records of tropical Pacific state, such as that presented in this work, to assess the relationship between volcanism and ENSO.

Climate model predictions of the climate system's response to continued greenhouse emissions depend crucially on accurate simulation of ENSO's response to external forcing. Recent work suggests that recent ENSO properties reflect a sensitivity to anthropogenic forcing (*19*, *20*, *33*), a finding supported by select climate models simulations of future climate change (*34*, *35*). Both modeling and data-based assessments of climate change impacts on ENSO must overcome the high degree of intrinsic variability, a detection threshold that is not met in the present study with respect to volcanic forcing. Whereas models can rely on ensembles to elevate signal-to-noise ratios, in the paleoclimate record, as in reality, we are limited to one realization. This ultimately limits our ability to detect changes in ENSO derived from model-based targets. However, the sign, structure, and magnitude differ between volcanic versus greenhouse forcing, ultimately limiting the relevance of the volcanic-forcing response of ENSO to potential responses of ENSO to greenhouse gas forcing.

Finally, this work highlights a role for high-resolution paleoclimate reconstructions and model simulations of LM volcanism in the assessment of potential geoengineering schemes designed to offset greenhouse warming in coming decades. There are few results from natural experiments available that facilitate investigations of the climate system response to sulfate aerosol loading. The volcanic response of major climate modes such as ENSO is key to assessing regional climate impacts under solar radiation management scenarios. As such, our work suggests that continued efforts toward data-model comparisons of the effects of volcanic eruptions on regional climate over the LM are critical to a robust assessment of the climatic effects of sulfate aerosol–induced geoengineering scenarios.

REFERENCES AND NOTES

1. A. T. Wittenberg, *Geophys. Res. Lett.* **36**, L12702 (2009).
2. S. Stevenson, B. Otto-Bliesner, J. Fasullo, E. Brady, *J. Clim.* **29**, 2907–2921 (2016).
3. F. S. R. Pausata, L. Chafik, R. Caballero, D. S. Battisti, *Proc. Natl. Acad. U S A* **112**, 13784–13788 (2015).
4. F. S. R. Pausata, C. Karamperidou, R. Caballero, D. S. Battisti, *Geophys. Res. Lett.* **43**, 8694–8702 (2016).
5. M. E. Mann, M. A. Cane, S. E. Zebiak, A. Clement, *J. Clim.* **18**, 447–456 (2005).
6. J. Emile-Geay, R. Seager, M. Cane, E. Cook, G. H. Haug, *J. Clim.* **21**, 3134–3148 (2008).
7. N. Maher, S. McGregor, M. H. England, A. S. Gupta, *Geophys. Res. Lett.* **42**, 6024–6033 (2015).
8. M. Khodri *et al.*, *Nat. Commun.* **8**, 778 (2017).
9. F. Lehner, A. P. Schurer, G. C. Hegerl, C. Deser, T. L. Frölicher, *Geophys. Res. Lett.* **43**, 2851–2858 (2016).
10. S. Stevenson, J. T. Fasullo, B. L. Otto-Bliesner, R. A. Tomas, C. Gao, *Proc. Natl. Acad. Sci. U.S.A.* **114**, 1822–1826 (2017).
11. M. Plazzotta, R. Séférian, H. Douville, B. Kravitz, J. Tjiputra, *Geophys. Res. Lett.* **45**, 5663–5671 (2018).
12. J. Brad Adams, M. E. Mann, C. M. Ammann, *Nature* **426**, 274 (2003).
13. K. Anchukaitis *et al.*, *Geophys. Res. Lett.* **37**, n/a (2010).
14. J. Li *et al.*, *Nat. Clim. Chang.* **3**, 822–826 (2013).
15. J. Emile-Geay, K. M. Cobb, M. E. Mann, A. T. Wittenberg, *J. Clim.* **26**, 2302–2328 (2013).
16. S. Guillet *et al.*, *Nat. Geosci.* **10**, 123–128 (2017).
17. K. M. Cobb, C. D. Charles, D. E. Hunter, *Geophys. Res. Lett.* **28**, 2209–2212 (2001).
18. K. M. Cobb, C. D. Charles, H. Cheng, R. L. Edwards, *Nature* **424**, 271–276 (2003).
19. K. M. Cobb *et al.*, *Science* **339**, 67–70 (2013).
20. P. R. Grothe *et al.*, *Geophys. Res. Lett.* (2019); https://doi.org/10.1029/2019GL083906.
21. M. Sigl *et al.*, *Nature* **523**, 543–549 (2015).
22. M. Toohey, M. Sigl, *Earth Syst. Sci. Data* **9**, 809–831 (2017).
23. F. Lavigne *et al.*, *Proc. Natl. Acad. Sci. U.S.A.* **110**, 16742–16747 (2013).
24. A. Burke *et al.*, *Earth Planet. Sci. Lett.* **521**, 113–119 (2019).
25. C. Gao *et al.*, *J. Geophys. Res. Atmos.* **111** (D12), D12107 (2006).
26. T. J. Crowley *et al.*, *PAGES News* **16**, 22–23 (2008).
27. B. L. Otto-Bliesner *et al.*, *Bull. Am. Meteorol. Soc.* **97**, 735–754 (2016).
28. S. Dee *et al.*, *J. Adv. Model. Earth Syst.* **7**, 1220–1247 (2015).
29. In the case of the Samalas eruption (Fig. 4D), models show a warming in the eruption year; note that simulated NINO34 indices were annually averaged from July 1 to June 30 to center the winter El Niño response (as in the coral data). CESM applies volcanic forcing in April of each calendar year (*2*, *25*), and thus the 'year 0' response is a by-product of the time-averaging method.
30. A. N. LeGrande, K. Tsigaridis, S. E. Bauer, *Nat. Geosci.* **9**, 652–655 (2016).
31. M. Stoffel *et al.*, *Nat. Geosci.* **8**, 784–788 (2015).
32. A. Meyer, D. Folini, U. Lohmann, T. Peter, *J. Clim.* **29**, 1325–1338 (2016).
33. Y. Liu *et al.*, *Nat. Commun.* **8**, 15386 (2017).
34. W. Cai *et al.*, *Nat. Clim. Chang.* **5**, 849–859 (2015).
35. W. Cai *et al.*, *Nature* **564**, 201–206 (2018).
36. G. A. Schmidt *et al.*, *Geosci. Model Dev.* **4**, 33–45 (2011).
37. D. M. Thompson, T. R. Ault, M. N. Evans, J. E. Cole, J. Emile-Geay, *Geophys. Res. Lett.* **38**, L14706 (2011).

ACKNOWLEDGMENTS

We thank M. Toohey for assistance with the evolv2k dataset, A. LeGrande and J. Russell for valuable insights on this work, and P. Grothe for assistance with coral chronological assignments. **Funding:** This research was supported by the Peter Voss Postdoctoral Fellowship in the Institute at Brown for Environment and Society, Brown University, as well as the University of Texas at Austin, Institute for Geophysics Postdoctoral Fellowship, both awarded to S.D.; by NSF Marine Geology and Geophysics awards 0752091, 1502832, and 1836645 to K.C.; NSF OCE award 0752585 to C.D.C. and K.C.; and NOAA grant NA18OAR4310426 to J.E.G. **Author contributions:** S.D., K.C., J.E.G., and T.A. formulated research questions. K.C. and C.D.C. collected, sampled, and analyzed oxygen isotopes in the coral data with assistance from L.E. and H.C. S.D. performed analysis on coral data, generated figures, and extracted model output with guidance from K.C., J.E.G., and T.A. All authors contributed to the writing of the manuscript. **Competing interests:** The authors declare no competing interests. **Data and materials availability:** All data and code are available in the supplementary materials and are publicly available on the National Climatic Data Centers website at https://www.ncdc.noaa.gov/paleo/study/27490.

SUPPLEMENTARY MATERIALS

science. /content/367/6485/1477/suppl/DC1 Section S1: Materials and Methods
Section S2: Data and Matlab Code
Tables S1 to S5
Figs. S1 to S9
References (*38*–*48*)

1 March 2019; accepted 2 March 2020
10.1126/science.aax2000

PLANT SCIENCE

Peptide signaling for drought-induced tomato flower drop

S. Reichardt[1], H.-P. Piepho[2], A. Stintzi[1]*, A. Schaller[1]*

The premature abscission of flowers and fruits limits crop yield under environmental stress. Drought-induced flower drop in tomato plants was found to be regulated by phytosulfokine (PSK), a peptide hormone previously known for its growth-promoting and immune-modulating activities. PSK formation in response to drought stress depends on phytaspase 2, a subtilisin-like protease of the phytaspase subtype that generates the peptide hormone by aspartate-specific processing of the PSK precursor in the tomato flower pedicel. The mature peptide acts in the abscission zone where it induces expression of cell wall hydrolases that execute the abscission process. Our results provide insight into the molecular control of abscission as regulated by proteolytic processing to generate a small plant peptide hormone.

The abscission of leaves, flowers, and fruits is a regulated process that is indispensable for both vegetative and reproductive plant development. Premature abscission of reproductive organs, however, reduces fruit set and crop productivity. Early flower drop is observed in many plant species when resources are limited and under conditions of environmental stress. Drought and heat cause premature flower and fruit drop, a problem likely to be exacerbated by global warming (*1*–*3*). Here we explore the function of a subtilisin-like protease in activating a small peptide that acts as a signal for flower abscission in tomato plants.

Insight into the regulatory mechanisms of organ abscission has been obtained mainly in two model systems: flower drop in tomato and the abscission of floral organs in *Arabidopsis* (*4*, *5*). The abscission of tomato flowers occurs at an abscission zone in the fruit stem (the pedicel; Fig. 1A) and is controlled by plant hormones. During undisturbed flower and fruit development, basipetal auxin transport results in a constant supply of auxin that keeps the abscission zone inactive to prevent abscission. When auxin flow is reduced upon fruit maturation, the abscission zone is sensitized to the action of ethylene (*5*, *6*), and ethylene signaling is then required to trigger abscission (*7*, *8*). In *Arabidopsis*, the abscission of sepals, petals, and stamens is delayed but not blocked in ethylene-insensitive mutants, indicating that ethylene controls the timing but is not indispensable for abscission in this system (*9*). Abscission of *Arabidopsis* flower organs rather depends on a small peptide that is proteolytically released from the INFLORESCENCE DEFICIENT IN ABSCISSION (IDA) precursor by subtilisin-like serine proteinases (subtilases) (*10*, *11*). The mature IDA peptide activates a receptor complex comprising one of the two redundant receptor kinases HAESA or HAESA-like 2 and SERK co-receptors, to trigger a mitogen-activated protein (MAP) kinase cascade regulating the expression of hydrolytic and cell wall–modifying enzymes necessary for the breakdown of the pectin-rich middle lamella and cell separation (*12*–*16*). The IDA signaling pathway also mediates the environmentally controlled shedding of cauline leaves in *Arabidopsis* (*17*). By contrast, the molecular mechanisms for stress-induced abscission of flowers and fruits still are poorly understood.

To understand how peptide signaling is involved in stress-induced flower and fruit drop in tomato, we generated transgenic plants overexpressing different subtilases as candidate peptide precursor–processing proteases (*11*). Premature abscission of flowers was observed in plants overexpressing phytaspase 2 (*Sl*Phyt2, *Solyc*04g078740; Fig. 1, A and B, and fig. S1). When these plants were exposed to drought stress (fig. S2), flower drop increased to 70% as compared to 50% in the wild type (Fig. 1C). Flower drop reached only 20 to 30% in transgenic plants silenced for *SlPhyt2* expression (Fig. 1C and fig. S3), resulting in increased fruit set in *SlPhyt2* knockdown lines as compared to overexpressors and wild type (fig. S4). The extent of flower drop correlated with *Sl*Phyt2 expression and activity in knockdown and overexpressing lines (Fig. 2, A and B, and fig. S3), implying a function for *SlPhyt2* in drought-induced abortion of flower and fruit development in tomato. Indeed, *SlPhyt2* expression was induced in response to drought stress in flower pedicels proximal to the abscission zone and in the leaf vasculature (Fig. 2, C and D).

We further analyzed *Sl*Phyt2 function in an inflorescence explant bioassay. Removal of the auxin source by cutting off the flower triggers abscission in this system (*6*). Flower removal induced expression of *SlPhyt2* in the proximal pedicel (Fig. 3A) before the onset of abscission (Fig. 3C). Pedicel abscission was faster than normal in *SlPhyt2*-overexpressing plants and delayed in knockdown plants (Fig. 3C). The data mirror the drought-induced flower-drop phenotype observed in transgenic overexpressing and knockdown plants (Fig. 1). Thus, flower abscission is limited by *SlPhyt2* expression.

Next, we asked how *Sl*Phyt2 functions in relation to auxin and ethylene. We analyzed expression of early auxin-dependent genes that lead to the acquisition of ethylene sensitivity and activation of the abscission zone (*IAA3*, *ERF4*, *TPRP*) (*6*). Also included were regulatory genes in the late ethylene response (*ERT10*, *PK7*) (*6*), and tomato abscission–related polygalacturonase (*TAPG4*) as one of the

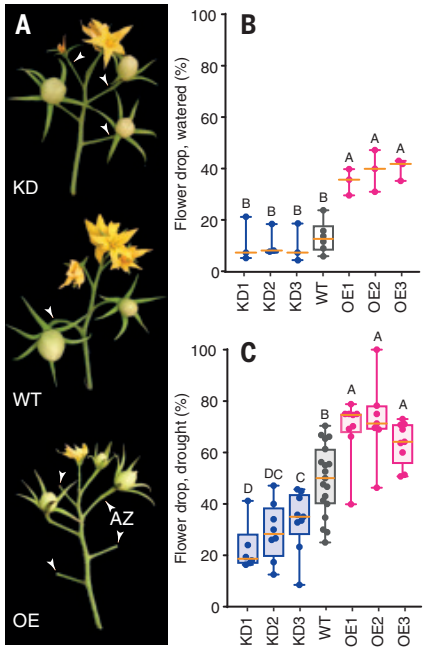

Fig. 1. Flower drop is enhanced under drought stress in a *Sl*Phyt2-dependent manner. (**A**) Inflorescence phenotype of *SlPhyt2*-silenced (knockdown, KD) and overexpressing plants (OE) compared to wild type (WT). OE plants abscise flowers prematurely at the pedicel abscission zone (AZ, arrowhead). (**B** and **C**) Flower drop was analyzed in KD (blue), OE (magenta), and WT (gray) plants under well-watered (B) and drought conditions (C). Flower drop was scored repeatedly until fruit set and is shown as the percentage of abscised flowers of all flowers or fruits per inflorescence (values for individual inflorescences are given in the raw data and statistics supplement). Each data point represents one experimental plant, showing the mean abscission value of all inflorescences on this plant [three plants for each of the transgenic lines and 6 wild-type plants in (A); at least 6 plants for the transgenic lines and 19 wild-type plants in (B)]. Total number of flowers and abscised flowers per genotype are given in the raw data supplement. Data were analyzed by fitting a generalized linear mixed model (GLMM). Genotype least squares means with a common letter are not significantly different (α = 0.05).

[1]Department of Plant Physiology and Biochemistry, University of Hohenheim, Stuttgart, Germany. [2]Biostatistics Unit, Institute of Crop Science, University of Hohenheim, Stuttgart, Germany.
*Corresponding author. Email: andreas.schaller@uni-hohenheim.de (A.Sc.); annick.stintzi@uni-hohenheim.de (A.St.)

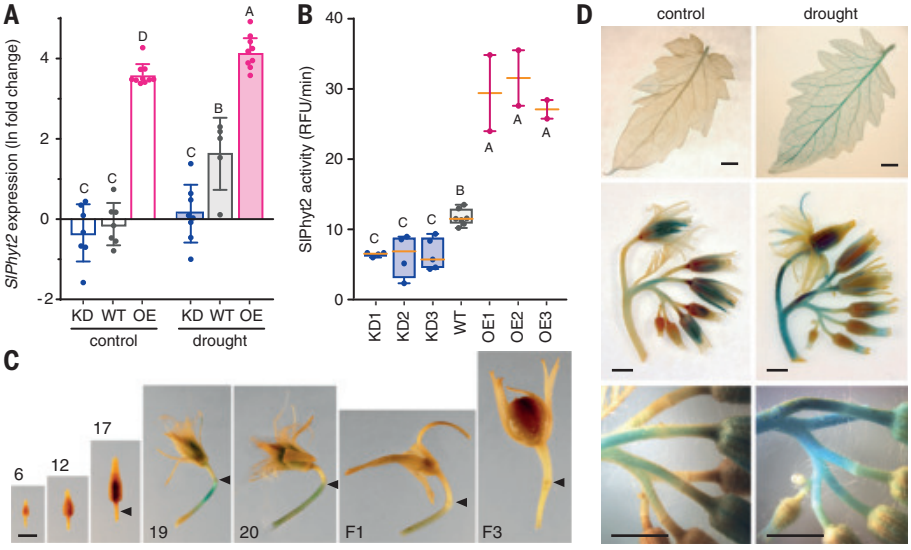

Fig. 2. *SlPhyt2* expression is induced by drought stress. (**A**) *SlPhyt2* expression is induced in leaves of drought-stressed (color-shaded bars) WT plants (gray) and overexpressing plants (magenta) but not in knockdown plants (blue); bars show mean expression levels ± SD as ln fold change relative to the watered WT control (open bars). (**B**) Phytaspase activity in cell wall extracts of leaves from drought-stressed plants is reduced in knockdown and increased in overexpressing plants as compared to wild type. Means (A) and medians (B) with no letter in common are significantly different (*t* test). (**C**) Histochemical staining of $SlPhyt2_{pro}$::GUS activity in the proximal pedicel of developing tomato flowers; numbers indicate developmental stages according to (*30*). Arrowheads mark the abscission zone. Early abscission was typically observed between flower stages 18 and 20. (**D**) GUS staining in leaves and inflorescences of control and drought-stressed plants. Scale bars in (C) and (D) represent 5 mm.

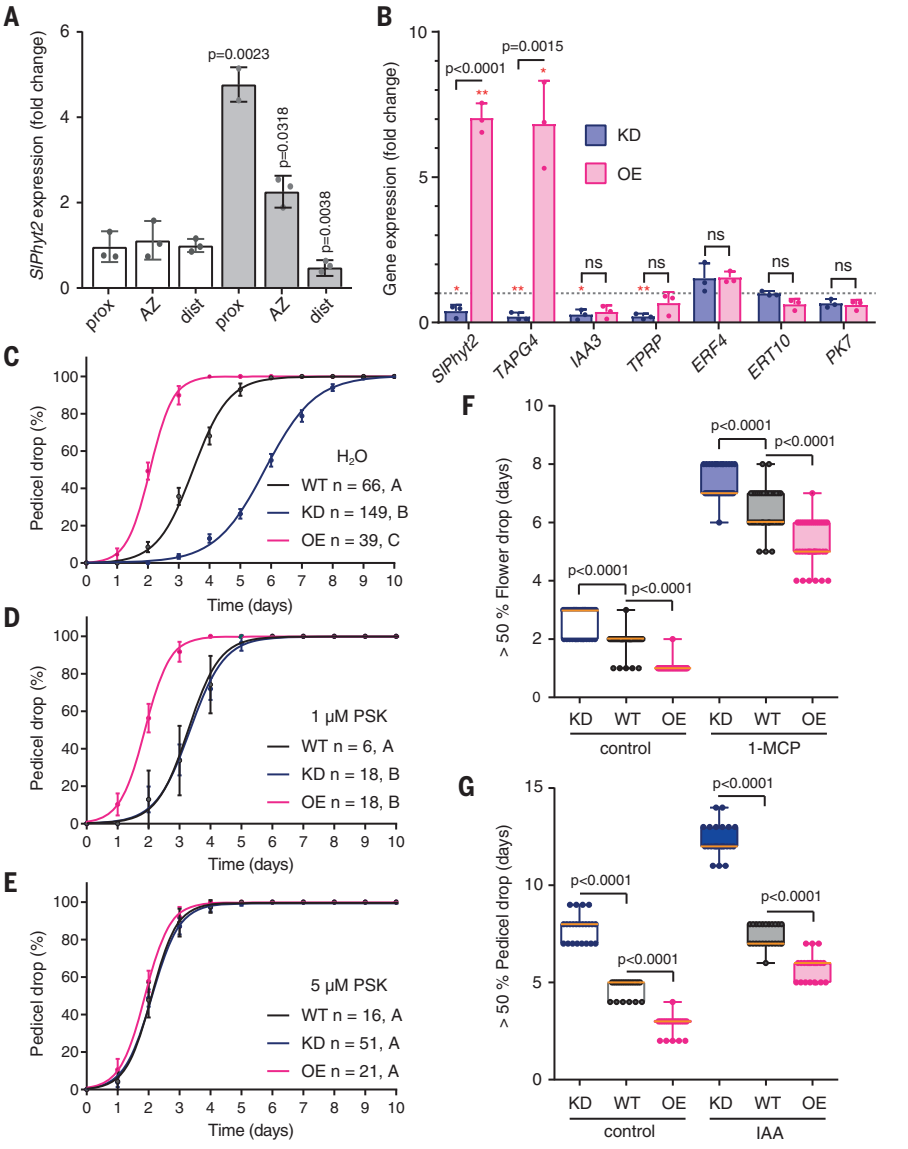

Fig. 3. Abscission is regulated by *Sl*Phyt2 and PSK in an auxin- and ethylene-independent manner. (**A**) Induction of *SlPhyt2* expression in the proximal (prox) compared to the distal (dist) pedicel after flower removal analyzed by quantitative polymerase chain reaction (qPCR) before (open bars, control) and 14 hours after flower removal (gray bars) normalized to abscission zone (AZ) control (mean ± SD; *P* values mark significant differences to the abscission zone control; *t* test). (**B**) qPCR analysis of *SlPhyt2* expression in abscission zone + 5 mm of the flanking pedicel compared to *TAPG4* and phytohormone response markers. Gene expression in knockdown (blue) and overexpressing plants (magenta) is shown relative to wild type normalized to 1 (dashed line; mean ± SD). Red asterisks mark significant differences between transgenic plants and wild type (*t* test). *P* values are shown for significant differences between knockdown and overexpressing plants (*t* test). (**C** to **E**) Pedicel abscission assayed over time for *SlPhyt2* knockdown, overexpressing, and WT plants in a detached-flower bioassay (error bars indicate 95% confidence interval; *n* = number of inflorescences analyzed; drop curves marked by the same letter are not significantly different at $\alpha = 0.05$). (C) Control in H_2O; (D) 1 µM PSK; and (E) 5 µM PSK. (**F** and **G**) Bioassay for abscission in knockdown, overexpressing, and WT inflorescence explants showing the time (day) until >50% of pedicels had abscised. (F) 1-MCP–treated inflorescences compared to controls in ambient air. (G) 50 µM indole-3-acetic acid (IAA)-treated inflorescences compared to solvent-treated controls; Mann Whitney test based on ranks.

executors of abscission (*6*). *TAPG4* transcript levels correlated with higher expression of *SlPhyt2* in the abscission zone and pedicel of overexpressing plants and with reduced expression in knockdown plants as compared to wild type (Fig. 3B). Expression of early auxin- and late ethylene-dependent genes was unaffected in the transgenic lines (Fig. 3B). Likewise, there was no difference in ethylene emission or concentration of the ethylene precursor ACC (1-aminocyclopropane-1-carboxylic acid) in *SlPhyt2* knockdown and overexpressing plants as compared to the wild type (fig. S5). Furthermore, treatment with the ethylene antagonist 1-MCP (1-methylcyclopropene) or resupply of auxin to the cut surface of the pedicel delayed abscission to a similar extent in the transgenic lines and wild-type plants, although the differences in the rate of abscission between knockdown, overexpressing, and wild-type plants persisted (Fig. 3, F and G, and figs. S6 and S7). *TAPG4* expression may thus be controlled by *Sl*Phyt2 in an auxin- and ethylene-independent manner, possibly by a peptide hormone.

To identify the hypothetical peptide, we analyzed the substrate specificity of *Sl*Phyt2. We added to this subtilase a C-terminal hexa-His tag, expressed the construct in *Nicotiana benthamiana*, and purified the tagged protein from cell wall extracts by metal chelate affinity chromatography (fig. S8A) and gel filtration. Substrate specificity of the recombinant protein was analyzed in a proteomics assay (Proteomics Identification of Cleavage Sites, PICS) (*18*, *19*). Using a substrate library of more than 10,000 peptides, we found that *Sl*Phyt2 was selective for Asp in P1 (the position immediately upstream of the scissile bond) and showed a preference for hydrophobic amino acids both upstream and downstream of the cleavage site (in P2, P3, and P2′; Fig. 4A). The precursors of known peptide hormones were scanned for this recognition motif, resulting in the identification of two candidate *Sl*Phyt2 substrates: the precursor of systemin, an 18–amino acid peptide involved in the wound response and herbivore defense signaling in tomato (*20*), and the precursor of phytosulfokine (PSK), a disulfated pentapeptide that regulates plant growth (*21*). Although prosystemin is processed by *Sl*Phyt2 in an Asp-specific manner in vitro (*22*), we did not observe any defect in wound signaling or herbivore defense in *SlPhyt2* knockdown plants (fig. S9), excluding prosystemin as a physiologically relevant *SlPhyt2* substrate in vivo. We therefore addressed the possibility that *Sl*Phyt2 is responsible for maturation of PSK as a signal for pedicel abscission in tomato.

There are eight genes in the tomato genome encoding precursors of PSK, all having Asp in P1 upstream of the conserved PSK sequence, and hydrophobic amino acids in P2 (Leu) and P2′ (Ile; Fig. 4B). Several of these genes (*SlPSK1, SlPSK4*, and *SlPSK6*) are expressed in abscission zones with highest expression levels for *SlPSK1* (fig. S10A). We found that expression of *SlPSK1* and *SlPSK6* is coinduced with *SlPhyt2* by drought stress (fig. S10B). A synthetic, extended PSK peptide comprising the disulfated PSK pentapeptide [(sY)I(sY)TQ] and five additional precursor-derived amino acids at its N terminus (EAHLD) was cleaved by *Sl*Phyt2 in an Asp-specific manner, releasing mature PSK in vitro (Fig. 4C and fig. S11). Substitution of the cleavage-site Asp by Ala rendered the PSK precursor peptide resistant to proteolytic cleavage by *Sl*Phyt2, indicating that Asp is required for cleavage site recognition and processing (Fig. 4D and fig. S11).

Mature PSK induced pedicel abscission in the inflorescence explant bioassay in a dose-dependent manner. At 5 μM PSK, the response was saturated and indistinguishable in PSK-treated knockdown, wild-type, and overexpressing plants (Fig. 3, C to E). PSK treatment also induced expression of *TAPG2* and *TAPG4* and down-regulated the expression of genes that maintain the abscission zone in an inactive state (Fig. 4E). The data verify PSK as a signal for pedicel abscission in tomato and suggest a role for *Sl*Phyt2 in precursor processing and PSK maturation in vivo. The requirement of *Sl*Phyt2 for PSK biogenesis was confirmed in the detached flower bioassay. In wild-type inflorescences, the N-terminally extended PSK precursor peptide induced pedicel abscission, whereas the protease-resistant variant of PSK was inactive (Fig. 4F and fig. S12). In *Sl*Phyt2-deficient knockdown plants, both resistant and cleavable precursor peptides were inactive, indicating that the cleavage site Asp and *Sl*Phyt2 are both required for biogenesis of the PSK abscission signal (Fig. 4F and fig. S12).

Drought stress–induced coexpression of *SlPhyt2* and *PSK* precursor genes in the pedicel, Asp-dependent cleavage of the precursor peptide by recombinant *Sl*Phyt2 in vitro, flower-drop in *SlPhyt2* overexpressors, and the inability of *SlPhyt2*-silenced plants to respond to PSK precursor peptides confirm *Sl*Phyt2 as the subtilase processing the PSK precursor into active PSK peptide. Unlike other plant proteases known to convert precursors into active peptide growth factors (*11*, *23*, *24*), *Sl*Phyt2 has a regulatory function in signal biogenesis. We propose (model, fig. S13) that stress-induced

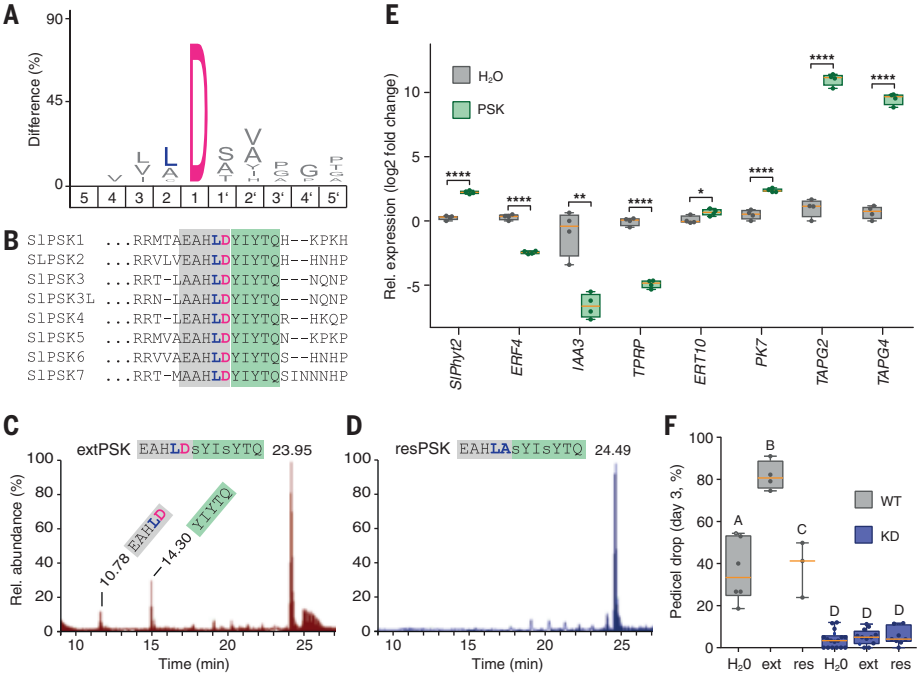

Fig. 4. Formation of PSK as an abscission signal depends on Asp-specific cleavage of the precursor by *Sl*Phyt2 in vivo. (**A**) iceLogo showing amino acid residues preferred by *Sl*Phyt2 upstream (positions 1 to 5) and downstream (positions 1′ to 5′) of the cleavage site. (**B**) C terminus of the eight PSK precursors encoded in the tomato genome; sequence of the PSK peptide highlighted in green. (**C** and **D**) Ion chromatograms showing cleavage products generated by *Sl*Phyt2 from N-terminally extended PSK (extPSK) (C) and a phytaspase-resistant D-to-A variant of the same peptide (resPSK) (D). (**E**) qPCR expression analysis of *TAPG* and phytohormone response marker genes in abscission zones of PSK-treated (5 μM; green) compared to control inflorescences (gray). (**F**) Abscission bioassay showing the percentage of pedicel drop on day 3 after flower removal in WT (gray) and knockdown inflorescences (blue) treated with extPSK (ext), resPSK (res) or water (H_2O). Treatments sharing no letter are significantly different (*t* test). Single-letter abbreviations for the amino acid residues are as follows: A, Ala; C, Cys; D, Asp; E, Glu; F, Phe; G, Gly; H, His; I, Ile; K, Lys; L, Leu; M, Met; N, Asn; P, Pro; Q, Gln; R, Arg; S, Ser; T, Thr; V, Val; W, Trp; and Y, Tyr.

flower drop is controlled by the subtilase *Sl*Phyt2, expressed in the pedicel for PSK production. PSK then drives abscission by induction of cell wall hydrolases in the abscission zone.

Thus, we add the peptide PSK to the suite of known abscission signals. Developmental abscission of ripe fruits is controlled by the phytohormones auxin and ethylene, and possibly by the IDA peptide (*25*). Premature flower drop in response to environmental stress, an event of agricultural concern, is triggered by PSK in tomato. How PSK interferes with auxin and ethylene-mediated regulation of abscission zone activity remains to be investigated. IDA is unlikely to contribute to stress-induced flower drop. There is no phytaspase cleavage site in tomato IDA precursors. Also, expression of the five *IDA* precursor genes is very low in abscission zones (fig. S10A) and unresponsive to drought stress (fig. S10B). PSK is known for its growth-promoting activity (*21*, *26*, *27*), which may be as relevant to abscission as PSK-induced cell separation. Enlargement of abscission zone cells provides the shear force for organ detachment after hydrolysis of the middle lamella (*4*, *25*). The induction of cell expansion and expression of cell wall hydrolases by the PSK peptide thus may both contribute to the execution of abscission. Although PSK is found in both monocots and dicots, phytaspases, the subtype of subtilases that includes *Sl*Phyt2, are less broadly distributed. An expanded phytaspase clade is found in the nightshade family (the Solanaceae, including tomato and potato) and a few other eudicot families (Ranunculaceae, Fabaceae, Lamiaceae, and Phrymaceae) but is absent from other families (e.g., Brassicaceae) (*18*, *28*, *29*). Whether PSK-mediated regulation of abscission is restricted to the phytaspase-bearing lineages or is more widely distributed in flowering plants remains an open question.

REFERENCES AND NOTES

1. R. K. Pandey, W. A. T. Herrera, J. W. Pendleton, *Agron. J.* **76**, 549–553 (1984).
2. M. Sawicki, E. Aït Barka, C. Clément, N. Vaillant-Gaveau, C. Jacquard, *J. Exp. Bot.* **66**, 1707–1719 (2015).
3. M. M. Peet, D. H. Willits, R. Gardner, *J. Exp. Bot.* **48**, 101–111 (1997).
4. O. R. Patharkar, J. C. Walker, *J. Exp. Bot.* **69**, 733–740 (2018).
5. Y. Ito, T. Nakano, *Front. Plant Sci.* **6**, 442 (2015).
6. S. Meir *et al.*, *Plant Physiol.* **154**, 1929–1956 (2010).
7. M. B. Lanahan, H. C. Yen, J. J. Giovannoni, H. J. Klee, *Plant Cell* **6**, 521–530 (1994).
8. J. Q. Wilkinson *et al.*, *Nat. Biotechnol.* **15**, 444–447 (1997).
9. S. E. Patterson, A. B. Bleecker, *Plant Physiol.* **134**, 194–203 (2004).
10. M. A. Butenko *et al.*, *Plant Cell* **15**, 2296–2307 (2003).
11. K. Schardon *et al.*, *Science* **354**, 1594–1597 (2016).
12. X. Meng *et al.*, *Cell Rep.* **14**, 1330–1338 (2016).
13. S. K. Cho *et al.*, *Proc. Natl. Acad. Sci. U.S.A.* **105**, 15629–15634 (2008).
14. J. Santiago *et al.*, *eLife* **5**, e15075 (2016).
15. C. E. Niederhuth, O. R. Patharkar, J. C. Walker, *BMC Genomics* **14**, 37 (2013).
16. G.-E. Stenvik *et al.*, *Plant Cell* **20**, 1805–1817 (2008).
17. O. R. Patharkar, J. C. Walker, *Plant Physiol.* **172**, 510–520 (2016).
18. S. Reichardt *et al.*, *Sci. Rep.* **8**, 10531 (2018).
19. O. Schilling, C. M. Overall, *Nat. Biotechnol.* **26**, 685–694 (2008).
20. G. Pearce, D. Strydom, S. Johnson, C. A. Ryan, *Science* **253**, 895–897 (1991).
21. Y. Matsubayashi, Y. Sakagami, *Proc. Natl. Acad. Sci. U.S.A.* **93**, 7623–7627 (1996).
22. R. E. Beloshistov *et al.*, *New Phytol.* **218**, 1167–1178 (2018).
23. A. Schaller *et al.*, *New Phytol.* **218**, 901–915 (2018).
24. T. Hander *et al.*, *Science* **363**, eaar7486 (2019).
25. R. B. Aalen, M. Wildhagen, I. M. Stø, M. A. Butenko, *J. Exp. Bot.* **64**, 5253–5261 (2013).
26. M. Sauter, *J. Exp. Bot.* **66**, 5161–5169 (2015).
27. F. Ladwig *et al.*, *Plant Cell* **27**, 1718–1729 (2015).
28. Y. Xu *et al.*, *Sci. Rep.* **9**, 12485 (2019).
29. A. Taylor, Y.-L. Qiu, *Mol. Plant Microbe Interact.* **30**, 489–501 (2017).
30. V. Brukhin, M. Hernould, N. Gonzalez, C. Chevalier, A. Mouras, *Sex. Plant Reprod.* **15**, 311–320 (2003).

ACKNOWLEDGMENTS

We thank W. Schulze (Plant Systems Biology, University of Hohenheim) and the Core Facility Hohenheim for mass spectrometric analyses; G. Felix (University of Tübingen) for help with the ethylene and ACC measurements; L. A. Lafleur, D. Repper, and U. Glück-Behrens for technical assistance; and the staff of the Service Unit Hohenheim Greenhouses for maintenance of experimental plants. We also thank P. Winterhagen (Institute of Crop Science, University of Hohenheim) for the gift of 1-MCP, and Commonwealth Scientific and Industrial Research Organization (CSIRO) Plant Industry for the pHANNIBAL/pKANNIBAL vector system. **Funding:** This work was supported by a grant from the German Research Foundation (DFG) to A.Sc. (SCHA 591/8-1). **Author contributions:** All authors contributed to the design of the study. S.R., A.St., and A.Sc. performed the experiments. Data were analyzed by all authors. A.Sc. and A.St. prepared the figures with contributions from S.R. The manuscript was written by A.Sc. with contributions from all authors. All authors agreed with the final version. **Competing interests:** The authors declare no competing interests. **Data and materials availability:** All data are available in the main text or the supplementary materials.

SUPPLEMENTARY MATERIALS

science.sciencemag.org/content/367/6485/1482/suppl/DC1
Materials and Methods
Figs. S1 to S13
References (*31*–*49*)
Raw Data and Statistics

19 September 2019; accepted 27 February 2020
10.1126/science.aaz5641

OCEAN CIRCULATION

Interglacial instability of North Atlantic Deep Water ventilation

Eirik Vinje Galaasen[1]*, Ulysses S. Ninnemann[1], Augustin Kessler[2], Nil Irvali[1], Yair Rosenthal[3], Jerry Tjiputra[2], Nathaëlle Bouttes[4], Didier M. Roche[4,5], Helga (Kikki) F. Kleiven[1], David A. Hodell[6]

Disrupting North Atlantic Deep Water (NADW) ventilation is a key concern in climate projections. We use (sub)centennially resolved bottom water $\delta^{13}C$ records that span the interglacials of the last 0.5 million years to assess the frequency of and the climatic backgrounds capable of triggering large NADW reductions. Episodes of reduced NADW in the deep Atlantic, similar in magnitude to glacial events, have been relatively common and occasionally long-lasting features of interglacials. NADW reductions were triggered across the range of recent interglacial climate backgrounds, which demonstrates that catastrophic freshwater outburst floods were not a prerequisite for large perturbations. Our results argue that large NADW disruptions are more easily achieved than previously appreciated and that they occurred in past climate conditions similar to those we may soon face.

Atlantic Meridional Overturning Circulation (AMOC) and North Atlantic Deep Water (NADW) ventilation represent a low-probability, high-impact tipping point in the climate system (*1*), with implications for the distribution and sequestration of anthropogenic CO_2 and heat and for Atlantic-wide patterns of climate and sea level (*2*–*4*). Although the consequences of any changes are clearly severe, the probability of instabilities in the rate or pathways of NADW ventilation remains highly uncertain. Both simple and complex models suggest large changes are possible but also that a strong overturning, like that found in the modern ocean, may be more difficult to disrupt than an overall weaker circulation (*4*–*6*). Likewise, most models simulate moderate to no reduction in AMOC in response to future source region buoyancy increases (*1*), but these models may be biased toward stability (*7*) and struggle to reproduce the rich spectrum of variability revealed by a decade of observations (*8*, *9*). Testing these physical and conceptual models, and, more generally, the stability of NADW ventilation in warm climates, requires empirical constraints beyond those provided by the current state of ocean circulation.

Given a background climate that is similar to that of today, the modern mode of deep Atlantic ventilation with strong NADW influence (Fig. 1) appears to be stable on long multi-millennial time scales. Proxy reconstructions indicate that modern NADW ventilation pathways persisted with little multi-millennial

[1]Department of Earth Science and Bjerknes Centre for Climate Research, University of Bergen, Bergen, Norway. [2]NORCE Norwegian Research Centre, Bjerknes Centre for Climate Research, Bergen, Norway. [3]Institute of Marine and Coastal Sciences and Department of Earth and Planetary Sciences, Rutgers University, New Brunswick, NJ, USA. [4]Laboratoire des Sciences du Climat et de l'Environnement, LSCE/IPSL, CEA-CNRS-UVSQ, Université Paris-Saclay, Gif-sur-Yvette, France. [5]Earth and Climate Cluster, Department of Earth Sciences, Vrije Universiteit Amsterdam, Amsterdam, Netherlands. [6]Godwin Laboratory for Paleoclimate Research, Department of Earth Sciences, University of Cambridge, Cambridge, UK.
***Corresponding author. Email: eirik.galaasen@uib.no**

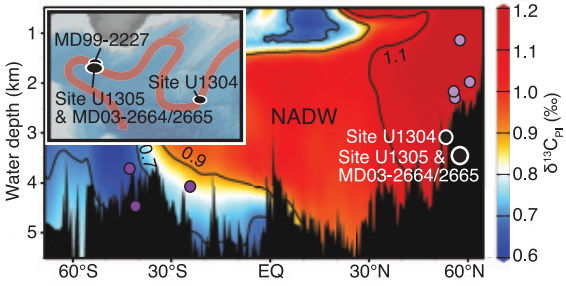

Fig. 1. Core locations. IODP Site U1305 (57°29′N, 48°32′W; 3459 m), MD03-2664 (57°26′N, 48°36′W; 3442 m), MD03-2665 (57°26′N, 48°36′W; 3440 m), and IODP Site U1304 (53°03′N, 33°32′W; 3082 m) projected on a western Atlantic north-south section of preindustrial $\delta^{13}C$ ($\delta^{13}C_{PI}$) (*22*), plotted using Ocean Data View. Core sites depicted in the data composites of Fig. 3C are included (light and dark purple circles). Inset, plotted using GeoMapApp, shows the key subpolar core sites including MD99-2227 (58°21′N, 48°37′W; 3460 m) and the main spreading pathways of Nordic Seas–sourced deep water contributing to lower NADW (red). EQ, equator.

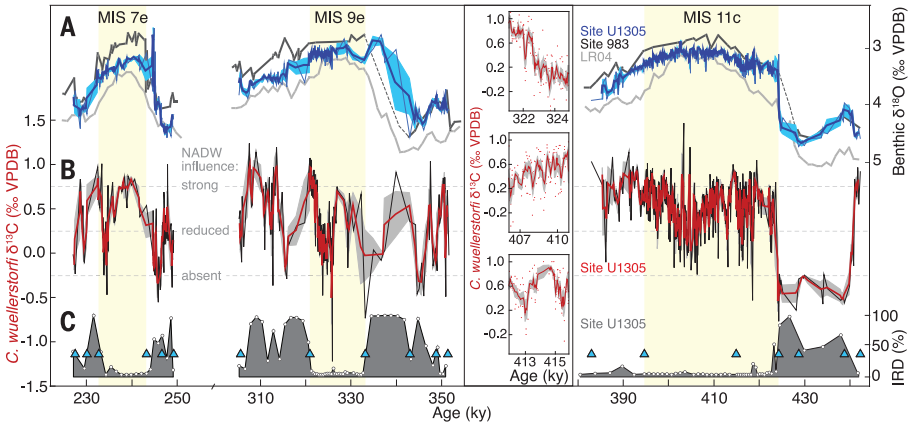

Fig. 2. IODP Site U1305 MIS 7e, 9e, and 11c *C. wuellerstorfi* stable isotope and ice-rafting records. (**A**) Benthic $\delta^{18}O$ from IODP Site U1305 (thin blue line, sample average of replicate measurements; bold dark blue, three-point running mean; shading, the standard error of the three-point window), age model tuning target ODP Site 983 (60°23′N, 23°38′W; 1983 m) (black; dashed lines denote prolonged gaps) (*33*), and LR04 for reference (gray) (*34*). (**B**) Site U1305 *C. wuellerstorfi* $\delta^{13}C$ (black, sample average; red, three-point running mean; shading, standard error of three-point window) with dashed horizontal lines denoting approximate levels of inferred NADW influence. (**C**) Position of age model tie points (triangles) and Site U1305 IRD (percent of >150 μm entities; black and gray) (*19*). All records are on the LR04 time scale (*19*). The sample spacing gives the benthic stable isotope records a nominal time resolution of ~70 years during the interglacial benthic $\delta^{18}O$ plateaus (shaded yellow). Insets show examples of the *C. wuellerstorfi* $\delta^{13}C$ variability [coloring as in (B), individual data as dots]. VPDB, Vienna Pee Dee Belemnite standard.

variability in recent interglacial periods (*10*–*14*). By contrast, pronounced AMOC variability has occurred on time scales of a decade or less in observations (*8*, *9*), which suggests that strong mean overturning is composed of substantial variance. However, little is known about NADW variability on the intermediary time scales, which leaves the variability within a long-term vigorous mean ventilation state poorly defined. There are few proxy reconstructions that depict higher-frequency variability, and those that are available are largely confined to the last two interglacials, the Holocene and Marine Isotope Stage (MIS) 5e. During these periods, the largest changes in deep Atlantic ventilation involving reductions of NADW influence occurred on relatively short centennial time scales and were focused around intervals with wasting of continental ice sheet remnants from the preceding glaciation (*10*, *12*, *15*). This includes the century-long NADW reduction at 8.2 thousand years (ky) before present (B.P.) that followed the freshwater outburst flood from glacial Lake Agassiz (*12*). The absence of similarly large changes in the last ~8 ky of the Holocene (*12*) has supported the notion of vigorous and stable ventilation as generally representative of interglacial boundary conditions.

Beyond the last two interglacials, little is known about centennial-scale variability in NADW, despite its relevance for delimiting the natural variability of ocean ventilation and the frequency of large NADW reductions under different background climates. The most recent interglacials, MIS 5e, 7e, 9e, and 11c, are particularly relevant, as these periods had similar climate boundary conditions to the current MIS 1. These interglacials also encompass intervals of high-latitude warmth, Greenland Ice Sheet (GrIS) retreat, and sea level exceeding the modern (*16*–*18*). These case examples provide an opportunity to test the robustness of NADW ventilation under various source-region conditions, including those similar to future projections (*1*). In this work, we reconstruct northwest Atlantic bottom water $\delta^{13}C$ to trace NADW influence (Fig. 1) over MIS 7e, 9e, and 11c and to provide a detailed perspective on NADW ventilation instability during recent interglacials.

Our epibenthic foraminifera *Cibicidoides wuellerstorfi* (sensu stricto) $\delta^{13}C$ record (*19*) from the International Ocean Drilling Program (IODP) Site U1305 (57°29′N, 48°32′W; 3459 m water depth) at the Eirik Drift is situated to monitor lower NADW entering the deep Atlantic (Fig. 1). Given the potential for uncertainty in $\delta^{13}C$ reconstructions (*20*), we only consider changes in the running mean of three samples [averaging five data points; see (*19*)] and signals outside the standard error of data within this window to reflect bottom water $\delta^{13}C$ variability. With negligible influence from organic carbon fluxes (*21*), this method provides a proxy for past changes in the ventilation and distribution of water masses (*20*, *22*). The Eirik Drift bottom water $\delta^{13}C$ record indicates large changes in deep Atlantic carbon chemistry during the interglacial $\delta^{18}O$ plateaus of MIS 7e, 9e, and 11c (Fig. 2). Each interglacial contained abrupt changes in bottom water $\delta^{13}C$ as large [≤1.0‰ (per mil)] as those of the bordering glacial terminations and inceptions (Fig. 2) and similar to those occurring after freshwater outburst floods, such as the ~8.2 ky B.P. event (*12*) and during MIS 5e (*10*). Absolute values range from near-modern NADW levels (≥0.8‰; Fig. 1) to those typical of the glacial deep Atlantic (*13*, *14*, *23*, *24*). Although similar in magnitude, the frequency, timing, and duration of these changes differ among individual interglacial periods. Low bottom water $\delta^{13}C$ values persist for a millennium or more during late MIS 7e [~233.5 to 243.5 ky; on our age model, (*19*)] and during mid- to late MIS 9e (~323.0 to 326.0 ky), whereas large (~0.5‰) multi-centennial variability punctuated MIS 11c superimposed on multi-millennial trends.

Low bottom water $\delta^{13}C$ values at Site U1305 likely reflect reduced NADW influence and changes in deep Atlantic ventilation patterns. Reduced (high-$\delta^{13}C$) NADW influence and incursions of (low-$\delta^{13}C$) Southern source water (SSW) explain many features of the observed variability, including (i) the spatial consistency of intermittently low $\delta^{13}C$ observed at different deep sites (Site U1304 and U1305; Fig. 3); (ii) the abruptness of the $\delta^{13}C$ changes as the NADW-SSW water mass boundary shifted across the core sites; (iii) the shift of Site U1305 $\delta^{13}C$ toward the millennially averaged values found near the northern or the southern source regions (Fig. 3); and (iv) the association of high

(low) *C. wuellerstorfi* $\delta^{13}C$ with high (low) *C. wuellerstorfi* B/Ca in selected Eirik Drift samples (fig. S6) (*19*).

We further use a transient interglacial (115 to 125 ky) simulation (*19*) with the isotope-enabled intermediate complexity iLOVECLIM Earth system model (*25*) to assess potential links between variability in deep Atlantic $\delta^{13}C$, NADW distribution, and AMOC. Simulated centennial-scale episodes of NADW shoaling and SSW expansion produce $\delta^{13}C$ reductions in the deep Atlantic that strongly match the magnitude, rate, and duration of the variability observed in our (Fig. 4) and other reconstructions (*10*, *12*–*14*), consistent with the inference

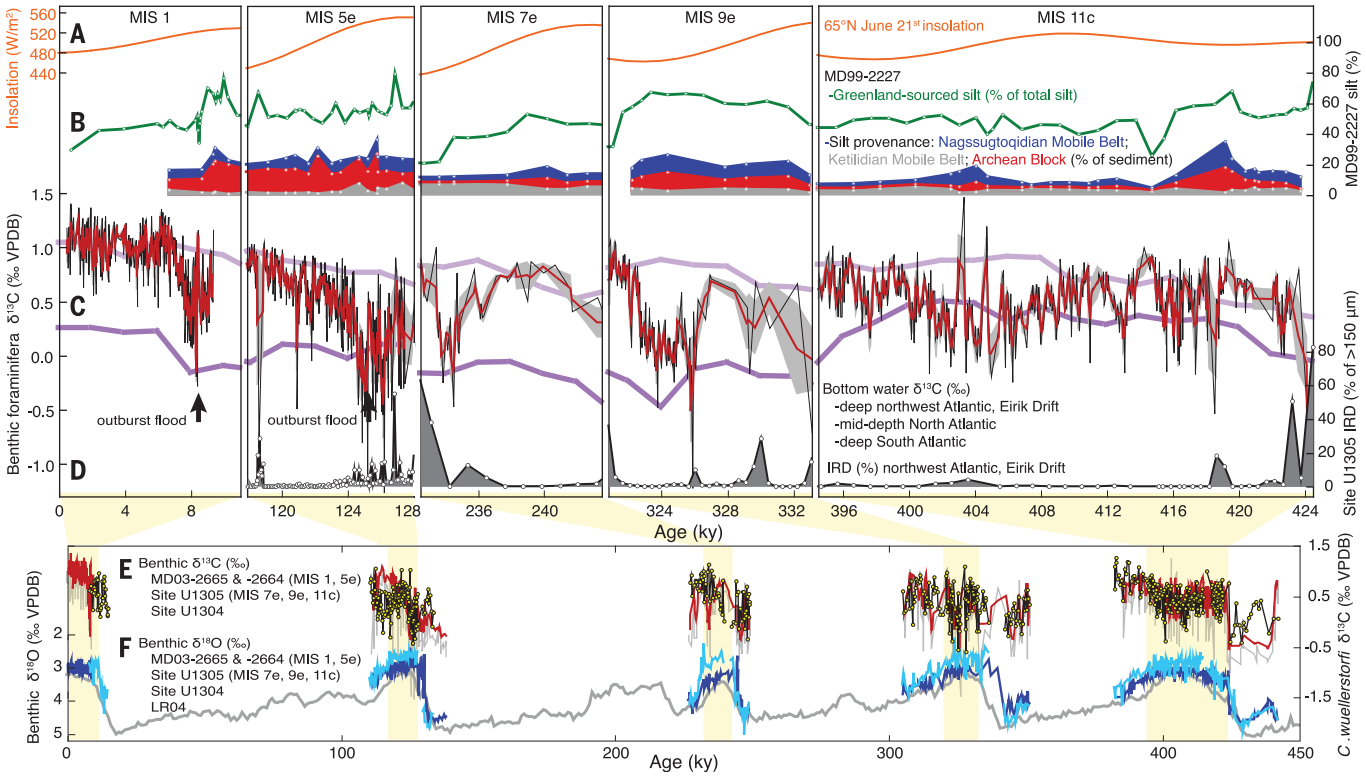

Fig. 3. Variability in NADW ventilation during interglacials MIS 1 to 11c. (**A** to **D**) Focused on the interglacial $\delta^{18}O$ plateaus: (A) 65°N insolation at 21 June (orange) (*35*); (B) core MD99-2227 records of GrIS sediment discharge showing silt sourced from Precambrian Greenland terranes (green, percent of total silt) (*32*) and from different Greenland provenances (percent of sediment: colored, see text inset) (*18*, *32*, *36*); (C) bottom water $\delta^{13}C$ reconstructions from mid-depth North (light purple) (*23*) and deep South Atlantic composites (dark purple) (*37*) (see Fig. 1 for locations) and from the deep Eirik Drift [MIS 1: (*12*); MIS 5e: (*10*); MIS 7e, 9e, and 11c: this study] (coloring as in Fig. 2) with arrows denoting freshwater outburst floods as determined in (*10*, *12*); and (D) Eirik Drift IRD records [MIS 5e: (*10*); MIS 7e, 9e, and 11c: (*19*)]. (**E** and **F**) Glacial-interglacial records of (E) *C. wuellerstorfi* $\delta^{13}C$ from the Eirik Drift [as in (C); gray line, sample average; red line, three-point mean] and IODP Site U1304 (black and yellow, sample average) (*15*, *38*) (resolution, U1305: ~70 years; U1304: ~300 years); (F) Benthic foraminifera $\delta^{18}O$ from the Eirik Drift and Site U1304 (colored, see inset; references as for $\delta^{13}C$) and LR04 (gray) (*34*). All records are plotted on the LR04 time scale (*19*).

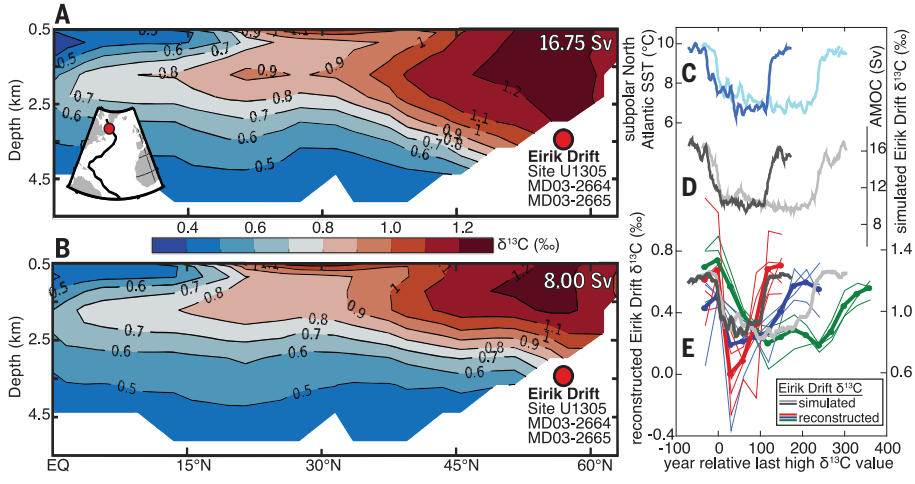

Fig. 4. Modeled and reconstructed deep Atlantic $\delta^{13}C$ changes. (**A** and **B**) The iLOVECLIM simulated $\delta^{13}C$ distribution and Eirik Drift core location (red circle) along a north-south transect (inset) averaged for years with (A) strong, modern-like AMOC (>2σ; 16.75 ± 0.70 sverdrup mean; *n* = 460 model years) and NADW distribution; and (B) weaker AMOC (<2σ; 8.00 ± 0.42 sverdrup mean; *n* = 63 model years) and shoaled NADW [see (*19*) for details]. Sv, sverdrup. (**C** to **E**) Across two simulated NADW shoaling events (10-year mean values): (C) subpolar North Atlantic mean sea surface temperature (SST; light and dark blue); (D) AMOC stream function at 27°N (light and dark gray); and (E) Eirik Drift bottom water $\delta^{13}C$ changes [light and dark gray; magnitude similar for different preformed $\delta^{13}C$ values, see (*19*)] compared to the reconstructions by aligning at the last high $\delta^{13}C$ values. To illustrate common features that account for interglacial differences in preformed $\delta^{13}C$ values, the reconstructed events are shown as the average (bold lines) of multiple events (thin lines) at 30-year steps (obtained by linear interpolation), binned according to durations of ≤100 (red; *n* = 5), 101 to 200 (blue; *n* = 4), and 201 to 300 years (green; *n* = 3).

that the $\delta^{13}C$ variability reflects changes in NADW distribution. These large deep Atlantic $\delta^{13}C$ changes, which are similar in magnitude to glacial millennial-scale changes (*23*, *24*), were achieved without a total collapse of but with a marked (~16 to ~8 sverdrup) decrease in AMOC strength, and they were accompanied by cooling in the subpolar North Atlantic (Fig. 4).

Our results call for a reconsideration of the long-held notion of warm-climate stability in deep Atlantic carbon chemistry and ventilation. This view of stability likely remains true for the (multi-)millennial mean state, as previously depicted by lower-resolution records that lack the fidelity to resolve the shorter time scale characteristic of interglacial NADW reductions (Fig. 3). High-resolution records are naturally biased toward the youngest strata and the current interglacial, the Holocene. Yet, when contextualized against the late Pleistocene interglacials, the Holocene stands out as having had the most stable lower NADW ventilation of the last 0.5 million years (Fig. 3), which was only strongly curtailed at ~8.2 ky B.P. (*12*). Bottom water $\delta^{13}C$ and NADW reductions similar to those at ~8.2 ky B.P. were prevalent features of prior interglacials, and these features even occasionally lasted for millennia (Fig. 3). Ventilation patterns changed repeatedly from one similar to the modern pattern (Fig. 1) to one with reduced NADW and incursions of SSW in the deep North Atlantic (~3.4 km), which is similar to the change illustrated by our model simulation (Fig. 4).

The short duration of interglacial NADW reductions might indicate a change in the intrinsic ocean dynamics operating under different background climate states. The interglacial deep Atlantic is clearly better ventilated than the glacial on long equilibrium time scales (*11*, *13*, *14*, *23*, *24*). However, the magnitude of ventilation pattern changes that are possible appears to be similar in (de)glacial (*11*, *24*, *26*) and interglacial periods when variability in lower NADW is considered at shorter time scales (Fig. 3). The centennial-scale duration and transient nature of most interglacial NADW reductions (Fig. 3 and Fig. 4) suggest that the modern ventilation pattern tends to recover quickly when perturbed and is similar to the AMOC recovery time scale seen in many numerical models forced with buoyancy increases (*4*). With this in mind, the longer-lasting NADW reductions in MIS 7e (~233.5 to 234.5 ky), 9e (~323 to 326 ky), and late 11c (~401 to 408 ky) either required more sustained forcing or suggest that the recovery time scale following perturbations is not fixed. Most interglacial NADW reductions were still short-lived compared with those associated with glacial (Dansgaard-Oeschger) variability (*24*), which suggests that either NADW ventilation behaved differently or the persistence of any forcing changed, depending on the climate state. One possible explanation for this time scale difference is the extensive glacial expansion of high-latitude sea ice, which could promote a baseline increase in SSW ventilation (*27*) and prolong the duration of northern ventilation anomalies (*28*). A lack of strong sea ice responses could also explain the potentially muted climate variability in interglacial compared with glacial climates (*10*, *13*, *14*, *29*), despite the presence of NADW variability. However, more high-resolution climate records spanning past interglacials are needed to conclusively evaluate the impacts of warm-climate NADW reductions and delineate its role relative to feedbacks, such as sea ice responses, in driving interglacial climate variability.

Model simulations suggest that future warming and freshwater addition from an intensified hydrological cycle and ice sheet melting could increase source region buoyancy and curtail convective NADW renewal (*1*, *4*). The common occurrence of NADW reductions in past interglacials (Fig. 3) clearly demonstrates the potential for large changes in deep Atlantic ventilation and allows us to explore the triggers for perturbations. NADW reductions during the last two interglacial periods were mainly confined to the early warm interglacial phases, concurrent with high northern hemisphere summer insolation and known freshwater outburst floods that accompanied the final retreat of residual glacial ice sheets (Fig. 3) (*10*, *12*, *30*, *31*). Although stratigraphically belonging to interglacial periods—to the extent that they are related to wasting vestiges of glaciation—these anomalies are likely best viewed, mechanistically, as the final episodes of deglaciation. By contrast, NADW reductions in MIS 7e, 9e, and 11c occurred in the mid- and late interglacial phases under low summer insolation (Fig. 3) and after any likely deglacial freshwater influences. This implies that NADW reductions can occur without the excess buoyancy input provided by wasting residual glacial ice sheets or the influence of large continental ice sheets on atmospheric circulation. However, interglacial ice sheet activity might still have played a role in regulating the stability of NADW ventilation during some intervals. NADW reductions in MIS 7e, 9e, and 11c often coincided with, or were preceded by, the input of ice-rafted debris (IRD) at Site U1305 (Fig. 3), which indicates a supply of icebergs and fresh water proximal to the NADW source region. Furthermore, the prolonged NADW reduction of MIS 9e was associated with elevated southern GrIS sediment discharge and MIS 1 stability was associated with low GrIS activity (*32*), whereas particularly strong GrIS retreat in MIS 11c (*16*, *18*) occurred alongside persistent NADW variability (Fig. 3). These observations are consistent with ice sheet activity and freshwater addition intermittently influencing the formation or downstream density of lower NADW. However, variability in NADW ventilation, IRD input, and GrIS discharge also occurred independently of each other (Fig. 3), which implicates additional controls on NADW ventilation and supports models that suggest that convective instability is possible with relatively small buoyancy input if delivered to the convection regions (*6*).

Our results suggest that we should consider rapid and large changes in NADW ventilation not only as a possibility (*10*, *12*, *30*) but even as an intrinsic feature of centennial-scale variability in warm climate states. This has implications for constraining the potential for and cause of changes in the modern Atlantic. First, it supports the concerns that disregarding large variability in simulations may have biased future AMOC projections toward stability (*7*). The possibility of large, natural variability on decadal (*8*, *9*) to centennial time scales (Fig. 3) also complicates the attribution of variability in the deep Atlantic, but the characteristics of this variability may be used to differentiate between natural and anthropogenic changes in the coming century. Although past changes were predominantly multi-centennial, there are also climate and ocean conditions that can drive longer NADW reductions, as evidenced, for example, by the ~3000-years-long anomaly in mid-MIS 9e (Fig. 3). Specifically what these conditions were remains unclear, but the triggers for NADW instability have clearly operated across the range of recent interglacial climate conditions. Recognizing this requires moving beyond the notion of vigorous and stable deep Atlantic ventilation as representative of warm climate states (*1*, *5*, *11*) and toward conceptual and numerical models that can account for pronounced variability across various time scales and climate states.

REFERENCES AND NOTES

1. T. F. Stocker *et al*., Eds., *Climate Change 2013: The Physical Science Basis: Working Group I Contribution to the Fifth Assessment Report of the Intergovernmental Panel on Climate Change* (Cambridge Univ. Press, 2013).
2. M. W. Buckley, J. Marshall, *Rev. Geophys.* **54**, 5–63 (2016).
3. C. L. Sabine *et al*., *Science* **305**, 367–371 (2004).
4. T. F. Stocker, A. Schmittner, *Nature* **388**, 862–865 (1997).
5. H. Stommel, *Tellus* **13**, 224–230 (1961).
6. T. F. Stocker, D. G. Wright, *Nature* **351**, 729–732 (1991).
7. M. Hofmann, S. Rahmstorf, *Proc. Natl. Acad. Sci. U.S.A.* **106**, 20584–20589 (2009).
8. M. A. Srokosz, H. L. Bryden, *Science* **348**, 1255575 (2015).
9. M. S. Lozier *et al*., *Science* **363**, 516–521 (2019).
10. E. V. Galaasen *et al*., *Science* **343**, 1129–1132 (2014).
11. J. F. Adkins, E. A. Boyle, L. Keigwin, E. Cortijo, *Nature* **390**, 154–156 (1997).
12. H. K. F. Kleiven *et al*., *Science* **319**, 60–64 (2008).
13. J. F. McManus, D. W. Oppo, J. L. Cullen, *Science* **283**, 971–975 (1999).
14. D. W. Oppo, J. F. McManus, J. L. Cullen, *Science* **279**, 1335–1338 (1998).
15. D. A. Hodell *et al*., *Earth Planet. Sci. Lett.* **288**, 10–19 (2009).
16. A. de Vernal, C. Hillaire-Marcel, *Science* **320**, 1622–1625 (2008).
17. Past Interglacials Working Group of PAGES, *Rev. Geophys.* **54**, 162–219 (2016).
18. A. V. Reyes *et al*., *Nature* **510**, 525–528 (2014).

19. See the supplementary materials.
20. A. Schmittner *et al*., *Paleoceanography* **32**, 512–530 (2017).
21. B. Corliss, X. Sun, C. Brown, W. Showers, *Deep Sea Res. Part I Oceanogr. Res. Pap.* **53**, 740–746 (2006).
22. M. Eide, A. Olsen, U. S. Ninnemann, T. Johannessen, *Global Biogeochem. Cycles* **31**, 515–534 (2017).
23. L. E. Lisiecki, M. E. Raymo, W. B. Curry, *Nature* **456**, 85–88 (2008).
24. L. G. Henry *et al*., *Science* **353**, 470–474 (2016).
25. N. Bouttes, D. M. Roche, V. Mariotti, L. Bopp, *Geosci. Model Dev.* **8**, 1563–1576 (2015).
26. J. F. McManus, R. Francois, J. M. Gherardi, L. D. Keigwin, S. Brown-Leger, *Nature* **428**, 834–837 (2004).
27. R. Ferrari *et al*., *Proc. Natl. Acad. Sci. U.S.A.* **111**, 8753–8758 (2014).
28. G. Vettoretti, W. R. Peltier, *J. Clim.* **31**, 3423–3449 (2018).
29. B. Martrat *et al*., *Science* **317**, 502–507 (2007).
30. C. R. W. Ellison, M. R. Chapman, I. R. Hall, *Science* **312**, 1929–1932 (2006).
31. J. A. L. Nicholl *et al*., *Nat. Geosci.* **5**, 901–904 (2012).
32. R. G. Hatfield *et al*., *Earth Planet. Sci. Lett.* **454**, 225–236 (2016).
33. M. E. Raymo *et al*., *Paleoceanography* **19**, PA2008 (2004).
34. L. E. Lisiecki, M. E. Raymo, *Paleoceanography* **20**, PA1003 (2005).
35. J. Laskar *et al*., *Astron. Astrophys.* **428**, 261–285 (2004).
36. E. J. Colville *et al*., *Science* **333**, 620–623 (2011).
37. L. E. Lisiecki, *Clim. Past* **6**, 305–314 (2010).
38. C. Xuan, J. E. T. Channell, D. A. Hodell, *Quat. Sci. Rev.* **142**, 74–89 (2016).

ACKNOWLEDGMENTS

We thank the scientific party and crew of R/V *JOIDES Resolution* IODP Expedition 303, the curatorial staff at the IODP Bremen core repository for core sampling assistance, and D. Richmond for assistance with processing MIS 9e samples. **Funding:** This work was funded by grants from the Research Council of Norway (RCN) through the project THRESHOLDS (RCN grant 254964) and data generation at FARLAB (RCN grant 245907). **Author contributions:** U.S.N. and E.V.G. designed the project, and all coauthors helped conceptualize the study; E.V.G. processed the sediment samples and conducted the benthic and planktic foraminifera stable isotope analyses; N.I. conducted the IRD analyses; A.K., J.T., N.B., and D.M.R. designed and performed the iLOVECLIM simulation; Y.R. performed the B/Ca analyses; and E.V.G. led the writing effort and coordinated input from all coauthors. **Competing interests:** None declared. **Data and materials availability:** The data are available in the supplementary materials.

SUPPLEMENTARY MATERIALS

science.sciencemag.org/content/367/6485/1485/suppl/DC1
Materials and Methods
Supplementary Text
Figs. S1 to S7
References (*39*–*57*)
Data S1

5 July 2019; accepted 11 February 2020
10.1126/science.aay6381

Robert Bosch Stiftung

Are you conducting research that is both environmentally and socially relevant?

Are you an excellent researcher with forward-thinking ideas and an inter- or transdisciplinary research approach?

If yes, we would like to invite you to apply for the

Robert Bosch Junior Professorship

Research into the Sustainable Use of Natural Resources

together with a German university or research institution of your choice. Applicants of all nationalities are welcome.

Areas addressed

We are looking for an outstanding young scientist who wants to find new approaches to clarify and tackle global challenges with regard to the sustainable use of natural resources. The research should focus on developing and emerging countries. We are especially interested in applications that also consider human behaviour in this context. Research approaches may be based in the humanities, the social or the natural sciences.

Scope

The successful applicant will be awarded a grant worth up to 1 million euros for a five-year period, in order to set up a research group in a German research institution or university. The funds can be allocated flexibly towards covering salaries and research costs.

Candidate profile

- excellent doctorate degree, completed no more than 5 years prior to the application closing date of 3 May 2020 (adjusted for documented parental leave)
- compelling independent past scientific achievements and publications in peer-reviewed journals
- international research experience
- excellent proficiency in English
- non-German applicants should be prepared to learn German.

The application closing date is **3 May 2020**.

For further information and to apply please visit:
www.bosch-stiftung.de/juniorprofessorship

10 ways that *Science* Careers can help advance your career

1. Register for a free online account on **ScienceCareers.org**.
2. Search thousands of job postings and find your perfect job.
3. Sign up to receive e-mail alerts about job postings that match your criteria.
4. Upload your resume into our database and connect with employers.
5. Watch one of our many webinars on different career topics such as job searching, networking, and more.
6. Download our career booklets, including Career Basics, Careers Beyond the Bench, and Developing Your Skills.
7. Complete an interactive, personalized career plan at "my IDP."
8. Visit our Employer Profiles to learn more about prospective employers.
9. Research graduate program information and find a program right for you.
10. Read relevant career advice articles from our library of thousands.

Visit **ScienceCareers.org** today — all resources are free

SCIENCECAREERS.ORG

ScienceCareers
FROM THE JOURNAL SCIENCE AAAS

By **Michael Palladino**

Stepping up to leadership

Four years after I received tenure, the dean of science at my primarily undergraduate institution called to tell me he planned to retire. "I'm recommending you as my replacement," he said. I didn't think much of it until a few months later, when the provost and president asked to speak with me. They said they thought I was a strong candidate for dean and asked whether I was interested. I was flattered. But I wondered, "Why me? Why now?" I was a relatively young faculty member, and I would have to oversee academics in disciplines well outside my own. I wasn't sure I was qualified—or whether I wanted such a drastic change in my professional life.

I loved my job. I could not wait to come to campus every day. I enjoyed the classes I was teaching. And I was midway through a federal research grant, with a lab full of talented and enthusiastic undergraduate research students. We were publishing in good journals and presenting at conferences.

But I took the inquiry seriously and spoke with colleagues to get their perspective. They convinced me that perhaps others saw something in me that I did not see in myself. I had served in leadership positions within a few national organizations, such as the Council on Undergraduate Research, and they thought that my leadership skills would be valuable within our own institution. My colleagues also encouraged me to think about the opportunity I'd have to advance issues that were important to me and other scientists.

"The dean position [gave] me a chance to have a wider impact."

In the end, I decided I couldn't pass it up. I became a scientist because I wanted to have an impact, to make a difference. If I stayed in my current position, I might earn a few more grants, publish more papers, and teach a larger number of students. But the dean position would give me a chance to have a wider impact.

Teaching and research were still important to me, so I negotiated an arrangement that would allow me to continue teaching at least one course each year and maintain a scaled-back research agenda. To make this possible, the university hired a full-time associate dean, who lessened some of my administrative workload.

When I started, I made it a priority to learn how individual departments worked and what they saw as their top needs. I didn't go in thinking I had all of the answers. Instead, I surrounded myself with smart people, and I listened to what they had to say. That approach was especially helpful when dealing with academic departments I was less familiar with.

Gradually, I started to see how the university operated beyond my home department—biology—and to see where it could grow. I worked to hire more faculty members and fund a $48 million project to expand and renovate the science building. I also secured external funding for a summer research program that gave undergraduate students a taste of what it's like to work in a lab. The work felt rewarding because I enjoyed supporting faculty and watching our students learn and grow.

The transition hasn't always been easy, however. Juggling the increased demands on my time has been especially challenging. I feel as though I'm constantly switching between different hats—my teaching hat, my research hat, my administrator hat—and it can be dizzying. I've had to make some difficult—and not universally popular—decisions, including to merge the computer science and software engineering departments. And I've noticed a shift in my relationships with colleagues: Some have kept me at a greater distance than before, whereas others have sought me out because they want to ask me for something.

Overall, though, my career transition has been positive—so much so that I moved into a vice provost position 7 years after accepting the deanship. I'd strongly encourage other academics to be open to unexpected opportunities in administration, even ones that you may not think you're ready for. With the changing climate of higher education, institutions desperately need thoughtful, strategic leaders with the communication and organizational skills to lead and inspire their fellow academics. ■

Michael Palladino is a former vice provost for graduate studies at Monmouth University in New Jersey. In May, he'll be vice president for academic affairs and dean of the faculty at Bloomfield College.

ILLUSTRATION: ROBERT NEUBECKER

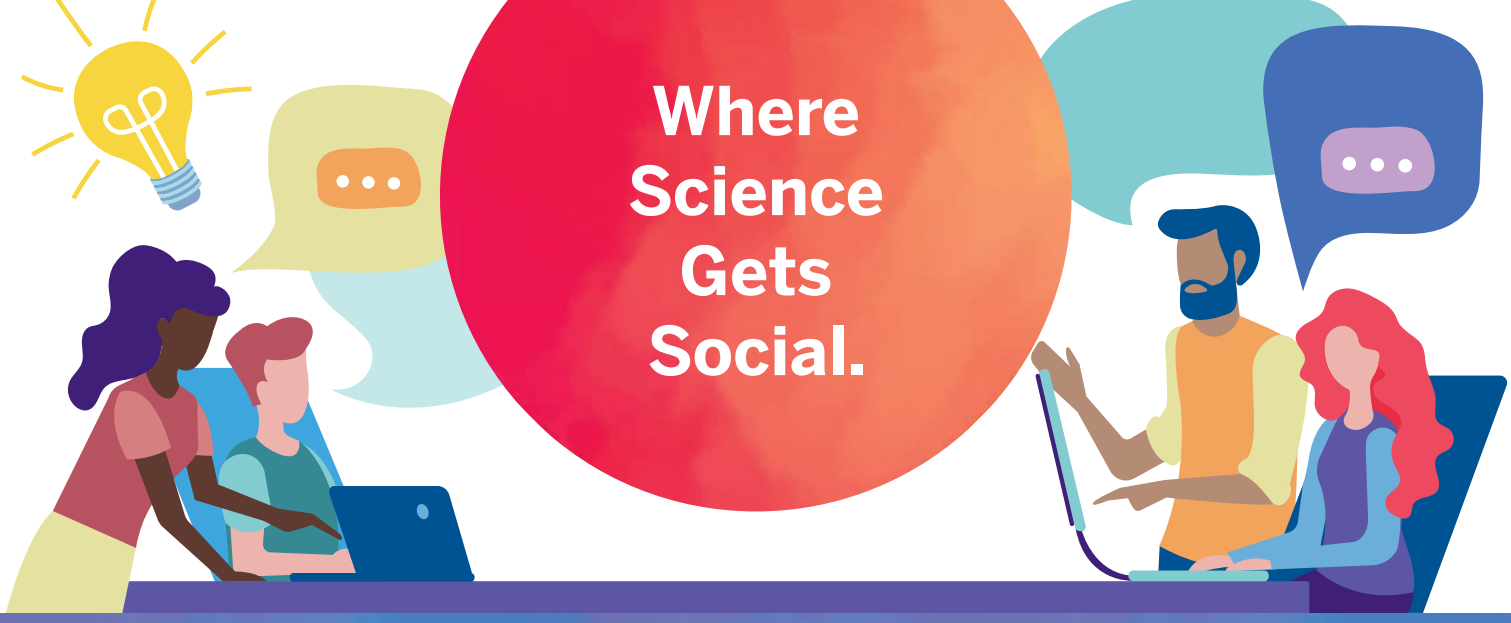

AAAS.ORG/COMMUNITY

AAAS' Member Community is a one-stop destination for scientists and STEM enthusiasts alike. It's "Where Science Gets Social": a community where facts matter, ideas are big and there's always a reason to come hang out, share, discuss and explore.

Member COMMUNITY
AAAS

AMERICAN ASSOCIATION FOR THE ADVANCEMENT OF SCIENCE

Bispecific Antibody Generation

Custom Antibody Engineering Services

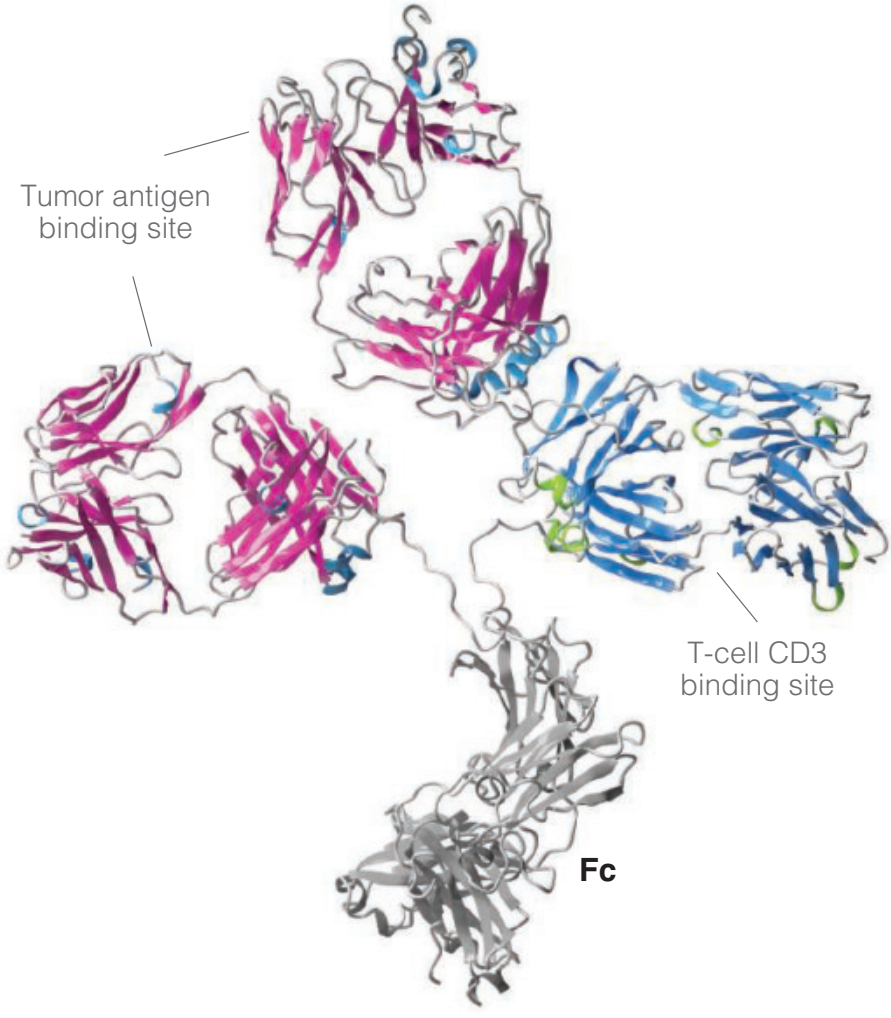

With nearly 20 years of experience, ProMab can help streamline your antibody project from start to finish

Custom Antibody Solutions

- Hybridoma Sequencing
- Antibody Humanization
- Antibody Producing Stable Cell Line
- Rabbit Monoclonal Antibody
- Human Monoclonal Antibody
- Mouse / Rat Monoclonal Antibody

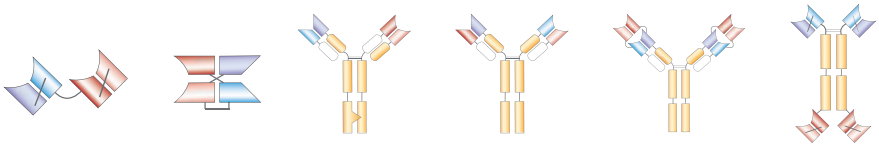

Discover more | www.promab.com

ProMab Biotechnologies, Inc.
2600 Hilltop Dr, Building B, Suite C320, Richmond, CA 94806
1.866.339.0871 | info@promab.com